



Dispersion of Grain Refiner Particles in Molten Aluminium

by Einar Jon Asbjornsson, M.Sc.

Thesis submitted to the University of Nottingham
for the degree of Doctor of Philosophy, July 2001.

Abstract

Nine types of Al-Ti, Al-Ti-C and Al-Ti-B master alloy rods have been investigated by metallography and also by LiMCA measurements after the dissolution of the alloys in an aluminium melt. The results show the presence of TiC and TiB_2 particle clusters in the Al-Ti-C and Al-Ti-B alloys, respectively. The size of the clusters as measured by LiMCA was in the range of 20-100 μ m. The percentage of the total TiB_2 and TiC additions to the melt that was found in the clusters was up to 2.8%. EDX analysis of the TiC particle clusters showed the presence of oxygen, presumably in the form of aluminium oxide, and the TiB_2 clusters also contained oxygen, fluorine and potassium.

Al-5Ti-1B master alloys from different manufacturers contain different quantities of impurities containing oxide and fluoride salts. Furthermore, the distribution of phases varies, especially with respect to texturing of the TiB_2 particles, and the impurities show a varying degree of association with the TiB_2 texture lines. The Al-Ti-C master alloys also showed texturing but the main difference was observed in their oxide content. The quantity of clusters as determined by LiMCA can be related to the microstructure of the master alloys, further supporting the conclusion that oxide plays an important role in cluster formation in the Al-Ti-C rods and the impurities containing oxide and fluoride salts in the Al-Ti-B rods. The LiMCA tests also confirm that further agglomeration of the clusters and particles occurs in the aluminium melt both for Al-Ti-C and Al-Ti-B master alloys.

The flow conditions and particle distribution in an aluminium melt in launders was modelled using CFD for two launder designs. In the first design the effect of vortex formation in the dead-zone at a corner of the launder was demonstrated. Particle dispersion from a point source simulating the dissolution of a master alloy rod was modelled for the second launder. An effective distribution was achieved within 1000 mm from the source of particle introduction, this distance being less than that required for the dissolution of the soluble $TiAl_3$ particles from the master alloys. LiMCA measurements in the first launder and chemical analysis of samples taken from the flowing melt support the flow and particle distribution modelling.

Acknowledgements

The work presented in this thesis constitutes a part of a scheme for co-operative research between the School of Mechanical, Materials, Manufacturing Engineering and Management at the University of Nottingham and the Science Institute of the University of Iceland. The work was carried out under the joint supervision of Professor D.G. McCartney at the University of Nottingham and Professor T.I. Sigfusson at the University of Iceland. The scheme was supported by Alusuisse - Lonza Technical Centre in Chippis, Switzerland, and the London & Scandinavian Metallurgical Company Ltd. in Rotherham, England.

The present part of the scheme was started in July 1996 and ended in October 1999. The work was carried out at the School of Mechanical, Materials, Manufacturing Engineering and Management at the University of Nottingham. The experimental work was conducted at Alusuisse - Lonza experimental cast house in Chippis and at the metallurgical laboratory of the London & Scandinavian Metallurgical Company Ltd. in Rotherham. Finally, some of the metallurgical analysis and computational analysis were carried out at the Science Institute of the University of Iceland.

I would like to express my gratitude to the following for invaluable assistance during the course of this project:

Professors D. G. McCartney and T. I. Sigfusson for their interest, advice and encouragement during this investigation.

Alusuisse - Lonza Technical Centre and London & Scandinavian Metallurgical Company Ltd. for their support and provision of facilities.

Dr. P. Pouli and Dr. T. Gudmundsson at Alusuisse - Lonza and Dr. M. Kearns and Mr. D. Bristow, London & Scandinavian Metallurgical Company Ltd. for their advice and discussions. The invaluable help of my predecessor in this joint research scheme, Dr. T. Gudmundsson at Alusuisse - Lonza, during the experimental work at Chippis must be especially acknowledged.

Mr. M. Mayor and Mr. M. Rywalski, laboratory technicians at Alusuisse - Lonza, for their assistance in the experimental work.

Icelandic Aluminium Ltd. for assistance and advice on practical problems in aluminium cast houses.

The Technological Institute of Iceland, especially Mr. I. O. Thorbjornsson, for the provision of facilities during the writing-up period.

Finally, I would like to thank my son, Asbjorn, and all my family for their patience during these years.

Contents

1	Introduction	1
2	Literature review	4
2.1	Manufacture of aluminium products	4
2.2	Molten metal processing	5
2.2.1	Impurities in molten aluminium	6
2.2.2	Removal by settling	7
2.2.3	Removal by gas fluxing	8
2.2.4	Removal by filtering	9
2.2.5	Grain refining	9
2.3	Structure of grain refining master alloys	11
2.3.1	Al-Ti master alloys	11
2.3.2	Al-Ti-B master alloys	12
2.3.3	Al-Ti-C master alloys	13
2.4	Measurement of inclusions in molten aluminium	14
2.4.1	The PoDFA method	14
2.4.2	The PoDFA procedure	14
2.4.3	Detectable inclusions and size range	15
2.4.4	Sample analysis	15
2.4.5	Polishing of PoDFA samples	18
2.4.6	Experimental use	18
2.4.7	The LiMCA method	19
2.4.8	Theory	19
2.4.9	The LiMCA results	20
2.4.10	Experimental use	22
2.4.11	Comparison of PoDFA and LiMCA	23
2.5	Experimental studies of inclusions in molten aluminium	23
2.6	Fluid dynamics modelling of flow launders	24
2.6.1	Modelling of flow conditions	25
2.7	Summary	26
2.8	Figures	29
3	Microstructure of grain refining master alloys	42
3.1	Experimental methods	43
3.1.1	Scanning electron microscopy	43
3.2	The Al-6Ti master alloy	44

3.3	The Al-5Ti-1B master alloy	44
3.4	The Al-3Ti-0.2B master alloy	47
3.5	The Al-3Ti-0.15C master alloys	47
3.6	The Al-6Ti-0.03C master alloy	49
3.7	Discussion	49
3.8	Figures	52
4	LiMCA measurements of the dissolution of master alloys	76
4.1	Experimental setup	77
4.1.1	Experimental procedure	77
4.1.2	Chemical analysis	77
4.1.3	Metallographic samples	78
4.1.4	Master alloys	79
4.2	The Al-6Ti master alloy	79
4.2.1	Experimental results	79
4.2.2	Discussion of the Al-6Ti master alloy	81
4.3	The Al-6Ti-0.03C master alloy	82
4.3.1	Experimental results	82
4.3.2	Discussion of the Al-6Ti-0.03C master alloy	84
4.4	The Al-3Ti-0.15C master alloy	85
4.4.1	Experimental results	85
4.4.2	Discussion of the Al-3Ti-0.15C master alloy	87
4.5	The Al-5Ti-1B master alloy	89
4.5.1	Experimental results	90
4.5.2	Discussion of the Al-5Ti-1B master alloys	93
4.6	The Al-3Ti-0.2B master alloy	99
4.6.1	Experimental results	99
4.6.2	Discussion of the Al-3Ti-0.2B master alloys	100
4.7	Further analysis of LiMCA results	100
4.8	Summary	101
4.9	Figures	104
5	Computational fluid dynamics modelling of launder systems	130
5.1	Flow modelling of the first launder	130
5.1.1	Numerical model	131
5.1.2	Model parameters	132
5.1.3	Boundary conditions	132
5.1.4	Mesh structure	133
5.2	Results and discussion for the first launder	133
5.3	Flow modelling of the second launder	134
5.3.1	Model parameters, boundaries and mesh structure	134
5.4	Results and discussion for the second launder	135
5.5	Particle tracking	136
5.5.1	Equations for position	136
5.5.2	Momentum equation for particle transport	136
5.5.3	Turbulent dispersion	137

5.6	Results and discussion of particle tracking	138
5.7	Effect of the grain refining rod	140
5.8	Further discussion	141
5.9	Tables and figures	143
6	Investigation of dissolution of master alloys in launders	163
6.1	Casting parameters	163
6.2	Sampling of flowing melts	164
6.3	Chemical analysis	165
6.4	LiMCA measurements	167
6.5	Discussion	168
6.6	Figures	173
7	Conclusions	181
8	Future work	184
	Bibliography	186
A	Supplement to Chapter 4	191
B	Supplement to Chapter 6	196
	Nomenclature	199
	Publications and lectures	201
	List of Tables	202
	List of Figures	204

Chapter 1

Introduction

Grain refining master alloys are widely used to modify the grain structure of aluminium castings produced in the direct chill casting process. The aluminium billets used for rolling ultra thin sheets (down to $6\mu\text{m}$ thickness) are an example of products that need to have a fine grain size in order to achieve the required mechanical properties.

The beneficial effect of grain refiners has been known for a long time, but in recent years problems have been encountered which are partly associated with the grain refiner addition. These are tearing of the ultra thin aluminium sheets during rolling and the appearance of grey-lines in rolled products. Both these phenomena were at first associated with impurities or inclusions resulting from the aluminium production process but in recent years the possible effect of particles from the grain refiner has received more attention.

In direct chill casting units, the molten aluminium is transferred from the holding furnace to the casting machine in a transfer launder. The grain refiner, in the form of a rod, is fed continuously into the stream of molten aluminium in the launder. The rod melts and releases grain refining particles into the melt.

There are three main classes of master alloys, Al-Ti alloys, Al-Ti-B alloys and Al-Ti-C alloys. All three contain small soluble $TiAl_3$ particles and the latter two also contain small, practically insoluble, TiB_2 and TiC particles, respectively, embedded in an aluminium matrix. It is especially the hard and insoluble TiB_2 and TiC particles which can possibly cause problems in the final rolled aluminium products.

In 1993, a scheme of co-operative research was started by the School of Mechanical, Materials, Manufacturing Engineering and Management at the University of Nottingham and the Science Institute of the University of Iceland. The purpose was to investigate the behavior of grain refiners in aluminium castings. The project was supported by Alusuisse - Lonza Technical Centre in Chippis, Switzerland, and the London & Scandinavian Metallurgical Company Ltd. in Rotherham, England. The former is an aluminium producer and large packaging company and the latter is a leading producer of grain refining materials.

The companies also took an active part in scheme by providing facilities for experimental work at the Alusuisse - Lonza experimental cast house in Chippis and at the metallurgical laboratory of the London & Scandinavian Metallurgical Company Ltd. in Rotherham. Their experts have also taken an active part in meetings and discussions on the progress of the work.

The first part of the scheme was a study of the agglomeration of TiB_2 particles in liquid aluminium. The results showed that the TiB_2 particles can agglomerate with the help of fluoride salts in the master alloy rods. Therefore, the agglomerates can possibly produce a more deleterious effect in the final aluminium products than single TiB_2 particles. This part of the project was completed in 1996.

The second part of the scheme was started in 1996 and constitutes the present work. The main object of this study was to answer the following questions:

- Is there a difference in the distribution of TiB_2 and TiC particles in master alloys from different producers?
- Do the insoluble TiB_2 or TiC particles agglomerate in molten aluminium after the dissolution of the grain refiner?
- Is there a difference in the agglomeration behaviour between master alloys of the same type from different producers?
- Do the flow conditions in the melt have an effect on the agglomeration behaviour?
- Can the flow conditions and particle distribution in transfer launders be visualized using computational fluid dynamics modelling in order to optimize the location of the grain refiner addition?

The experimental work and computational analysis employed to fulfill the aims of the project can be divided into the following four categories:

The microstructure of master alloys.

The microstructure of nine types of master alloys from different producers has been investigated using optical microscopy and scanning electron microscopy. Chemical analysis of the alloys has also been done. The main purpose of this work is to compare the particle size and distribution of the phases given by the nominal composition. In addition, the aim is to clarify if the quantity and distribution of additional impurity phases, e.g. salts and oxides, are different between products from different manufacturers.

LiMCA measurements of particle distribution in aluminium melts.

The LiMCA device is particle detection instrument which can measure the number and size of particles in aluminium melts down to a size of $20\mu\text{m}$. This instrument was employed to study the change in particle concentration when

different types of master alloys were dissolved in a stirred aluminium melt in a crucible. The effect of time on the particle distribution was also investigated to look for evidence of agglomeration of the master alloy particles in the melt. The effect of flow conditions were also investigated. In all, nine types of master alloys were tested. The study included chemical analysis of the master alloys and melts. Metallurgical tests were also employed.

Computational fluid dynamics modelling of launders systems.

Computational fluid dynamics techniques were employed for the modelling of flow conditions of molten aluminium in two launders with different geometries. Subsequently, the distribution and flow of particles in the melt in the launders were analysed. The modelling was performed in a commercial software package, CFX version 4.1.

Measurements of dissolution of master alloys in launders.

The experiments included chemical analysis of samples taken near addition points of the grain refiner rod and LiMCA measurements of the particle distribution in a launder. The results are compared with the results of the computational fluid dynamics analysis of flow conditions and particle distribution in the launder.

In this thesis, the literature relevant to the work presented is reviewed and discussed in Chapter 2. As this work concerns a subject of industrial importance, the results of some previous studies are proprietary and not available in the open literature. The experimental work and computational analysis are presented in Chapter 3–6 and the results summarized in Chapter 7. Finally, Chapter 8 contains suggestions for future work.

Chapter 2

Literature review

The production of aluminium has been a growing industry for the past century and the range of products where aluminium and its alloys are finding applications has steadily increased. Many of these products, such as extremely thin metal foils, place a high demand on the quality of the base metal as regards impurities and grain structure in order to maintain the requisite standard of surface texture and product continuity.

The present project concerns the effect of the addition of grain refining master alloys on the observed number and size of particles in molten aluminium after processing in casthouses. In this chapter the casthouse processes for cleaning the aluminium melt from the electrolytic production cells are reviewed and the inclusions normally obtained in aluminium are described. The different types of grain refining master alloys and their effects are discussed along with the available methods for measurements of particle size, number and distribution in molten aluminium. A review of previous studies on the behavior of inclusions in aluminium melts is also included. Finally, the theory of modelling of flow conditions and particle distribution in launder systems for flowing melts is presented along with previous work on such models.

2.1 Manufacture of aluminium products

Aluminium is the third most abundant element on the earth's surface after oxygen and silicon. The metal was first produced in 1835 by Oersted. In 1886, the electrolytic reduction of alumina (Al_2O_3) dissolved in molten cryolite was independently discovered by Charles Hall in Ohio, USA, and Paul Heroult in France. All primary aluminium production is based on their method, called the Hall-Heroult process. Figure 2.1 shows a typical version of the Hall-Heroult cell [1]. Alumina refined from bauxite is dissolved in molten cryolite in an electrolytic cell with various fluoride salt additions. When electric current is passed through the cell, the cryolite reacts with the alumina and pure aluminium is formed at the

cathode. The molten aluminium is then decanted from the cell and transported to the casthouse for further treatment.

In the casthouse the molten aluminium undergoes treatment to reduce the level of impurities and gases in the melt. A typical single furnace casthouse process line is shown in Figure 2.2. The treatment includes settling in the furnace, gas fluxing, degassing and filtering. These processes are discussed further in Section 2.2. After this treatment the impurity level is typically down to approximately 0,3-0,5%.

In the casthouse a grain refining master alloy is normally added to the melt in order to modify the grain structure of the cast product. The alloys are usually in the form of a rod which is continuously fed into the melt in the transfer launder between the furnace and the casting machine. The effect of the master alloy addition on the particle content of the melt, including their size and distribution, is the main concern of the present project as previously discussed.

The casting machines in the casthouses produce primary aluminium ingots in different forms for subsequent remelt or direct fabrication purposes. The most common is the direct chill casting machine in which billets are continuously cast by relatively fast water cooling of the melt. By this, optimum properties of the billets are obtained as regards the distribution of impurities and the grain structure. The billets are then cut up into appropriate sizes which are transported to the metal products manufacturer for final processing.

The final processing of the primary aluminium includes all the normal metal processing techniques such as casting, extrusion and rolling as shown in Figure 2.3, which gives an overview of the aluminium manufacturing process. In the production of thin metals foils (0,007-0,009 mm) by rolling, the surface quality and the continuity of the final product is imperative. Even the smallest of holes in a foil seriously affects its quality for instance for food packaging applications. The absence of large particles or inclusions in the aluminium base metal for such applications is therefore of a major priority for the aluminium manufacturer.

2.2 Molten metal processing

In the aluminium production process, the molten aluminium from the electrolytic cells is transported to a casthouse where it is transformed into a solidified product. This product is then transported away for further processing. The main products of casthouses are alloyed billets for rolling mills, alloyed cylindrical billets for extrusion and unalloyed ingots for remelt.

The casting units are similar in most casthouses, they consists of furnaces, transfer launders with various inline treatment units and a casting machine on a casting pit. The main difference between casting units lies in the number of furnaces in each line. A single furnace system has one furnace, were both alloying

and metal preparation for the casting is performed. Figure 2.2 shows a single furnace casting line. In a two furnace system, there is one furnace for alloying and another one for metal preparation. In the project described in this thesis, the experiments in launders were performed in a single furnace casting line. Typical practice of metal handling through a single furnace system is the following:

- Molten aluminium from the electrolytic cell is poured from a crucible into a flow channel leading to the furnace. In the flow channel, the molten metal passes through a filter, which removes both slag and inclusions. After the furnace has been filled with molten metal, the chemical composition of the melt is measured and alloying elements added to achieve the planned composition.
- The furnaces are often equipped with a gas fluxing rotor system. If the molten metal needs to be fluxed with gas for cleaning (see Section 2.2.3), the rotor heads are dipped into the bath. There they rotate at high speed and distribute the gas, usually argon or a mixture of argon and chlorine. After the fluxing, there is a holding time, when the melt is undisturbed for a period of time. This allows inclusions in the melt to settle on the bottom or the walls. Inclusions can also float to the top where they enter the slag. After the holding time, drosses are removed from the melt surface and casting can start.
- When the casting begins, the furnace is tilted and molten aluminium flows along the flow channel, towards the casting pit (see Figure 2.2). On the way the molten metal may pass through some inline treatment units if they are installed. These inline treatment units are generally a degassing system and a filter box. The purpose of these is to clean impurities from the molten metal. Also, a grain refining master alloy is usually added to the melt in the flow channel to modify the grain structure of the solidified product. The grain refiner is in the form of a rod which is fed continuously into the molten metal where it melts down and disperses. At the end of the flow channel, the molten metal enters the casting machine, where the metal solidifies.

A more detailed description of specific parts of the casting process are presented in subsequent sections of this chapter.

2.2.1 Impurities in molten aluminium

A major concern in production of aluminium, is the control of impurities in the molten metal. There are various sources of impurities. Some originate in the electrolytic cell, but scrap metal, alloying elements and grain refining master alloys also contain impurities all of which enter the melt. Table 2.1 shows the level

of impurities in aluminium produced with two different methods of electrolysis. One is the normal Hall-Heroult process but the other the three-layer electrolytic process, which is occasionally used to produce high purity aluminium [2]. In the latter the electrolyte consists of a mixture of aluminium, sodium and barium halides. The pure aluminium cathode floats on the top of the electrolyte. The anode is made of aluminium with enough copper added to make it denser than the electrolyte. The electrolysis is carried out in a cell similar to standard production cells except the anode is at the bottom and the cathode at the top.

Impurities can be divided into four different groups. These are:

Volatile elements. Volatile elements are elements such as hydrogen and sodium, with a high vapor pressure. When a metal with a high hydrogen content solidifies, hydrogen pores are formed. Figure 2.4 shows a typical relation between hydrogen content and porosity in sand-cast aluminium. The porosity degrades the mechanical properties of the metal and can cause blistering of sheet metal during hot rolling.

Reactive elements. Reactive elements are elements that can be removed from molten metal by adding argon, chlorides, salts, boron and other chemicals. These reactive elements include calcium, lithium and titanium.

Non-reactive elements. A non-reactive element, always present in molten aluminium, is iron. Iron is very difficult to remove from the molten metal. It has been reported that Al_mFe intermetallics [3], cause an undesirable fir-tree structure in ingots as shown in Figure 2.5 [2].

Inclusions. Inclusions in molten aluminium can be either in liquid state or in solid state. Inclusions can, even in low numbers, have an effect on the properties of the cast product. They can cause holes in thin foils, usually in foils with thickness less than $50\mu m$. Inclusions can also cause fracturing of wires during the latter stages of the drawing process.

There are several methods available to remove impurities from molten aluminium. The main methods are settling, gas fluxing and filtering. There is a large number of producers of equipment for gas fluxing and filtering with many different versions of these products. Therefore, only the principles behind each method are reviewed.

2.2.2 Removal by settling

Settling of inclusions is basically a simple process. It utilizes two effects, gravity and natural convection. Because of a difference in density between inclusions and the molten aluminium, the inclusions either sink to the bottom, if they are denser than the molten metal, or float towards the surface if they are less dense.

Table 2.1: A comparison between aluminium metals from a Hall-Heroult electrolytic cells and three-layer electrolysis with respect to impurities [2].

<i>Impurity</i>	<i>Typical concentration (mass p.p.m)</i>	
	Electrolytic cells	Three-layer electrolysis
Mg	10-40	< 1
Si	300-700	1-5
Ti	30-50	< 1
V	100-200	< 1
Fe	500-2000	1-10
Ni	10-30	< 1
Cu	5-30	< 1
Zn	20-200	< 1
Ga	80-180	1

Natural convection is the result of differences in temperature in the melt. There are always colder regions near the walls and at the surface, and this is the driving force for natural convection. Natural convection can move inclusions toward the walls where they get attached. Natural convection and thermal diffusion promote collision of inclusions, and this can lead to agglomeration. The agglomerates are larger than individual particles and therefore sink faster in the melt. As the agglomerates grow larger, collisions with smaller particles are more likely on the way down, and this can lead to faster removal of inclusions in the melt.

Settling can only be performed in a furnace or in a crucible, because the melt is never stationary in a flow channel.

2.2.3 Removal by gas fluxing

Hydrogen is an impurity which has to be removed down to a specific level in molten aluminium. It promotes the formation of pores in the metal when it solidifies. The most efficient method to remove hydrogen from molten aluminium is to use gas fluxing or degassing units. The object with degassing units is to form small gas bubbles, which are released at the bottom of the molten metal from where they float to the surface. Dissolved hydrogen diffuses into these bubbles as they rise to the surface. Degassing units can be in a furnace or in the flow channels in special units.

The simplest way to construct a degassing unit is the utilization of porous plugs. Orifices are distributed in the bottom of a furnace and gas is fed to them through a piping system in the refractory lining of the furnace [4].

A more common method for distributing gas bubbles in a molten metal, is by using spinning rotors. The design of rotor heads varies as every manufacturer

has their own special design [5, 6]. One of the principal design parameters is the rotor speed, which can vary from 10–700 rpm.

The main effect of gas fluxing is the removal of hydrogen. It is usual to use argon gas for the fluxing. Additional effects are obtained if chlorine gas is used, since it reacts with dissolved sodium and removes it. Small inclusions also collide with the gas bubbles, attach to their surface and float with them to the surface. Fluxing by gas bubbles also generates turbulence in the melt which stirs the melt and ensures a homogeneous distribution of the remaining inclusions and alloying elements.

2.2.4 Removal by filtering

Filters are used to remove inclusions from the melt. The principle is to feed the molten metal through a porous medium, through which the inclusions cannot pass. The main difference between different types of filters is the type of the porous medium. All filters are available with different porosities.

The most common filters are ceramic foam filters (CFF), which are made of alumina. The pore size of the filters ranges between 0.5–2 mm. The filter is placed in a filter box in the flow channel. Figure 2.6 shows a sectional view of a two stage ceramic foam filter [7].

Deep bed filters (DBF) are more complex. They are made of a steel cage, refractory linings, alumina balls and alumina grains. Figure 2.7 shows a new compact design of DBF [8]. The filter contains 600 kg of grains on top of ca. 600 kg of alumina balls. The molten metal enters the steel cage and sinks to the bottom through the grains and alumina balls. When the molten metal reaches the bottom, it is pumped out of the cage with a gas-lift pump.

The efficiency of deep bed filters is better than for ceramic foam filters. However, CFF are much easier to operate and are more flexible, presumably because a reservoir of liquid metal must remain in DBF filter. Flexibility is useful when different alloys are cast on the same casting line. The efficiency of filters decreases with time. With use, the pores gradually fill up with inclusions which finally clog the filter.

2.2.5 Grain refining

Aluminium and aluminium alloys are frequently grain-refined during solidification in order to promote the formation of an equiaxed grain structure in the cast metal and thereby eliminate columnar grain formation. Equiaxed grain structure is generally imperative for the subsequent forming of the solidified metal. This grain structure is commonly achieved by adding approximately one kilo per tonne of a grain refining master alloy to the melt just prior to casting [9, 10]. Figure 2.8 shows the effect of the grain refiner addition.

Although it is generally accepted that the grain refiner addition introduces nucleation sites into the molten alloy, the precise mechanism of grain-refinement is still not well understood as discussed in review articles on this subject [9–11]. The basic model for explaining the grain refining mechanism postulates, that the inoculant disperses numerous potent insoluble or sparingly soluble heterogeneous nuclei into the melt and that a large number of these sites become active on cooling and nucleate the solid phase. The master alloys, therefore, contain a large number of these small particles embedded in an aluminium matrix. The matrix melts down when the master alloy is introduced into the aluminium melt and releases the particles.

All master alloys also contain $TiAl_3$ particles which are soluble in the melt. The beneficial effect of dissolved titanium as a restricting element for the growth of the α -Al phase is well known [10, 12] but the actual nucleation mechanism of the insoluble particles is still under investigation. Undissolved $TiAl_3$ particles may also serve as nuclei for the solid phase.

Most of the master alloys in current use contain either small insoluble or sparingly soluble TiB_2 or TiC particles in addition to $TiAl_3$. The role of these particles is to act as the nuclei for grain formation. Dissolved titanium is considered to have beneficial effect on the grain refining properties of the TiB_2 particles [13].

In industrial practice Al-Ti-B master alloys are the most widely used grain refiners with a typical composition of 5% titanium and 1% boron (Al-5Ti-1B) giving addition levels (by weight) of 50ppm Ti and 10ppm B [14]. Insoluble titanium diboride particles, which have the form of hexagonal platelets approximately $2\mu\text{m}$ by $0.5\mu\text{m}$ thick, are introduced by Al-Ti-B master alloy additions. It is recognized, however, that many of the added platelets are redundant, in that they do not act as nucleation centres for the solidifying aluminium, and hence become undesirable, hard inclusions in the final product [12, 15].

Al-Ti master alloys are also employed as grain-refiners, with normal addition levels of 0.01 to 0.02 wt%Ti, i.e. well below the peritectic composition of the Al-Ti phase diagram (see Figure 2.9), which occurs at 0.15wt%Ti [16]. Such alloys have, in the past, been found to behave inconsistently and to be much less effective than Al-Ti-B master alloys. Recently, however, enhanced performance has been achieved by using Al-Ti based master alloys containing up to 0.15 wt%C and low boron levels (< 0.003 wt%B) [17–19]. Inherently, such alloys contain a very low volume fraction of insoluble particles. Therefore, they are particularly attractive for use in applications where aluminium metal cleanliness and freedom from hard inclusions is of crucial importance [18]. Despite the number of papers reporting the good grain refining performance of Al-Ti-C master alloys [20, 21], relatively little is known about the level of insoluble particles introduced.

2.3 Structure of grain refining master alloys

There are three main classes of master alloys available to the aluminium industry:

- Al-Ti master alloys
- Al-Ti-B master alloys
- Al-Ti-C master alloys

The master alloys are produced both in waffle form, for additions in holding furnaces, and in 9.55 mm diameter rod form. The rod is mainly used in direct chill casting units. The rod is fed continuously into the stream of molten aluminium in the transfer launder between the holding furnace and the casting machine.

All master alloys contain titanium in the form of $TiAl_3$ particles. These particles are soluble in the aluminium melt as previously discussed. In addition, most master alloys presently used contain either TiB_2 or TiC particles which are insoluble or sparingly soluble in the melt. The size and the distribution of these particles in the master alloy and subsequently in the melt is a subject of major importance to the grain refining of aluminium. In the following section, the metallurgy of the three classes of master alloys will be reviewed.

2.3.1 Al-Ti master alloys

Grain refining of aluminium with titanium is the oldest form of grain refining and it was discovered more than fifty years ago [22]. Al-Ti master alloys are produced by adding salt of K_2TiF_6 to molten aluminium at an appropriate temperature. They contain titanium well above the peritectic concentration which is 0.15% Ti (see Figure 2.9). Therefore, the Al-Ti master alloys contain large tetragonal $TiAl_3$ particles in an α -aluminium matrix. The size distribution of $TiAl_3$ particles usually ranges from approx. 20 to 100 μm in diameter and they are soluble in molten aluminium. Small $FeAl_3$ particles are also usually found in the Al-Ti master alloy but any effect of these particles is not considered relevant [10].

In the experimental part of this project, the aim is to use the LiMCA device (see section 2.4.7) to gain information on particles released when a master alloy is melted. For being detectable with the LiMCA device, the $TiAl_3$ particles must have much higher electrical resistivity than molten aluminium, which has electrical resistivity of $25 \cdot 10^{-6} \Omega cm$. Only one reference [16] has been found on the electrical resistivity of $TiAl_3$ particles and there it was given as $> 0.16 \Omega cm$. This difference in resistivity indicates that $TiAl_3$ particles should be detectable with the LiMCA device. The same reference gives the density of $TiAl_3$ particles as $3370 kg/m^3$. They are therefore, denser than molten aluminium (approx. $2300 kg/m^3$), which means that they will tend to settle toward the bottom in an aluminium melt prior to dissolution.

2.3.2 Al-Ti-B master alloys

The most common grain refiners are the Al-Ti-B master alloys which have been used commercially for over 25 years. Despite comprehensive studies, the mechanism of grain refinement with Al-Ti-B master alloys is not fully understood. Detailed overviews of the proposed mechanism of grain refining with Al-Ti-B master alloys can be found in the literature [10, 11, 13].

The typical microstructure of Al-Ti-B master alloys contains large $TiAl_3$ particles and many smaller diboride particles in a matrix of α -aluminium. Both the $TiAl_3$ and TiB_2 morphologies and distribution are sensitive functions of the master alloy processing conditions and production methods [23].

There are two main types of Al-Ti-B master alloys, Al-5Ti-1B, containing 5%wt Ti and 1%wt B and Al-3Ti-0.2B, containing 3%wt Ti and 0.2%wt B .

The Al-Ti-B master alloys are produced by adding salts of K_2TiF_6 and KBF_4 in the appropriate mole ratio into molten aluminium at a temperature between 700°C and 800°C [24]. The reactions between the molten aluminium and the salts are as follows:



which creates TiB_2 particles and



which creates $TiAl_3$ particles.

The $TiAl_3$ particles were described in Section 2.3.1. The TiB_2 particles are small, practically insoluble, particles with a hexagonal structure. Their density is $4520\text{kg}/\text{m}^3$. Figure 2.10 shows a schematic picture of a TiB_2 particle. This structure can be seen in polished samples of Al-Ti-B master alloys, at high magnification in an scanning electron microscope (SEM). Figure 2.11 shows a TiB_2 particle cluster in a Al-5Ti-1B master alloy, which clearly demonstrates the hexagonal structure.

Bunn [25] used polished samples, SEM and image analysis, and Bailey [26] chemically extracted the TiB_2 particles from the aluminum matrix to investigate the size distribution of TiB_2 in master alloys. The results from latter study are shown in Figure 2.12. The size range of the particles is ranging from approx. $0.1\mu\text{m}$ to $10\mu\text{m}$. The results from Bunn [25] show a slightly narrower distribution, i.e. ranging up to $6\mu\text{m}$. The particle size is, therefore, well below the $20\mu\text{m}$ detection limit of the LiMCA device (see section 2.4.7). Thus, the important factor for the LiMCA experiments in the present study is whether TiB_2 clusters are formed either in the melt or in the master alloy and if they reach a size above $20\mu\text{m}$. Gudmundsson [27] has examined the Al-5Ti-1B master alloy and detected clusters up to $25\mu\text{m}$. He concluded that the TiB_2 particle clusters were

glued together with fluoride salts (see Equations 2.1 and 2.2).

Another consideration for the detectability of TiB_2 particle clusters with the LiMCA device, is the electrical resistivity of TiB_2 particles. As discussed in Section 2.4.10, the electrical resistivity of TiB_2 is very close the resistivity of molten aluminium, which means there must be some other phases in the TiB_2 clusters to allow their detection. There are three possible additional phases, $TiAl_3$, oxide and residual fluoride salts. All of these have a much higher electrical resistivity than molten aluminium and could, therefore, make TiB_2 clusters detectable with the LiMCA device.

2.3.3 Al-Ti-C master alloys

Growing demand by the aluminium industry for effective grain refiners with lower volume fraction of borides and good grain refining properties in melts containing zirconium, chromium and lithium has led to the development of Al-Ti-C master alloys [10]. The former elements have been found to poison the effect of boron containing master alloys. The grain refining efficiency of Al-Ti-C master alloys has been under investigation [19, 21] and the results have been satisfactory for materials where the grain refining efficiency of Al-Ti-B master alloys is poor.

The typical microstructure of Al-Ti-C master alloys contains large $TiAl_3$ particles and many smaller TiC particles in a matrix of α -aluminium. The production methods of commercially available Al-Ti-C master alloys are proprietary although it is believed that titanium containing scrap metal from the aircraft industry is used as a source for titanium. The scrap metal is cut using cutting fluid as a lubricant which is not cleaned off the cuttings before addition and it becomes a source of carbon. Additional carbon is added by proprietary methods. This production method eliminates the large addition of salts, which are believed to influence the agglomeration of TiB_2 particles [27].

The $TiAl_3$ particles were described in Section 2.3.1. The TiC particles are small practically insoluble particles with an octahedral structure [19]. Figure 2.13 shows a schematic picture of a TiC particles. The density of TiC particles is 4930kg/m^3 .

The size distribution of TiC particles has been reported by Whitehead [20]. The measurements were carried out in a SEM with image analysis software. The average diameter of the TiC particles was ranging from 0.1 to $1.8\mu\text{m}$. Agglomerates of TiC were not detected in that study. However, Mayes [19] and Hoefs [21] reported agglomerates of TiC up to $2\mu\text{m}$ in diameter.

The electrical resistivity of TiC has been reported as between $50\text{--}200\Omega\text{cm}$ [28] which is two to eight times higher than that for molten aluminium. This is hardly enough difference to allow detection of TiC clusters by the LiMCA device without additional high resistivity phases in the clusters. There are no fluoride salts employed in the production of these alloys, so that the main possibility of

additional phases are $TiAl_3$ and oxide.

2.4 Measurement of inclusions in molten aluminium

Detection of inclusions in molten aluminium alloys has been advancing for the past years. The reason for this is a greater demand for high quality gauge and critical surface quality applications. A growing demand of quality control, which includes data sampling, has directed studies towards both advancing the old detection methods and creating new ones.

This section gives an overview of two different measurement techniques, used to measure inclusions in liquid aluminium. This includes a description of the fundamentals of each procedure and discussion of their advantages and limitations. This section also discusses how these methods can be used in experiments to evaluate information on the dispersion of grain refining particles in launders.

The methods, most widely used by the aluminium industry to measure inclusions in liquid aluminium, are the PoDFA (*Porous Disc Filtration Apparatus*) method and the LiMCA (*Liquid Metal Cleanliness Analyser*) method. These methods are very different from each other. The PoDFA method is an off-line method requiring the removal of a molten metal sample whereas the LiMCA method is an on-line method for direct measurements in the molten metal flow.

2.4.1 The PoDFA method

The PoDFA (*Porous Disc Filtration Apparatus*) method has been under development since 1960 and is now commonly used in the aluminium industry. Other similar methods are also available, such as the LAIS methods [29]. All these methods are based on filtering and produce similar results.

2.4.2 The PoDFA procedure

The main principle of the PoDFA method is to force a molten metal sample through a porous refractory alumina disc. The solids present as inclusions in the molten metal are caught on the alumina disc. Figure 2.14 shows TiB_2 particles caught on the PoDFA filter.

The procedure is as following [27] :

1. A crucible with a hole in the bottom, which is covered with a PoDFA disc, approx. 25mm in diameter, is preheated to 700–750°C .
2. The sample is collected with a dipper, the sample size should be 1000–2000g. The sample is poured into the crucible. The crucible is tilted to

allow smooth transfer of the sample into the crucible and to avoid unnecessary shock of the filter disc as shown in Figure 2.15.

3. The crucible is placed in a pressure chamber with a hole in the bottom. The pressure in the PoDFA bell is maintained at 68 to 76 kPa until at least 500 g of metal, preferably 1500 g measured to the nearest 0.1 kg, has passed through the alumina disc. The filter collects the inclusions.
4. The solidified metal is removed from the crucible and sectioned such that 5–10 mm of the metal above the disc is kept attached to the disc.
5. The filter disc and the aluminium are cut into two equal pieces and a 5 mm slice is made from one of the halves.
6. The 5 mm slice is mounted in thermosetting resin and polished according to a prescribed polishing procedure.
7. The sample is examined metallographically. This procedure is described in section 2.4.4.

2.4.3 Detectable inclusions and size range

With the PoDFA technique, it is possible to distinguish between various types of inclusions. Some inclusions need special polishing methods to be detectable, for instance if the inclusion is soluble then the sample has to be dry polished instead of the wet polishing methods normally used.

The size range of particles in the filter can be from $1\mu\text{m}$ to $1000\mu\text{m}$. Particle sizes as low as $0.2\mu\text{m}$ have been reported as measured with filter techniques [29].

In Table 2.2 a list of the common types of inclusions present in molten aluminium has been compiled together with a short description of each inclusion type. An overview of this kind has not been found in the literature.

2.4.4 Sample analysis

Observation by optical microscopy of the metallographic cross-section of the disc permits identification of different types of inclusions. When expressed as total concentration of inclusions per kilogram of metal filtered (mm^2/kg), an indication of the metal cleanliness is obtained. Equation 2.3 shows the evaluation formula for the STIC (Standard Inclusions Content) value.

The inclusions tend to penetrate the filter disc for a short distance. To ensure that most of these are included in the evaluation, the edge of the disc is scanned to a depth of 0.5 mm. Less than 10% of the total number of inclusions should penetrate deeper than 0.5 mm in the filter disc, otherwise the PoDFA sample must be rejected. The evaluation of the area of the inclusion concentration will only include inclusions present down to 0.5 mm into the disc. In practice it is not common to see inclusions penetrate deeper than 0.5 mm.

Table 2.2: A list of detectable inclusions in molten aluminium. Size is in μm .

Inclusion	Type	Size	Form	Origin	
<i>Borides</i>	TiB_2	0.1-5	Rectangular or hexagonal discs	Grain refining	
	$TiVB_2$	2-10	Rectangular or hexagonal discs	Grain refining	
	AlB_2	1-25	Rectangular or hexagonal discs	Grain refining	
	AlB_{12}	1-25	Polygonal or irregular lumps	Grain refining	
	$AlTiB$		Irregular	Grain refining	
<i>Chlorides</i>	$AlCl_3$	2-25	Irregular shaped holes	Fluxing with chlorine.	
	$MgCl_2$			Introduction of salt	
	$NaCl$				
	$CaCl_2$				
<i>Nitrides</i>	AlN	10-50	Strings of fine and coarse particles	Insufficiently cleaned furnace	
<i>Fluorides</i>	NaF		Spherical	Cryolite	
	KF				Introduction of salts
<i>Carbides</i>	Al_4C_3	1-25	Angular crystals. Flat and very sharp fine needles	In the melt, reaction with cathode & anode wood	
	Al_4C_4B	1-30	Fine needles		
<i>Graphides</i>	SiC	1-10	Flakes and larger equiaxed Jagged or round particle	Contact with carbon	
<i>Oxides</i>	$\alpha - Al_2O_3$	1-10	Large compact particles	refractory Alumina from smelter.	
	$\gamma - Al_2O_3$	< 1			Small dispersed particles
	MgO		1-10	Thin film or group of films	Contact with air
			1-10	Thin film or group of films	Mg in contact with air
			> 10	Patches of small particles	
	Al_2MgO_4		< 8	Cuboides	Mg alloys
			1-50	Large Spinel	
			> 10	Spherical spinels	Refractory
	FeO	1-5	Crystal of spinels	Refractory	
	1-100	Irregular	From alloying rust		
MnO	1-100	Irregular	From alloying		

The frame used as an assistant tool in the counting of the inclusions is 1mm x 1mm at 50X magnification and is divided into 100 smaller squares. The counting is done by evaluating the size of the area of each small square covered by the inclusions. One important rule for the counting process is:

Any area of aluminium with maximum width of less than 20 μm surrounded by inclusions is included as part of the inclusions concentrate area. For scattered inclusions particles smaller than 3 μm in diameter, the spacing must be included if it is less than 5 μm .

This means that the counting can be affected by the size distribution of the inclusions in the sample, i.e. a large number of smaller particles can show more scatter in the sample than a few bigger particles.

The equation for the calculation of the STIC value is:

$$\begin{array}{r}
 \text{Total Inclusion} \\
 \text{Concentrate Area} \\
 \text{per Kilogram} \\
 (\text{mm}^2/\text{kg})
 \end{array}
 = \frac{
 \begin{array}{r}
 \text{Total Number} \\
 \text{of Squares} \\
 \text{Measured}
 \end{array}
 \times
 \begin{array}{r}
 \text{Area per Small} \\
 \text{Square at Chosen} \\
 \text{Magnification} \\
 (\text{mm}^2)
 \end{array}
 \times
 \begin{array}{r}
 \text{Nominal} \\
 \text{Chord} \\
 \text{Length} \\
 (\text{mm})
 \end{array}
 }{
 \begin{array}{r}
 \text{Weight of} \\
 \text{Filtered Metal} \\
 (\text{kg})
 \end{array}
 \times
 \begin{array}{r}
 \text{Chord Length} \\
 \text{Measured} \\
 (\text{mm})
 \end{array}
 }
 \quad (2.3)$$

where the chord length is the length of the filter.

The result is reported to no more than three significant figures. Experience has shown a reproducibility of about $\pm 15\%$ (95% confidence level) on evaluations made on the same samples by different metallographers [30]. There is no data available to confirm this statement, but it is considered to be valid by the industry [31].

The chord length is measured with a precision of ± 0.2 mm. In equation 2.3 the nominal chord length is divided by the measured chord length to eliminate the effect from cutting precision, i.e. the cutting line is not directly through the center of the sample. This is natural but some samples have a measured chord length larger than the nominal length which means that the filter diameter is bigger than the nominal length. Therefore, to obtain this effect in the equation, it should be the square value of nominal length divided with the square of the measured length.

Magnification is kept as low as possible. A sample with a high STIC requires less magnification than a sample with a low STIC value. At 50X magnification, 12–13 frames must be evaluated, at 100X it is 48–52 and at 200X it is 192–208. This is the basic procedure to evaluate the total count of inclusions in each sample. In practice, however, an experienced metallographer does not count the inclusions in the sample frame to frame, but scans over the area and only to stop at points where the inclusions are.

Useful data for statistical analysis of the results is not common as it is difficult to get many different metallographers to examine the same samples in order to compare the results. It is also difficult to get many samples from the same batch, shortage of equipment makes it impossible to filter statistically a sufficient number of samples simultaneously. It is not possible to take comparable samples from the same batch over a period of time as they can not be expected to have the same inclusion content.

2.4.5 Polishing of PoDFA samples

The procedure for polishing PoDFA samples is not clearly defined, it is mainly based on the experience of the person polishing the samples.

There are two methods possible for the polishing, i.e. conventional polishing and dry polishing. The aim of dry polishing is to avoid dissolution of inclusions, which are soluble in water, such as salts. This is not vital for PoDFA samples intended solely for evaluation of the STIC value, but it is more important when further analyzing of the samples is required.

Dry polishing has been done two ways, either by leaving out the lubricant or by using other lubricants than water which do not dissolve the soluble element.

An experiment performed by Campbell [32] showed that when polishing a grain refiner rod with diamond polishing, which is a dry polishing method without lubricant, the surface on the Ti-B-Al samples was affected. The results show that the Diamond Polish surfaces had excess TiB_2 particles i.e. approximately 5 times greater than the expected from the boron concentration of the alloy. This condition is most likely caused by the following:

1. During the Diamond Polish procedure, the wheel impregnated with diamond, is not flushed with liquid. Therefore, material removed from the surface of the sample during the polishing operation, including TiB_2 particles, remains on the wheel and is active during the polishing procedure. During this period, TiB_2 particles may be reduced in size.
2. The TiB_2 particles that remain on the wheel are redeposited into the soft aluminium surface.

This shows that it is difficult to polish a PoDFA sample with this dry method, if the aim is to evaluate the STIC value.

Studies on using other lubricants than water have not been found in the literature.

2.4.6 Experimental use

In the present experiments, it was first planned to take PoDFA samples from various locations in transfer launders, and preferably to obtain a sample from

precise locations in the flow stream. This proved to be impossible with the PoDFA technique, since the dipper used to obtain a sample is relatively large compared to the size of the launders. Putting a dipper into the launder, therefore, disturbs the profile of the metal flow, and this seriously affects the representative value of the obtained sample.

There have also been problems using the PoDFA technique on commercial pure aluminium as used in the present study, since the filter can break loose from the aluminium [31].

One possible way to use the PoDFA is to measure the time needed to plug the filter. Doutré [33] has shown that the results provided by this technique were found to reflect the level of small particles ($< 5\mu\text{m}$) and were unaffected by the much lower concentration of larger, more harmful inclusions. This can be interesting since TiB_2 particles are expected to be $< 5\mu\text{m}$. The PoDFA II method or the Prefil-Footer is based on this principle [34].

2.4.7 The LiMCA method

The LiMCA method is a new technique compared to the filtering techniques. The first device came in use 1986 and in 1993 a smaller and more practical version called LiMCA II appeared on the market [34].

The LiMCA method is a suitable shop floor technique for monitoring the melt quality [35] by measuring the quantity of non-metallic inclusions in the melt. Further applications of the LiMCA method are filter quality measurements, settling time measurements and evaluation of furnace cleaning methods. Those applications are described in several references [7, 36–42].

2.4.8 Theory

As seen in Figure 2.16, the principle of the LiMCA device is to measure changes in the resistance across an orifice (a few micro-ohms out of total resistance of 2 milli-ohms), while molten metal is drawn through it. A non-conducting particle causes this change in the resistance and this results in a short (typically 0.2 millisecond) and small variation in the voltage across the orifice. Typical values of the voltage change are from $20\ \mu\text{V}$ to $10\ \text{mV}$. These measurements are performed with a powerful signal processing box to exclude noise.

The processing box then counts the number of pulses measured over each measurement period, usually 20–30 sec and stores the voltage difference for each point. The number of counts is usually displayed as [K/Kg] or thousands of particles per kilo of melt. It must be noted that the denotation for expressing this value varies in the literature between k/kg, K/kg and K/Kg. The denotation K/Kg is employed in the computer on the LiMCA device and it has also been employed in this study. The software can then calculate the size for each point

with the LiMCA equation, which is derived by [43]:

$$\rho_{eff} = \rho \left(1 + \frac{3}{2}f + \dots \right) \quad (2.4)$$

where f is the volume fraction of the particle and ρ is the resistivity

$$R_1 = \frac{\rho L}{A} = \frac{4\rho L}{\pi D^2} \quad (2.5)$$

$$f = \frac{V_{sphere}}{V_{cylinder}} = \frac{2d^3}{3D^2L} \quad (2.6)$$

By putting eq. 2.6 into eq. 2.4 and using eq. 2.5 gives the resistance of a cylinder with a non-conducting sphere contained within:

$$R_2 = \frac{4\rho_{eff}L}{\pi D^2} = \frac{4\rho L}{\pi D^2} \left(1 + \frac{d^3}{D^2L} + \dots \right) \quad (2.7)$$

$$R_2 - R_1 = \Delta R = \frac{4\rho d^3}{\pi D^2} \quad (2.8)$$

Working with voltage gives

$$\Delta V = \Delta R * I = \left(\frac{4\rho d^3}{\pi D^4} I \right) \quad (2.9)$$

which leads to

$$d^3 = \Delta V \left(\frac{\pi D^4}{4\rho I} \right) \quad (2.10)$$

where ΔV = amplitude of voltage pulse (volts)

d = diameter of the inclusion (meters)

D = diameter of the probe orifice (meters)

ρ = electric resistivity of molten aluminium = $25 \times 10^{-8} \Omega m$ at $700^\circ C$

I = current (amperes)

This equation 2.10 is known as the LiMCA equation. It must be stated again that the particles must be perfectly non-conducting for this equation to be valid.

2.4.9 The LiMCA results

The following list views the sensitivity of the LiMCA device.

<i>Dynamic range:</i>	Particle size 20–300 μm . Particle density 0.05 – 1000 K/Kg.
<i>Sample size:</i>	Adjustable – typically 17.5 g/metal per data point.
<i>Size resolution:</i>	Region of 5 μm .
<i>Reproducibility:</i>	At low inclusions concentrations, dominated by statistical noise and $\pm 10\%$ at high inclusion concentration.
<i>Data rate</i>	Adjustable – typically one data point per minute.

The first notable limit is the size range. Particles under 20 μm cannot be measured because the difference in voltage over the orifice becomes too small for them being classified from the noise. Figure 2.17 shows how the voltage difference over the orifice decreases rapidly when the particles get smaller. The upper range is simply because the orifice is usually 300 μm so that bigger particles cannot penetrate through. If the orifice diameter was larger, for instance 400 μm , then it would be possible to measure bigger particles but the lower limit would also increase. Also by decreasing the orifice diameter it would be possible to detect smaller particles, but experience has shown that the orifice will then plug too often to make this approach feasible.

The lower limit for the particle density is simply one particle per sample or approx. 0.05 K/Kg, depending on the sample size. For a sample of 17.5 g, this means one particle in 17.5 g of metal results in 0.057 K/Kg.

The statistical noise level is determined by the number of inclusions in each sample [44]. By statistical methods, it can be shown that if there is a certain density of particles in a medium, and a sample of a given size is extracted from this medium, a particle count in the sample will distribute according to a normal Gaussian distribution defined by the following parameters:

$$\begin{aligned}\mu &= \beta S \\ \sigma &= \sqrt{\mu}\end{aligned}\tag{2.11}$$

where μ is the mean of the distribution
 σ is the standard deviation of the distribution
 β is the density of particles in the population
 S is the size sample

As stated before, the manufacturer of LiMCA states that the limit of residual reproducibility due to the intrinsic limitations of the instrument is $\pm 10\%$ or σ_h . To correctly predict the reproducibility of the data points at low inclusions levels, it is necessary to combine the effect of both statistical noise and instrumental imperfection. This can be done by combining the two normal distributions. This is done with:

$$\sigma_{total} = \sqrt{\sigma^2 + \sigma_h^2}\tag{2.12}$$

In Figure 2.18 the overall reproducibility per data point is plotted as a function of melt cleanliness, with a sample size of 17.5 g. The statistical reproducibility gradually drops down to zero as the particle density increases. The instrumental reproducibility is constant at 10%. The overall reproducibility tends asymptotically towards 10% at high inclusions.

Figure 2.19 shows the importance of having as large sample size as possible when monitoring melts with low inclusions density. With higher densities this becomes less important.

2.4.10 Experimental use

The LiMCA device is very powerful tool for on-line monitoring of inclusions in flow channels. It could therefore, be most suitable for the forthcoming experiments, especially because it is possible to place the sampling point very accurately in the flow channel as compared to the PoDFA technique. But there are questions which must be answered first. First is the question "What is the LiMCA really measuring?". In this project TiB_2 inclusions are those of main interest. The electrical resistance of TiB_2 is not well established. In Mohanty [35] the electrical resistivity of TiB_2 is given as $9.0 * 10^{-6} \Omega cm$ compared to $25 * 10^{-6} \Omega cm$ for molten aluminium. In other words, TiB_2 is reported to be more conductive. According to this, the LiMCA peaks should be negative, which is hardly ever seen in practice. In Kirk-Othmer [45], the electrical resistivity for TiB_2 is given as $28.4 * 10^{-6} \Omega cm$ at $20^\circ C$. It is normal to estimate that the resistivity increases with increasing temperature, so this would lead to positive peaks. Despite the resistivity values quoted by Mohanty, negative pulses were obtained from only one type of grain refiner (Al-3Ti-1B) in his experiments on grain refiner particle distribution with the LiMCA device and most of the peaks were positive. In the Mohanty experiments, the Ti addition was usually below the peritectic composition, so it can be expected that the $TiAl_3$ particles from the grain refiner will be dissolved (see Section 2.3.1). Therefore, it can be concluded that the LiMCA was measuring the TiB_2 particles or particle clusters. Then the second problem arises in that the individual TiB_2 particles should be in the size range $1-5 \mu m$, which is not considered detectable with the LiMCA device. Therefore, the conclusion must be drawn, that the TiB_2 particles enter the melt in clusters from the grain refiner, because it is unlikely that such large clusters will be formed in the melt over a period of 5 minutes employed by Mohanty. One of the conclusions drawn from the Mohanty's experiment is therefore that TiB_2 particles can enter the melt in large clusters and their resistivity of the clusters is usually higher than the resistivity for molten aluminium.

Table 2.3: Comparison of the LiMCA and PoDFA techniques [46]

<i>LiMCA</i>	<i>PoDFA</i>
Real-time data	Data delayed by hours to days
Continuous measurement	Non-continuous
Portable equipment	Fixed sampling equipment
Inclusion density	Inclusion density
Size distribution of inclusions	Nature of inclusions
Technologically complex	Technologically simple
Totally operator-independent	Discipline needed to make it analyst-independent

2.4.11 Comparison of PoDFA and LiMCA

BOMEM Inc. lists the difference between LiMCA and PoDFA as shown in Table 2.3 [46]. The table highlights common views on the main difference between the methods and most important is the fact that the LiMCA is an on-line technique with continuous measurements. This has given rise to common misunderstanding, however, since the LiMCA measurements are not continuous over the period of a whole cast. They are strictly only continuous within each sampling cycle, which is around 20–30 seconds. Then the measurements stop when the device is pumping the sample out of the tube. But this is more a question of definition, the main advantage of the LiMCA device over the PoDFA method is this ability to sample a large number of data for each cast and to be able to see the results while measurements are taking place.

There are two main areas where the LiMCA is insufficient. One is measuring particles less than $20\mu m$ in diameter and the other is not being able to distinguish between different types of inclusions. With current equipment it is not possible to detect smaller particles, unless the noise filtering in the signal processing unit becomes more advanced, and this is unlikely in the near future. Also distinguishing between different types of inclusions cannot be done solely by measuring difference in voltage. There is hardly any available data on the electrical conductivity of TiB_2 , TiC and $TiAl_3$, which are the particles of main interest in this project. But even with such data being available, a distinction could not be made based on the LiMCA process alone.

2.5 Experimental studies of inclusions in molten aluminium

The LiMCA device was developed for measuring inclusions in aluminium melts in cast-houses as previously discussed. Martin and Guthrie [47] have used LiMCA to study the settling of inclusions in casting furnaces. Figure 2.20 shows the

effect of settling on the inclusions concentration at the exit of a tilting furnace. The settling effect in the furnace in this cast was considered to be best described by the following equation:

$$N_{20} = 45,000 \times e^{-t/15} + 10,000 \times e^{-t/120} \quad (2.13)$$

where t is the time in minutes.

In their work Martin and Guthrie [47] also generated inclusions in aluminium melts in an experimental furnace by making suitable additions of a rod-shaped grain refiner alloy of the type Al-5Ti-1B. According to their results, once the grain refiner melts and becomes mixed in the bath of aluminium, titanium diboride particles are precipitated in the 2-3 μm diameter range. However, agglomerates of such particles will report in the range 10 μm diameter to as much as 100 μm in diameter. The particles larger than 20 μm were detected by the LiMCA device in their work. An alternative method of generating inclusions was to add a master alloy containing 4% boron. They state that the boron combines with residual titanium and vanadium in the melt to form $(Ti - V)B_2$ inclusions which can also be detected by the LiMCA device. It is not clear from the studies of Martin and Guthrie if they consider the TiB_2 agglomerates to form in the melt or to be present in the master alloy, but their results further support the choice of the LiMCA device for the present study.

In the present project [48] LiMCA measurements of the inclusion concentration in launders have been studied as a function of time into the casts. Figures 2.21 and 2.22 show two such curves which demonstrate the effect of settling in the furnace by measuring in the launder when pouring from the furnace. All the casts studied could be described by the same general form of equation as employed by Martin and Guthrie [47]:

$$N_{20} = A_1 \times e^{-t/k_1} + A_2 \times e^{-t/k_2} \quad (2.14)$$

where A and k are constants which are different for different casts. No single overall equation could be found using the available data for the different casts.

2.6 Fluid dynamics modelling of flow launders

Computational fluid dynamics techniques (CFD) have been advancing for the past two decades. The reason for this is the huge increase in computer power which allows more complex calculations with ever increasing speed, whereas the basic methods of solution have largely stayed the same.

In the aluminium industry, the main use of CFD methods has been in the design of new casting machines [49]. The governing factors in the design procedure are the temperature loss in the launders and the solidification of the molten

metal in the molds. These areas, especially the solidification process, have been subject of many research projects in the past [49] but in recent years, with more advanced modelling packages becoming available, other parts of the casting process have gained more attention.

2.6.1 Modelling of flow conditions

Before modelling the flow of molten aluminium in a launder system, the characteristics of the flow must be analyzed. It is essential to determine whether the flow is laminar or turbulent, as this affects the choice of model used for the calculations. One difference between laminar and turbulent flow is that the velocity profiles are different. Also in laminar flow, there are no fluctuations or eddy currents in the flow which can have a large effect on particle dispersion in the launder system. A schematic representation of a turbulent velocity profile near a wall boundary is shown in Figure 2.23 [50]. The velocity profile becomes relatively flat at some distance from the wall. This region is commonly called the turbulent core. In the region nearest to the wall, viscous forces dominate and this results in a steep velocity gradient, called the laminar sub-layer. In between these two regions is the buffer layer, where both turbulent and viscous effects are important.

To determine whether the flow is laminar or turbulent, the Reynolds number is calculated for the launder, which is to be modelled. The Reynolds number is defined as [51]

$$Re = \frac{VD\rho}{\mu} \quad (2.15)$$

where V is the average velocity, D is the effective diameter of the launder, ρ is the density of molten aluminium and μ is the dynamic viscosity. If the Reynolds number is large ($Re > 2000$) the flow in a pipe is generally turbulent [51]. Calculations for both the launder systems to be modelled in the present work, resulted in Reynolds numbers approx. 10,000, which is well above the limit of turbulent flow and therefore the turbulent model was included in the flow calculations.

Results from studies on the flow of molten aluminium and particle dispersion in launder systems have not been widely published in the literature. The main reports on flow and particle distribution in launder systems have been studies of molten steel in rectangular launders. The aim of these studies has been to optimize the flotation of particles to the surface by adding flow modifiers into the launders [52–56]. The results from modelling launder systems transferring molten steel cannot be used directly as a reference for the flow of molten aluminium. The launder systems used in the steel industry are very different from the launder systems in this project and the properties of molten steel are different from that of molten aluminium as shown in Table 2.4. The difference lies both in the density and more importantly in the viscosity of the melt.

Table 2.4: Properties of molten aluminium and steel in launders.

<i>Metal</i>	<i>Temperature</i> [°C]	<i>Density</i> [kg/m ³]	<i>Viscosity</i> [kg/ms]
Aluminium	700	2380	1.2×10^{-3}
Steel	1580	7000	6.7×10^{-3}

The results of modelling the flow of molten aluminium in a launder and comparison with a physical model has been presented by Shen [57]. A launder system was modelled numerically with a $k - \epsilon$ numerical model for turbulent flow (see Section 5.1.1) and compared to a 1/3 scale water model. Figure 2.24 shows the computed velocity vectors in the vicinity of a bend in the launder. The results from the water model and the numerical calculations were found to be compatible. However, compared to the present study, the launder geometry was very different and the boundary conditions were chosen differently. In his work, Shen treated the top surface as a free surface to ease comparison with the water model. However, this approach may not be appropriate given the formation of oxide on the surface of molten aluminium.

Numerical modelling of the flow of molten aluminium through deep bed filters has also shown that the numerical results obtained with a standard $k - \epsilon$ turbulence model [58] have been verified with water models [59]. This further supports the use of this type of a model for aluminium melts in launders. Hence it is clear that the work to date on modelling launders with molten aluminium has shown promising results and offers the potential for further application.

2.7 Summary

The aims of the present project were described in Chapter 1. It is interesting to summarise the main points of the literature survey and to compare these with planned work:

- There are three main classes of master alloys containing different types of particles in an aluminium matrix. They are:
 - Al-Ti alloys containing soluble $TiAl_3$ particles in a size range of 20-100 μ m.
 - Al-Ti-B alloys containing soluble $TiAl_3$ particles in a size range of 20-100 μ m and insoluble or sparingly soluble TiB_2 particles in a size range of 0.1-10 μ m.
 - Al-Ti-C alloys containing $TiAl_3$ particles in a size range of 20-100 μ m and insoluble or sparingly soluble TiC particles in a size range of 0.1-1.8 μ m.

All three classes are employed in the present study.

- Studies of the particle distribution in the master alloy rods have shown that the TiB_2 particle can form clusters in the rods. Clusters up to $25\mu\text{m}$ have been found and fluoride salts were considered to act as a form of a glue in the clusters. Small TiC clusters have also been reported in Al-Ti-C alloy rods with a size up to $2\mu\text{m}$. No studies have been found in the open literature on the difference in particle distribution between the same type of master alloy rods from different manufacturers. The particle distribution in master alloy rods will be investigated in the present study with special emphasis on the formation of clusters of TiB_2 and TiC particles. Master alloys from different manufacturers are included to compare both the particle distribution and also the presence and distribution of additional phases such as fluoride salts and oxide.
- Two standard methods for measuring the inclusions content of an aluminium melt are available. They are the PoDFA method and the LiMCA method. The PoDFA method consists of taking a sample from the melt and measuring the inclusion content by microscopy. The LiMCA method, on the other hand, is an on-line method for direct measurements of the molten metal flow. The method is based on measuring the difference in the resistance across an orifice through which the melt under investigation is drawn. The on-line LiMCA method is considered to be more appropriate for the present study of particle distribution in stirred and flowing melts.
- There are two main limitations of the LiMCA method. One is that the inclusions must have a much higher resistivity than the aluminium melt for them to be detected. The second is that even with practically non-conducting inclusions, the minimum inclusion size that can be detected is approximately $20\mu\text{m}$. This has not affected the use of the LiMCA for quality control in aluminium cast houses. However, these limitation raise questions regarding the suitability of the method for the present work considering the small particle size of the TiB_2 and TiC particles in the master alloys. Furthermore, the TiB_2 and TiC particles have a similar resistivity to the aluminium melt so that any clusters formed by these particles must also contain some high resistivity additional phases such as salts or oxide to become detectable. The presence of fluoride salts has been observed in TiB_2 clusters in master alloys.
- The LiMCA method has been employed for measuring the change in the particle distribution in aluminium melts with the addition of Al-Ti-B master alloys. Changes in the inclusion content of the melt were observed with the master alloy addition. This supports the selection of the LiMCA

method for the present work and that the TiB_2 particles form clusters which can be detected by the LiMCA device despite their resistivity.

- No studies have been found in the literature on the agglomeration of TiB_2 and TiC particles after they enter the aluminium melt from the master alloy. However, the addition of Al-5Ti-1B master alloy has been used to generate agglomerates up to $100\mu m$ in a study of the settling of inclusions in aluminium melts in furnaces. It is not clear whether the agglomerates originated in the master alloy rods or were formed in the melt. The possible agglomeration of TiB_2 and TiC particles in the melt will be investigated in the present study.
- The flow conditions in transfer launders will affect the distribution of particles from the master alloy addition in the melt. Computational fluid dynamics techniques have shown promising results for modelling flow in transfer launders for steel and aluminium melts and for the flow of aluminium through deep bed filters. This method, therefore, offers the potential for further application in particle distribution studies in flowing melt in transfer launders. Two launder designs are modelled in the present study and the results compared with LiMCA measurements of the particle distribution after master alloy addition to the melt in one of the launders.

2.8 Figures

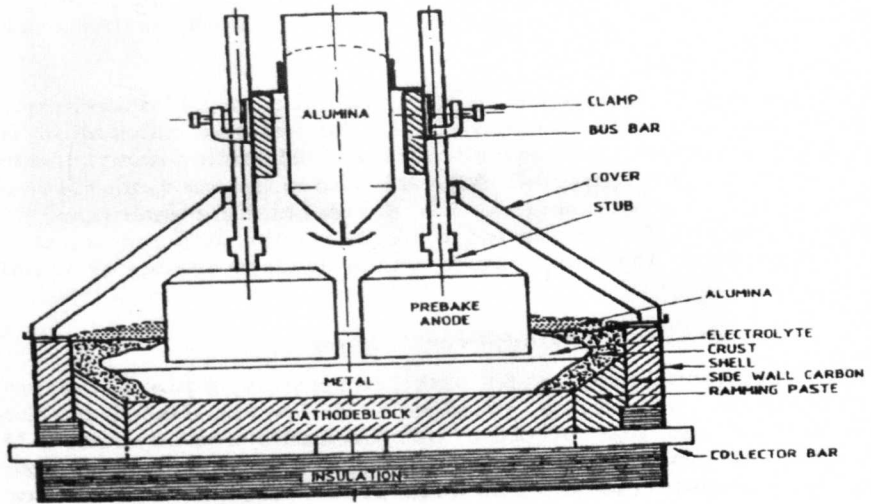


Figure 2.1: The Hall-Heroult reduction cell [1].

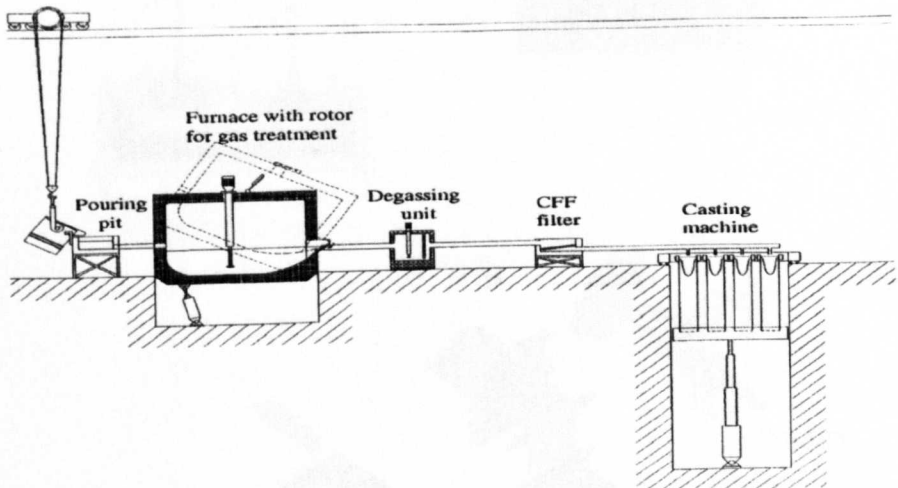


Figure 2.2: Casthouse layout.

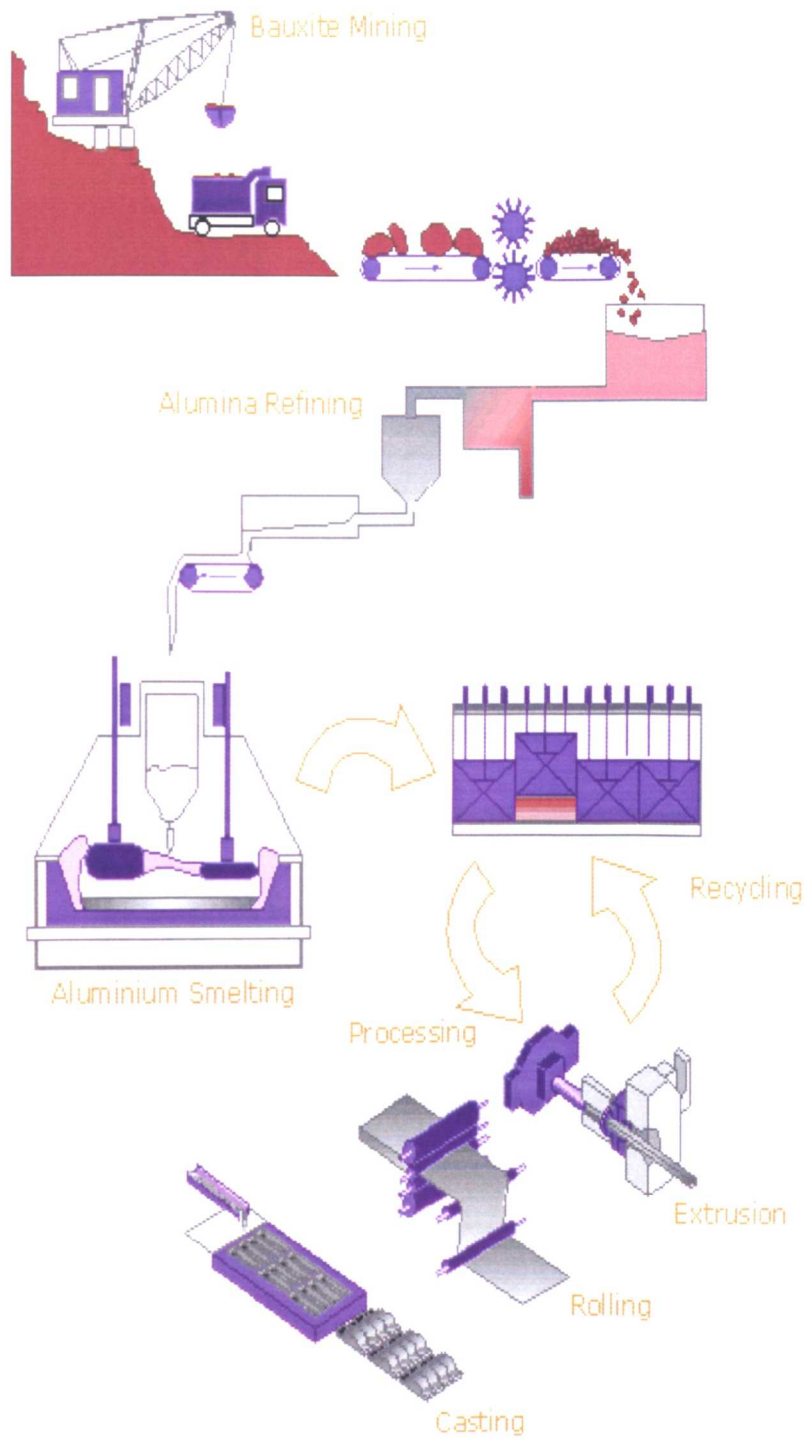


Figure 2.3: An overview of the aluminium manufacturing process [60].

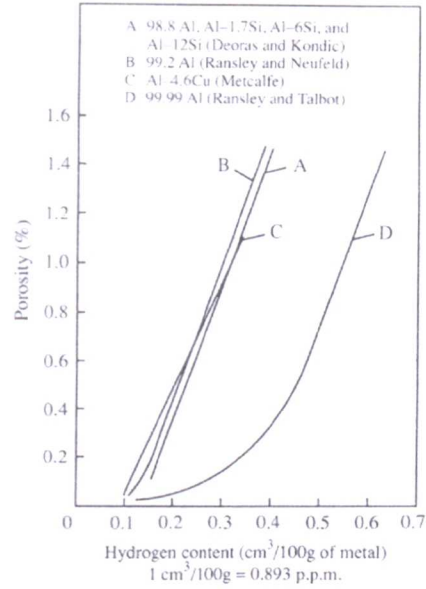


Figure 2.4: Relation between hydrogen content and porosity for sand-cast bars, 25mm diameter, of aluminium and aluminium alloys. [2]



Figure 2.5: A cross-section of an ingot showing a typical fir-tree structure. Etched in 10% NaOH at 70°C for 20 minutes. [2]

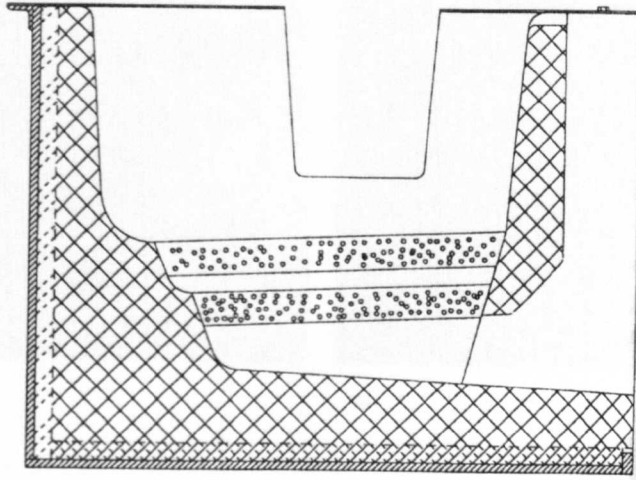


Figure 2.6: Sectional view of a staged ceramic foam filter. [7]

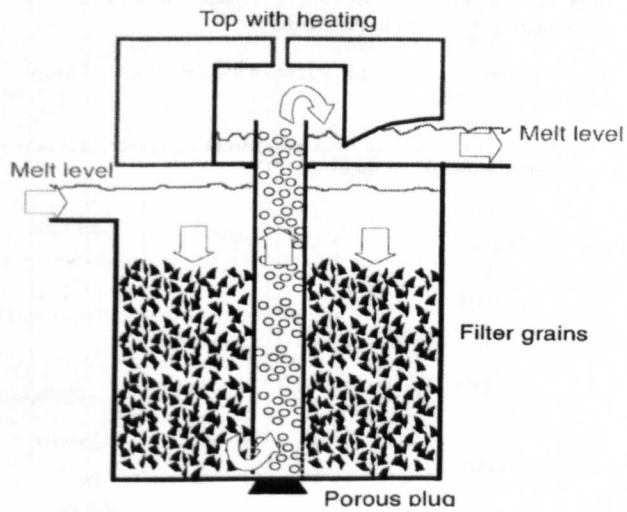


Figure 2.7: Cylindrical filter unit containing a gas-lift pump. The melt levels and flow pattern are indicated. [8]

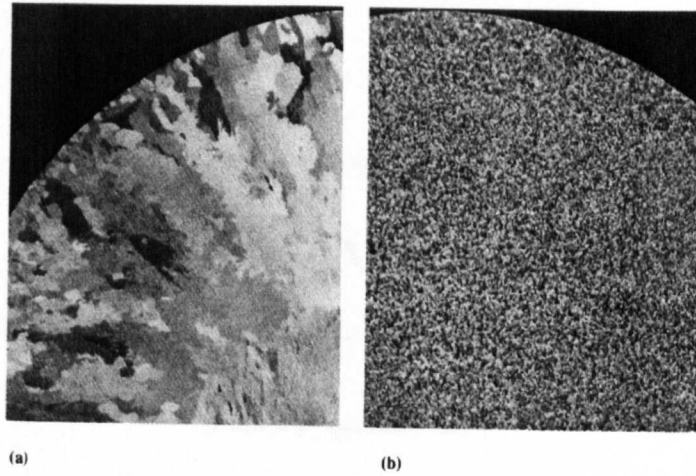


Figure 2.8: Portions of tranverse sections through two ingots of alloy 6061 that were direct chill semicontinuous cast.

(a) Ingot cast without a grain refiner. (b) Ingot showing fine equiaxed grain structure that was cast with a grain refiner [2].

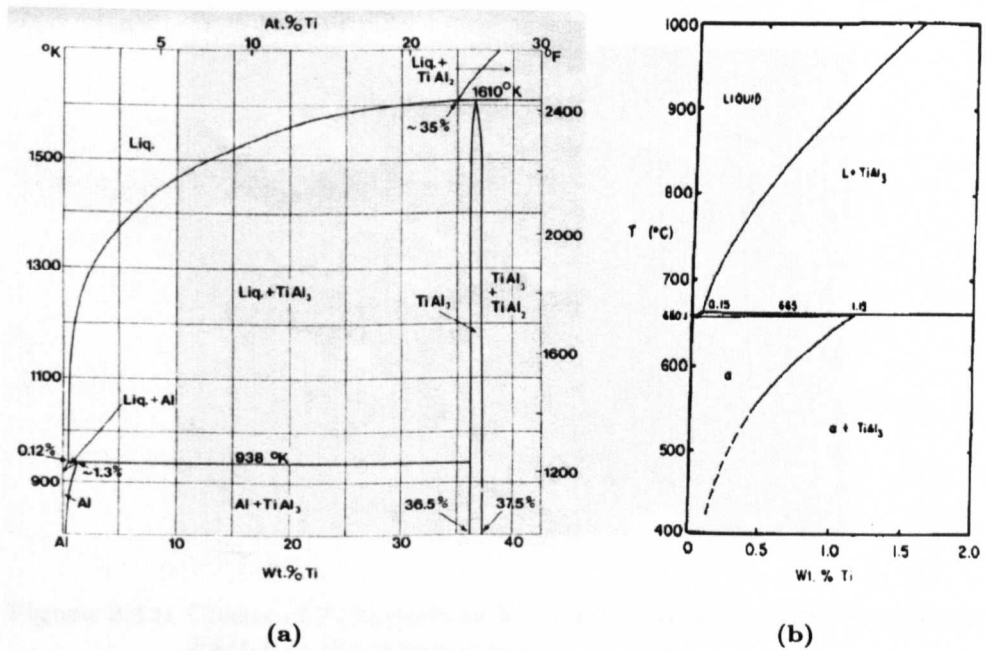


Figure 2.9: (a) The Al-Ti phase diagram [16]. (b) The aluminium rich end of the phase diagram

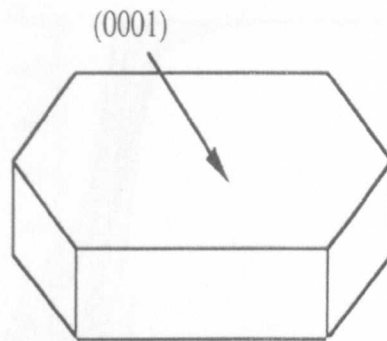


Figure 2.10: Schematic view of a hexagonal TiB_2 particle [25].

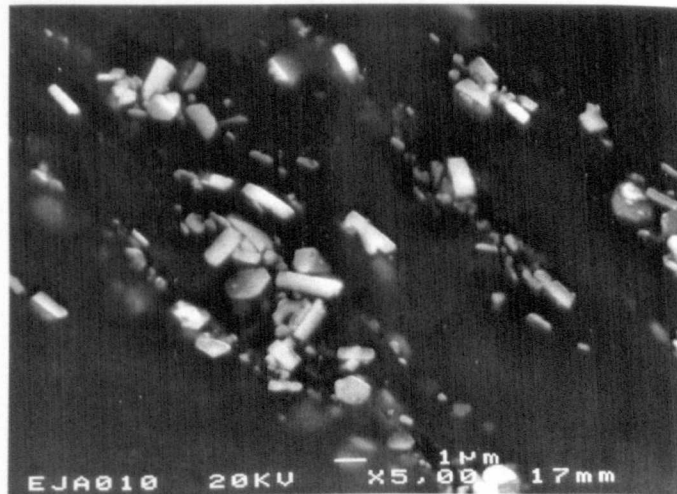


Figure 2.11: Cluster of TiB_2 particles in a Al-5Ti-1B master alloy denoted as B5/1-B in the present study.

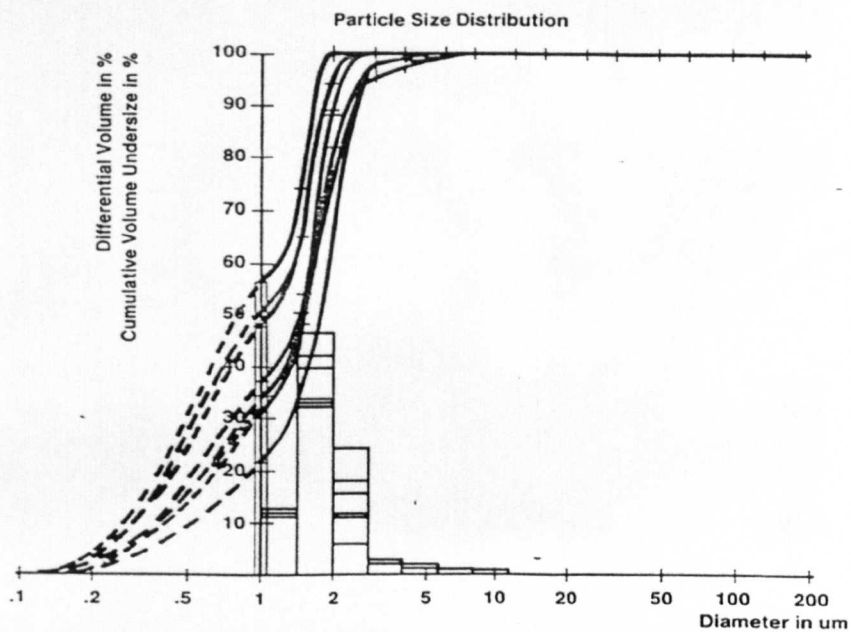


Figure 2.12: Size distribution of TiB_2 particles chemically extracted from an Al-5Ti-1B master alloy [26].

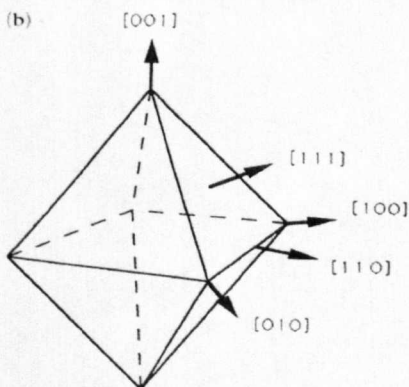


Figure 2.13: Schematic view of an octahedral TiC particle [19].

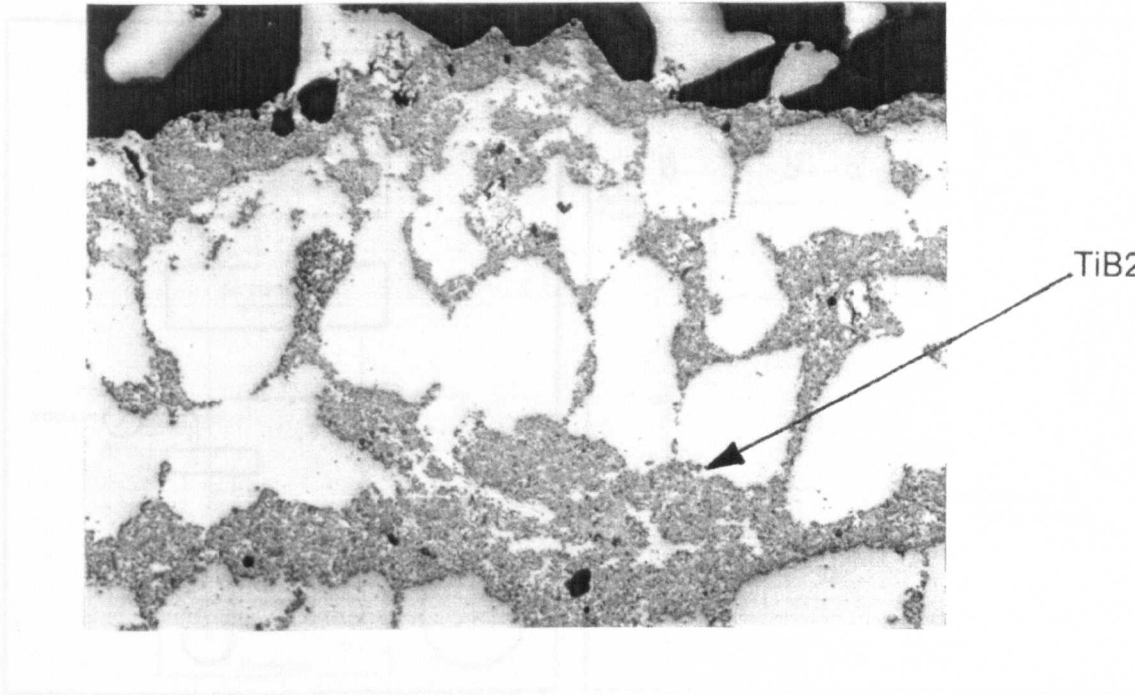


Figure 2.14: Cross-section of a PoDFA filter showing TiB_2 particles. The magnification is 200X.

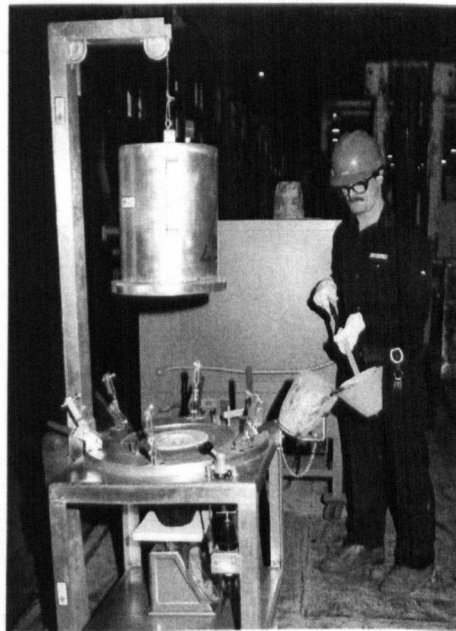


Figure 2.15: Pouring of a PoDFA sample.

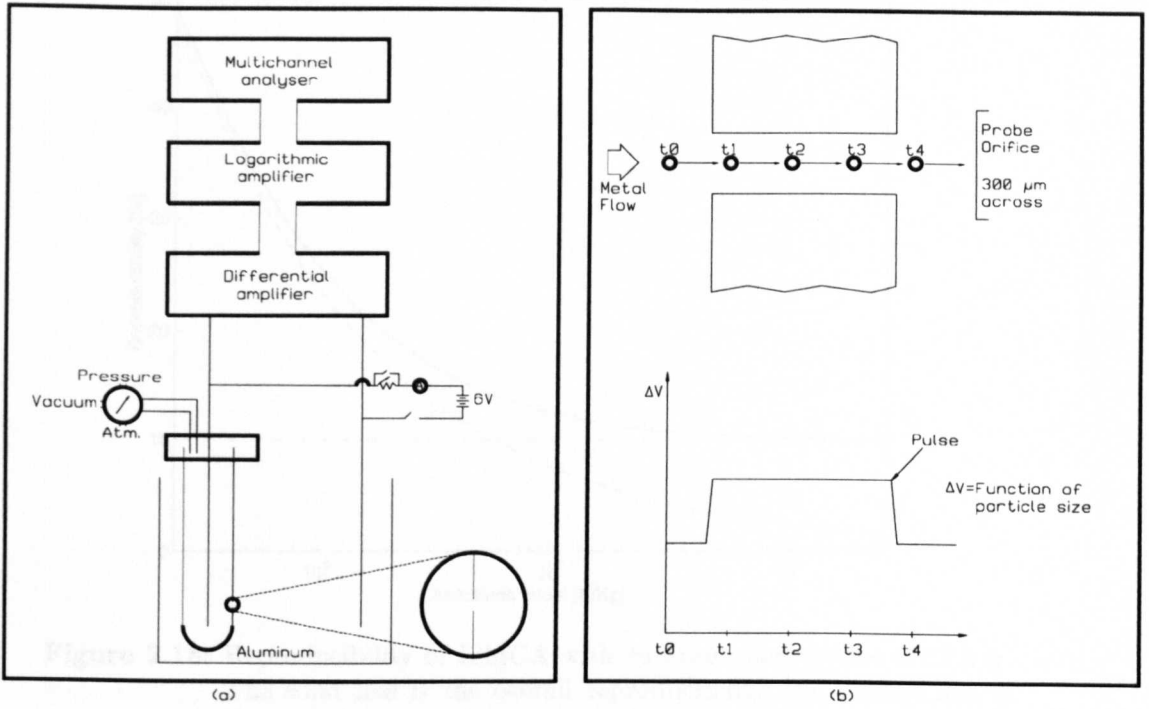


Figure 2.16: (a) Schematic of LiMCA operation. (b) Resistive pulse principle for the particle size measurement.

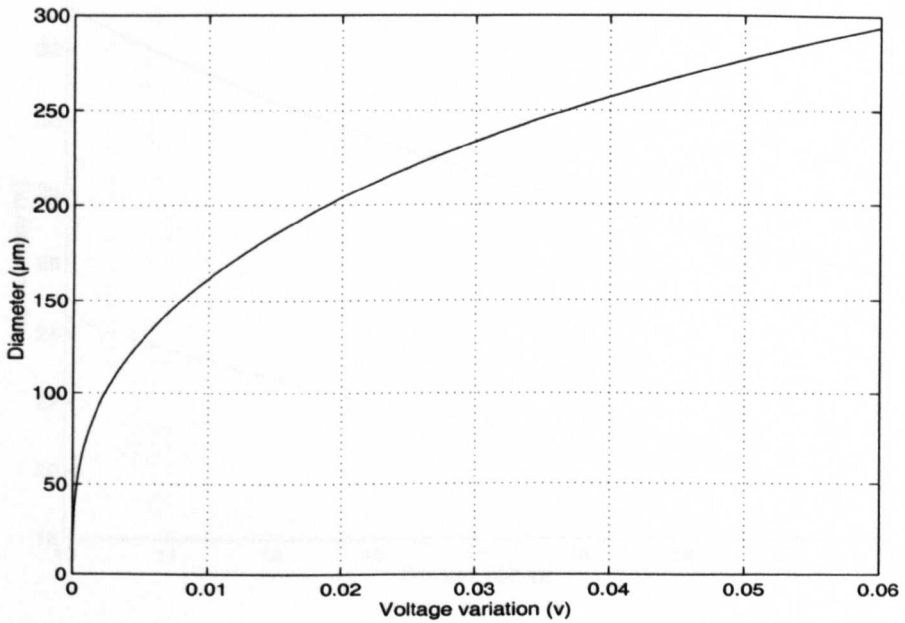


Figure 2.17: Diameter of the spherical particle as a function of the voltage variations.

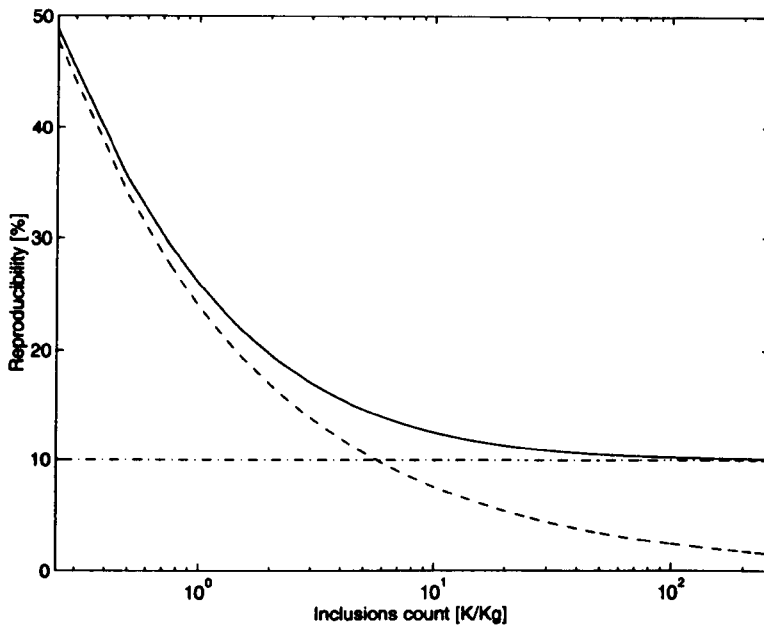


Figure 2.18: Reproducibility of LiMCA with constant sample size of 17.5 g. The solid line is the overall reproducibility, the dashed line is the statistical reproducibility and the dashed-dotted line is the instrumental reproducibility.

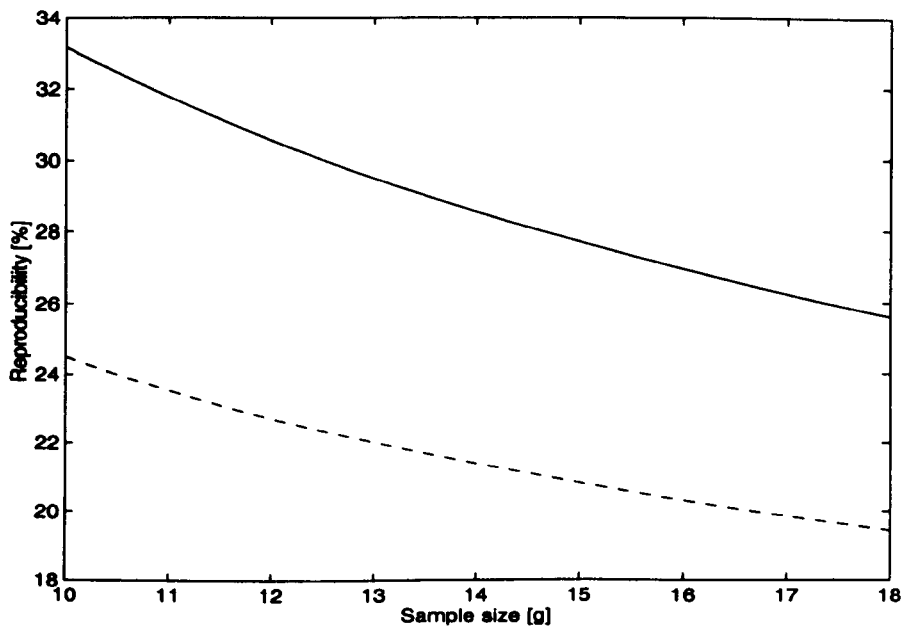


Figure 2.19: Reproducibility of LiMCA with constant inclusion count. Dashed line 2×10^3 inclusions per kilogram (2 K/Kg) and solid 1×10^3 inclusions per kilogram (1 K/Kg).

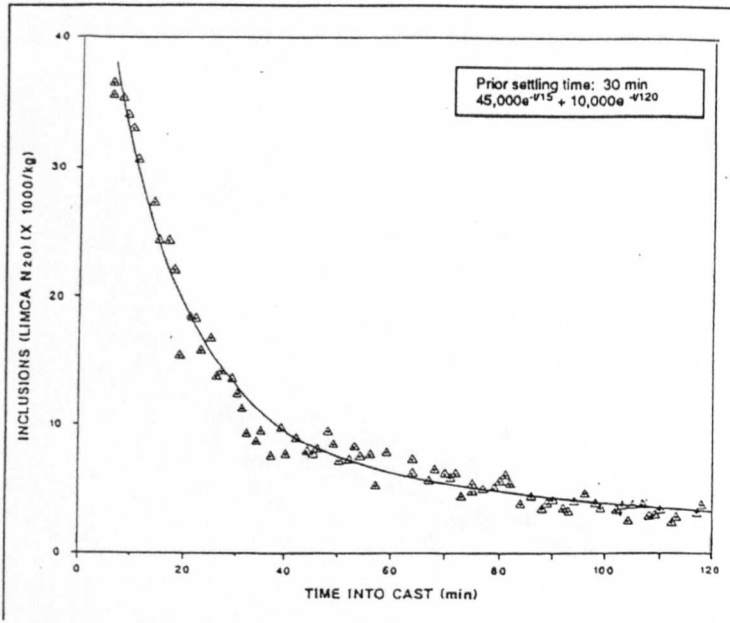


Figure 2.20: Effect of settling on the inclusions concentration measured by LiMCA at the exit of a tilting furnace [47].

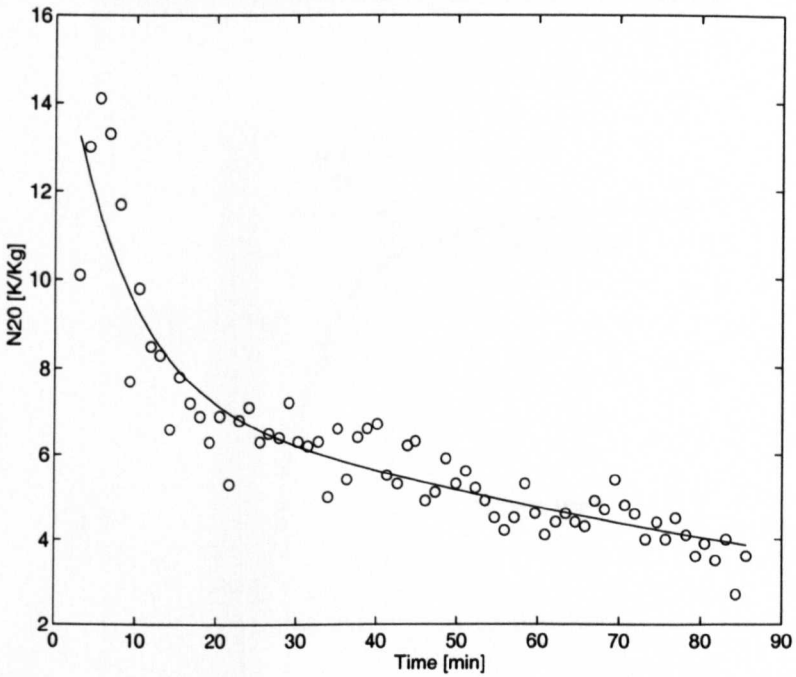


Figure 2.21: Effect of settling on the inclusions concentration measured by LiMCA in the launder of a manufacturing casthouse. Prior settling time 60 minutes. Grain refiner Al-5-Ti-1B.

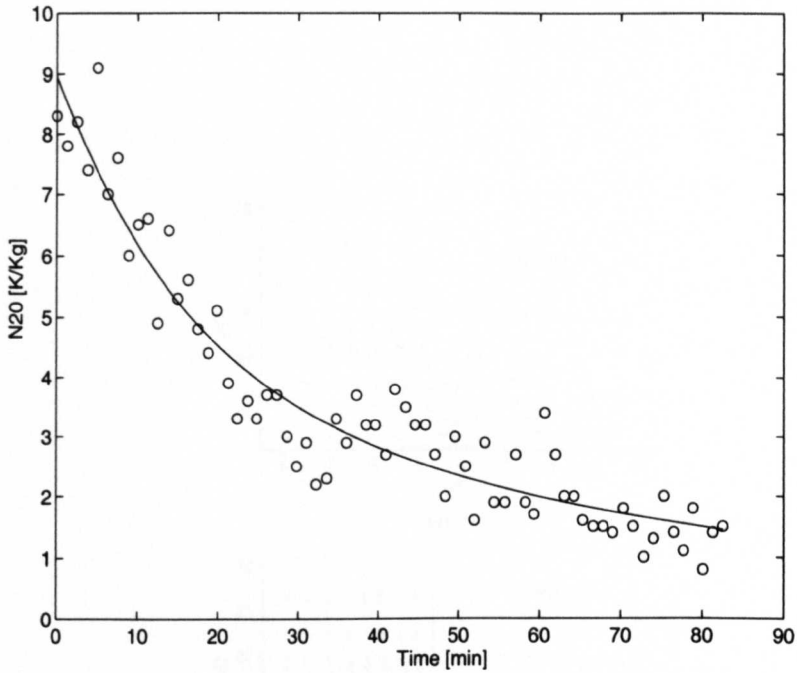


Figure 2.22: Effect of settling on the inclusions concentration measured by LIMCA in the launder of a manufacturing casthouse. Prior settling time 60 minutes. Grain refiner Al-5-Ti-1B.

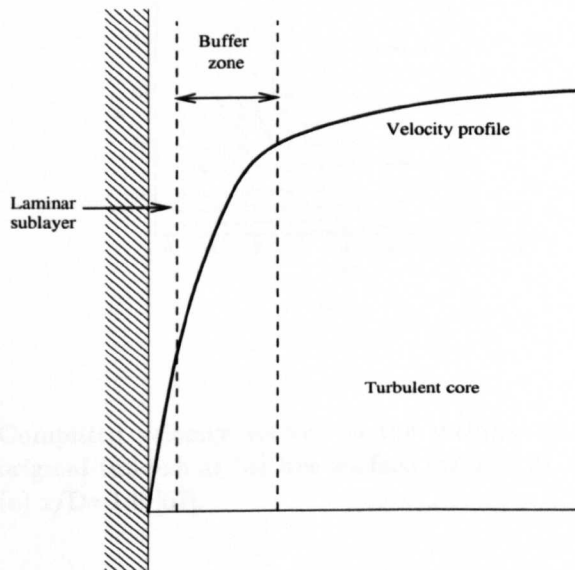
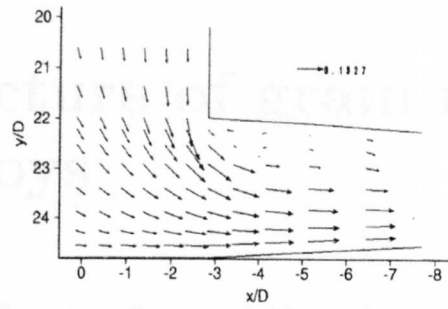
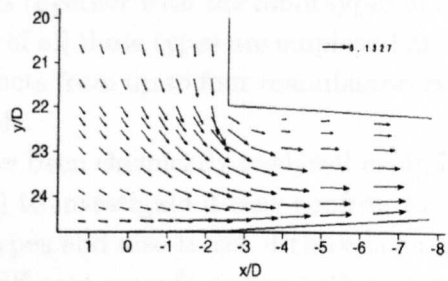


Figure 2.23: Estimated velocity profile for turbulent flow in the vicinity of a solid surface.

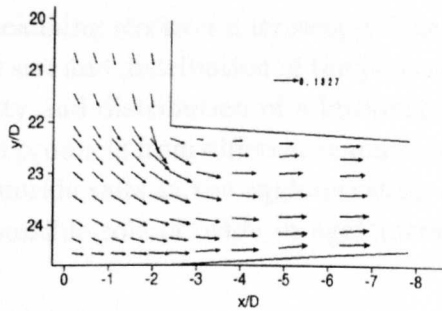
Chapter 3

Microstructure
master alloy

(a)



(b)



(c)

Figure 2.24: Computed velocity vectors in the vicinity of the bend for the original tundish at (a) free surface ($z/D=3.2$), (b) $z/D=2.4$, and (c) $z/D=1.6$ [57].

Chapter 3

Microstructure of grain refining master alloys

There are three classes of master alloys available to the aluminium industry. Table 3.1 shows these classes together with the main types of alloys available within each class. Master alloys of all these types are employed in the experimental part of this project with products from up to four manufacturers being tested for each type as shown in the table.

The master alloys have been chemically analyzed using ICP Optical Emission Spectrometry (ICP-OES) to investigate if they confirm to the nominal composition of their respective types and also to see if there is an appreciable difference between products from different manufacturers within each type.

Secondly, the microstructure of the master alloys has been investigated using optical microscopy and scanning electron microscopy. The main purpose of this is to compare the particle size and distribution of the phases. In addition, the aim is to clarify if the quantity and distribution of additional phases, e.g. salts and oxide, is different between products from different manufacturers. Finally, further evidence of the role of fluoride salts in the agglomeration of TiB_2 particles [27] will be sought and the possible role of oxide in agglomeration of TiC particles investigated.

Table 3.1: Classes and main types of master alloys.

<i>Class</i>	<i>Type</i>	<i>Nominal Composition</i>			<i>Number of products tested</i>
		<i>Ti</i> [wt %]	<i>B</i> [wt %]	<i>C</i> [wt %]	
Al-Ti	Al-6Ti	6	-	-	1
Al-Ti-B	Al-5Ti-1B	5	1	-	4
	Al-3Ti-0.2B	3	0.2	-	2
Al-Ti-C	Al-3Ti-0.15C	3	-	0.15	2
	Al-6Ti-0.03C	6	-	0.03	1

3.1 Experimental methods

The metallography of the master alloys was performed using an optical microscope (OM) and a scanning electron microscope (SEM) fitted with an energy-dispersive x-ray spectrometer (EDX). In the following the equipment, techniques and use of the instruments will be described.

3.1.1 Scanning electron microscopy

The scanning electron microscope (SEM) is a very flexible tool for analysis of the microstructure of metallic materials. The most important factors for versatility are high resolution and high depth of focus, which allows examination of samples with an uneven surface.

A schematic view of the typical design of a SEM is shown in Figure 3.1. The electron optical column consists of the electron gun and two or more electron lenses. The electron gun (normally with a tungsten filament) accelerates electrons down the column, through the lenses and scanning coils. The acceleration voltage is usually 1-50keV. The lenses in the column focus the beam to a small diameter. The diameter can vary from 1-10nm, depending on the resolution of the instrument [61]. The electron beam scans the specimen in similar way as in a cathode ray tube (CRT) used for image formation on a television set. The position of the beam is controlled with the scanning coils and it deflects the beam along closely spaced lines. The electrons excited by the electron beam and emitted from the specimen are collected in an electron detector. The current of the electrons hitting the detector is smaller than the primary beam current and must be amplified. The amplified signal controls the brightness of the beam in a CRT, which is synchronized with the primary beam in the column. The output for the user is then an image on a monitor of the surface of the specimen [62].

When the electron beam hits the specimen, electrons and other radiation are emitted from the specimen. Figure 3.2 shows the types of signals which are relevant for the analysis in the present project [62], i.e. the backscattered electrons, secondary electrons and x-rays.

Backscattered electrons are produced by single large angle or multiple small-angle elastic scattering. The energy distribution of backscattered electrons depends on the primary energy of the incident electrons, the number of outer-shell electrons, the atomic number of the material and the surface inclination of the specimen [62]. Therefore, yield energy spectrum and depth of escape of backscattered electron is proportional to the atomic number of the material.

Secondary electrons are formed by interaction of the primary electrons with loosely bound atomic electrons. The energy spectrum of the secondary electrons is independent of the energy of incident electrons and the specimen material. An important characteristic of secondary electrons is their shallow

Table 3.2: Chemical analysis of the Al-6Ti master alloy.

Master alloy	Element (wt %)										
	Si	Fe	Cu	Mn	Mg	Cr	Ni	Zn	Ti	B	C
Al-6Ti	.07	.15	<.01	.1	<.01	<.01	<.01	<.01	6.16	<.01	<.001

sampling depth, a direct consequence of the low kinetic energy with which they are generated.

X-rays excited by the electron beam generate two types of spectra. The spectra used for energy-dispersive x-ray spectrometer (EDX) is characteristic radiation with a distinct line spectrum. The depth of information from the specimen ranges from 1-10 μ m, depending of the energy in the primary electron beam and the atomic weight of the specimen. In this project, the EDX detector on the SEM instrument used could detect boron and all elements with a higher atomic number.

The size of samples for SEM analysis can vary from few square millimeters to square centimeters. The size is controlled by the size of the vacuum chamber. The surface of the samples can be rough, the focus length is ranging from 1 μ m to 2mm depending on the magnification [62]. The samples must conduct electricity, otherwise the electrons cannot penetrate it and give the response signal.

The majority of the SEM work presented in this chapter, was done on a Cambridge Instruments SEM, with an EDX detector from Oxford Instruments, model 5431. The EDX detector can detect elements down to boron. However, detection of boron is not reliable with this instrument, boron peaks and carbon peaks usually overlap, which makes analysis difficult. The instrument has a digital imaging unit for photography.

3.2 The Al-6Ti master alloy

Al-6Ti master alloy from one producer was used in the experimental part of the project. The chemical analysis is given in Table 3.2. Figure 3.3 shows a cross section of the master alloy used. Large $TiAl_3$ particles are seen and a few small $FeAl_3$ particles in an α -aluminium matrix.

The size of the $TiAl_3$ particles is ranging from 20 to 100 μ m.

3.3 The Al-5Ti-1B master alloy

The Al-5Ti-1B master alloys tested in this study, were manufactured by four different producers, A,B,C and D. The marking of each type is as follows: The first letter indicates the the secondary addition element in the master alloy, which is B for boron, the numbers indicate the titanium-boron ratio and the last letter

Table 3.3: Chemical analysis of the Al-5Ti-1B master alloys.

Master alloy	Element (wt %)										
	Si	Fe	Cu	Mn	Mg	Cr	Ni	Zn	Ti	B	C
<i>B5/1-A</i>	.06	.16	<.01	.1	<.01	<.01	<.01	<.01	5.05	1.03	<.001
<i>B5/1-B</i>	.06	.12	<.01	<.01	<.01	<.01	<.01	<.01	4.95	0.99	<.001
<i>B5/1-C</i>	.07	.11	<.01	.1	<.01	<.01	<.01	<.01	4.98	1.01	<.001
<i>B5/1-D</i>	.06	.09	<.01	.1	<.01	<.01	<.01	<.01	5.00	0.98	<.001

stands for the producer. Therefore, *B5/1-C* is an Al-5Ti-1B master alloy from producer C.

Information on the production method of each type of master alloy and processing parameters are proprietary and cannot be used to distinguish between different types. The chemical analysis of the four types is given in Table 3.3.

In the work of Gudmundsson [27], it was suggested that salts present in the Al-5Ti-1B master alloy act as a gluing compound in the TiB_2 clusters. To investigate this further, samples of master alloys *B5/1-A* and *B5/1-C* were fractured and analyzed in a scanning electron microscope. The samples were fractured longitudinally and examined unpolished, to prevent dissolution of water soluble substances. Figure 3.4 shows a TiB_2 cluster marked with an "A" in the *B5/1-B* alloy. The size of the cluster is approximately 20 μm . This is the largest cluster observed by microscopy in the TiB_2 containing master alloys in this study. The EDX spectra of the marked spots are shown in Figures 3.5 to 3.7. The spectra show the existence of both fluorine (F) and potassium (K) within the TiB_2 cluster and some oxygen is also detected. The EDX spectra from other clusters in this sample produced similar results, although the titanium peaks were sometimes higher. Figure 3.8 shows a TiB_2 cluster marked with an "A" in the *B5/1-A* alloy. The EDX spectra of the marked spots are shown in Figures 3.9 and 3.10. The spectrum for spot A within the cluster shows the existence of fluorine (F), potassium (K) and oxygen (O). The spectrum for spot B which is outside the cluster only shows aluminium and titanium which is consistent with the α -phase of the base metal. Three other TiB_2 clusters from the *B5/1-A* alloy were analyzed and the results were consistent with the first one. Samples of master alloys *B5/1-C* and *B5/1-D* were subsequently analyzed and gave the same results. This shows that TiB_2 particle clusters in the Al-5Ti-1B master alloys contain fluoride salts. The origin of the salts is in the substances used in the production as described in Equations 2.1 and 2.2. The effect of the salts was not analyzed further in this study.

As seen in Figures 3.5 and 3.9 the clusters also contain oxygen presumably indicating the presence of oxide. This was also reported by Gudmundsson [27]. The possible role of oxides in the TiB_2 cluster formation has not been discussed in the literature.

Table 3.4: Analysis of the microstructure of the Al-5Ti-1B master alloys.

Master alloy	Average size of $TiAl_3$ [μm]	Texturing of TiB_2	Inclusions (Oxides/salts)
<i>B5/1-A</i>	50	Slight	Many
<i>B5/1-B</i>	35	High	Few
<i>B5/1-C</i>	35	High	Few
<i>B5/1-D</i>	45	None	Few

The four different master alloys were sectioned longitudinally and polished for examination. The microstructure is shown in Figures 3.11, 3.12, 3.13 and 3.14. They show the microstructure at two different magnifications, 50x and 200x. The large particles seen are $TiAl_3$ particles and the small ones are TiB_2 . Also seen in the figures are a few dark spots containing impurities which are discussed below.

There are a few characteristics which differ between types of master alloys. The first difference is the size of the $TiAl_3$ particles. The largest $TiAl_3$ particles are detected in the *B5/1-A* master alloy. There, the average size of the $TiAl_3$ particles is 50 μm but in *B5/1-D* it is 45 μm and in *B5/1-B* and *B5/1-C* it is only 35 μm .

Another difference is the level of texturing of the TiB_2 particles. The texturing is an effect of the production method which is possibly rolling when texturing is observed. Master alloys *B5/1-B* and *B5/1-C* show obvious texturing and alignment of the diboride particles along the length of the master alloy rod as shown in Figures 3.12 and 3.13. There is some texturing in master alloy *B5/1-A* but it is less than for the previous two. The TiB_2 particles are well dispersed in *B5/1-D*.

The inclusions seen in the microstructure of the master alloys were also analyzed. Their quantity was highest in *B5/1-A*. Figures 3.15 and 3.17 show a backscatter images of these spots. The color of the inclusions indicates an element lighter than aluminium. The spots were chemically analyzed using EDX and Figures 3.16 and 3.18 show the results. There is a large amount of oxygen present in the inclusions and this indicates oxides, probably aluminium oxide. The spectra also show the presence of potassium and fluorine indicating the presence of potassium aluminium fluoride salts originating from the TiB_2 production reaction (see Equation 2.1). The spectra also show the presence of titanium and boron. These elements can either be due to the presence of TiB_2 particles in close connection with the inclusions or it can also be suggested that the inclusions may contain some unreacted salts from the TiB_2 formation process.

Finally, Table 3.4 summarizes the main difference between the four types of Al-5Ti-1B master alloys.

Table 3.5: Chemical analysis of the Al-3Ti-0.2B master alloys.

Master alloy	Element (wt %)										
	Si	Fe	Cu	Mn	Mg	Cr	Ni	Zn	Ti	B	C
<i>B3/.2-A</i>	.03	.13	<.01	<.01	<.01	<.01	<.01	<.01	2.84	0.20	<.001
<i>B3/.2-B</i>	.02	.09	<.01	<.01	<.01	<.01	<.01	<.01	1.49	0.10	<.001

3.4 The Al-3Ti-0.2B master alloy

The Al-3Ti-0.2B master alloys tested came from two producers and they are labelled *B3/.2-A* and *B3/.2-B*. The chemical analysis is given in Table 3.5. The chemical analysis revealed that *B3/.2-B* did not have the expected chemical composition. The level of titanium and boron was only fifty percent of the value stamped on the coil. This master alloy was, therefore, not included further in the experimental programme.

The *B3/.2-A* master alloy was sectioned and polished for examination. The microstructure is shown in Figures 3.19 which show the microstructure at different magnification. The large particles seen are $TiAl_3$ particles and the TiB_2 particles are the small particles. The quantity of $TiAl_3$ particles in *B3/.2-A* is similar to the Al-5Ti-1B master alloys but the quantity of TiB_2 particles is much less. The distribution of titanium between the $TiAl_3$ and TiB_2 phases in Al-Ti-B master alloys can be seen in Table 6.2.

3.5 The Al-3Ti-0.15C master alloys

The Al-3Ti-0.15C master alloys employed in the present study were produced by two manufacturers and the alloys are labelled *C3/.15-A* and *C3/.15-B*. Master alloy *C3/.15-A* was specially prepared for this project with a high oxide content but *C3/.15-B* is commercially available.

Information on the production methods for each type of the master alloys and the processing parameters are proprietary and cannot be used to distinguish between the two types. The chemical analysis is given in Table 3.6. The relatively high iron content is noteworthy. This indicates addition of some iron containing compounds to these master alloys, possibly similar to the ferrotitanium or ferrocantitanium alloys used by the steel industry.

The examination procedure for fractured master alloy samples described in Section 3.3 was also used on the Al-3Ti-0.15C master alloys. Figure 3.20 shows a TiC cluster marked with "A" in the *C3/.15-B* rod. The cluster is approximately 15 μm in size. Spot B is at the side of the cluster in the α -phase of the base metal. The EDX spectra for the marked spots are shown in Figure 3.21 and Figure 3.22. The spectrum for spot A shows the existence of titanium, carbon and oxygen in the cluster and no traces of salts which was expected because

Table 3.6: Chemical analysis of the Al-3Ti-0.15C master alloys.

Master alloy	Element (wt %)										
	Si	Fe	Cu	Mn	Mg	Cr	Ni	Zn	Ti	B	C
<i>C3/.15-A</i>	.03	.96	<.01	<.01	<.01	<.01	<.01	<.01	3.16	<.01	.128
<i>C5/.15-B</i>	.05	.97	<.01	<.01	<.01	<.01	<.01	<.01	3.09	<.01	.138

of the production method for Al-Ti-C master alloys. The spectrum for spot B shows only aluminium and titanium which is consistent with the α -phase of the base metal. Figure 3.23 shows a TiC cluster marked with "A" in the *C3/.15-A* rod. Spot B is at the side of the cluster in the α -phase. The EDX spectra of the marked spots are shown in Figure 3.24 and Figure 3.25. The results are the same as for the *C3/.15-B* master alloy.

The TiC clusters were analyzed further using polished samples of the master alloys. Figure 3.26 shows a TiC particle cluster found in the *C3/.15-A* master alloy. The size of the cluster is around $10 \times 20\mu m$ which is much larger than previously reported in literature. Figures 3.27, 3.28 and 3.29 show the EDX spectra of the spots marked in Figure 3.26. Titanium and carbon and oxygen are detected. This leads to the assumption that TiC clusters are associated with oxides, although the quantity of oxygen is low in the clusters.

Figure 3.30 shows a backscatter image of TiC particle clusters in *C3/.15-A*. The large blocky particles are $TiAl_3$ particles. Two groups of TiC are seen, one long and narrow at the top, which is longer than the figure shows and another in the middle of the picture, which is $90 \times 50\mu m$. The difference between these groups and the cluster shown in Figure 3.26, is the black underlying phase in the former. Figure 3.31 shows the EDX spectrum of the whole surface in Figure 3.30. Titanium and carbon are clearly detected and the oxygen level is significant. Figures 3.32, 3.33 and 3.34 show the EDX spectra for the measurement points in Figure 3.30. Aluminium, titanium, oxygen, carbon and iron are detected. The most important finding is that the black phase seen in Figure 3.30 is oxygen rich, presumably in the form of oxide. The TiC particles appear to have a tendency to accumulate in areas where oxide is present in the master alloy.

The microstructure of *C3/.15-A* and *C3/.15-B* is shown in the optical micrographs in Figures 3.35 and 3.36. The large particles are $TiAl_3$ and the small particles are carbides. The size of the $TiAl_3$ particles is similar in both master alloys but they are possibly slightly smaller and better dispersed in *C3/.15-B*. The level of texturing of the TiC particles is similar, and not unlike the texturing of the TiB_2 particles in the Al-Ti-B master alloys. The Al-3Ti-0.15C alloys are, therefore, possibly also rolled during production.

The main difference between the two master alloys appears to be in the oxide content. Large oxides strings (up to $1000\mu m$) are present in the *C3/.15-A* master alloy as seen in Figure 3.35 (200x), but such strings are not seen in *C3/.15-B*.

Table 3.7: Chemical analysis of the Al-6Ti-0.03C master alloy.

Master alloy	Element (wt %)										
	Si	Fe	Cu	Mn	Mg	Cr	Ni	Zn	Ti	B	C
C6/.03-A	.03	.15	<.01	<.01	<.01	<.01	<.01	<.01	5.83	<.01	.034

3.6 The Al-6Ti-0.03C master alloy

One Al-6Ti-0.03C master alloy was employed in this project. The chemical analysis is given in Table 3.7. The master alloy was sectioned and polished for examination using the same procedure as before. The microstructure is shown in Figure 3.37. The large particles seen are $TiAl_3$ and inclusions are also visible. The TiC particles were not observed by optical microscopy. The microstructure is similar to that of the Al-6Ti master alloy, it has the same amount of titanium and the carbon content is so small that only a very low percentage of the titanium is in the form of TiC particles.

3.7 Discussion

The chemical analysis of the master alloys show that in all cases except one the actual composition is in good agreement with the nominal composition. In that single case, the measured composition is exactly half the nominal composition stamped on the rod. This is most probably a manufacturing defect and this emphasizes the need for rigid quality control in master alloy production and use. Apart from this particular case, the same types of products from different manufacturers give essentially the same chemical analysis.

The investigation of the microstructure of the master alloys shows that the $TiAl_3$ particles have similar general characteristics in all the alloys investigated. Their average size ranges from 35-50 μ m and the maximum size observed was approximately 100 μ m.

The TiB_2 particles in the Al-Ti-B master alloys appear to be similar in size in all types examined by optical microscopy. Their distribution is, however, significantly different due to the difference in the level of texturing of the TiB_2 particles, i.e. the level of alignment along definite lines in the longitudinal direction of the rods. This feature is possibly the result of rolling in the manufacture of the rods or other production methods which give a similar effect. The texturing results in a concentration of the TiB_2 particles along specific lines in the rods. This effect seems likely to promote particle agglomeration both in the rod itself and during the addition into the melt in a launder.

The presence of oxygen, fluorine and potassium was confirmed in TiB_2 particle clusters observed in the Al-5Ti-1B master alloys. The size of these clusters was up to 20 μ m which is similar to those found by Gudmundsson [27].

In the work of Gudmundsson [27] he concluded that potassium aluminium fluoride salts act as a form of glue in the agglomeration of the TiB_2 particles in master alloys. The presence of such salts is confirmed in the clusters analyzed in the present work but they also contain oxides, presumably aluminium oxides. The effect of the oxide will be further discussed below.

In the micrographs of the TiB_2 containing master alloys, the impurities in the alloys are usually seen to be associated with the TiB_2 particles. Their analysis show the presence of oxygen, fluorine and potassium. These can be explained as being aluminium oxide and potassium aluminium fluoride salts from TiB_2 production reaction. In addition they show the presence of titanium and boron. The latter elements can either be due to the presence of TiB_2 particles in a close connection with the impurities or it can also be proposed that the impurities may contain some unreacted salts from the TiB_2 formation process. A comparison between the EDX spectra for the TiB_2 particle clusters and the impurities reveals that they show essentially the same features. Therefore, it seems likely that the latter may become a further source of the same type of glue for TiB_2 particle agglomeration as found in the TiB_2 clusters. They can become effective during the melting process in the launder or in the aluminium melt due to their close association with the TiB_2 particles.

The number, size and distribution of the impurities differs between the Al-5Ti-1B master alloys. The reason for this is not clear. The impurities show a similar tendency towards texturing as the TiB_2 particles. The B5/1-A master alloy shows by far the largest quantity of impurities and they are most often in close combination with the TiB_2 particles in the rod. The reason for the observed difference in the quantity of the impurities is not known, but it seems more likely that this is due to an increased oxide content of the master alloy than to an increase in the fluoride salt content. The fluoride salt addition should be similar for the same final $TiAl_3$ and TiB_2 content in the master alloys.

The Al-Ti-C master alloys contain no fluoride salts resulting from the TiC formation. The TiC particles, on the other hand, appear to show an affinity for oxides. The TiC particle clusters that were found in alloy C3/.15-A, which was specially prepared for this study with a relatively high oxide content, all contain oxide, presumably aluminium oxide. The oxide, therefore, appears to promote the particle agglomeration as suggested by industry [23]. TiC clusters up to $2\mu\text{m}$ in size have been previously reported [19, 21]. However, the cluster size observed in present work is much larger, i.e. well above $20\mu\text{m}$. The Al-Ti-C alloys also show the presence of impurities which now mainly contain aluminium oxide. The two Al-3Ti-0.15C master alloys contain a relatively high amount of iron and some iron was also detected in the impurities. Any effect of the iron in the agglomeration process is not apparent at the present time.

In looking at particle agglomeration in the master alloys and subsequently in the aluminium melt in a launder, the main observations in the present mi-

crostructure analysis are as follows:

The texturing in the particle distribution of the TiB_2 and TiC particles results in particle concentration along specific lines in the master alloy rods. The impurities in the alloys are usually distributed along the same lines. It seems likely that an increased level of texturing increases the tendency towards particle agglomeration if this tendency is present in the alloys. Discussion of the effect of texturing on the agglomeration rate has not been seen in the literature.

The presence of oxide in TiC particle clusters in Al-Ti-C master alloys has been confirmed. The oxide, presumably aluminium oxide, is in a solid form in aluminium melts both in the master alloy production and in the launder. In industry the oxide has been considered to promote particle agglomeration in these alloys [23]. The present study supports this. Increased oxide content of the Al-Ti-C master alloys, e.g. in the form of impurities, should therefore increase the probability of particle agglomeration. The binding mechanism between the two relatively inert components, i.e. Al_2O_3 and TiC , is not clear.

The presence of oxide and potassium aluminium fluoride salts has been confirmed in the TiB_2 particle clusters. A similar composition is found in the impurities which are usually associated with TiB_2 particles. Gudmundsson [27] has proposed that a thin fluid potassium aluminium fluoride film on the surface of the TiB_2 particles in a melt acts as a glue for the particle agglomeration. The influence of the oxide, presumably aluminium oxide, in the film is not included in the model as it is in a solid form in the melt. A variation of this model is to assume that some unreacted salts from the TiB_2 formation process are present at the TiB_2 particle surface after their production and these subsequently form a bond though a further reaction at the particle interfaces. The present analysis of the TiB_2 containing master alloys could support both these models. It seems likely, however, considering the observations of the role of oxide in the TiC particle agglomeration, that there can be other forces present involving the oxide as discussed for the TiC particles above. In general it can be said, however, that an increase in the quantity of impurities in the Al-Ti-B master alloys will probably increase the rate of particle agglomeration. A discussion of this effect has not been seen in the literature.

3.8 Figures

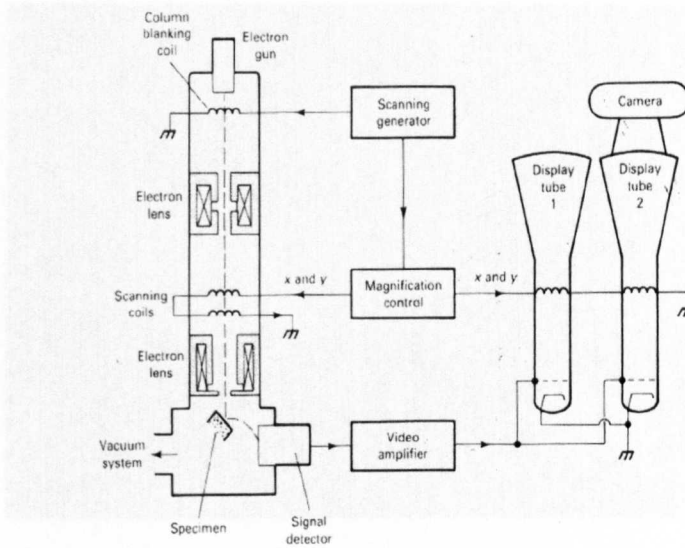


Figure 3.1: Typical design of a scanning electron microscope (SEM) for secondary electron imaging [62].

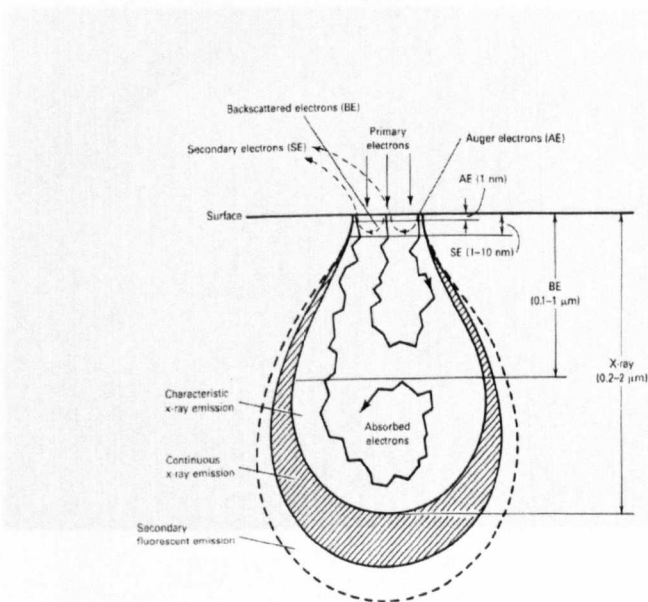
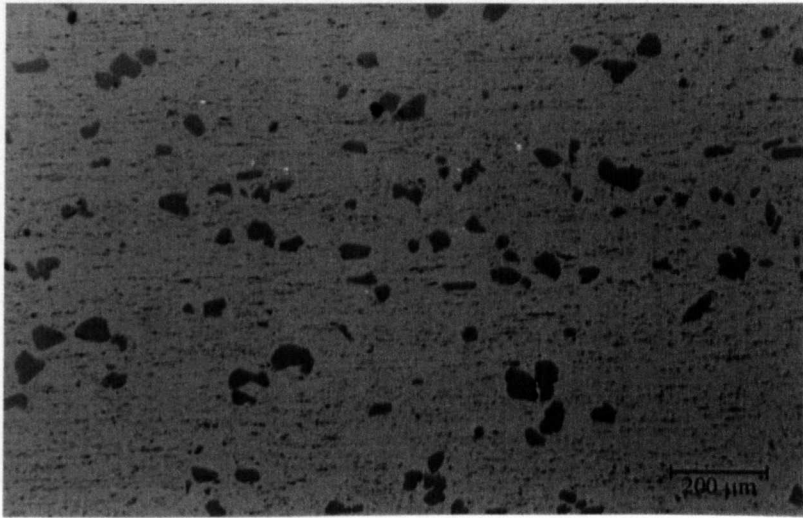
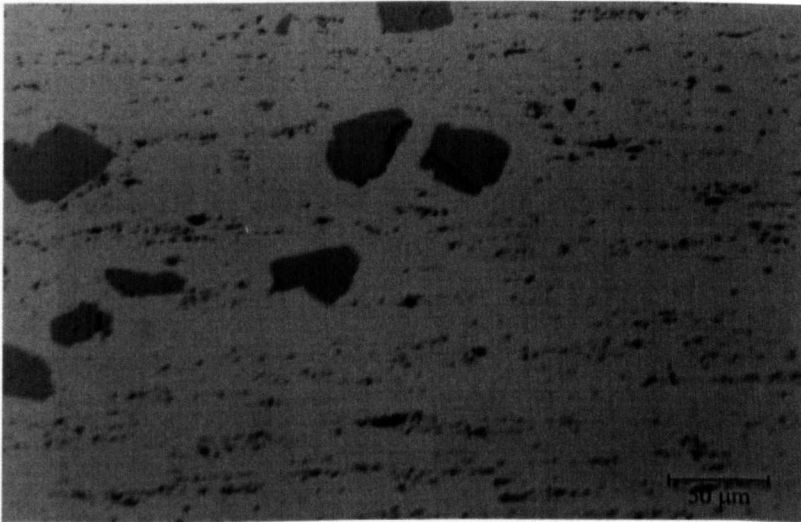


Figure 3.2: Types of electron-beam-excited electrons and radiation used in a SEM and the depth of the region below the specimen surface from which information is obtained [62].



(a) 50x



(b) 200x

Figure 3.3: Polished surfaces of the Al-6Ti master alloy. Magnification 50x and 200x. The grey particles are $TiAl_3$ and the dark spots are impurities.



Figure 3.4: TiB_2 cluster in the *B5/1-B* master alloy. EDX spectra of spots A, B and C, are shown in Figures 3.5, 3.6 and 3.7.

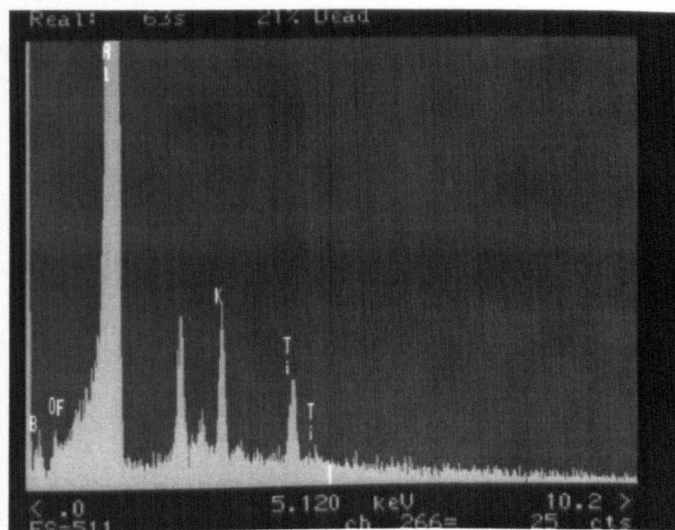


Figure 3.5: The EDX spectrum of spot A in Figure 3.4. The unmarked large peak between Al and K is 2xAl peak.

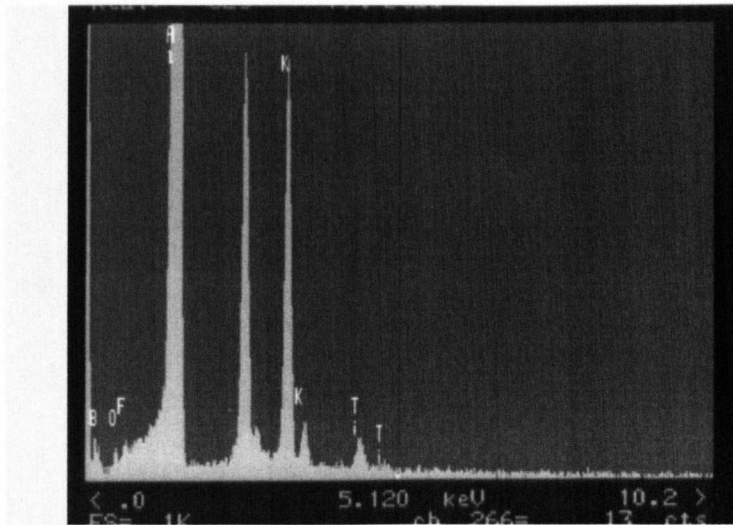


Figure 3.6: The EDX spectrum of spot B in Figure 3.4. The unmarked peak between Al and K is 2xAl.

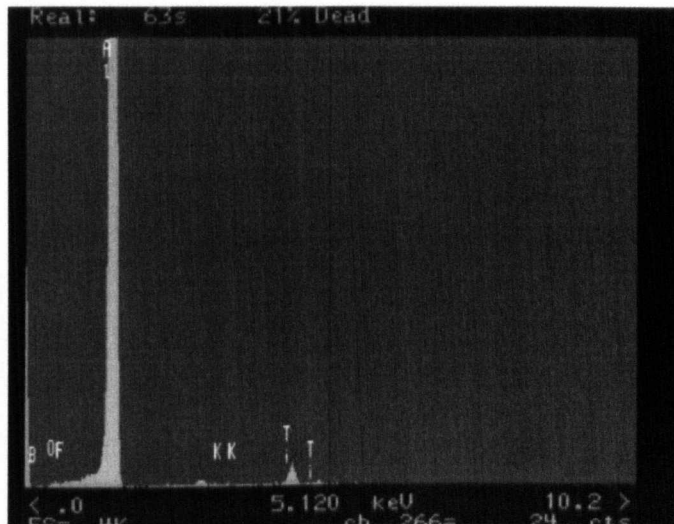


Figure 3.7: The EDX spectrum of spot C in Figure 3.4.

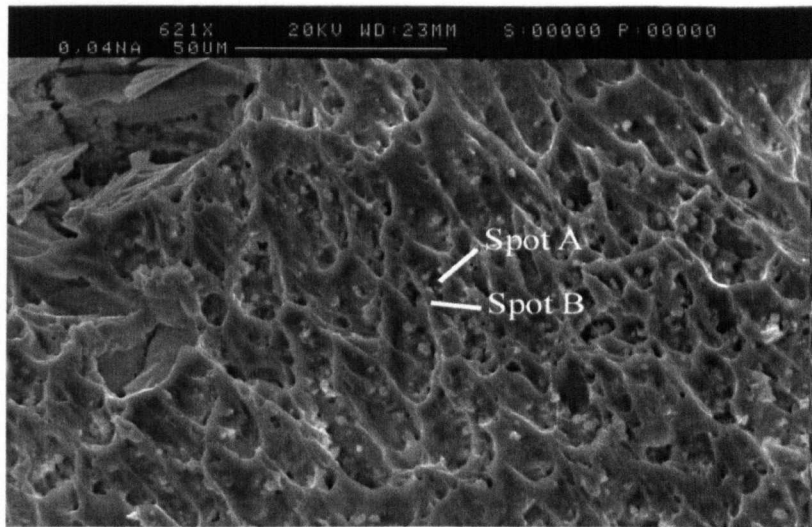


Figure 3.8: TiB_2 cluster in the $B5/1-A$ master alloy marked "A". EDX spectra of spots A and B which is in the α -phase, are shown in Figures 3.9 and 3.10.

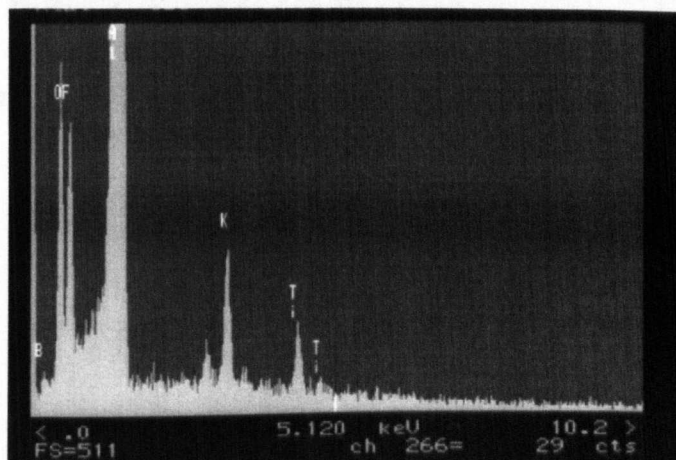


Figure 3.9: The EDX spectrum of spot A in Figure 3.8. The unmarked peak between Al and K is $2xAl$.

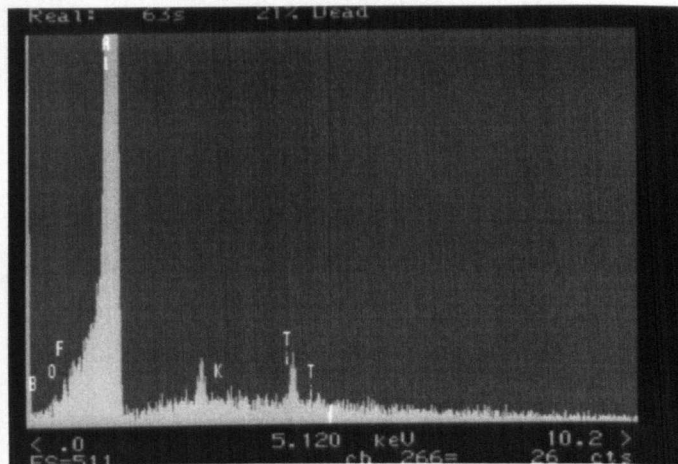
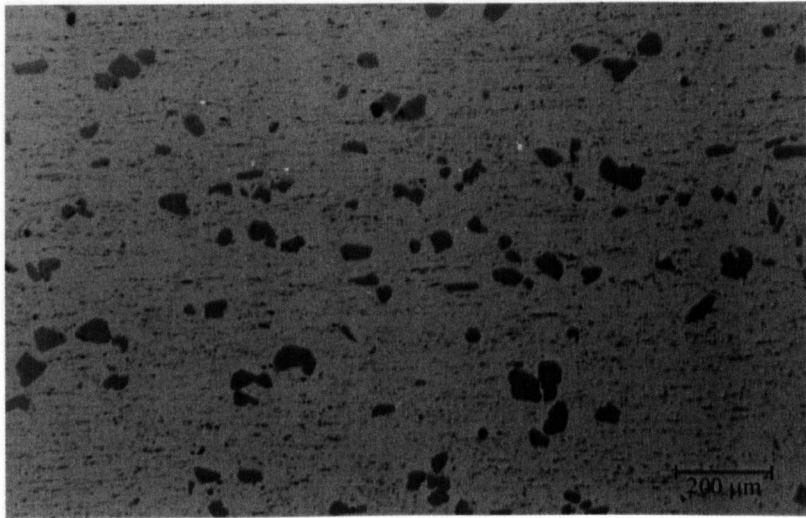
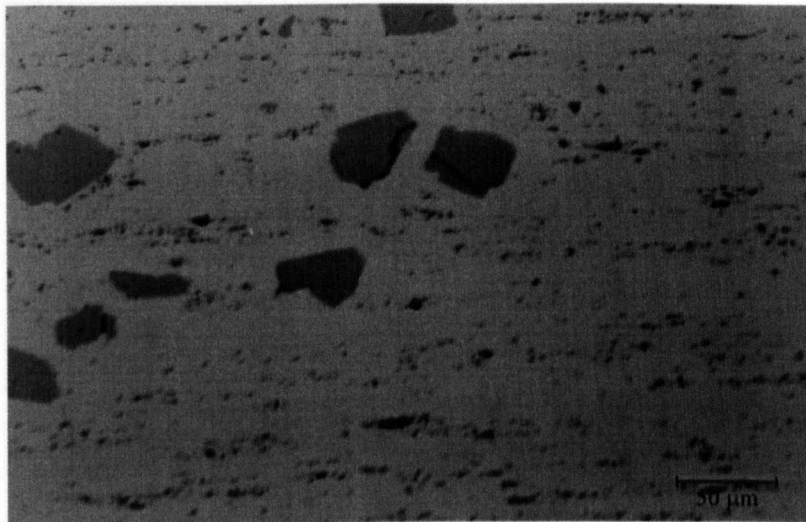


Figure 3.10: The EDX spectrum of spot B in Figure 3.8. The unmarked peak between Al and K is 2xAl.

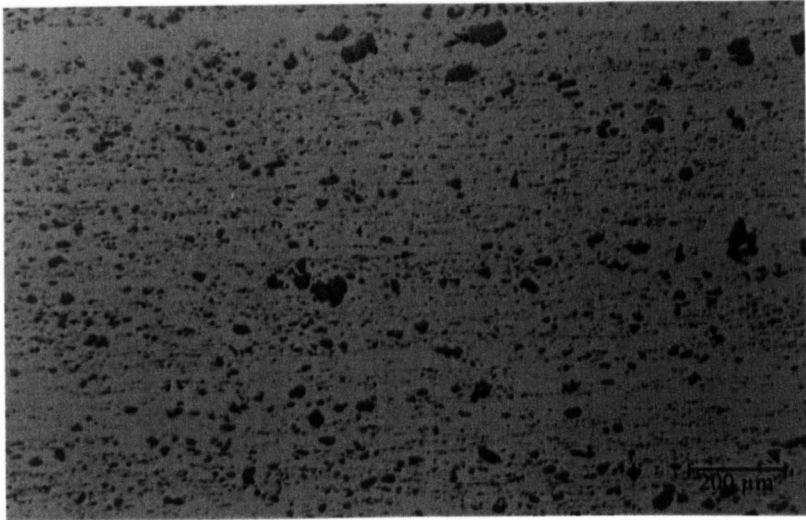


(a) 50x

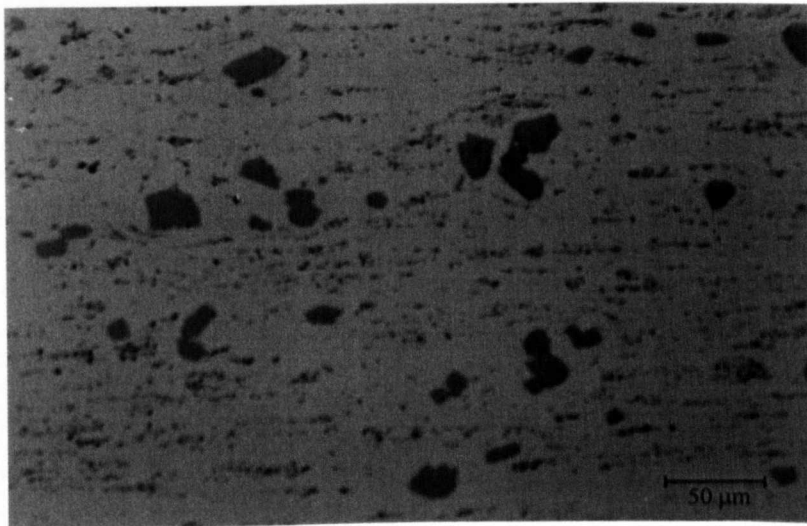


(b) 200x

Figure 3.11: Polished surfaces of the *B5/1-A* master alloy. Magnification 50x and 200x. The large particles are $TiAl_3$ and the small particles are TiB_2 . The dark spots are inclusions containing aluminium oxide and fluoride salts.

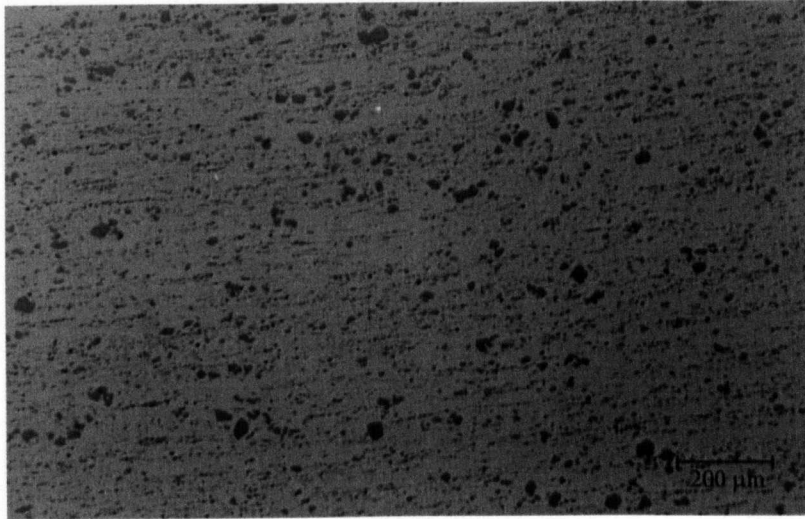


(a) 50x

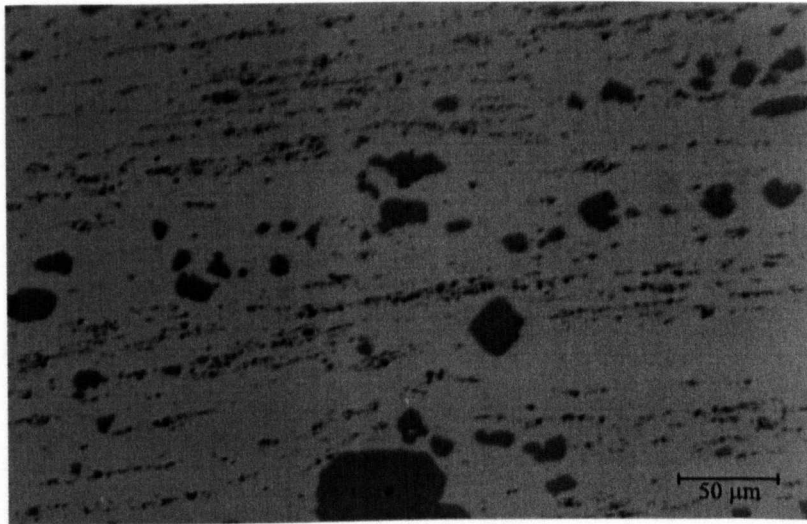


(b) 200x

Figure 3.12: Polished surfaces of the *B5/1-B* master alloy. Magnification 50x and 200x. The large particles are $TiAl_3$ and the small particles are TiB_2 . The dark spots are inclusions containing aluminium oxide and fluoride salts.

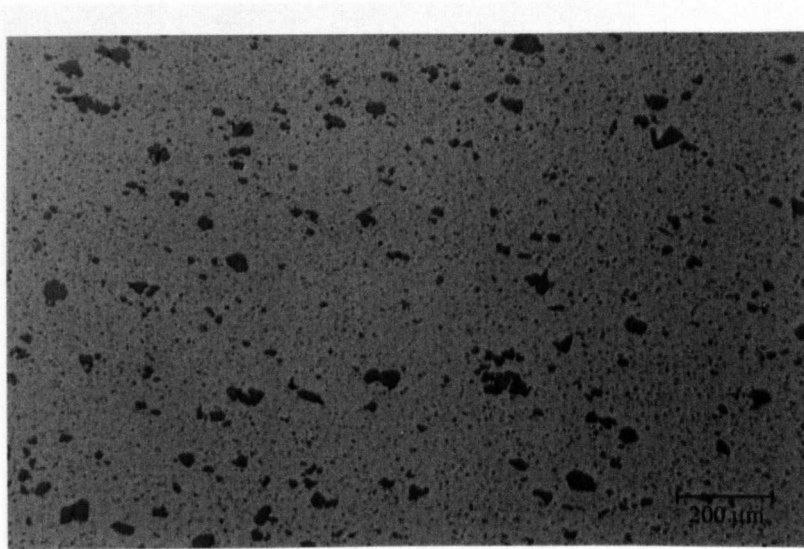


(a) 50x

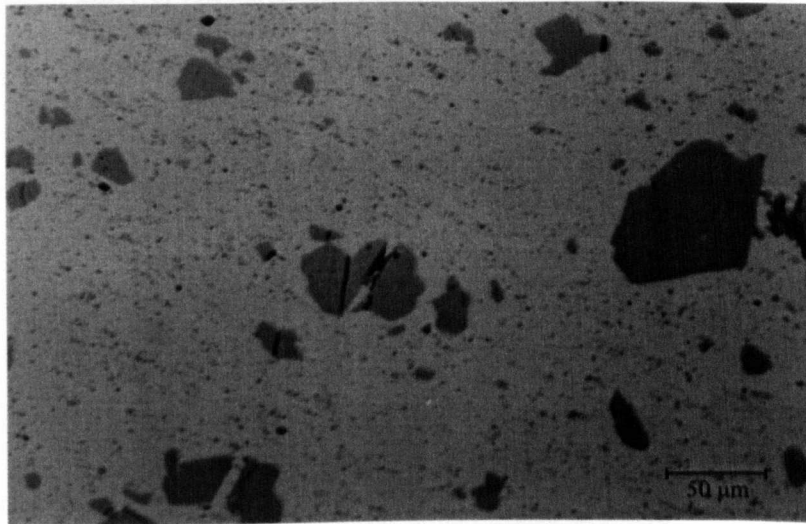


(b) 200x

Figure 3.13: Polished surfaces of the *B5/1-C* master alloy. Magnification 50x and 200x. The large particles are $TiAl_3$ and the small particles are TiB_2 . The dark spots are inclusions containing aluminium oxide and fluoride salts.



(a) 50x



(b) 200x

Figure 3.14: Polished surfaces of the *B5/1-D* master alloy. Magnification 50x and 200x. The large particles are $TiAl_3$ and the small particles are TiB_2 . The dark spots are inclusions containing aluminium oxide and fluoride salts.

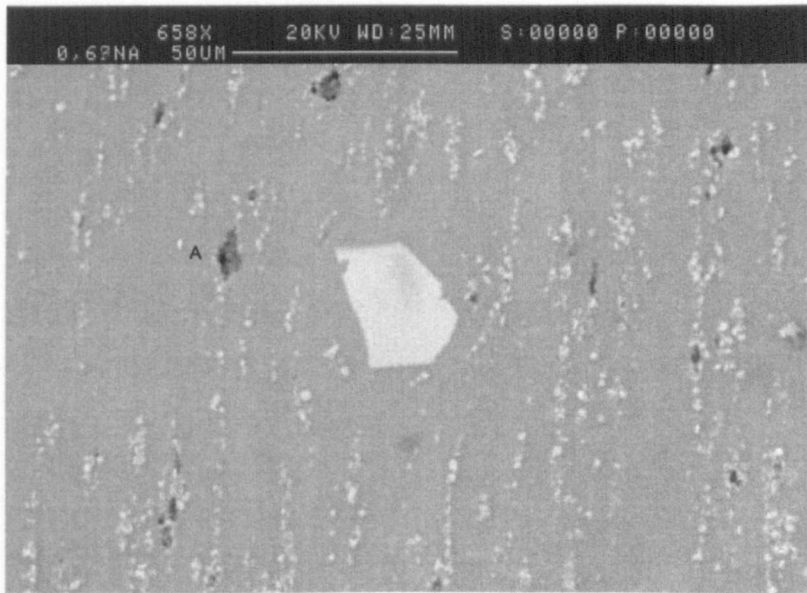


Figure 3.15: Backscatter view of polished sample of the B5/1-A master alloy. EDX spectrum of the inclusion marked with an A is shown in Figure 3.16. The large blocky particle is $TiAl_3$ and the small white particles are TiB_2 .

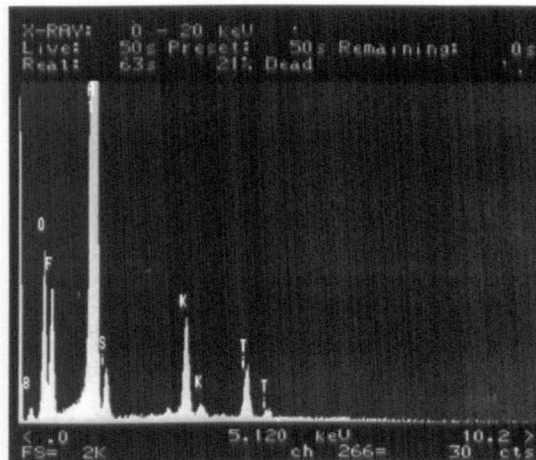


Figure 3.16: The EDX spectrum of spot A in Figure 3.15.

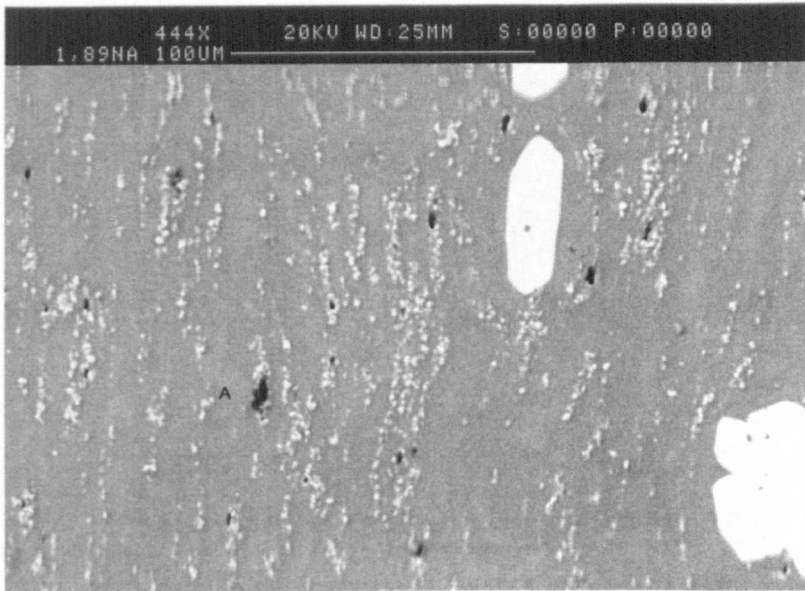


Figure 3.17: Backscatter view of polished sample of the B5/1-A master alloy. EDX spectrum of the inclusion marked with an A is shown in Figure 3.18. The large blocky particles are $TiAl_3$ and the small white particles are TiB_2 .

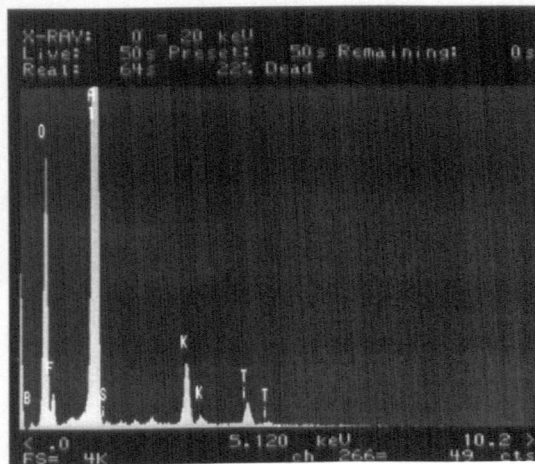
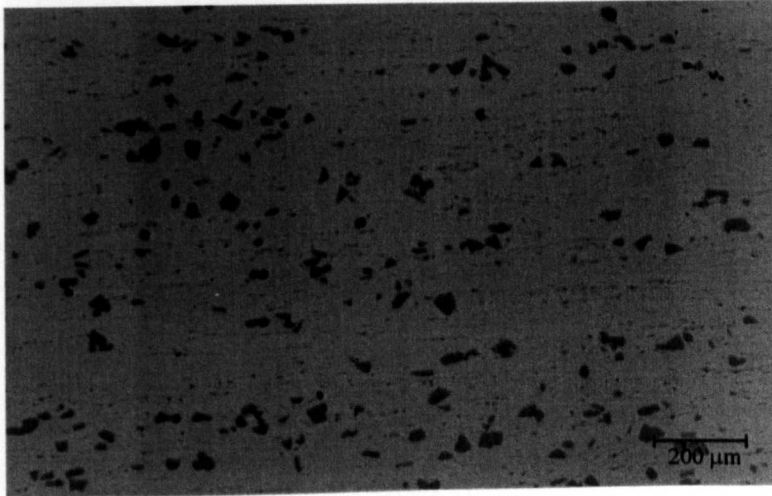
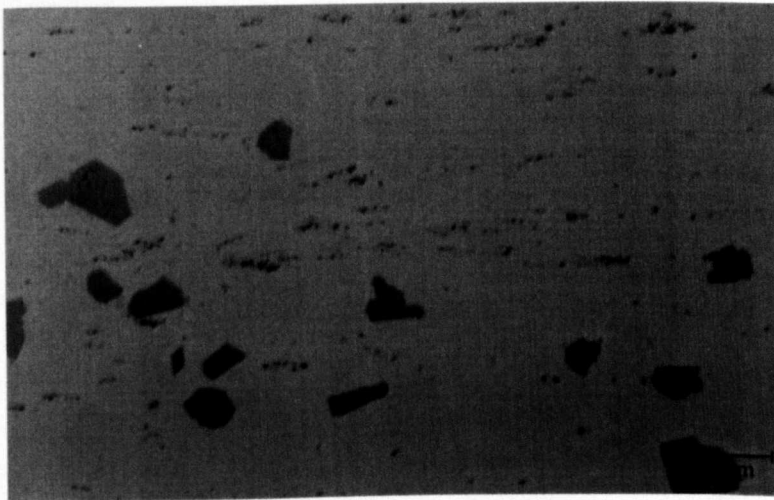


Figure 3.18: The EDX spectrum of spot A in Figure 3.17.



(a) 50x



(b) 200x

Figure 3.19: Polished surfaces of the *B3/.2-A* master alloy. Magnification 50x and 200x. The large particles are $TiAl_3$ and the small particles are TiB_2 . The dark spots are inclusions containing aluminium oxide and fluoride salts.

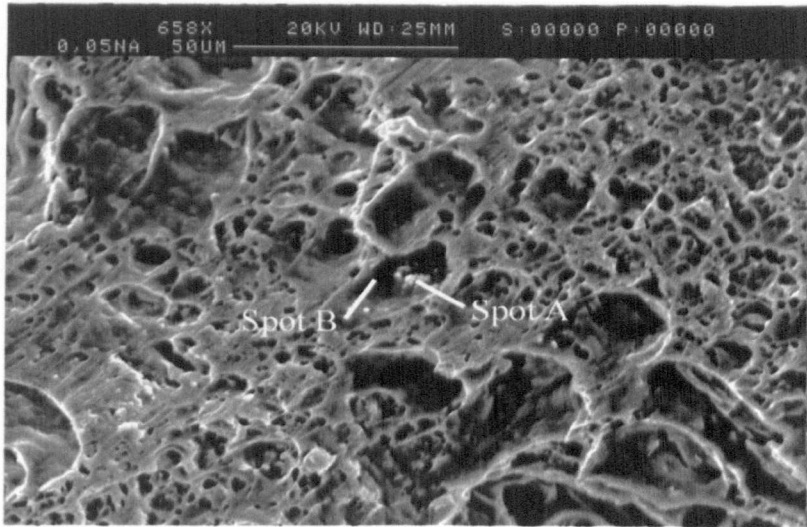


Figure 3.20: *TiC* cluster in the *C3/.15-B* rod marked "A". EDX spectra of spots A and B which is in the α -phase, are shown in Figures 3.21 and 3.22.

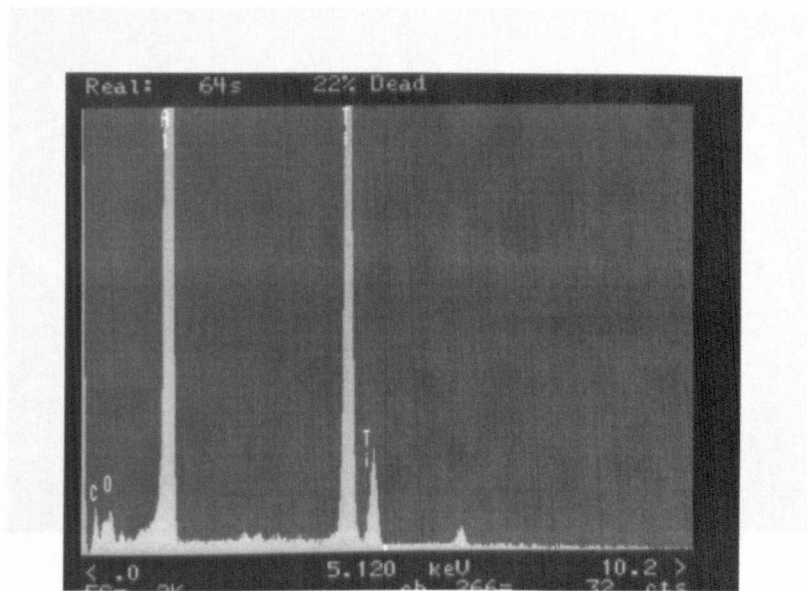


Figure 3.21: The EDX spectrum of spot A in Figure 3.20.

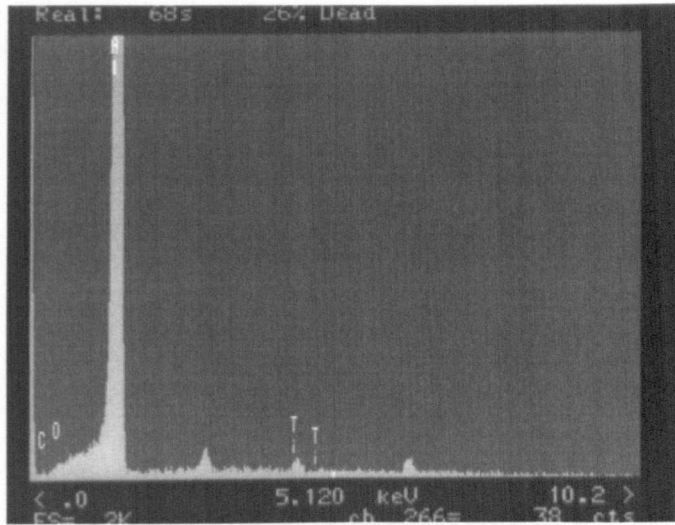


Figure 3.22: The EDX spectrum of spot B in Figure 3.20.

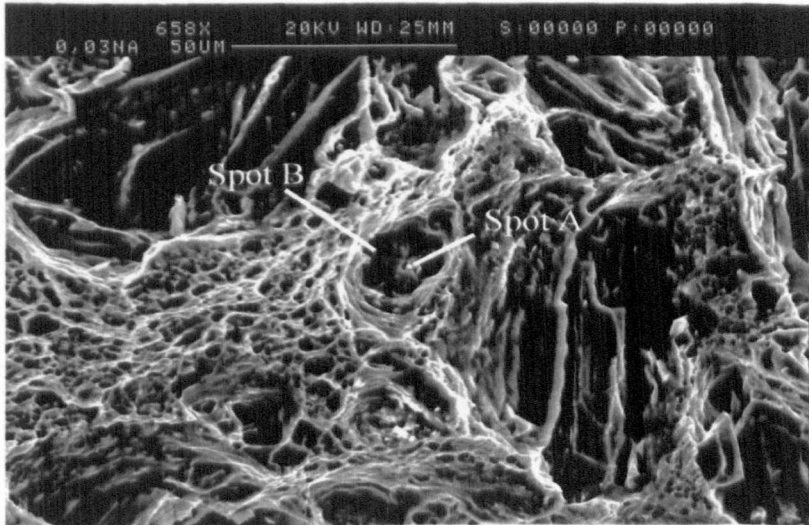


Figure 3.23: TiC cluster in the $C3/.15-A$ rod marked "A". EDX spectra of spots A and B which is in the α -phase, are shown in Figures 3.24 and 3.25.

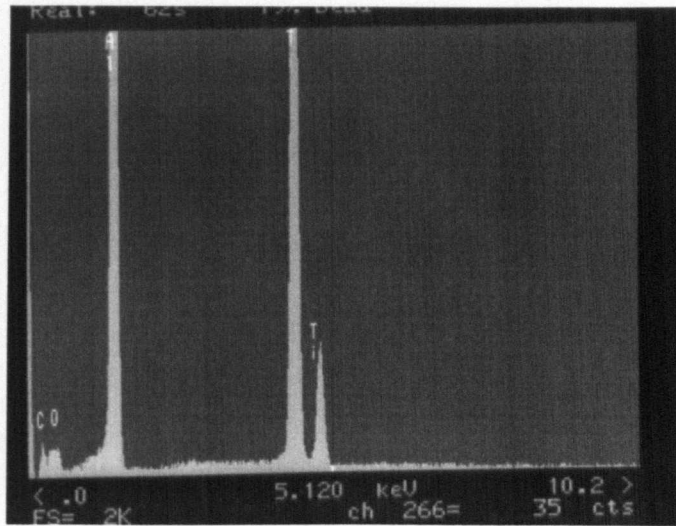


Figure 3.24: The EDX spectrum of spot A in Figure 3.23.

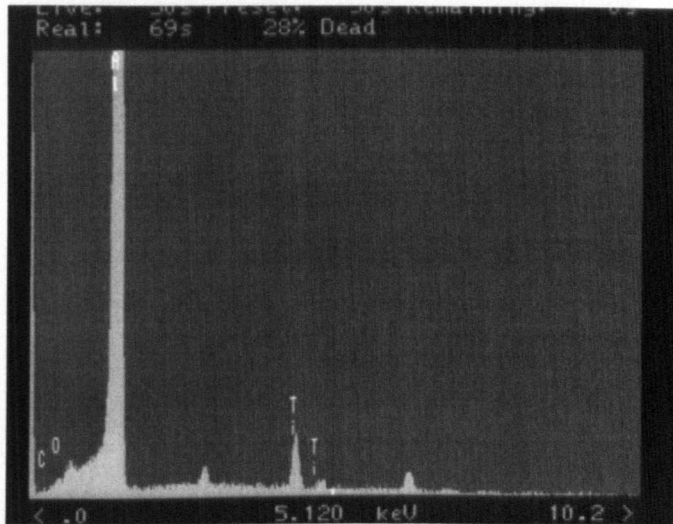


Figure 3.25: The EDX spectrum of spot B in Figure 3.23.

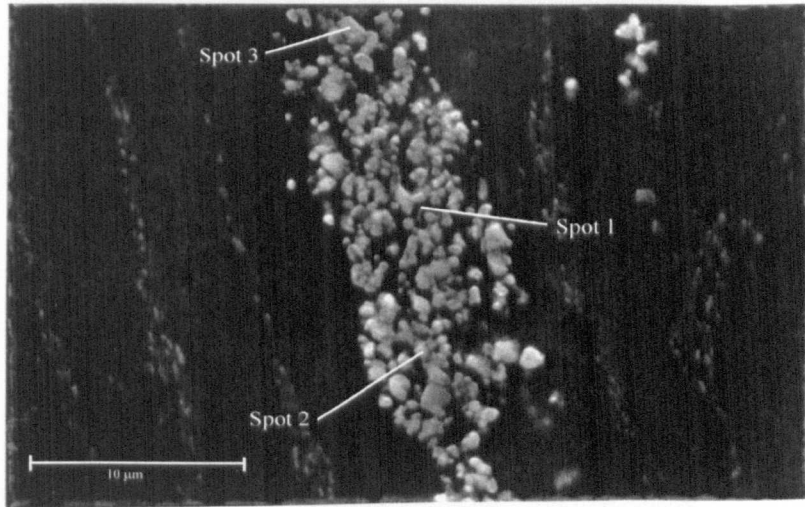


Figure 3.26: *TiC* particle cluster in *C3/.15-A*. The size of the cluster is $10 \times 20 \mu\text{m}$. EDX spectra of spots 1, 2 and 3, are shown in Figures 3.27, 3.28 and 3.29.

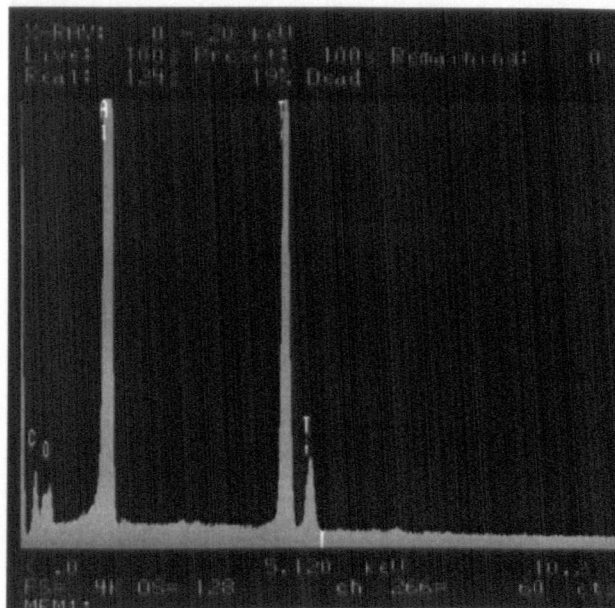


Figure 3.27: EDX spectrum of spot 1 in Figure 3.26.

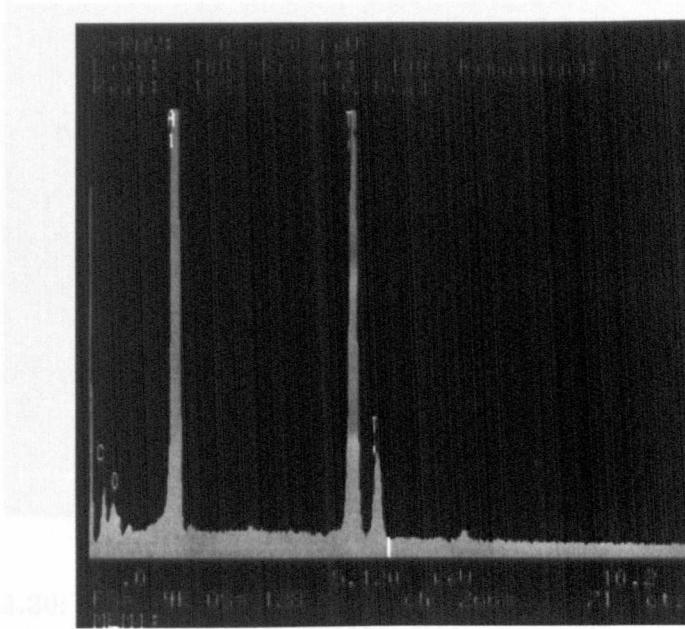


Figure 3.28: EDX spectrum of spot 2 in Figure 3.26.

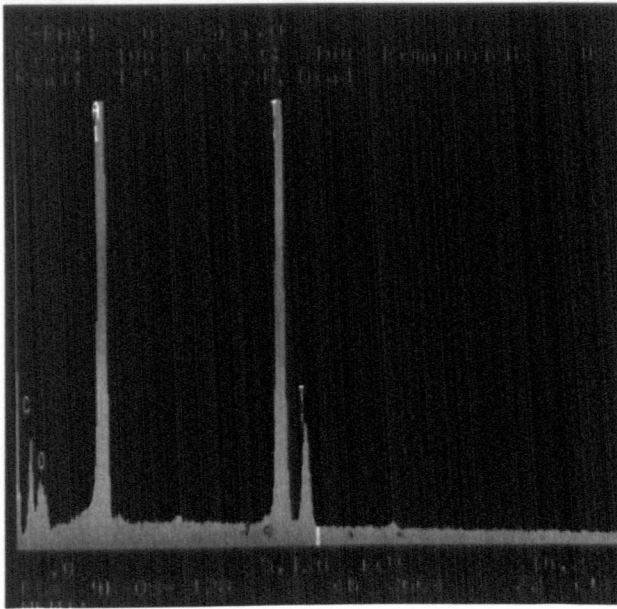


Figure 3.29: EDX spectrum of spot 3 in Figure 3.26.

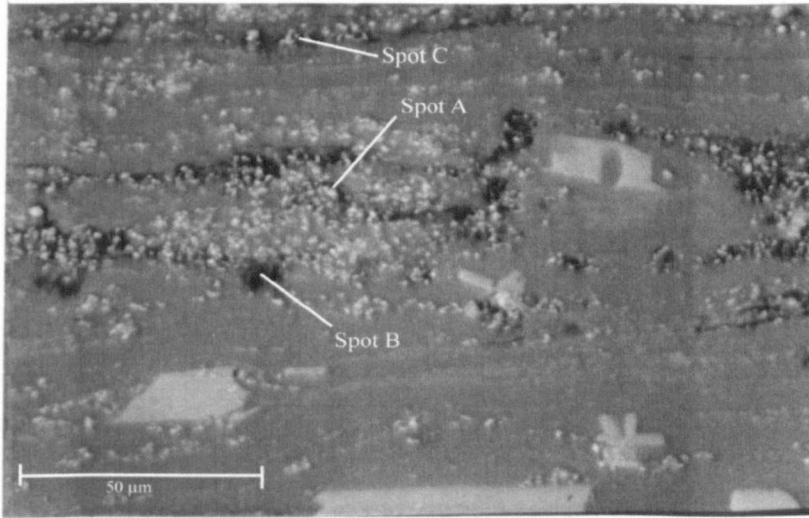


Figure 3.30: Backscatter image of TiC particle clusters in $C3/.15-A$. The large block particles are $TiAl_3$. Two groups of TiC are seen, one long and narrow at the top and one $90 \times 50 \mu m$ in the middle. EDX spectra of spots A, B and C, are shown in Figures 3.32, 3.33 and 3.34.

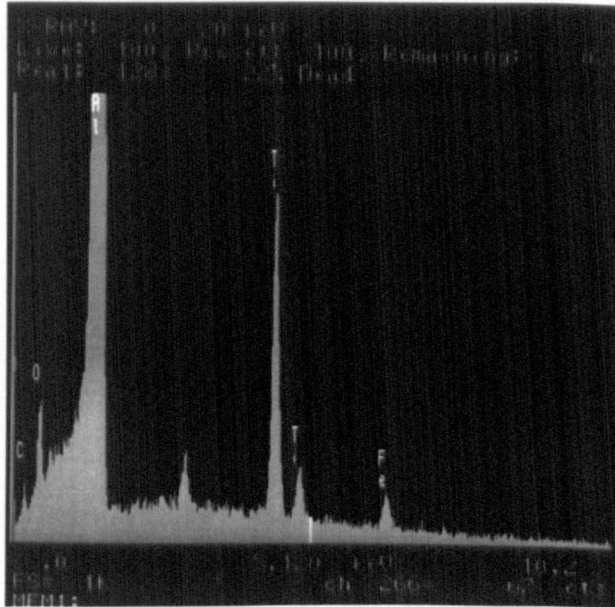


Figure 3.31: EDX spectrum of the whole surface in Figure 3.30. A significant level of oxygen is observed. The unmarked peak between Al and Ti is $2xAl$.

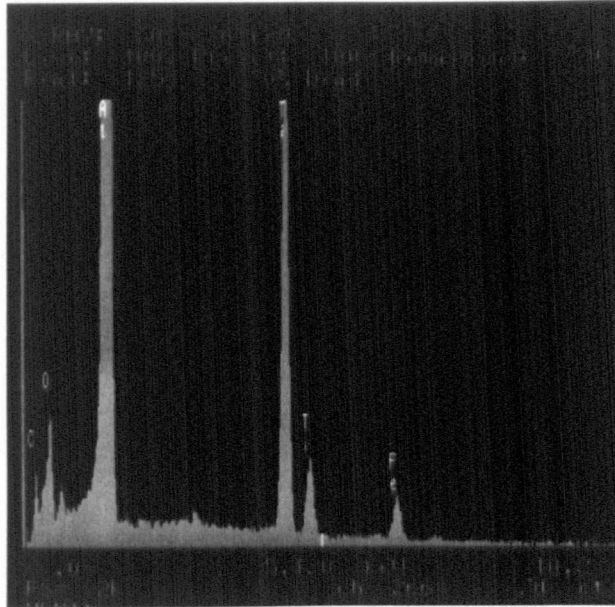


Figure 3.32: EDX spectrum of spot A in Figure 3.30. A significant level of oxygen is observed.

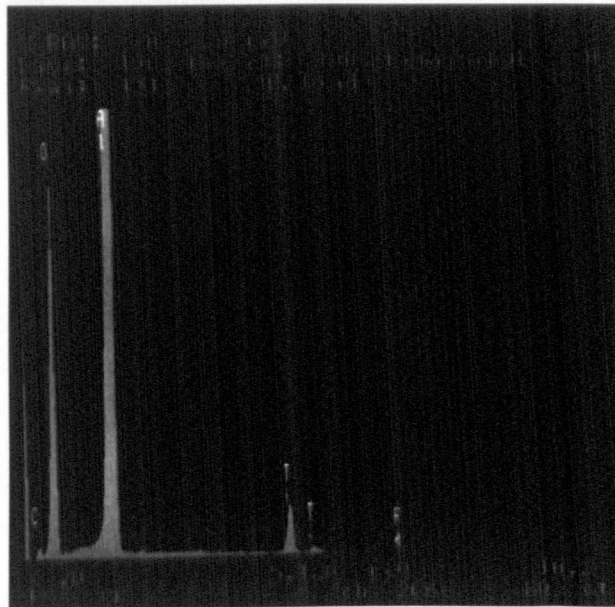


Figure 3.33: EDX spectrum of spot B in Figure 3.30. A significant level of oxygen is observed.

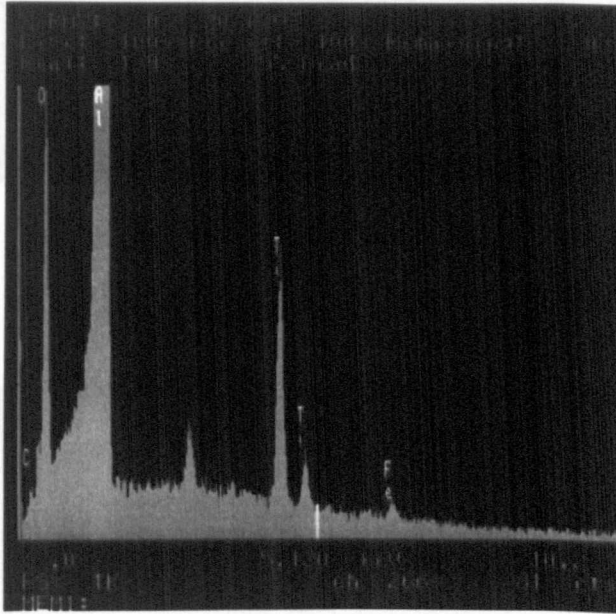
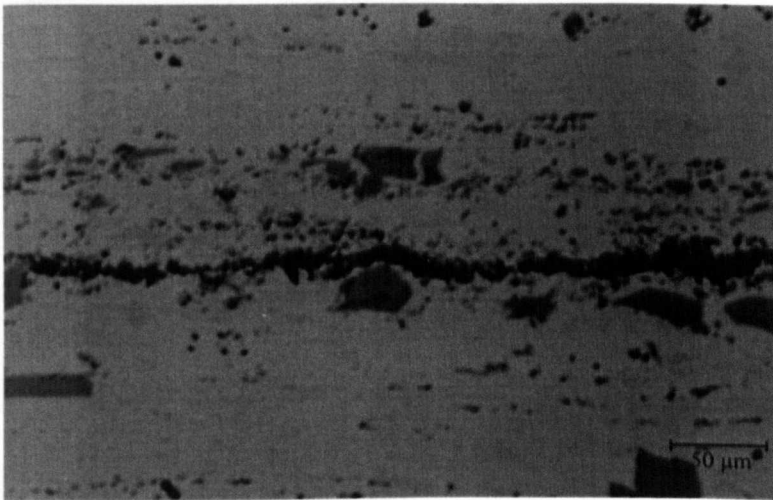


Figure 3.34: EDX spectrum of spot C in Figure 3.30. A significant level of oxygen is observed. The unmarked peak between *Al* and *Ti* is $2xAl$.

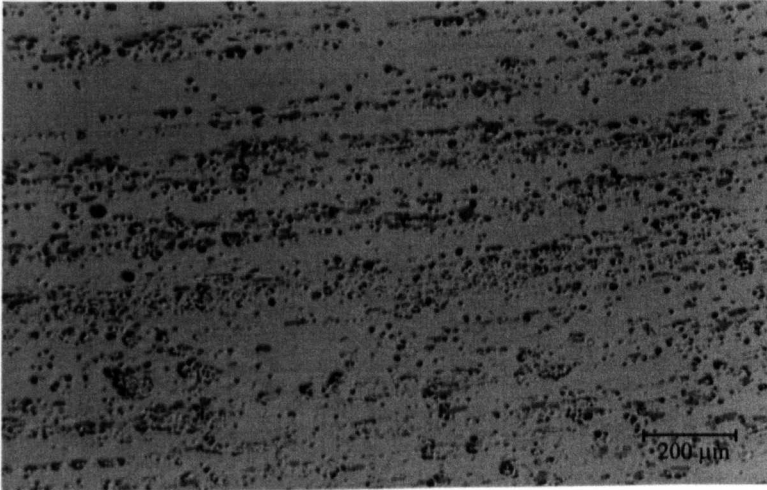


(a) 50x

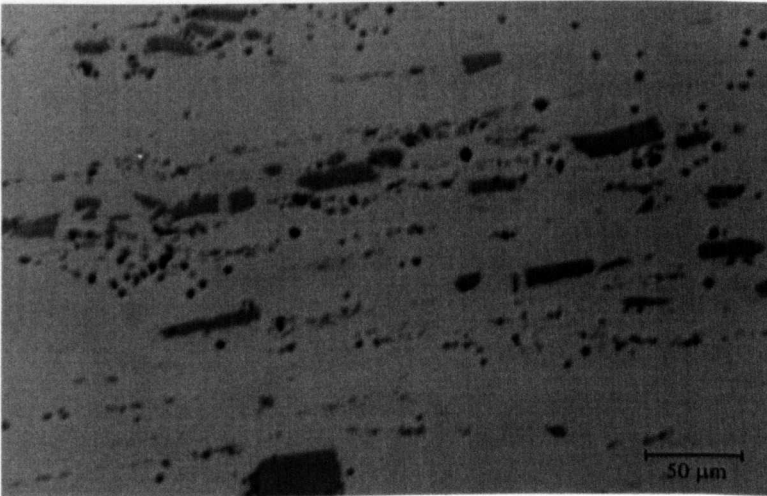


(b) 200x

Figure 3.35: Polished surface of the *C3/.15-A* master alloy. The large particles are $TiAl_3$ and the small ones are TiC . The dark streaks and spots are oxides.

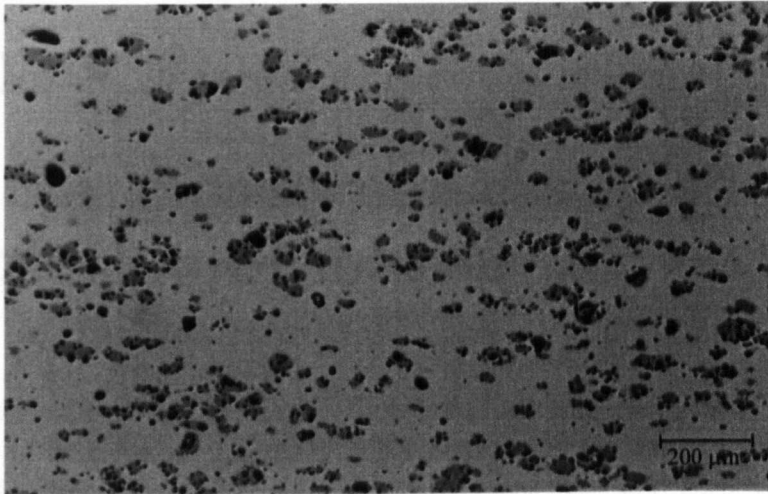


(a) 50x

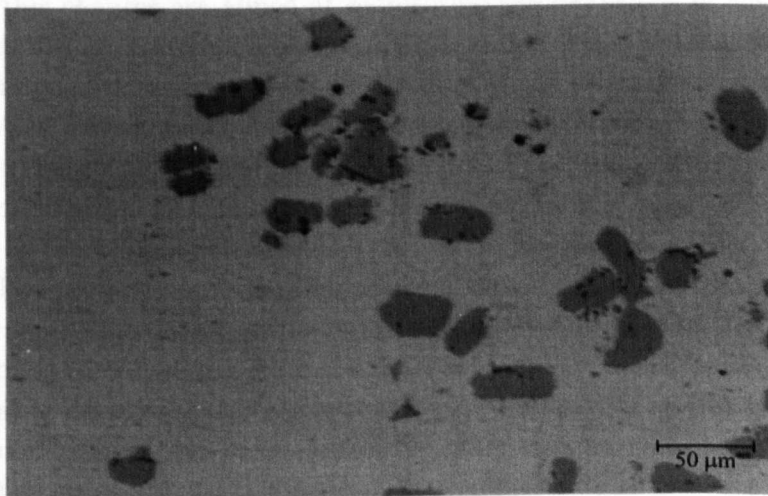


(b) 200x

Figure 3.36: Polished surface of the *C3/.15-B* master alloy. The large particles are $TiAl_3$ and the small ones are TiC . The dark spots are oxides.



(a) 50x



(b) 200x

Figure 3.37: Polished surface of Al-6Ti-0.03C master alloy. The large particles are $TiAl_3$ and the the dark spots are oxides. No TiC particles can be distinguished.

Chapter 4

LiMCA measurements of the dissolution of master alloys

When master alloys are melted from their solid form into molten aluminium, various types of particles are released into the melt, as described in Section 2.3 and Chapter 3. These depend upon the type of master alloy and each serves a specific purpose in the grain refining process. There are two main types of particles found in master alloys, i.e. soluble particles ($TiAl_3$) in almost spherical form, ranging from approx. 20–100 μm in diameter, and insoluble or sparingly soluble particles (TiB_2 or TiC) with a diameter less than 10 μm . The experiments discussed in this chapter are aimed at monitoring the behaviour of these particles when released into a molten aluminium bath under controlled conditions. They are also designed to further the understanding of the operational characteristics of the LiMCA device under these well controlled conditions.

In this study the particle behaviour is principally examined in terms of a particle count given as a function of time. The particle count is traditionally expressed by the LiMCA software as K/Kg or thousands of particles per kilogram of melt. The particle count is often referred to as N20, which means that only particles larger than 20 μm are included as discussed in Section 2.4.9. The size distribution is also available from the data acquired by LiMCA. Metallographic samples taken during the experiments are also examined in an effort to elucidate the dissolution/dispersion behaviour of the grain refiners.

The main limitation to this experimental procedure, is that the LiMCA device can only detect particles larger than 20 μm . Therefore, the TiB_2 and TiC particles, originating in the master alloy are not detected unless they have agglomerated into clusters.

The main objectives of this part of the study were, therefore, as follows:

- To investigate the dissolution of the large soluble $TiAl_3$ particles down to a size of less than 20 μm .
- To investigate if the small insoluble particles are introduced in clusters

larger than $20\mu\text{m}$ from the master alloy.

- To investigate the possible agglomeration of the small insoluble particles with time in the melt.

In order to achieve these objectives, the master alloy additions and concentrations are much larger than normally practised in cast-houses.

4.1 Experimental setup

The experimental equipment consists of an induction furnace, 8 kg crucible, pneumatic motor, K-type thermocouple, graphite rotor and the LiMCA device. A schematic drawing of the setup is shown in Figure 4.1. The rotor enters the melt at an angle. This is necessary to ensure a satisfactory flow pattern in the crucible and to have enough space for the LiMCA head to enter the melt. The approximate flow pattern is shown in Figure 4.2. The maximum rotor speed was established to be 60 RPM, because above 60 RPM the flow conditions in the melt are too severe for the LiMCA device. For most of the experiments, a rotor speed of 60 RPM was chosen to ensure good distribution of particles in the melt. Photographs of the experimental setup are shown in Figures 4.3 and 4.4.

4.1.1 Experimental procedure

For each experiment, 7.5 kg of commercially pure aluminium were weighed and melted in the crucible. Then portions of the master alloy rod required for the experiment were weighed. After the pure aluminium had melted in the crucible, the rotor was started. The melt was stirred for ten minutes while the furnace was set to maintain the preferred melt temperature of 715°C . When the temperature had stabilized in the crucible, the LiMCA head was dipped into the melt and the measurements started. After approximately ten minutes a satisfactory base line for the inclusion count for the original melt was normally reached and the addition of the master alloy began. The time intervals between additions were set before each experiment. The majority of the experiments had five additions of master alloy and the time interval between additions was 20 minutes. This time interval was selected after some preliminary experiments. Finally after the addition of all the prepared master alloy portions, the LiMCA head was withdrawn from the melt and the rotor stopped.

4.1.2 Chemical analysis

During each experimental run, samples for chemical analysis were taken. There were two methods used for obtaining samples. At the beginning of each experimental run, before the addition of the master alloy but with the rotor running, a

Table 4.1: List of the experiments.

Experiment	Grain Refiner		Additions		Speed [RPM]
	class	type	size	no.	
<i>Ti-1</i>	Al-6Ti		0.03% Ti	10	60
<i>Ti-2</i>	Al-6Ti		variable	5	60
<i>TiC-1</i>	Al-6Ti-0.03C		0.05% Ti	1	60
<i>TiC-2</i>	Al-6Ti-0.03C		0.05% Ti	5	60
<i>TiC-3</i>	Al-3Ti-0.15C	<i>C3/.15-A</i>	0.035% Ti	5	60
<i>TiC-4</i>	Al-3Ti-0.15C	<i>C3/.15-A</i>	0.035% Ti	1	60
<i>TiC-5</i>	Al-3Ti-0.15C	<i>C3/.15-B</i>	0.035% Ti	1	60
<i>TiB-1</i>	Al-5Ti-1B	<i>B5/1-B</i>	0.02% Ti	2	60
<i>TiB-2</i>	Al-5Ti-1B	<i>B5/1-B</i>	0.2% Ti	1	60
<i>TiB-3</i>	Al-5Ti-1B	<i>B5/1-B</i>	0.2% Ti	1	60
<i>TiB-4</i>	Al-5Ti-1B	<i>B5/1-D</i>	0.035% Ti	5	60
<i>TiB-5</i>	Al-5Ti-1B	<i>B5/1-C</i>	0.035% Ti	5	60
<i>TiB-6</i>	Al-5Ti-1B	<i>B5/1-B</i>	0.035% Ti	5	60
<i>TiB-7</i>	Al-5Ti-1B	<i>B5/1-A</i>	0.035% Ti	5	60
<i>TiB-8</i>	Al-5Ti-1B	<i>B5/1-B</i>	0.035% Ti	5	40
<i>TiB-9</i>	Al-5Ti-1B	<i>B5/1-A</i>	0.035% Ti	5	40
<i>TiB-10</i>	Al-5Ti-1B	<i>B5/1-C</i>	0.035% Ti	5	40
<i>TiB-11</i>	Al-3Ti-0.2B	<i>B3/.2-A</i>	0.02% Ti	9	60

sample was taken with a spoon at a depth of 30–40mm. The size of the sample was approx. 60g. The same type of sample was also obtained after the experimental run, with the rotor still running in order to get a measurement of the chemical composition at the final measurement point. The other method employed was to obtain samples during the experimental runs with a metal sucking device as shown in Figure 4.5. This device can obtain samples at a depth of 80mm without disturbing the melt. The number of those samples was limited, however, mainly because the sampling disturbed the LiMCA measurements.

In the chemical analysis, spark emission analysis was employed with a standard accuracy of $\pm 5\%$.

4.1.3 Metallographic samples

The samples used for the metallographic analysis were both the samples obtained with the metal sucking device and samples taken from the LiMCA tube. The samples from the LiMCA tube were taken at the end of each the experimental run, and they give an indication of the type of particles or clusters the LiMCA device is measuring at that point in time. The samples were polished and analyzed in an optical microscope and in a SEM, where the clusters could be chemically analyzed with an EDX detector.

4.1.4 Master alloys

The master alloys employed in this study have been described in Chapter 3. In all, nine types were tested. They are:

- The Al-6Ti master alloy. One type.
- The Al-6Ti-0.03C master alloy. One type.
- The Al-3Ti-0.15C master alloy. Types *C3/.15-A* and *C3/.15-B*.
- The Al-5Ti-1B master alloy. Types *B5/1-A*, *B5/1-B*, *B5/1-C* and *B5/1-D*.
- The Al-3Ti-0.2B master alloy. Types *B3/.2-A*.

Table 4.1 gives a summary of the experiments. The experiments were arranged in an ascending order with respect to the estimated probability of finding particles or particle clusters in the melt with the LiMCA device.

4.2 The Al-6Ti master alloy

In the first series of experiments the boride and carbide free Al-6Ti master alloy was added to the melt. The purpose of this was to determine if the stirrer and the master alloy additions draw oxides from the surface of the molten aluminium into the melt which could influence the LiMCA response. Two sets of experiments were carried out. In the first, *Ti-1*, ten even sized portions of Al-Ti master alloy were added into the melt and in the second, *Ti-2*, five portions of different sizes of the same master alloy were added.

4.2.1 Experimental results

The characteristics and chemical composition of the Al-6Ti master alloy were given in Section 3.2. The base metal was commercially pure aluminium with the chemical composition given in Table A.1 in Appendix I.

Experiment Ti-1: Ten portions of the Al-6Ti master alloy were successively added to the melt. The size of each portion increased the titanium content of the melt by 0.03 wt% Ti. Table A.2 in Appendix A shows the additions and the results of chemical analysis of samples taken during the experimental run. As previously described, the number of these samples had to be limited to prevent disturbances in the LiMCA measurements. Figure 4.6 shows a plot of particle counts versus time for the experiment. At the first eight addition points there is a large increase in the particle count, but it quickly returns close to the original base line. The transient peaks possibly result from the introduction of the large soluble $TiAl_3$ particles which are

then rapidly dissolved. The return to the original baseline indicates that the quantity of oxides drawn into the melt by the stirrer or the master alloy is very small or not detectable. Also, the $TiAl_3$ particles appear to dissolve completely shortly after each addition. After addition nine, when the titanium content increases from approximately 0.24 wt% to 0.27 wt% Ti, the particle count does not return to the base level. There are only a few valid measurement points after addition nine, because of blocking of the orifice in the LiMCA tube. These difficulties are probably because of $TiAl_3$ buildup around the orifice in the LiMCA probe. Therefore, it is not possible to estimate from this series the exact time when the irreversible increase in the particle count begins, i.e. the $TiAl_3$ particles stop dissolving completely. It is certain, however, that this does not start within the eight first additions.

Experiment Ti-2: The additions in this experiment were planned to prevent the blocking of the LiMCA tube orifice at the end of the run. A large first addition increased the titanium level of the melt to around 0.15 wt% Ti, a level which was reached with five additions in experiment *Ti-1*. The additions are listed in Table A.2 in Appendix A along with the chemical analysis. Figure 4.7 shows the particle count versus time for the experiment. After addition three, when the titanium content in the melt was approx. 0.24 wt% Ti, there was a slight increase in the particle count. After addition four, there is a much larger increase but it seems to decrease slowly with time. It was not possible to follow this decrease in the particle count further because the conditions for the LiMCA device were getting poor. Shortly after addition five, the LiMCA device stopped operating. The measurements in this test are therefore similar to *Ti-1* in that there is no rise in the permanent particle content with the addition of up to 0.24 wt% of titanium. Titanium concentration exceeding 0.24wt% Ti on the other hand results in a permanent increase in the particle count.

Samples taken for metallographic analysis after the experimental runs show a large number of $TiAl_3$ particles present in the melt. Figure 4.8 shows a large blocky $TiAl_3$ particle in a sample taken from the crucible fifteen minutes after experiment *Ti-1* ended. The length of the particle is $300\mu\text{m}$. It had not settled out probably because the rotational speed of the stirrer was increased after the LiMCA measurement stopped. Figure 4.9 shows a sample taken from metal retained in the LiMCA tube at the end of experiment *Ti-2*. The large particles seen in the figure are $TiAl_3$, as confirmed by EDX analysis shown in Figure 4.10. Only aluminium and a large quantity of titanium is detected. Figure 4.11 shows the EDX spectrum of the α -phase of the base metal. The titanium level is significantly lower. This shows that $TiAl_3$ particles can enter the LiMCA tube.

Other types of large inclusions, i.e. detectable by the LiMCA device, were not observed in these samples.

4.2.2 Discussion of the Al-6Ti master alloy

The results can be interpreted in terms of the Al-Ti phase diagram which is shown in Figure 2.9. It is clear from the phase diagram that at 715°C the $TiAl_3$ particles introduced into the melt are thermodynamically unstable until a Ti level of approx. 0.24 wt% is reached. Before this concentration is reached, the peaks in the LiMCA measurement in Figures 4.6 and 4.7 are believed to correspond to the introduction of principally $TiAl_3$ particles which rapidly dissolve. The count rate, therefore, quickly returns to near the original base value. It is apparent from this that no or very few insoluble inclusions larger than 20 μ m in size are being introduced into the melt either by the stirring or through the master alloy rod. However, when the titanium addition reaches approx. 0.24 wt% Ti the inclusion count increases markedly which corresponds to the retention of stable $TiAl_3$ in the melt. The value at which this occurs is in good agreement with what would be expected from the phase diagram. Similar work was reported by Mohanty [35] but there the inclusion count increased when the nominal titanium level exceeded 0.12 wt% Ti. Above this value the particle count increased drastically, causing a linear increase in the particle count with increasing titanium content. The temperature of the melts was similar, the work reported by Mohanty was conducted at 710°C instead of 715°C employed here. No apparent explanation can be found to clarify this difference in the experimental results and the present work is in good agreement with the well established Al-Ti phase diagram.

Samples from the melt obtained after the experiments, and sections from the LiMCA tubes, show only $TiAl_3$ particles larger than 20 μ m as confirmed by EDX analysis. No particles of other types were found in size above 5 μ m. Small inclusions (< 5 μ m) such as black spots (see Chapter 3) containing oxide and fluoride salts are also seen in the samples as expected. This leads to the conclusion that the LiMCA device is actually detecting the $TiAl_3$ particles. It also supports the earlier assumption, that the transient peaks after each addition of the master alloy arise from a detection of $TiAl_3$ particles which then dissolve rapidly. This agrees with the microstructural observations of this master alloy (see Section 3.2), which revealed that only soluble $TiAl_3$ particles and a moderately soluble Fe-bearing intermetallic could be identified.

After the solubility limit for $TiAl_3$ is reached (> 0.24 wt%), high peaks in the particle count are measured, but they subsequently slowly decrease. This decrease is probably due to settling of the particles rather than being the effect of slow dissolution of the $TiAl_3$ particles in the two phase region of the phase

diagram. The dissolution speed becomes lower when the titanium concentration approaches the solubility limit because the concentration difference in the melt and the solubility level affect the dissolution speed. However, under stirring conditions, the effect of the stirrer dominates the effect of the concentration difference so that equilibrium should be quickly reached. The settling of the $TiAl_3$ particles is quite fast, after addition four in Figure 4.7, the particle count decreases from 800 K/Kg to 200 K/Kg in twenty minutes. The $TiAl_3$ particles are 37% denser than molten aluminium and their measured size distribution in the final melt ranges from $20\mu m$ to $100\mu m$. The observed settling rate can, therefore, be expected. Settling due to gravity alone can be calculated following the Stokes law [51] for low Reynolds numbers, i.e. laminar flow around a sphere. By neglecting the rotation of the sphere and assuming a completely stagnant bath, then the drag force on the sphere is

$$F_D = 3\pi\mu V_0 d \quad (4.1)$$

where F_D is the drag force acting on the sphere, μ is the dynamic viscosity of the bath, V_0 is the terminal velocity and d diameter of the sphere. By adding the buoyancy force acting on the particle the terminal velocity of the particle can be solved as:

$$V_0 = \frac{gd^2(\rho_p - \rho_{Al})}{18\mu_{Al}} \quad (4.2)$$

where g is gravity, ρ_p the density of the sphere, ρ_{Al} density of molten aluminium and μ_{Al} the dynamic viscosity of molten aluminium. Figure 4.12 shows the Stokes settling for $TiAl_3$, TiB_2 and TiC particles in a stagnant aluminium bath.

4.3 The Al-6Ti-0.03C master alloy

In the second series of experiments the Al-6Ti-0.03C master alloy was added into the melt. The object was to observe the effect that TiC particles have on the particle count. This type of master alloy was chosen because of its similarity to the Al-6Ti master alloy employed in the first test. Two set of experiments were carried out. In the first, $TiC-1$, one portion of the master alloy was added into the melt and in the second, $TiC-2$, five portions of the same master alloy were added at fixed time intervals (see Table 4.1).

4.3.1 Experimental results

The characteristics and chemical composition of the Al-6Ti-0.03C master alloy are given in Section 3.6. The base metal was a commercially pure aluminium with the chemical composition given in Table A.1 in Appendix A.

Experiment TiC-1: One portion of the Al-6Ti-0.03C master alloy was added

into the melt. The portion increased the titanium content of the melt by 0.05 wt% Ti. Table A.3 in Appendix A shows the portion size and the titanium content of a sample taken at the end of the experimental run. The results are shown in Figure 4.13. The portion was added at minute 20 which is well indicated by a transient peak associated with soluble $TiAl_3$ particles originating in the master alloy. After the transient peak, the particle count returns to a new level approx. 5 K/Kg above the base value. Subsequently, the particle count starts to increase slowly to the end of the experimental run.

Experiment TiC-2: Five portions of the Al-6Ti-0.03C master alloy were added successively into the melt at fixed time intervals. The size of the portions increased the titanium content by 0.05 wt% Ti. Table A.3 shows the portions sizes and the titanium content of a sample taken at the end of the run. Figure 4.14 shows the particle count during the experiment. The first portion is added at minute twenty and the following ones at twenty minutes intervals. After the transient peak of the first addition has subsided there is a small increase in the particle count up the next addition. This is similar to the test behaviour in *TiC-1*. After additions two, three and four there is also a slight step increase in the count right after the transient peak has disappeared. The new particle count is relatively stable until the next portion is added. With the fifth addition the titanium content exceeds the solubility limit for $TiAl_3$ according to the Al-Ti phase diagram and a large increase in the particle count is detected.

The size distribution of the detected particles is also available from the LiMCA data as shown in Section 2.4.8. The calculation demonstrates whether the size distribution is changing in the course of the experiments. The particles are considered to be spheres and the distribution is normalized to simplify the comparison. The normalization equation is given by:

$$\hat{N}_{20-25\mu m,t}, \hat{N}_{25-30\mu m,t}, \dots, \hat{N}_{135-140\mu m,t} = \frac{N_{20-25\mu m,t}}{N_{20,t}}, \frac{N_{25-30\mu m,t}}{N_{20,t}}, \dots, \frac{N_{135-140\mu m,t}}{N_{20,t}}$$

where $\hat{N}_{20-25\mu m,t}$ is the normalized count of inclusions ranging from 20 to 25 μm at time t , $N_{25-30\mu m,t}$ is the detected count of inclusions ranging from 25 to 30 μm at time t and $N_{20,t}$ is the total number of detected inclusions at time t . This method eliminates the effect of the total number of detected particles when comparing the distribution at different times in a experimental run. Figure 4.15 shows the normalized particle distribution one, ten and twenty minutes after the addition shown in Figure 4.13. The values on the vertical scale represent fractions, a value of 0.2 is 20% of the total number of detected particles. The three curves are similar, indicating no detectable change in the particle distribution despite the fact that the total number of particles larger than 20 μm is gradually increasing.

Initial parameters for particle tracking using numerical simulation (see Chapter 5) can also be obtained from the LiMCA experiments. The method chosen is to display a size distribution, which is taken immediately after the transient peak, following the first addition, has disappeared. The value for each size interval is particles per kg of master alloy. Figure 4.16 shows the measured size distribution for the Al-6Ti-0.03C master alloy tested one minute after the addition. The measurements after 10 and 20 minutes give practically the same results. This shows that the master alloy is introducing particles other than $TiAl_3$ into the melt in sizes upto $100\mu m$, assuming that the carbon has not significantly affected the solubility of $TiAl_3$ from that observed in the experiments on the Al-Ti master alloy in Section 4.2. This is supported by the fact that a similar concentration of titanium, i.e. 0.24%, gave a large step increase in the particle count both in experiment *TiC-2* and in the Al-Ti experiment indicating a similar limit of solubility.

4.3.2 Discussion of the Al-6Ti-0.03C master alloy

The notable difference between tests with the Al-6Ti and Al-6Ti-0.03C master alloys is that after each addition of the Al-6Ti-0.03C master alloy, there is a step increase in the particle count corresponding to approximately 3-5K/Kg. This was not found after the Al-6Ti additions. Assuming that the carbon has not significantly affected the solubility of $TiAl_3$ as previously discussed, it should be expected that below 0.24 wt% Ti, the $TiAl_3$ particles dissolve within a few minutes at the most and, therefore, the increased particle count must arise from other phases within the Al-6Ti-0.03C master alloy. As discussed in Section 2.3.3, the size of TiC particles is less than approximately $2\mu m$ so that individual TiC particles are not responsible for the change in the LiMCA signal. The most probable explanation is that clusters of TiC particles are introduced into the melt by the Al-6Ti-0.03C master alloy. No clusters of TiC particles were found in the metallurgical analysis of this master alloy as discussed in Section 3.6. However, it seems likely that the clusters are TiC particles bonded together with oxide similar to those observed in the Al-3Ti-0.15C master alloy in Section 3.5.

Looking at Figure 4.13, the total weight of TiC added in 66g of the Al-6Ti-0.03C master alloy, is 0.099g. Using the density of $4930kg/m^3$, the total volume of TiC particles can be calculated as $2.6 \times 10^{-9}m^3$ in each kilogram of melt. On the other hand, the measured volume by LiMCA was $7.3 \times 10^{-11}m^3$ for each kilogram of melt shortly the transient peak has subsided. In other words the clusters represent 2.7% of the total TiC added. This means that the remaining mass of the TiC particles is either too small for detection, as it should be, or has settled on the walls on the crucible. The former is much more probable.

As in Section 4.2.1, the critical addition for stable $TiAl_3$ appears to be approx. 0.24 wt% Ti and this is consistent with the Al-Ti phase diagram of Figure 2.9.

The TiC particles, therefore, do not appear to change the solubility of $TiAl_3$ to a detectable extent.

Figure 4.13, for the single addition of the Al-6Ti-0.03C, shows that in addition to the step increase, the particle count slowly increases with time, indicating further agglomeration of the insoluble TiC particles in the melt. The rate of increase is approximately 0.2(K/Kg)/min. This effect is less apparent with the multiple additions.

The normalized size distributions at different time intervals in the experimental runs are practically identical. There is no significant increase of large inclusions as could be expected if it is assumed that agglomeration of the TiC particles is responsible for the gradual increase in the particle count. The most probable explanation, is that as the inclusions grow larger than $100\mu m$, they tend to settle out. Therefore, there is probably a dynamic equilibrium between the inclusions entering the measurable inclusions size range and the larger ones settling out, which results in a stable size distribution throughout the experimental run.

The results for the Al-6Ti-0.03C master alloy show both a greater quantity and size of clusters coming from the master alloy than expected considering previous work reported in the literature. The largest TiC agglomerates previously reported were approximately $2\mu m$ in diameter [19, 21]. Further agglomeration is also observed and this has not been reported before. This will be discussed further in Section 4.4.2.

4.4 The Al-3Ti-0.15C master alloy

In the third part of the experiments the Al-3Ti-0.15C class of master alloys was added into the melt. The objective was to observe the effect of additions with proportionally larger quantities of TiC particles than in the second test. Two types of master alloys were tested, one which was made specially for these experiments, *C3/.15-A*, and a commercially available master alloy, *C3/.15-B*. The former is reported by the manufacturer to have been produced using a process which is likely to have given a high oxide content and the microstructural observations on this alloy revealed the presence of large oxide strings (see Section 3.5). Three sets of experiments were carried out, both to examine the long term effect of repeated additions, and to compare the different master alloys.

4.4.1 Experimental results

The characteristics and chemical composition of the master alloys used is given in Section 3.5. The base metal was a commercially pure aluminium with an analysis given in Table A.1 in Appendix A.

Experiment TiC-3: Five portions of the *C3/.15-A* master alloy were added to the melt successively. The size of each portion increased the titanium content of the melt by 0.035 wt% Ti. Table A.4 in Appendix A shows the additions and the results from chemical analysis of samples taken during the experimental run. The results from the particle count are shown in Figure 4.17. When this figure is studied, it must be remembered that this master alloy was specially made for this experiment and it contains a large quantity of oxide strings (see Section 3.5). The transient peaks, after each addition are as before probably associated with the $TiAl_3$ phase and after these peaks settle, there is a step increase in the particle count. The step behaviour is most pronounced for the first three additions but with additions four and five it becomes more difficult to observe. The inclusion count has become extremely high which results in signal fluctuations. Between additions, the particle count also increases steadily with time, until the next portion is added. The final particle count after the five additions reaches 200 K/Kg.

Experiment TiC-4: One portion of the *C3/.15-A* master alloy was added to the melt. The portion increased the titanium content of the melt by 0.035 wt% Ti. Table A.4 in Appendix A shows the addition and the results of chemical analysis of a sample taken during the experimental run. The results from the particle count are shown in Figure 4.18. The particle count is similar to the particle count in experiment *TiC-3* after one addition. The particle count increases stepwise after the transient peak settles out, and after that it increases by 0.8 K/Kg every minute. The particle count is lower, however, after fifty minutes than observed after the two first additions shown in Figure 4.17.

Experiment TiC-5: One portion of the *C3/.15-B* master alloy was added to the melt. The portion increased the titanium content of the melt by 0.035 wt% Ti. Table A.4 in Appendix A shows the addition and the results from chemical analysis of a sample taken during the experimental run. The results from the particle count are shown in Figure 4.18. The expected transient peak in the particle count is missing in this experimental run, which is due to a failure in the measuring equipment. The orifice in the LiMCA tube was blocked and missed the first point. Otherwise, the results are similar to those in test *TiC-4* except that the step increase after the addition is smaller for the *C3/.15-B* master alloy and the rate of increase with time is slightly lower or 0.6 K/Kg every minute.

It is interesting to note that the test method detects a difference in the properties of the two master alloys with the same chemical classification. Thus, the addition of the alloy reported to be manufactured with a high oxide content re-

sulting in large oxide strings being observed by microscopy, produces a higher particle count.

Figure 4.19 shows a TiC cluster in a sample from the LiMCA tube taken at the end of experiment $TiC-3$. The sample is fractured and unpolished. Figures 4.20 and 4.21 show EDX spectra of points B and C in the cluster and Figure 4.22 shows the spectrum outside the cluster. The results clearly show that the cluster contains titanium, carbon and oxygen. This supports the assumption that the LiMCA is measuring TiC particle clusters and also the proposal that oxide plays a role in the cluster formation of the TiC particles.

4.4.2 Discussion of the Al-3Ti-0.15C master alloy

The Al-3Ti-0.15C master alloys contain $TiAl_3$ and TiC particles and there are also oxides present as discussed in Section 3.5. In the literature [20], the size of individual TiC particles has been reported as smaller than $2\mu m$, which is far below the detection limit for the LiMCA device. It is also stated that the TiC particles have practically no tendency to agglomerate [21], which means for this experiment, that the transient peak associated with the $TiAl_3$ phase should be detected, and then the particle count should return to the original base level. The largest TiC agglomerates previously reported are approximately $2\mu m$ in diameter [19, 21].

The particle count shown in Figure 4.17 clearly demonstrates that after addition of the $C3/.15-A$ master alloy, the particle count does not return to initial level. The particle counts has increased by approximately 13K/Kg immediately after the transient peak has settled and thereafter it is constantly increasing at a rate of approximately 1(K/Kg)/min. This means that there remain some detectable clusters of particles larger than $20\mu m$ from the master alloy addition and their number is increasing throughout the experiment. The most probable explanation is that the LiMCA is measuring clusters of TiC particles bonded together with oxide. The metallographic samples from the LiMCA tube show TiC particles combined with oxide and this further supports this conclusion (see Figure 4.19).

The particle count after one addition of master alloy $C3/.15-A$ and one addition of master alloy $C3/.15-B$ is shown in Figure 4.18. The increase in the particle count for the $C3/.15-A$ alloy is approximately 16K/Kg after the first transient peak has subsided whereas the increase is 7K/Kg for the $C3/.15-B$ alloy. The difference in the particle count between these two types of master alloys continues to range between 10 and 15K/Kg, i.e. the particle count for master alloy $C3/.15-B$ is 10-15K/Kg lower. The initial size distribution of the TiC particles in the master alloys is believed to be similar, but analyses have shown that there are larger oxide strings present in master alloy $C3/.15-A$ (see Section 3.5). This further supports the proposed theory that oxide is responsible

Table 4.2: A comparison of the percentage of TiC particles detected after the first step response and 30 minutes after the additions for the Al-Ti-C master alloys.

Experiment	Grain refiner	Added volume [m^3 per kg]	Percentage detected		Detected vol. 30 min [m^3 per kg]
			Step response	After 30 min	
$TiC-1$	Al-6Ti-0.03C	2.6×10^{-9}	2.7 %	4.2 %	0.11×10^{-9}
$TiC-4$	$C3/.15-A$	17.7×10^{-9}	2.8 %	5.6 %	1.0×10^{-9}
$TiC-5$	$C3/.15-B$	17.7×10^{-9}	0.56 %	1.4 %	0.25×10^{-9}

for aiding the formation of the clusters of TiC particles which the LiMCA device is detecting. This behaviour has not previously been reported for Al-Ti-C master alloys but it has been considered likely by industry [23].

An important method in the interpretation of the data is to examine the volume of the TiC particles, which the LiMCA device detects. The method employed here to calculate the volume, is to divide the data into $5\mu m$ intervals and then estimate the volume. For instance, the number of particles ranging from $20-25\mu m$ was set as the same number of $22\mu m$ particles. The value $22\mu m$ was chosen for this interval because the size distribution of TiC in the master alloy estimates more particles to be $20\mu m$ than $25\mu m$. The same method was used for all the intervals, i.e. $27\mu m$ average was chosen for the interval $25-30\mu m$.

To further explain the volume calculation, the volume of particles ranging from $20-150\mu m$ in diameter is analyzed. The particles are treated as spheres, which leads to the equation $V = (4/3)\pi r^3$, where V is the volume and r is the radius of the particle. Figure 4.36 shows the volume of particles ranging from $20-150\mu m$. It is important to understand for instance that one $100\mu m$ particle has the same volume as $5^3 = 125$ particles with a diameter of $20\mu m$. Therefore, the size distribution of the particles is extremely important when the volume is studied.

Figure 4.23 shows the volume of detected particles in units m^3 per kilogram of melt for the same experiments as shown in Figure 4.18. The volume of the particles detected with addition of master alloy $C3/.15-B$ is lower than the volume observed after addition of master alloy $C3/.15-A$ and the difference is almost constant similar to the difference in the particle count. This suggests that the size distribution of the detected particles from both master alloys is similar. Toward the end of each experiment, the volume increases significantly which means that the individual particles are getting larger towards the end of the runs.

The actual volume of TiC particles after the additions of 90g of master alloy is $1.77 \times 10^{-8} m^3$ per kilogram of melt using the density of $4930 kg/m^3$. Using the measured volume of $5 \times 10^{-10} m^3$ per kilogram, which is obtained after the

transient peak has subsided for master alloy *C3/.15-A*, 2.82% of the added *TiC* volume is detected by the LiMCA. A comparison with the results from the Al-6Ti-0.03C master alloy (2.7%) shows that almost the same percentage of the *TiC* particles participate in the clusters originating in the master alloys in both cases. The reason for this is not clear since no clusters were found by microscopy in the Al-6Ti-0.03C master alloy and the *C3/.15-A* alloy is characterized by a high content of oxide strings. A possible explanation can be that the normal ratio between oxide and *TiC* particles is higher in the low carbon alloy. On the other hand, the percentage increase for the *C3/.15-B* alloy is 0.56%.

Table 4.2 shows a comparison between the volume of *TiC* particles detected after the first step response and 30 minutes after the additions for the three Al-Ti-C master alloys. The volume of the detected particles increases with time and the increase is highest for the *C3/.15-A* alloy. The reason for this can possibly be attributed to the oxide content of this alloy indicating that the oxide plays an active role in the agglomeration process in the melt.

Figures 4.24 and 4.25 show the normalized size distribution of the detected particles, one, ten and twenty minutes after the additions of both types of master alloys. The figures are practically identical, which means that the detected particles have almost the same distribution. However, the percentage of particles ranging from 20-25 μm in diameter decreases as the time from the addition increases, i.e. the size distribution is shifting slightly towards larger particles with time.

Finally, the present work shows a completely different behaviour of cluster formation for *TiC* particles than previously reported in the literature. Clusters of *TiC* particles, presumably bonded together with oxide, are introduced into the melt by the master alloy addition and then further agglomeration is observed in the melt. The difference between the two Al-3Ti-0.15C master alloys shows that an increased oxide content increases the cluster formation and this is a further support of the proposed role of oxide in the agglomeration process.

4.5 The Al-5Ti-1B master alloy

In this series of experiments the Al-5Ti-1B master alloy was added to the melt. The experiments are aimed at clarifying the long term effect of the grain refiner addition and also at comparing master alloys from different producers. The effect of different rotational speeds is also studied. Ten sets of experiments were carried out (see Table 4.1), with tests on Al-5Ti-1B master alloys from four different producers. The master alloys are labeled as *B5/1-A*, *B5/1-B*, *B5/1-C* and *B5/1-D*.

4.5.1 Experimental results

The characteristics and the chemical composition of the master alloys are given in Section 3.3. The base metal was a commercially pure aluminium and the chemical analysis at the start of each experiment are shown in Table A.1 in Appendix A. The chemical analysis of the melt after the experiments are given in Table A.5 in Appendix A.

Experiment TiB-1: Two portions of the *B5/1-B* master alloy were added to the melt. The object was to add both portions with a small time interval into the melt and then to monitor the change in the particle count for a long period of time. Each portion increased the titanium content of the melt by 0.02wt% Ti. Table A.6 in Appendix A shows the weight of each portion and the time of addition. The results are shown in Figure 4.26. The solid line in the figure shows the particle count in K/Kg and the portions are added at minute 26 and minute 35. The transient peaks at the addition points are not large but clearly visible. The main reason for this is probably the combination of the small addition size and that only about 55% of the titanium is in the form of $TiAl_3$ particles (see Table 6.2). Another reason for the low peaks is that the dissolution of each addition starts 30-40 seconds before the acquisition of the sample which allows the addition to gain more time to dissolve before the measurements are taken. There are signs of a step increase in the particle count after the transient peak subsides. After the second addition the particle count slowly increases and ninety minutes after the second addition it peaks at 50 K/Kg. Then the inclusion count starts to decrease and after 180 minutes it has settled at the similar level as it was right after the second addition. It will be shown later that this is probably due to settling of the larger particles.

Experiment TiB-2: One large portion of *B5/1-B* master alloy was added to the melt. The aim was to monitor the inclusion count for 180 minutes after one large addition, which increased the titanium content by 0.2wt% Ti. Table A.6 in Appendix A shows the weight of the portion. The results are shown on Figure 4.26. Twenty five minutes after the addition, the LiMCA probe broke, leaving fractions in the melt, which terminated the experiment. After the addition at minute 26, a large transient peak is observed which settles within minutes. There is a step increase in the particle count of approximately 20K/Kg after the peak has subsided and, thereafter, the count increases by approximately 0.6(K/Kg)/min with time.

Experiment TiB-3: Experiment *TiB-2* was repeated in this test. Table A.6 in Appendix A shows the weight of the single master alloy portion. The results of the particle count versus time are shown in Figure 4.26. It was possible to measure for 120 minutes after the addition. The initial results

are similar to experiment *TiB-2*, but this time the inclusion count is seen to increase rapidly up to minute 140 where it has reached a value of approx. 100 K/Kg. Then the measurement stopped due to difficulties with the LiMCA device.

Experiment TiB-4: Five portions of *B5/1-D* master alloy were added to the melt. Each portion increased the titanium content by 0.035wt% Ti. Table A.7 in Appendix A shows the weight of each portion and also the total titanium concentration. The portions were added to the melt at twenty minutes intervals. The results are shown in Figure 4.27. The inclusion count is seen to increase slowly until the last portion was added. The last addition brings the final measured titanium addition up to 0.17wt% Ti, which is well under the measured solubility level for $TiAl_3$ particles. The last addition, however, caused a step increase in the count which raised the final value up to 50 K/Kg. The reason for this sudden increase is not clear.

Experiment TiB-5: Five portions of *B5/1-C* master alloy were added to the melt at twenty minutes intervals. Each portion increased the titanium content by 0.035wt% Ti. Table A.7 in Appendix A shows the weight of each portion. The results are shown in Figure 4.27. The inclusion count began with a step response behaviour, which was dominating after the first three additions. Step response means that immediately after each addition the inclusion count stabilizes at some constant higher level until the next portion is added. The first step was of the order of 10K/Kg. After the last two additions, there was considerable scatter in the data, but with clear indication of steps. The last values of the inclusion count reach over 100 K/Kg, with the measured wt% of Ti being 0.15wt% .

Experiment TiB-6: Five portions of *B5/1-B* master alloy were added to the melt at twenty minutes intervals. Each portion increased the titanium content by 0.035wt% Ti. Table A.7 in Appendix A shows the weight of each portion. The results are shown in Figure 4.27. The inclusion count only increased slowly throughout the experiment at a rate of approximately 0.3(K/Kg)/min. Practically no step response was observed. After the last addition the particle count was stable at a value of 25K/Kg.

Experiment TiB-7: Five portions of *B5/1-A* master alloy were added to the melt at twenty minutes intervals. Each portion increased the titanium content by 0.035wt% Ti. Table A.7 in Appendix A shows the weight of each portion. The results are shown in Figure 4.27. The inclusion count starts with a simple step response behaviour for the three first additions with the first step being approximately 28K/Kg. After the initial step response after additions four and five, the particle count increases for ten minutes

and then decreases back to the value observed right after the addition, probably due to particle settling.

In the three following experiments, the rotational speed of the rotor was changed from the previous experiments. The new rotor speed is 40 RPM instead of 60 RPM. The purpose of these experiments is to investigate the effect of stirring on the particle count in the crucible. The following experiments were conducted at 40 RPM:

Experiment TiB-8: Five portions of *B5/1-B* master alloy were added to the melt at twenty minutes intervals. Each portion increased the titanium content by 0.04wt% Ti. Table A.8 in Appendix A shows the weight of each master alloy portion. The results are shown in Figure 4.28. They are similar to the results in experiment *TiB-6*. The inclusion count increases slowly at a rate of 0.25(K/Kg)/min and there is practically no step response after each addition. After the final addition, the inclusion count reaches 20 K/Kg.

Experiment TiB-9: Five portions of *B5/1-A* master alloy were added to the melt at twenty minutes intervals. Each portion increased the titanium content by 0.04wt% Ti. Table A.8 in Appendix A shows the weight of each portion. The results are shown in Figure 4.28. The inclusion count shows a pronounced step response for each addition, the first step being approximately 22K/Kg. After the final addition, the inclusion count is stable at 110 K/Kg. The results are similar to experiment *TiB-7* except that the total particle count increases less rapidly.

Experiment TiB-10: Five portions of *B5/1-C* master alloy were prepared but only two were added to the melt. Each portion increased the titanium content by 0.04wt% Ti. Table A.8 in Appendix A shows the weight of each portion. The results are shown in Figure 4.28. Shortly after the second addition, the pneumatic motor broke down and the experiment had to be stopped. The particle count showed a tendency toward a step response behaviour after the first addition with the first step being approximately 8K/Kg. There was a slight decrease in the count shortly before the motor failure, which is probably due to a slower rotating speed before the failure.

Figure 4.30 shows a TiB_2 cluster in a sample from the LiMCA tube taken at the end of experiment *TiB-4*. The sample is fractured and unpolished. The cluster is approximately 20 μm in diameter. Figures 4.31 and 4.32 show EDX spectra of spots A and B in the cluster and Figure 4.33 shows the spectrum in spot 3 connecting the cluster. The results show that the cluster contains titanium and boron. No fluoride salts or oxide were detected in this cluster. Other TiB_2 clusters or inclusions larger than 20 μm , could not be found in the LiMCA tube samples available in this study.

4.5.2 Discussion of the Al-5Ti-1B master alloys

In these experiments, the master alloys contain $TiAl_3$ and TiB_2 particles both of which were detected with the LiMCA device. The $TiAl_3$ phase is soluble and consists of particles ranging from 20–100 μm . These particles are detected right after each addition, with a peak which then disappears rapidly, i.e. a transient response. The dissolution time of $TiAl_3$ is about one minute, which is the cycle time for the LiMCA device. This does not mean that the $TiAl_3$ particles are fully dissolved when they disappear, but there are none larger than 20 μm present after one minute. The individual TiB_2 particles range between 0.1–8 μm in diameter [26] and they should, therefore, not be detected in the melt. However, the master alloys are known to contain clusters of TiB_2 particles which are larger than 20 μm [27, 47]. They are therefore detectable by LiMCA and give a step response after the transient peaks have subsided. Due to the agglomerating behaviour reported for the TiB_2 particles it was also expected to find an increase in the particle count as a function of time. This increase was observed in some of the Al-5Ti-1B experiments, but master alloys from different producers, i.e. *B5/1-A*, *B5/1-B*, *B5/1-C* and *B5/1-D*, showed a slight difference in the particle count behaviour. The results are, however, clear in the support of TiB_2 particle clusters entering the melt from the master alloy and they also show that further agglomeration of these particles can take place in the melt.

Transient behaviour

The quantity of the $TiAl_3$ phase is the practically same in all four Al-5Ti-1B master alloys tested but the particle size distribution is different between alloy types as discussed in Section 3.3. The average $TiAl_3$ particle size was found to be largest in alloy *B5/1-A* or approximately 50 μm . It was 45 μm in alloy *B5/1-D* and 35 μm in alloys *B5/1-B* and *B5/1-C*. It is interesting to compare this order with the difference in height observed in the transient peak response in Figure 4.25. It is evident that the peak height follows the same order as the average $TiAl_3$ particle size, i.e. alloy $A > D > B \geq C$. The same order is found by comparing the peak heights in Figure 4.26 for alloys *B5/1-A*, *B5/1-B* and *B5/1-C*. Thus, it seems likely that the height of the peaks gives a comparison between the $TiAl_3$ particle size in the different Al-5Ti-1B master alloys.

Post-transient behaviour

The results from the comparison of the same class of master alloys from different producers in Figure 4.27 clearly show a different behaviour of the master alloys after the transient peaks subside. Two of the alloys, *B5/1-A* and *B5/1-C* show a step response in the particle count after each addition, with steps of approximately 28K/Kg and 10K/Kg, respectively, as shown in Table 4.3. Thus, there is

Table 4.3: The increase in the particle count produced by the step response after the first addition.

Experiment	Grain Refiner		Additions		Speed [RPM]	Particle count*
	class	type	size	no.		
<i>Ti-1</i>	Al-6Ti		0.03% Ti	10	60	0 K/Kg
<i>Ti-2</i>	Al-6Ti		variable	5	60	0 K/Kg
<i>TiC-1</i>	Al-6Ti-0.03C		0.05% Ti	1	60	5 K/Kg
<i>TiC-2</i>	Al-6Ti-0.03C		0.05% Ti	5	60	3 K/Kg
<i>TiC-3</i>	Al-3Ti-0.15C	<i>C3/.15-A</i>	0.035% Ti	5	60	13 K/Kg
<i>TiC-4</i>	Al-3Ti-0.15C	<i>C3/.15-A</i>	0.035% Ti	1	60	16 K/Kg
<i>TiC-5</i>	Al-3Ti-0.15C	<i>C3/.15-B</i>	0.035% Ti	1	60	7 K/Kg
<i>TiB-1</i>	Al-5Ti-1B	<i>B5/1-B</i>	0.02% Ti	2	60	2 K/Kg
<i>TiB-2</i>	Al-5Ti-1B	<i>B5/1-B</i>	0.2% Ti	1	60	18 K/Kg
<i>TiB-3</i>	Al-5Ti-1B	<i>B5/1-B</i>	0.2% Ti	1	60	16 K/Kg
<i>TiB-4</i>	Al-5Ti-1B	<i>B5/1-D</i>	0.035% Ti	5	60	1 K/Kg
<i>TiB-5</i>	Al-5Ti-1B	<i>B5/1-C</i>	0.035% Ti	5	60	10 K/Kg
<i>TiB-6</i>	Al-5Ti-1B	<i>B5/1-B</i>	0.035% Ti	5	60	1 K/Kg
<i>TiB-7</i>	Al-5Ti-1B	<i>B5/1-A</i>	0.035% Ti	5	60	28 K/Kg
<i>TiB-8</i>	Al-5Ti-1B	<i>B5/1-B</i>	0.035% Ti	5	40	1 K/Kg
<i>TiB-9</i>	Al-5Ti-1B	<i>B5/1-A</i>	0.035% Ti	5	40	22 K/Kg
<i>TiB-10</i>	Al-5Ti-1B	<i>B5/1-C</i>	0.035% Ti	5	40	8 K/Kg
<i>TiB-11</i>	Al-3Ti-0.2B	<i>B3/.2-A</i>	0.02% Ti	9	60	3 K/Kg

* The particle count after the transient peak from first addition subsides.

a large increase in the particle count right after the transient peaks settle. Afterwards the count increases slightly or remains relatively steady around that level. There seems to be some sort of a balance between further agglomeration and the settling of the TiB_2 particles after the initial step response. This is most clearly seen after the first additions. The other two master alloys show a very different behaviour. After each addition, the particle count reaches almost the same level as it was right before the addition but then continues to increase gradually. In this case, the master alloys only add a small and hardly detectable amount of TiB_2 clusters to the melt but some agglomeration occurs with time in the melt increasing the particle count.

The initial step increase, after the transient peak has receded, is higher after large additions than for small additions of the *B5/1-B* master alloy as shown in Figure 4.26. This further supports the conclusion that clusters are being introduced by the master alloy.

The results presented in Figure 4.28 show the particle count when the speed of the rotor has been decreased. The particle count is lower when the rotor is slowed down, but the general behaviour is the same for both rotor speeds. The same master alloys show a step response in the particle count, and the same a

gradual increase.

Figure 4.29 focuses on the particle count after the first addition in Figure 4.28. The particle count is highest with the *B5/1-A* rod and lowest with the *B5/1-B* rod. This figure shows clearly the difference between a step response and a gradual increase in particle count.

Figures 4.34 and 4.35 show the size distribution after the first addition in Figure 4.29. Figure 4.34 shows the average size distribution for a period of 15 minutes after the addition. The *B5/1-A* rod has the highest count for the smaller particles and *B5/1-B* the lowest. This is the same order as for the height of the step response. Above 40 μm , on the other hand, the difference between producers becomes small. By examining Figure 4.35, which shows the normalised size distribution for the same interval, it seems that even though the *B5/1-B* master alloy produces fewer particles above 20 μm they are larger on average. The *B5/1-B* master alloy has only 43% of the particles present in the melt in the size range of 20 – 25 μm while *B5/1-A* has 77% in that range and *B5/1-C* 88%. Another factor, which cannot be seen clearly in those figures is that the *B5/1-C* produces no particles above 70 μm , *B5/1-A* has none over 80 μm and *B5/1-B* has none over 110 μm . It is interesting to note here, that in the work of Martin and Guthrie [47] the size of the TiB_2 clusters measured after the addition of an Al-5Ti-1B master alloy to an aluminium melt in a furnace was 10-100 μm in diameter. This is, therefore, in good agreement with the present results.

The results clearly show that the addition of alloys *B5/1-A* and *B5/1-C* is introducing a much higher quantity of TiB_2 particle clusters into the melt than the addition of alloys *B5/1-B* and *B5/1-D*. The order of increased agglomerate content of the alloys is $A > C > B = D$. This is not the same order as for the peak response discussed above further supporting the conclusion that different particles are causing these responses.

The TiB_2 content of the alloys is practically the same but the difference in the agglomerate content can be related to the microstructure of the alloys. It is interesting to compare the particle count shown in Figure 4.27 with the metallogical analysis of these alloys presented in Section 3.3 and in Figures 3.11, 3.12, 3.13 and 3.14. Master alloy *B5/1-A* which gives the highest step response (28K/Kg) showed a slight degree of texturing of the TiB_2 particles but by far the highest quantity of impurities (black spots) containing fluoride salts and oxides. Also, the impurities were usually associated with the TiB_2 particles in this alloy. Master alloy *B5/1-C* gave the second highest step response (10K/Kg). This alloy showed a high degree of texturing of the TiB_2 particles and the impurities were mainly concentrated along the TiB_2 lines. Master alloys *B5/1-B* and *B5/1-D* showed practically no step response. The former has a high degree of texturing but the impurities are more randomly distributed than in master alloy *B5/1-C*. The latter, *B5/1-D*, showed no signs of texturing of the TiB_2 particles and also a

random distribution of the impurities. This comparison seems, therefore, to indicate that the observed particle count is dependent upon the distribution of the TiB_2 particles and impurities in the master alloys and also on the total quantity of impurities. It is difficult to generalise from these results alone, but they support the conclusion that a large quantity of impurities containing fluoride salts and oxides or a combined texturing of the impurities and TiB_2 particles increase the probability of cluster formation in the master alloys. Further agglomeration in the melt appears to be less dependent on the microstructure of the master alloys as expected.

Time dependence of distribution

The tests showing the long term effect of additions of different portions of $B5/1-B$ master alloy shown in Figure 4.26, support the theory that the TiB_2 particles are also agglomerating in the melt. The particle count increases as a function of time after addition of the master alloy into the melt and both large and small additions show the same behaviour, but on a different scale.

A feature supporting the agglomeration theory is the decrease in the particle count after 120 minutes in test $TiB-1$, when the smaller portions were added (see Figure 4.26). To explain this behaviour it must be remembered that settling of the largest particles is occurring throughout the experiments [51]. In order to compensate for the settling, particles smaller than $20\mu m$ must constantly agglomerate to increase the particle count. But after some time the available quantity decreases of both the smaller particles and also the impurities which are holding the agglomerates together, thereby decreasing the agglomeration rate. This results in a lower number of particles entering the detection zone. Therefore, at some point, the settling rate of the particles exceeds the agglomeration rate and results in decrease in the particle count.

The settling of the TiB_2 particles during the test can be evaluated from the chemical analysis before and after each experiment. The quantity of titanium added in the master alloy is compared with the quantity of titanium after the experiments with the starting value subtracted. Larger particles are more prone to settling than smaller ones, i.e. the settling rate is a function of particle size (see Figure 4.12). In the experiments, the addition of the $B5/1-A$ master alloy has resulted in the highest particle count, and the addition of $B5/1-B$ gave the lowest count. Therefore it is suitable to compare those two. With a rotational speed of 60 RPM, the expected quantity of titanium was 0.175 wt% Ti. The titanium content after the five additions of $B5/1-B$ master alloy was 0.15 wt% Ti, which is slightly lower than the target value, whereas with the $B5/1-A$ the titanium content is down to 0.13 wt% Ti. The decrease in the titanium content is mainly the result of TiB_2 settling, and the settling rate is therefore faster after additions of the $B5/1-A$ master alloy. This supports that there is a greater

number of large particles ($> 20\mu\text{m}$) being introduced by the *B5/1-A* master alloy. Looking at the same master alloy additions at 40 RPM, the same trend is observed. The target value is 0.2 wt% Ti. Now the titanium content, after the five additions of *B5/1-B* master alloy, is 0.16 wt% Ti, but after the *B5/1-A* additions, the measured titanium content is only 0.13 wt% Ti. One important result from this is that the settling rate is faster at 40 RPM than at 60 RPM. This means that when comparing the results at 40 and 60 RPM, the change in the agglomeration rate is not only affecting the results, but also the settling rate of the particles.

More useful information can be obtained if the volume of the particles in the melt is compared with the total volume of particles added to the melt. For the Al-5Ti-1B master alloy, the volume of TiB_2 particles can be calculated using the density of TiB_2 as $4520\text{kg}/\text{m}^3$. In one gram of Al-5Ti-1B master alloy there are 0.03214g of TiB_2 which can be converted to a volume of TiB_2 using the equation

$$V_{TiB_2} = \frac{0.03214 \times 10^{-3}\text{kg}}{4520\text{kg}/\text{m}^3} = 7.11 \times 10^{-9} \frac{\text{m}^3}{\text{per gram of GR addition}} \quad (4.3)$$

This means that when the addition is for instance 60g of Al-5Ti-1B master alloy, the total volume of TiB_2 added is

$$60\text{g} \times 7.11 \times 10^{-9} \frac{\text{m}^3}{\text{g}} = 4.266 \times 10^{-7}\text{m}^3 \quad (4.4)$$

The figures which show the volume of particles measured with the LiMCA device give the volume of particles per kilo of melt, not the total volume. Therefore, the calculated volume from the master alloy addition is divided with the quantity of the melt before comparison.

Figure 4.37 shows the percentage of the volume of TiB_2 particles detected after two small additions in experiment *TiB-1*. The total added volume of TiB_2 particles is $5.72 \times 10^{-8}\text{m}^3$ per kilo of melt. The maximum peaks are at values around $1.5 \times 10^{-9}\text{m}^3/\text{kg}$ which means the LiMCA was detecting 2.27% of the total volume added. This means that 97.73% of the volume is in particles smaller than $20\mu\text{m}$. These volume peaks occur eighty minutes after the second addition, but if the volume is examined five minutes after the second addition then only 0.53% of the volume is detected. It must be stressed that these calculation do not take into account the settling of the clusters during the experiments. The size distribution of the detected particles remains practically the same with time as discussed further in Section 4.7.

Figure 4.38 shows the the percentage of the volume of TiB_2 particles after one large addition in experiments *TiB-2* and *TiB-3*. The total volume of TiB_2 particles was $2.82 \times 10^{-7}\text{m}^3/\text{kg}$ in experiment *TiB-2* and $2.84 \times 10^{-7}\text{m}^3/\text{kg}$ in *TiB-3*. The highest peak was detected in experiment *TiB-3*, but the volume was

still increasing when the experiment stopped. The maximum value is approx. $3.1 \times 10^{-9} m^3/kg$ which means the LiMCA was then detecting 1.09% of the total volume added. This percentage would possibly have become higher if the measurements could have been continued.

These results clearly show that agglomeration is taking place in the melt and that the largest agglomerates are settling in the crucible during the course of the experiments.

Dependence of distribution in alloy types

Figure 4.39 shows the percentage of the TiB_2 volume detected in experiments *TiB-8* and *TiB-9*. The data series from experiment *TiB-10* was too short to be included. The percentage is lower for the *B5/1-B* rod, but the difference is much smaller than the particle count indicates. The reason for this is the particle size distribution. The size distribution of the *B5/1-A* in test *TiB-9* shows a much higher quantity of small particles (Figure 4.34) which results in a lower volume. Another feature is that the *B5/1-A* volume percentage seems to decrease slightly during the first 40 minutes after the first addition whereas the *B5/1-B* volume percentage slightly increases for the first 20 minutes and is relatively stable thereafter. This was not investigated further.

Figure 4.40 shows the percentage of the TiB_2 volume detected in experiments *TiB-4*, *TiB-5*, *TiB-6* and *TiB-7*. The level of the detected volume is now much higher than in the previous figure, even with smaller portion of master alloy added to the melt each time. The reason for this is the higher rotating speed. The flow conditions therefore, have a pronounced effect on the agglomeration and settling rate of the TiB_2 particles as previously discussed. On average, the volume percentage is lowest for the *B5/1-D* master alloy and *B5/1-B* is slightly higher. *B5/1-A* has the highest percentage, but the difference in volume between the master alloys is much lower than the differences in the particle count due to the particle size distribution.

Comparison with the Al-3Ti-0.15C master alloys

Table 4.4 shows a comparison between the volume of particles detected after the first step response for the Al-5Ti-1B and Al-3Ti-0.15C master alloys. The additions correspond to 0.035% increase in titanium. Using this addition size the volume of TiC particles is approximately 34% of the volume of the TiB_2 particles. The high oxide master alloy *C3/.15-A* gives the highest detected volume, further supporting the role of impurities such as oxide in the agglomeration process. The commercial carbon containing alloy, *C3/.15-B*, gives a similar percentage detected as the boride alloy giving the highest results, i.e. *B5/1-A*. On the other hand, the volume of the TiC particles is more in line with the results for the second lowest Al-5Ti-1B alloy, *B5/1-B*, due to the difference in the added

Table 4.4: A comparison of the detected volume of TiB_2 and TiC particles after the first step response for the Al-5Ti-1B and Al-3Ti-0.15C master alloys. The additions correspond to 0.035% increase in titanium.

Experiment	Grain refiner	Added volume [m^3 per kg]	Detected volume [m^3 per kg]	Percentage detected
<i>TiC-4</i>	<i>C3/.15-A</i>	1.77×10^{-8}	5.0×10^{-10}	2.8 %
<i>TiC-5</i>	<i>C3/.15-B</i>	1.77×10^{-8}	1.0×10^{-10}	0.56 %
<i>TiB-7</i>	<i>B5/1-A</i>	5.15×10^{-8}	3.1×10^{-10}	0.60 %
<i>TiB-6</i>	<i>B5/1-B</i>	5.15×10^{-8}	1.0×10^{-10}	0.19 %
<i>TiB-5</i>	<i>B5/1-C</i>	5.15×10^{-8}	2.1×10^{-10}	0.40 %
<i>TiB-4</i>	<i>B5/1-D</i>	5.15×10^{-8}	0.52×10^{-10}	0.10 %

volume. These results do not, therefore, show a significant difference between the commercial Al-3Ti-0.15C master alloy and the Al-5Ti-1B alloys.

4.6 The Al-3Ti-0.2B master alloy

In the final part of the experiments, an Al-3Ti-0.2B master alloy was employed. The experiment focuses on the long term effect of the grain refiner addition. The master alloy is labelled *B3/.2-A*.

4.6.1 Experimental results

The characteristics and chemical composition of the master alloy is given in Section 3.4. The base metal was commercially pure aluminium with chemical analysis shown in Table A.1 in Appendix A.

Experiment TiB-11: Nine portions of *B3/.2-A* master alloy were prepared.

Table A.9 in Appendix A lists the additions and Figure 4.41 shows the particle count for the experiment. The particle count rises with the first four additions with a slight indication of a step response, i.e. approximately 3K/Kg. After that it is almost stable at 20–30 K/Kg. After addition seven it starts to fall again, except for a peak in the signal when a new LiMCA probe is added. This disturbance is probably because of the oxide layer on top of the melt which goes into the melt when the new probe is dipped in again. The particle count settles on value of around 20 K/Kg, when an equilibrium between cluster formation and settling appears to have been achieved.

4.6.2 Discussion of the Al-3Ti-0.2B master alloys

The general behaviour of the Al-3Ti-0.2B master alloy is similar to that of the Al-5Ti-1B alloys. A step response is obtained with steps of a similar magnitude to the *B5/1-C* alloy, when the difference in the total TiB_2 content is taken into account (see Table 6.2). The effect of further agglomeration in the melt is also observed and the effect of settling in the latter stages of the experiment.

4.7 Further analysis of LiMCA results

There are several interesting possibilities for further analysis of the LiMCA measurements for each test run. Such analysis is beyond the scope of this project but some of the possibilities will be outlined as basis for future work.

Figure 4.42 shows the particle count for the large particles, i.e. ranging from 50 to $120\mu\text{m}$, measured in experiment *TiB-1* at different times. There were two almost simultaneous small additions of Al-5Ti-1B master alloy approximately at minute 35. The number of large particles is lowest at minute 40, but then the total particle count was also the lowest. There is little difference between the other curves, indicating that the number of the larger particles stays practically the same in the melt.

Figure 4.43 shows the normalized size distribution for the same size range as in Figure 4.42. There is some indication of a change in the particle size distribution as a function of time, with an increasing proportion of larger particles. However, this is not an indication of an increase in the number of these particles, but only that their number is increasing compared to the number of the smaller particles. Figure 4.44 shows the same data only focusing on the particle size range of 70 to $120\mu\text{m}$.

One method to illustrate the complexity of the data is to look at the percentage of particles larger than $110\mu\text{m}$ as a function of time. Figure 4.45 shows how the percentage of these particles changes with time. The time scale shown starts at minute forty in the run, since the grain refiner portions are introduced into the melt at minute 35. From this figure is not possible to deduce that the relative quantity of large particles is increasing with time.

A different approach is to look at the particle count for each size interval individually and estimate the best line fit through that. This is carried out with the normalized data. The best line fit can either been obtained from the whole data series or can be limited to some fixed time intervals. When this has been done for all the size ranges, the slope of the best line fit is plotted as a function of diameter. If the slope is positive, then the percentage of particles in the given size range is increasing. Conversely, if the slope is negative, the percentage is decreasing.

Figure 4.46 shows the slopes of the best line fit through the data from exper-

iment *TiB-1*. The original data showed an increase in particle count after the addition up to minute 120 when the particle count starts decreasing. Therefore, the data was analyzed before and after minute 120. The figure shows that after minute 120 the percentages of 20-25 microns particles is decreasing, but the percentages of larger particles is increasing.

Figure 4.47 shows the slopes of the best line fit through the data from experiment *TiB-3*. The original data showed a constant increase in the particle count, but the two time intervals examined here are chosen shortly after the addition and near the end of sampling. The figure shows that towards the end, the percentage of larger particles is increasing, similar to the behaviour in Figure 4.46, when the particle count was decreasing.

Figures 4.48 and 4.49 show the original data from experiments *TiB-1* and *TiB-3* presented in the form of an average particle diameter. This presentation is employed to examine if there is any change in the average particle diameter during the measurement runs. The average diameter is calculated by multiplying the number of particles in each size range with the diameter, adding it up for all size ranges and then dividing by the total number of particles. This is done for each measurement point in the data. The results show no indication of a change in the average diameter.

It is evident from these methods of analysis of the experimental data that detailed information can be obtained on particle behaviour in aluminium melts using the LiMCA method. Combining this with frequent metallographical analysis of the melts would help in further understanding of the agglomeration process observed in this project.

4.8 Summary

The results presented in this chapter have shown that the LiMCA device and the experimental setup developed in this project allow detailed measurements of particle behaviour after the addition of master alloys into aluminium melts. Table 4.3 gives an overview of the experiments. The main results can be summarized as follows:

- The dissolution of the large $TiAl_3$ particles can be monitored with the LiMCA device down to a size of $20\mu\text{m}$. The rate of dissolution is fast or of the order of 1-2 minutes. The addition of the Al-6Ti master alloy into the melt produced peak signals in the particle count, with the count returning to the original baseline in 1-2 minutes. The height of the peaks appears to give an indication of the size distribution of the $TiAl_3$ phase in the master alloy.
- Insoluble inclusions larger than $20\mu\text{m}$ are introduced into the melt by the Al-Ti-B and Al-Ti-C master alloys and they can be monitored with the

present experimental setup. The inclusions are most probably clusters of the small insoluble or sparingly soluble TiB_2 and TiC particles in the master alloys. The clusters often produce a step increase in the particle count from that prior to the addition after the $TiAl_3$ particles have dissolved. This indicates that the clusters are already present in the master alloy when it is dissolved in the melt. Further particle agglomeration in the melt was also detected.

- The Al-Ti-C master alloys showed both a step response behaviour directly after their introduction and also further agglomeration in the melt. The step response increased with an increased oxide content of the two Al-3Ti-0.15C master alloys tested but the rate of further agglomeration in the melt was similar. The measured volume of TiC particles after the transient peak had subsided indicated that 2.8% of the total added TiC particle volume ($1.77 \times 10^{-8} m^3/kg$) was in clusters in the high oxide alloy. The percentage was 0.56% for the commercial alloy using the same addition. The measured clusters were approximately 20-100 μm in diameter.

The low carbon Al-6Ti-0.03C master alloy also showed a step response behaviour but with a smaller step than the above alloys. The volume percentage of the TiC particles forming clusters was 2.7% of the total added TiC particle volume ($0.26 \times 10^{-8} m^3/kg$). This is a similar percentage to that of the high oxide Al-3Ti-0.15C master alloy.

Clusters of TiC particles associated with oxide, presumably aluminium oxide, were found by microscopy in a sample of the high oxide Al-3Ti-0.15C alloy taken from the LiMCA tube. Similar clusters were discussed in Section 3.5. The LiMCA measurements are, therefore, in an agreement with the metallurgical observations.

- Four types of Al-5Ti-1B master alloys were tested. Two of these showed a high step response, but the other two showed practically no such response except at extremely high addition rates. Further particle agglomeration in the melt was also detected for all types. The size range of the clusters was approximately 20-100 μm which is similar to that reported by Martin and Guthrie [47]. The volume percentage of the added TiB_2 particles measured after the transient peak has subsided ranged from 0.1% to 0.6% of the total added TiB_2 particle volume ($5.15 \times 10^{-8} m^3/kg$).
- The Al-3Ti-0.2B master alloys tested showed the same general behaviour as the Al-5Ti-1B alloys described above. It gives a step response and further agglomeration in the melt was also observed.
- An increased flow rate produced by an increased stirrer rotation speed, resulted in a higher particle count in the melt. This can be either due to

an increase in the rate of particle collisions or a reduced settling rate. This was not investigated further.

The most important finding of these experiments is the fact that some of the small insoluble particles in the master alloys are introduced in the form of clusters which can subsequently grow further in the melt. Similar clusters can also be formed in the melt itself. This behaviour of the grain refining particles has not been reported before for aluminium melts using the LiMCA device for particle detection. Master alloys from different producers show a different behaviour in this respect and this type of experiment can possibly be employed to improve the properties of master alloys in the future.

4.9 Figures

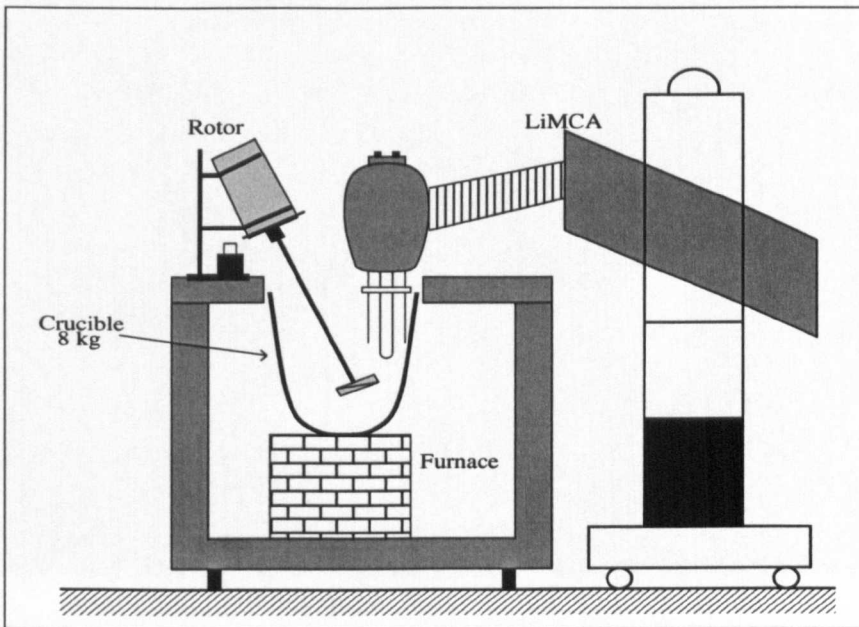


Figure 4.1: The experimental setup. The upper diameter of the crucible was 200mm and the depth of the melt was approximately 200mm. The width of the impeller head was 80mm and it was positioned approximately 150mm below the surface. The depth of the LiMCA probe was approximately 80mm.

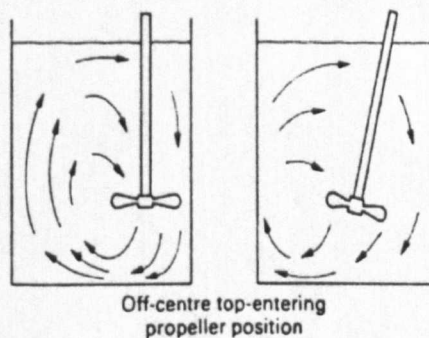


Figure 4.2: The flow profiles in a rectangular crucible [63], with rotor offset from centre.

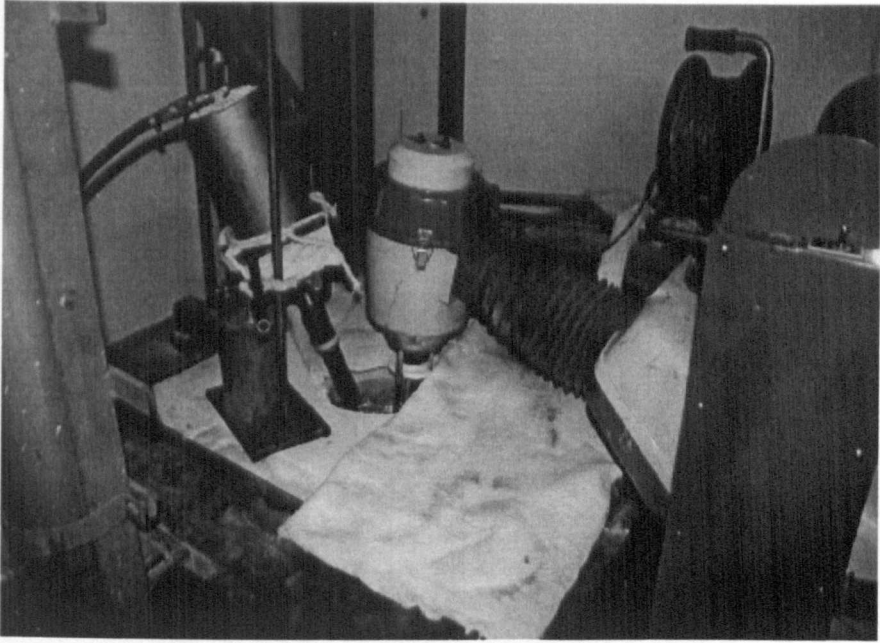


Figure 4.3: The experimental setup in operation. The impeller shaft is entering the melt on the left and the LiMCA head on the right.

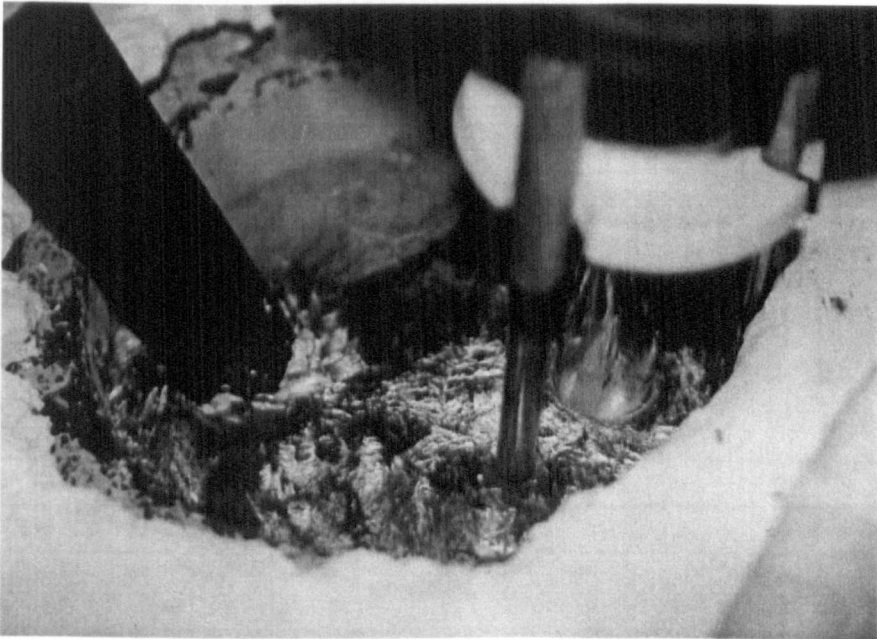


Figure 4.4: The experimental setup in operation, focusing on the LiMCA head entering the melt.



Figure 4.5: Metal sucking device.

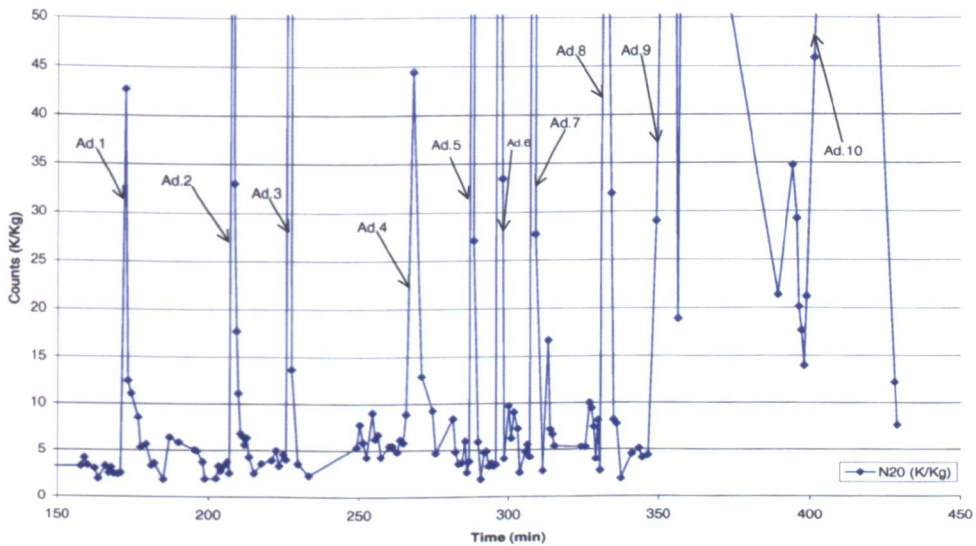


Figure 4.6: The particle count in experiment *Ti-1*. Grain refiner Al-6Ti. Each addition point is labelled with the number of the addition. The additions are shown in Table A.2.

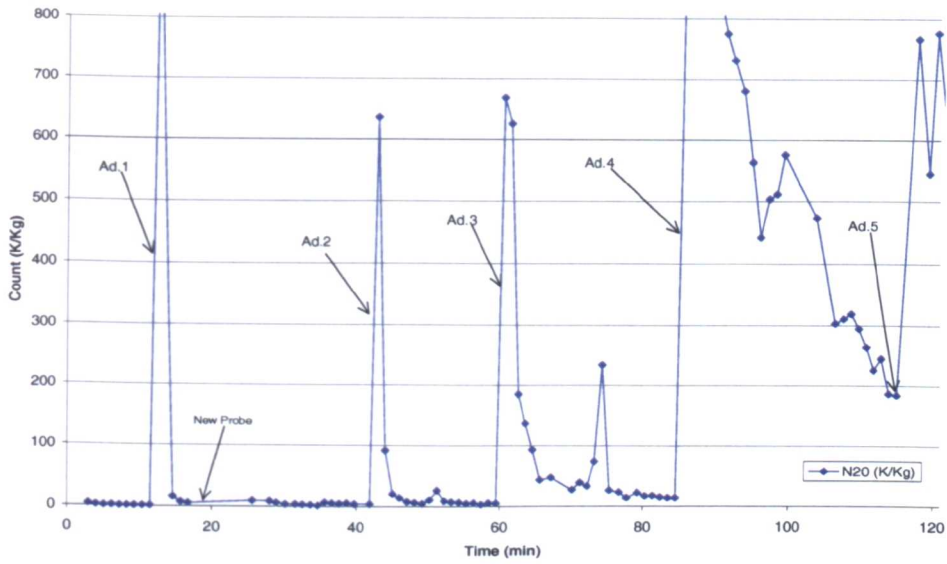


Figure 4.7: The particle count in experiment *Ti-2*. Grain refiner Al-6Ti. Each addition point is labelled with the number of the addition. The additions are shown in Table A.2.

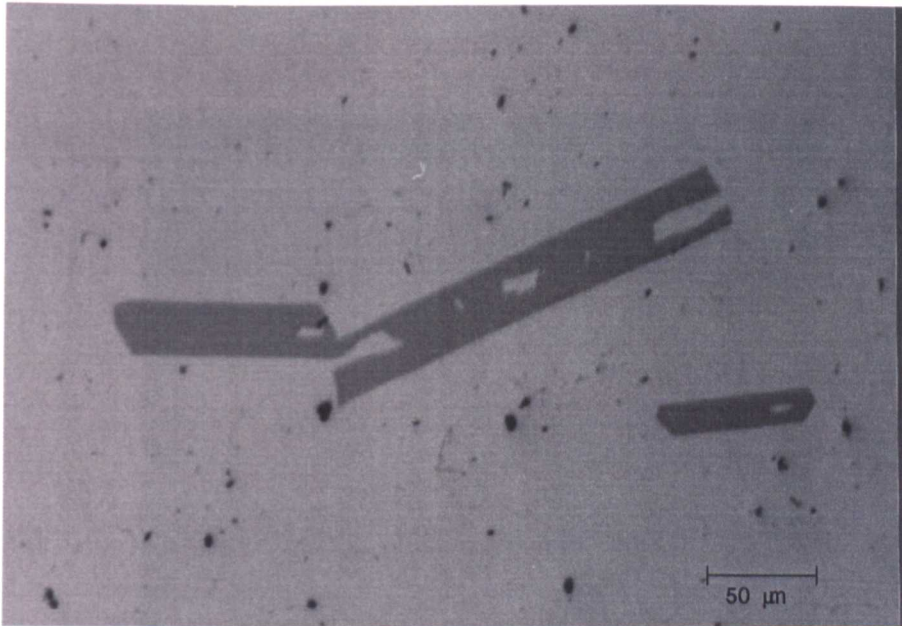


Figure 4.8: Cross-section of a sample taken with a metal sucking device, fifteen minutes after experiment *Ti-1*. The large grey blocky particles are $TiAl_3$. Magnification 200X.

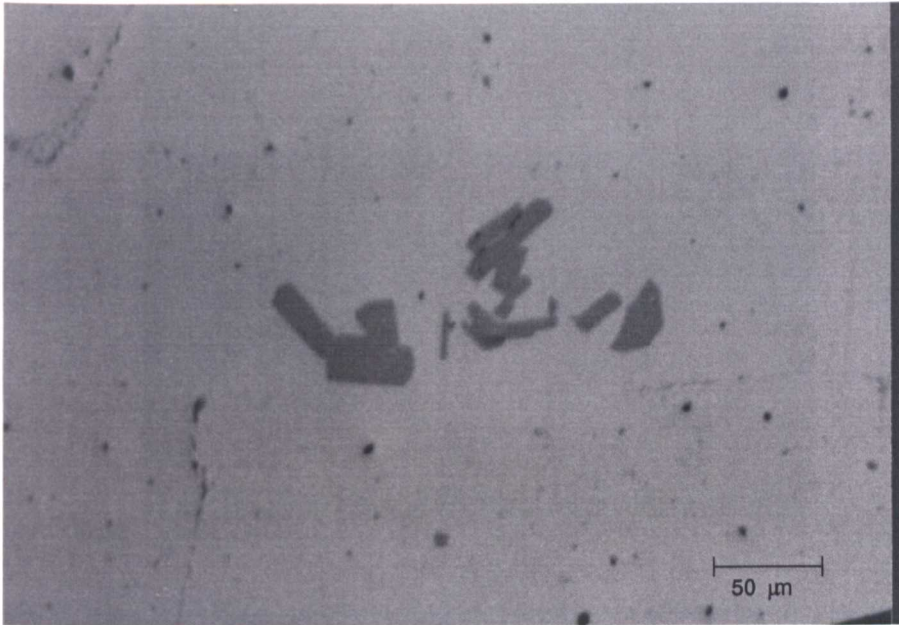


Figure 4.9: Cross-section of a sample taken from the LiMCA probe after experiment *Ti-2*. The large grey blocky particles are $TiAl_3$. Magnification 200X.

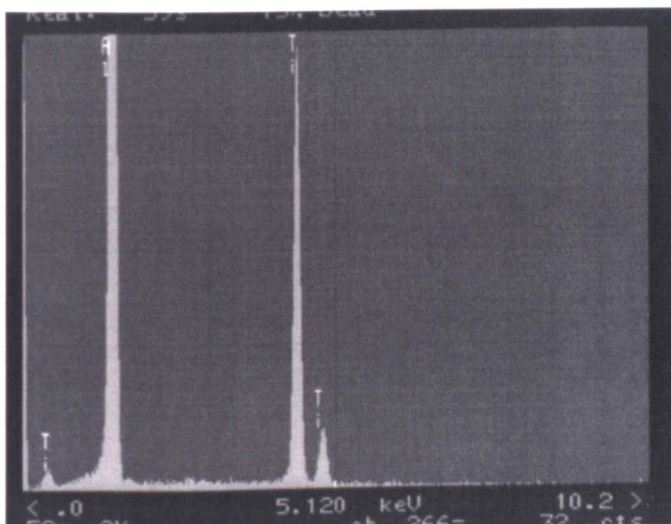


Figure 4.10: The EDX spectrum of the large particle in Figure 4.9.

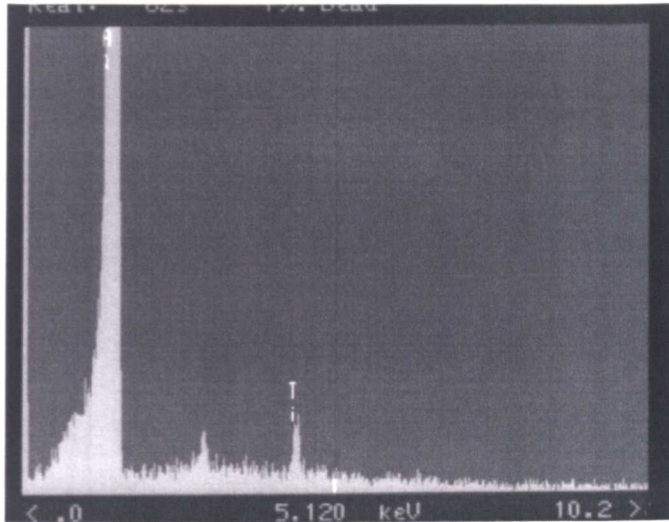


Figure 4.11: The EDX spectrum of the α -phase of the base metal in Figure 4.9. The unmarked peak between Al and Ti is $2xAl$.

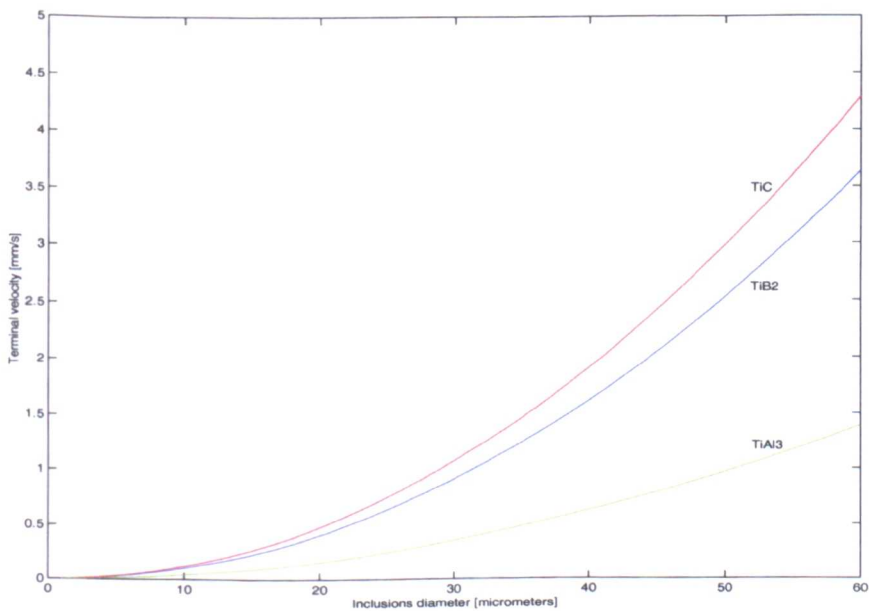


Figure 4.12: The Stokes settling rate for spherical particles in a stagnant aluminium bath.

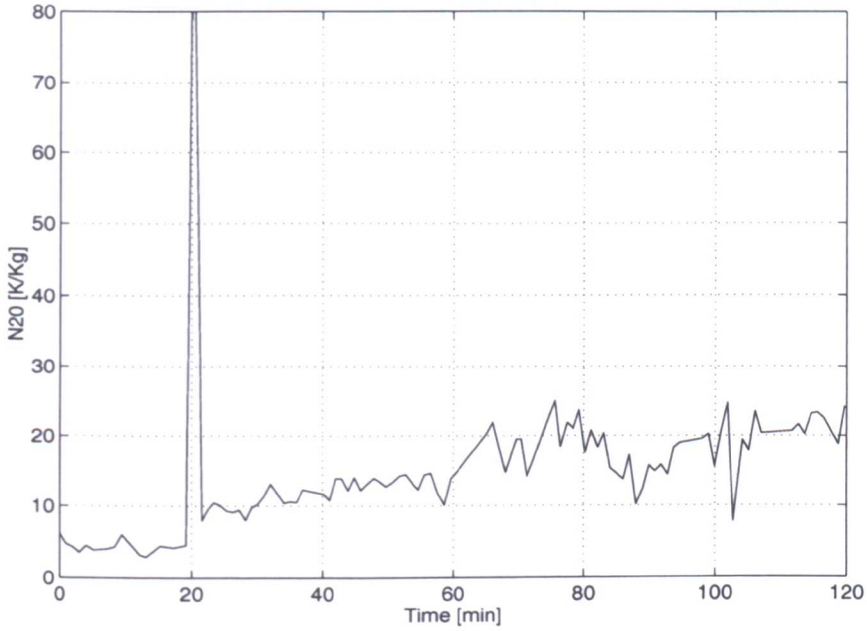


Figure 4.13: The particle count (N20 = Particles larger than $20\mu\text{m}$) in experiment *TiC-1*. Grain refiner Al-6Ti-0.03C. The additions are shown in Table A.3

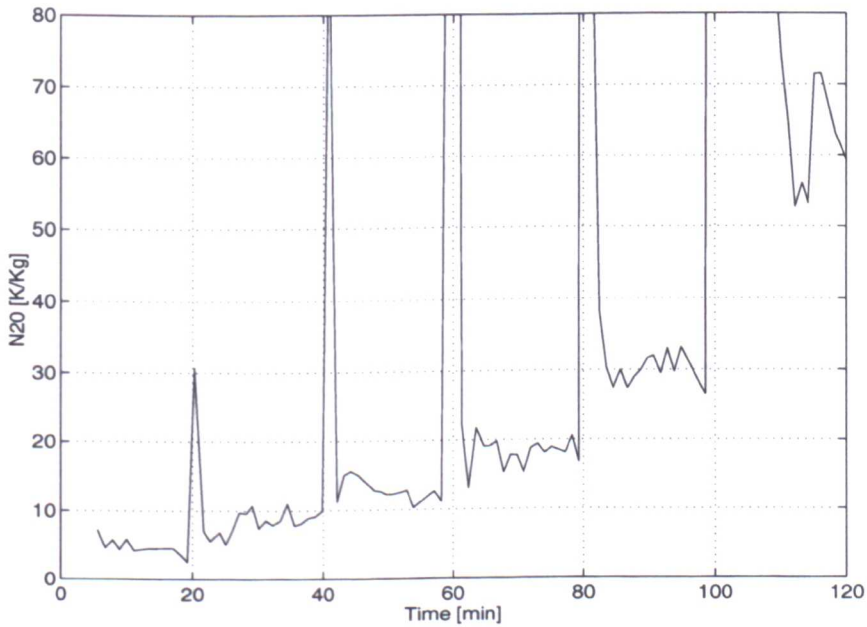


Figure 4.14: The particle count (N20) in experiment *TiC-2*. Grain refiner Al-6Ti-0.03C. The additions are shown in Table A.3

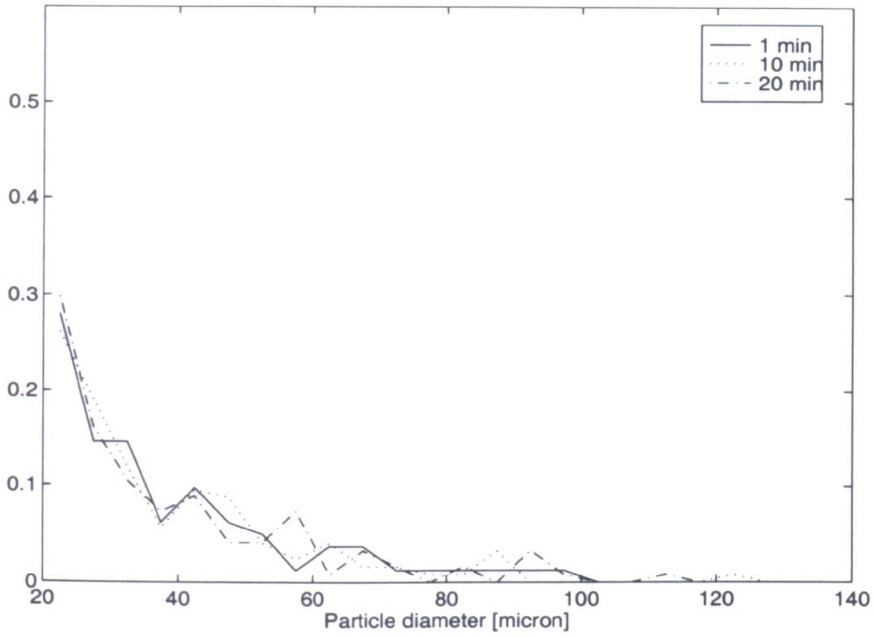


Figure 4.15: The normalized size distribution in experiment *TiC-1*, one, ten and twenty minutes after the addition, respectively.

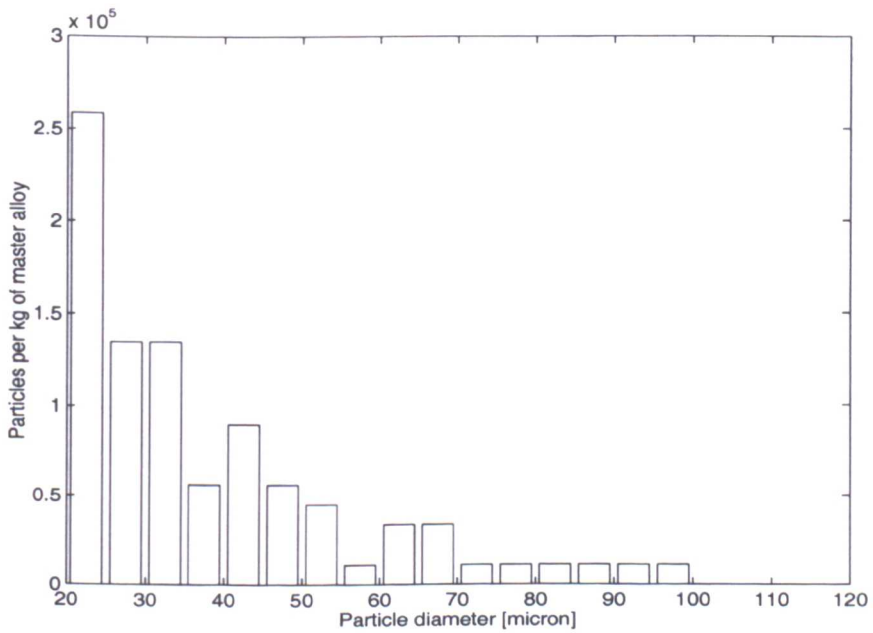


Figure 4.16: The particle count per kg of the Al-6Ti-0.03C master alloy in experiment *TiC-1* one minute after the addition of the master alloy.

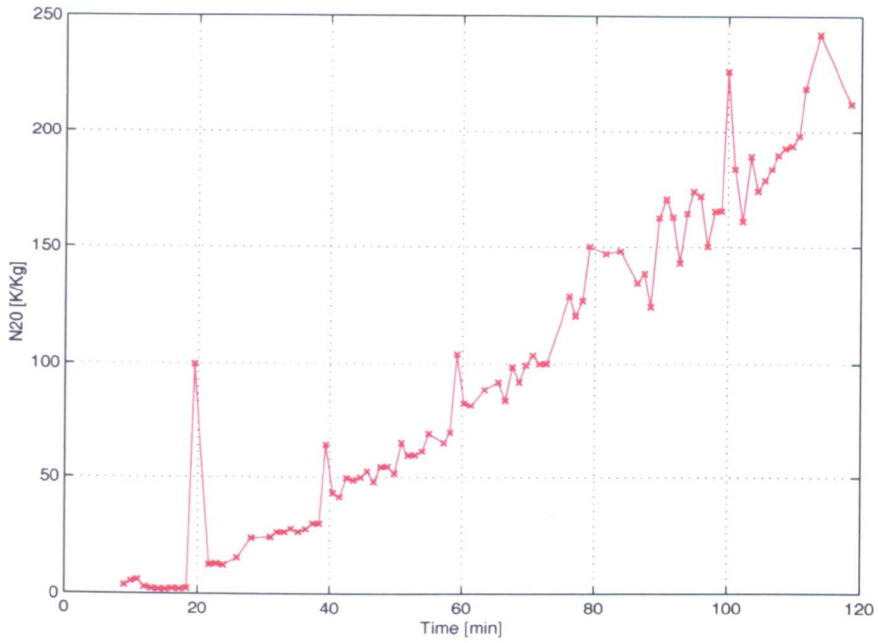


Figure 4.17: The particle count (N20) in experiment *TiC-3*. Grain refiner Al-3Ti-0.15C. The master alloy is of type *C3/.15-A*. The additions are shown in Table A.4

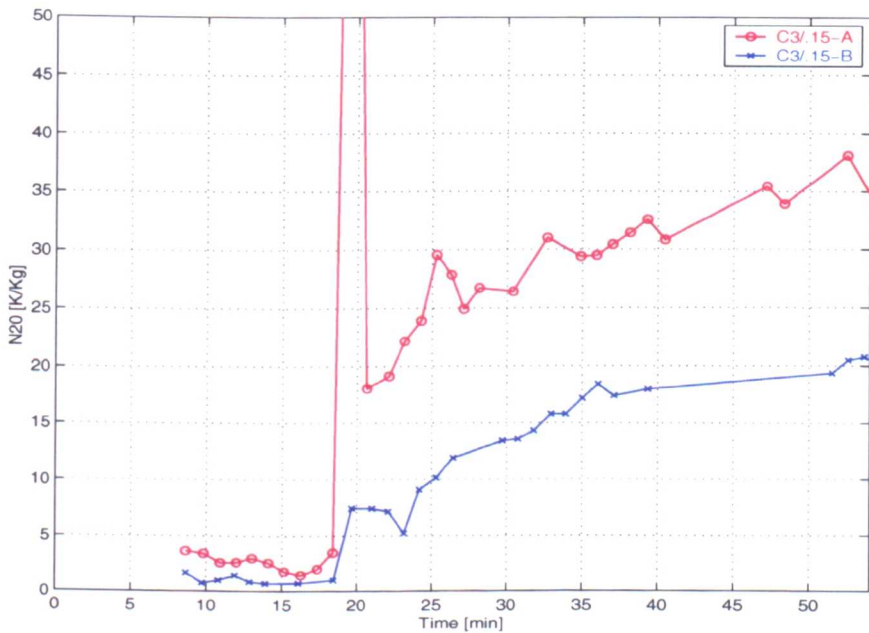


Figure 4.18: The inclusion count (N20) in experiment *TiC-4* and *TiC-5* Grain refiner Al-3Ti-0.15C. The additions are shown in Table A.4



Figure 4.19: A *TiC* cluster in fractured sample from the LiMCA tube taken at the end of experiment *TiC-3*. The sample is unpolished. EDX spectra at points A, B and C are shown in the following figures.

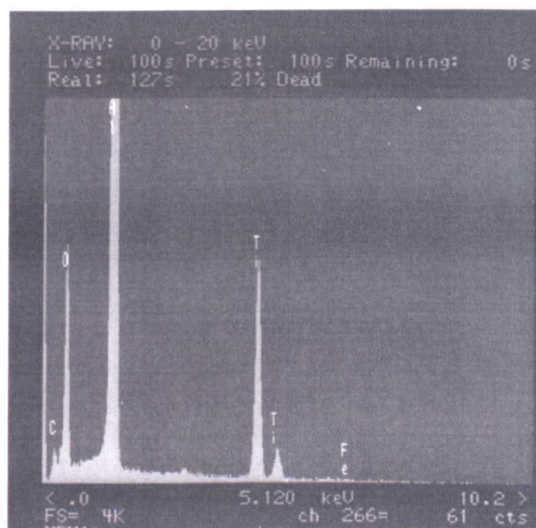


Figure 4.20: EDX spectrum at point B in the *TiC* particle cluster shown in Figure 4.19.

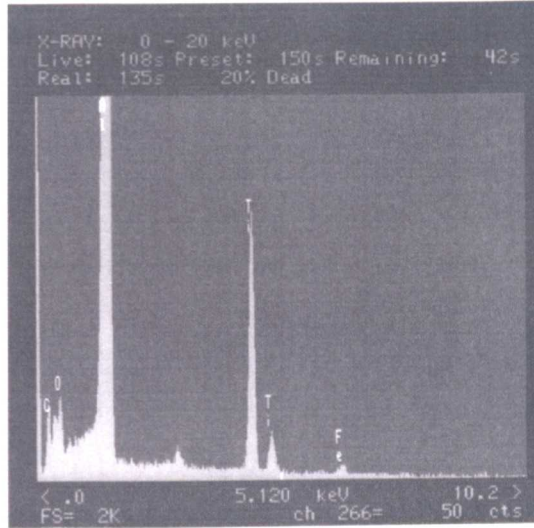


Figure 4.21: EDX spectrum at point C in the TiC particle cluster shown in Figure 4.19.

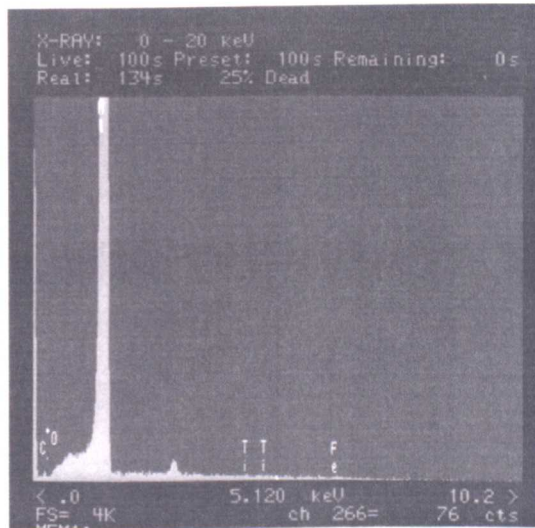


Figure 4.22: EDX spectrum at point A outside the TiC particle cluster shown in Figure 4.19.

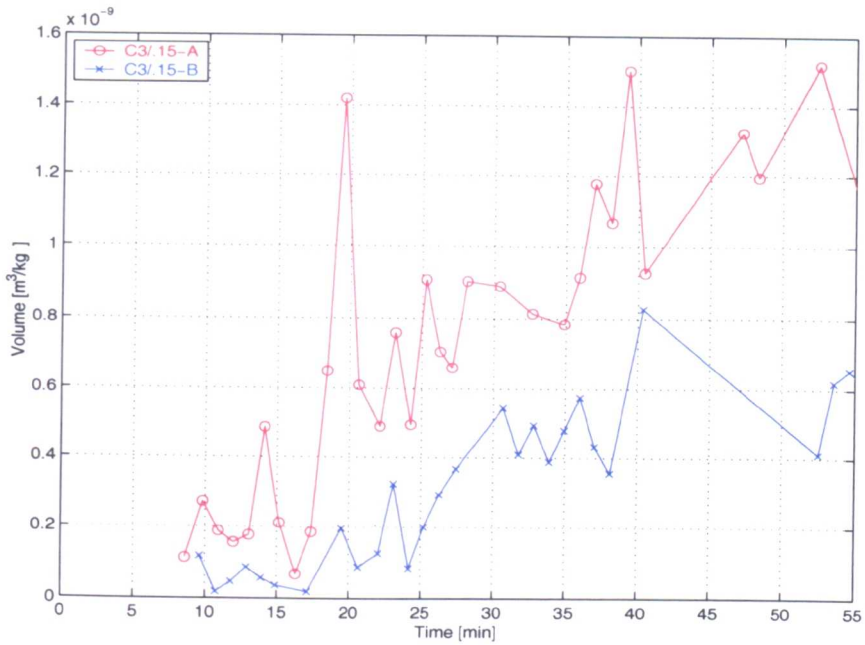


Figure 4.23: The volume of the detected particles shown in Figure 4.18.

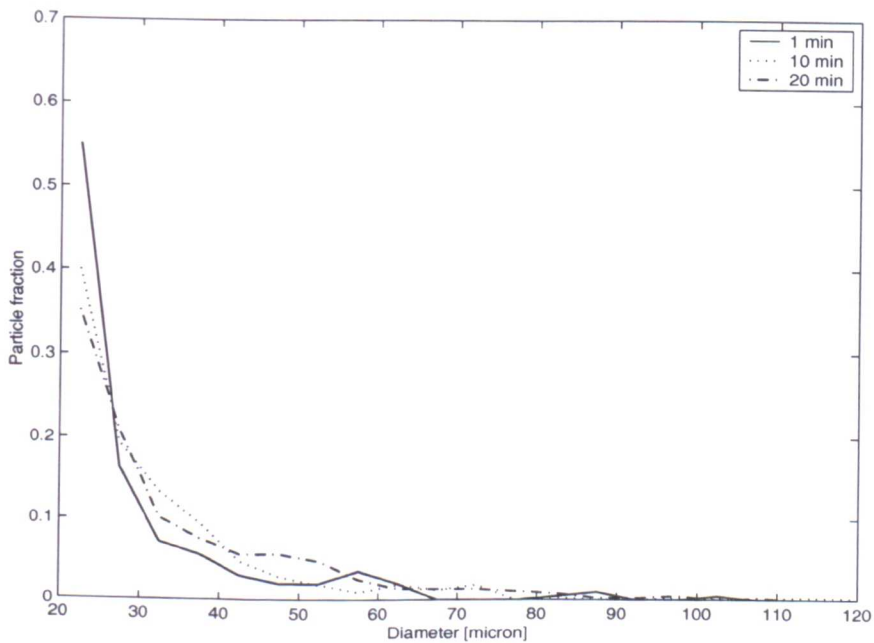


Figure 4.24: The normalized size distribution for the master alloy C3/.15-A in experiment *TiC-4*, calculated one, ten and twenty minutes after the additions shown in Figure 4.18

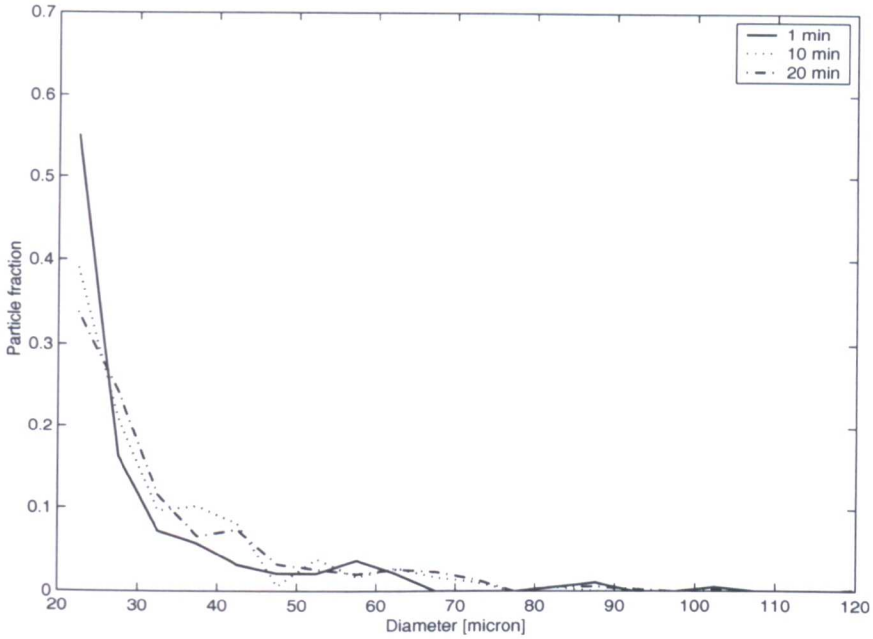


Figure 4.25: The normalized size distribution for the master alloy C3/.15-B in experiment *TiC-5*, calculated one, ten and twenty minutes after the additions shown in Figure 4.18

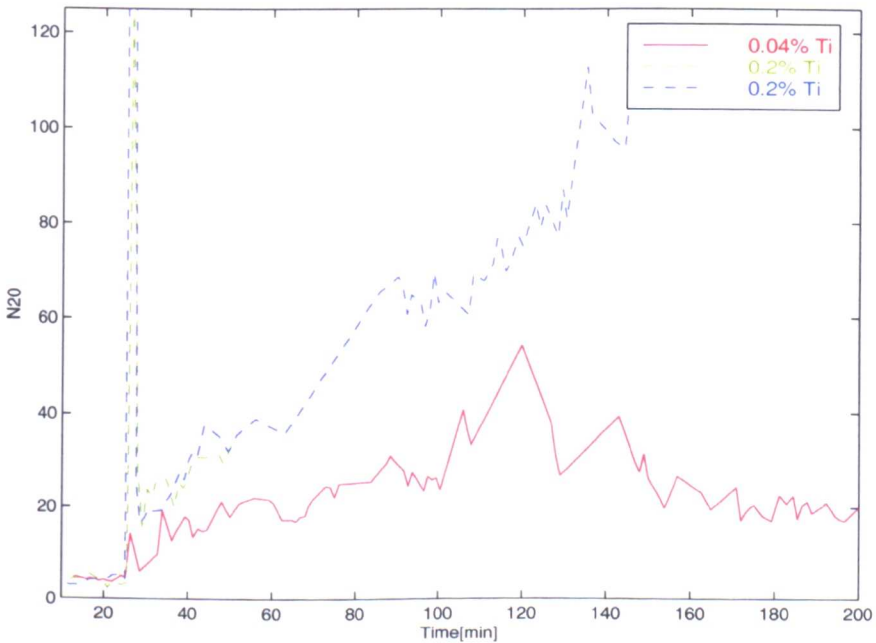


Figure 4.26: The particle count (N20) with two small additions in the beginning of the measurements (solid line, experiment *TiB-1*) and two series with high titanium content added in the beginning (dashed lines, experiments *TiB-2* and *TiB-3*). The master alloy was *B5/1-B*. The additions are shown in Table A.6.

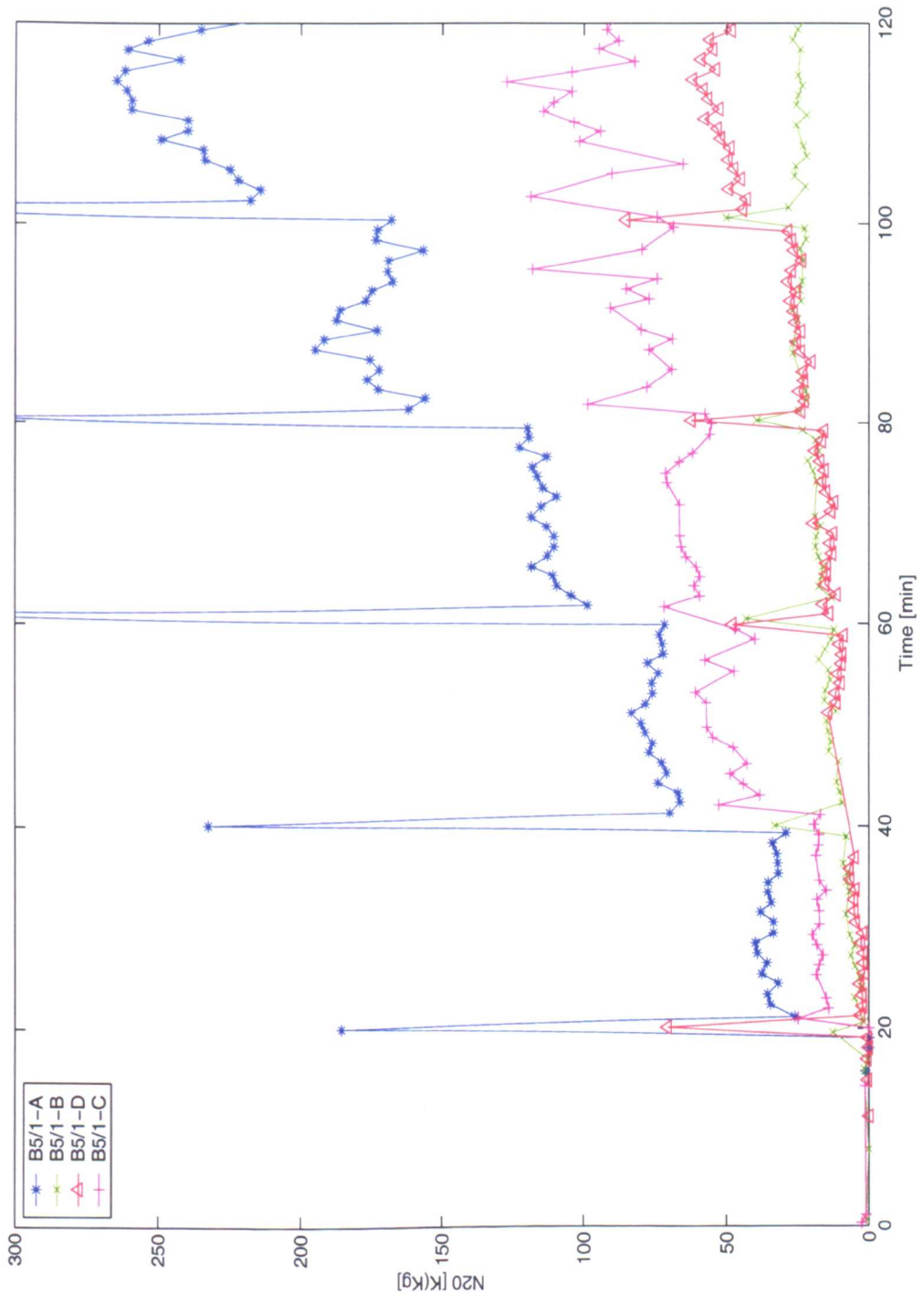


Figure 4.27: The particle count from experiments *TiB-4* to *TiB-7*, the additions give 0.035 wt% Ti at minutes 20, 40, 60, 80 and 100. The additions are shown in Table A.7.

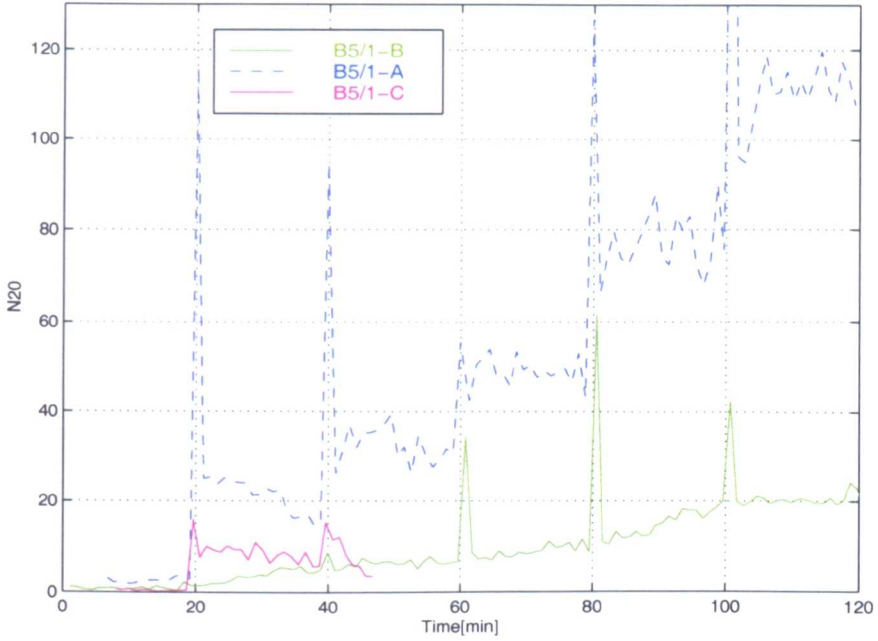


Figure 4.28: The particle count from experiments *TiB-8* to *TiB-10*, the additions give 0.04 wt% Ti at minutes 20, 40, 60, 80 and 100. The rotor speed is 40 RPM. The additions are shown in Table A.8.

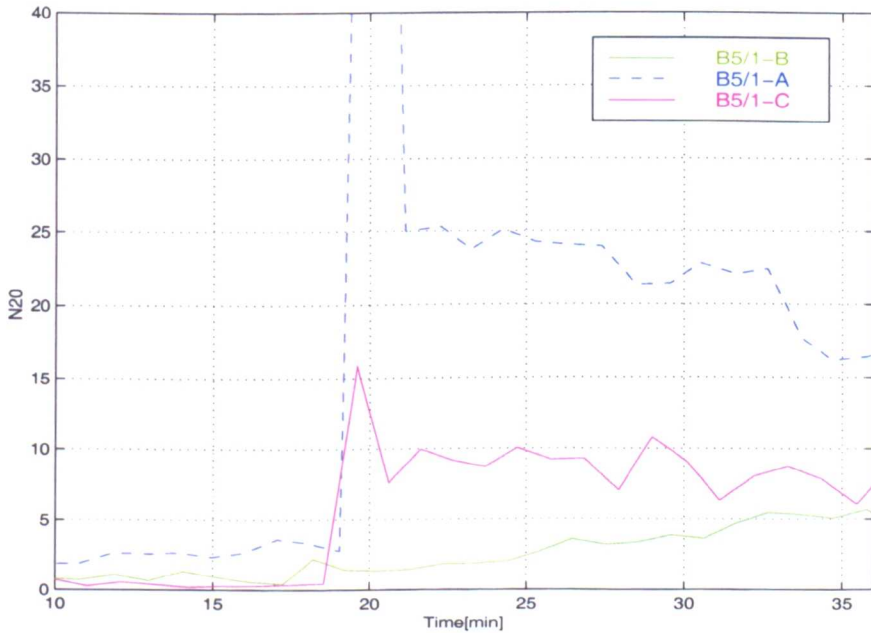


Figure 4.29: The particle count (N20) from Figure 4.28 showing only the first addition.



Figure 4.30: A TiB_2 cluster in fractured sample from the LiMCA tube taken at the end of experiment $TiB-4$. The sample is unpolished. EDX spectra at points A, B and C are shown in the following figures.

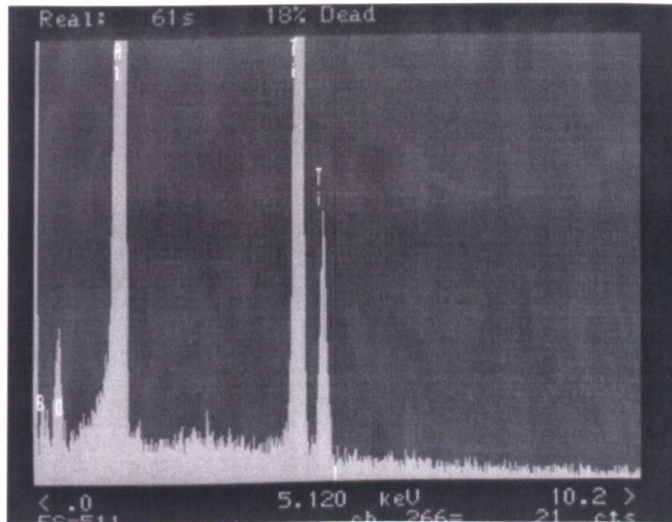


Figure 4.31: EDX spectrum at spot A in the TiB_2 particle cluster shown in Figure 4.30. The peak in the spectrum overlapping the symbol O is a low energy titanium peak ($L\alpha$).

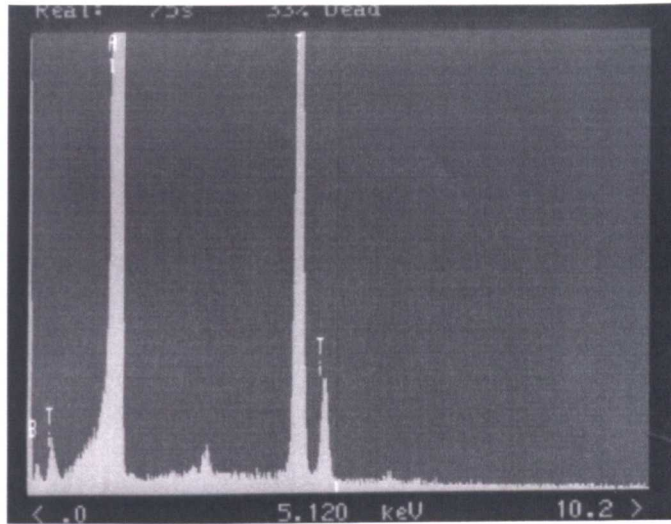


Figure 4.32: EDX spectrum at spot B in the TiB_2 particle cluster shown in Figure 4.30.

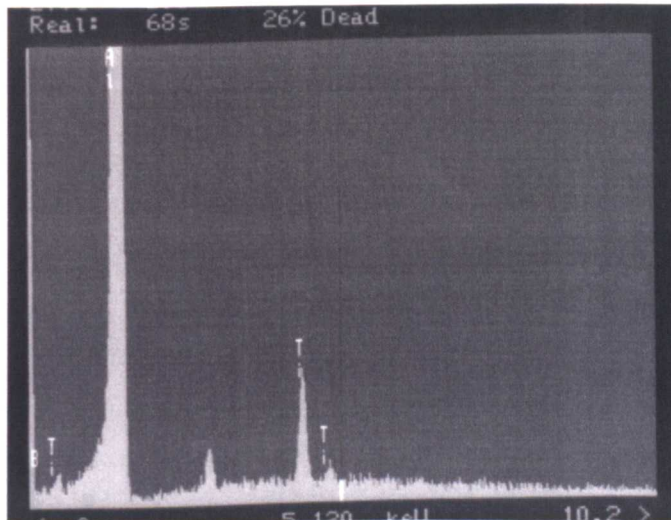


Figure 4.33: EDX spectrum at spot C inside the TiB_2 particle cluster shown in Figure 4.30.

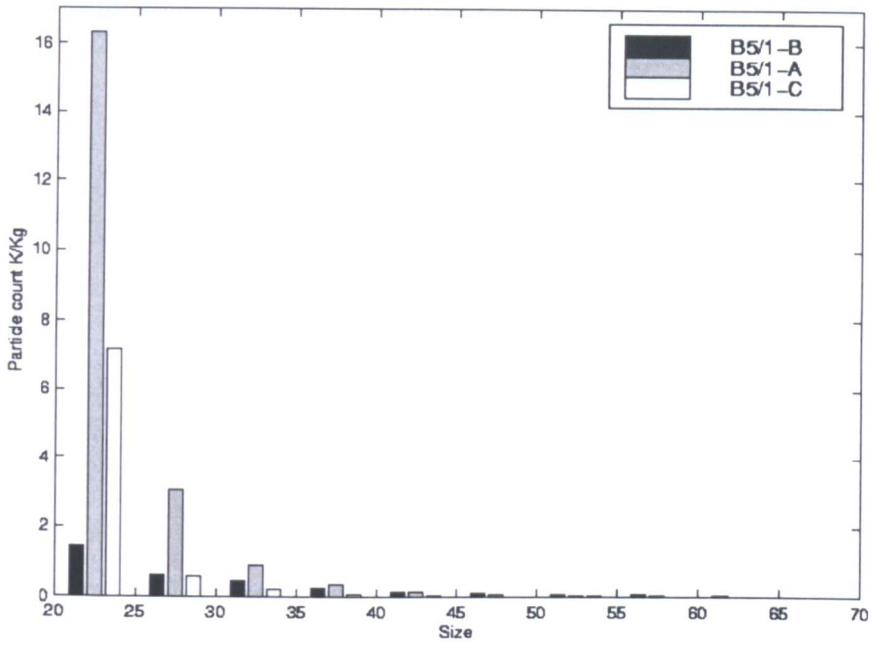


Figure 4.34: The average size distribution for each master alloy after the first addition in Figure 4.29.

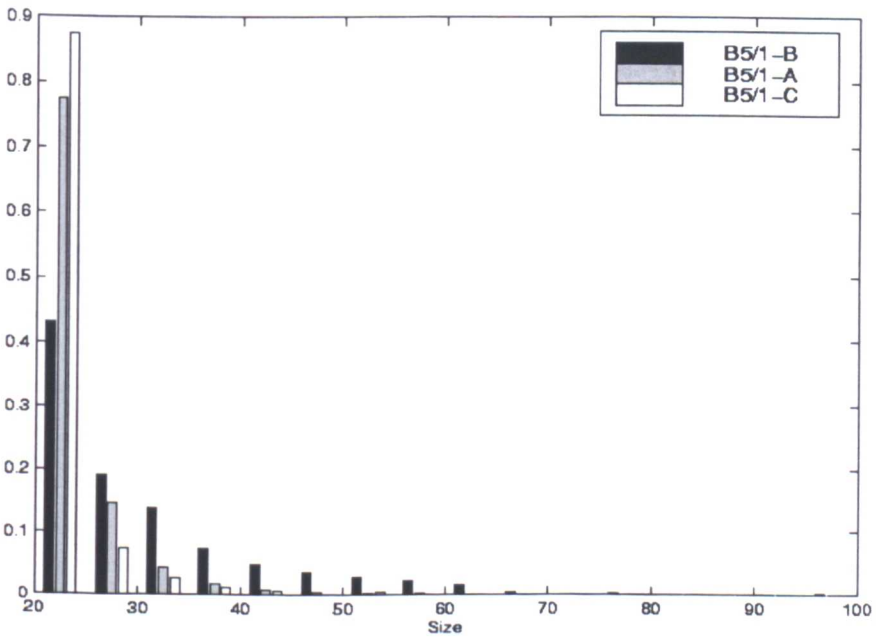


Figure 4.35: The normalized size distribution of detected particles for each master alloy after the first addition shown on Figure 4.29.

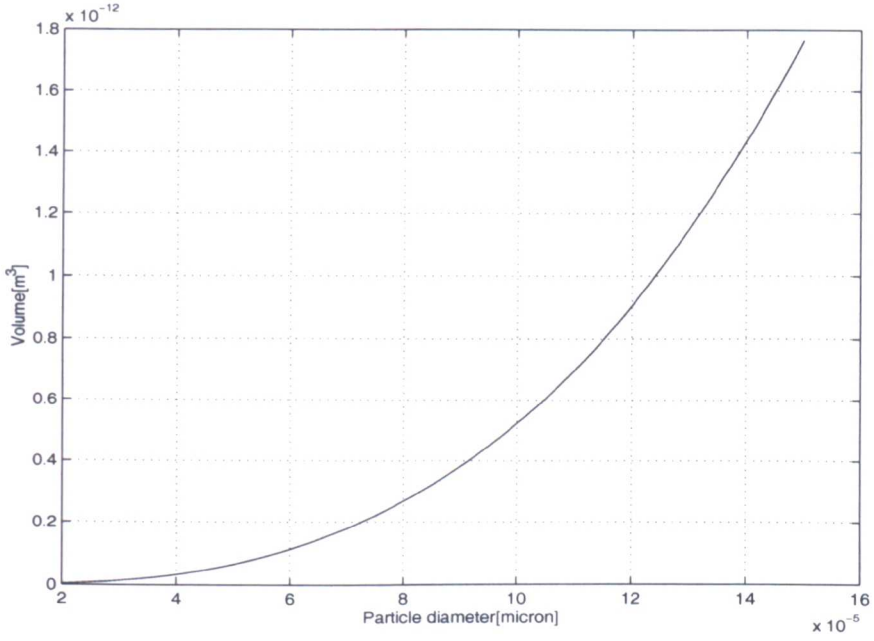


Figure 4.36: The volume of particles as a function of diameter, ranging from 20-150 μm .

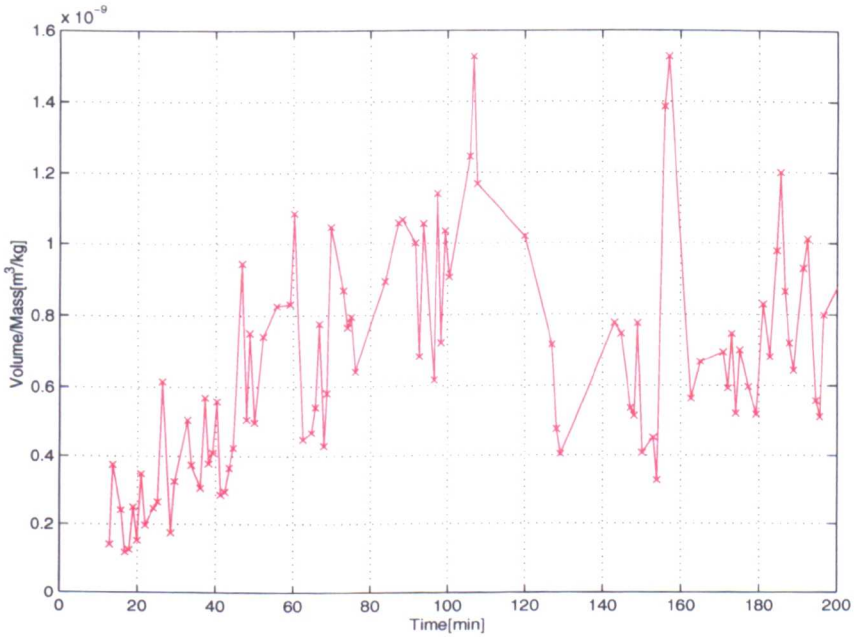


Figure 4.37: The estimated volume of TiB_2 particles detected in experiment $TiB-1$, shown in Figure 4.26.

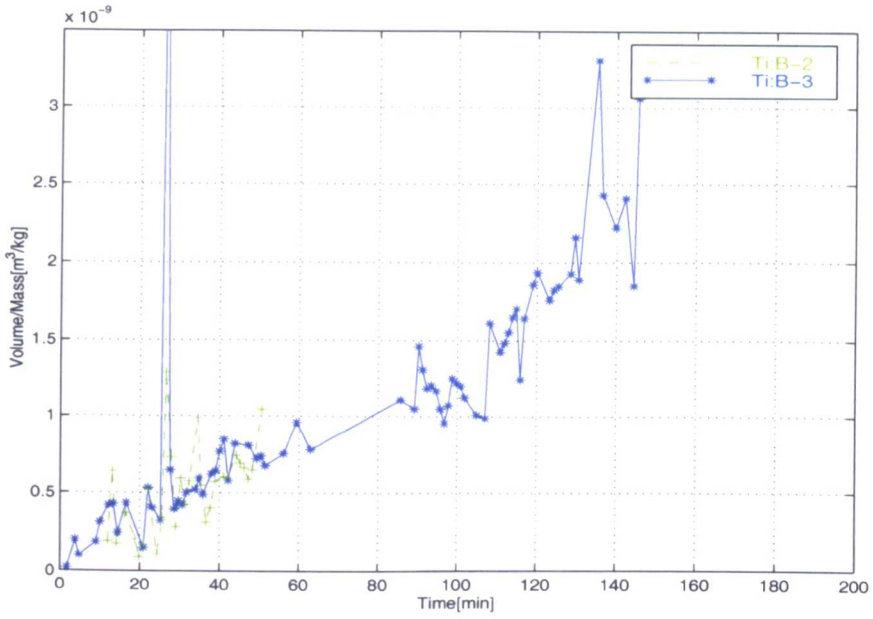


Figure 4.38: The estimated volume of TiB_2 particles detected in the experiments $TiB-2$ and $TiB-3$, shown in Figure 4.26.

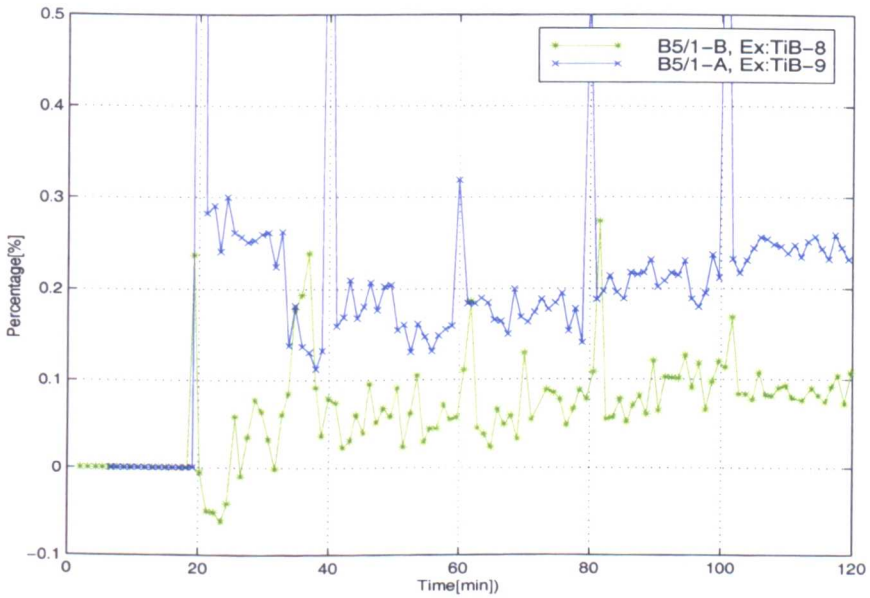


Figure 4.39: The percentage of total volume of TiB_2 particles added to the melt which are detected with LiMCA in the experiments shown in Figure 4.28.

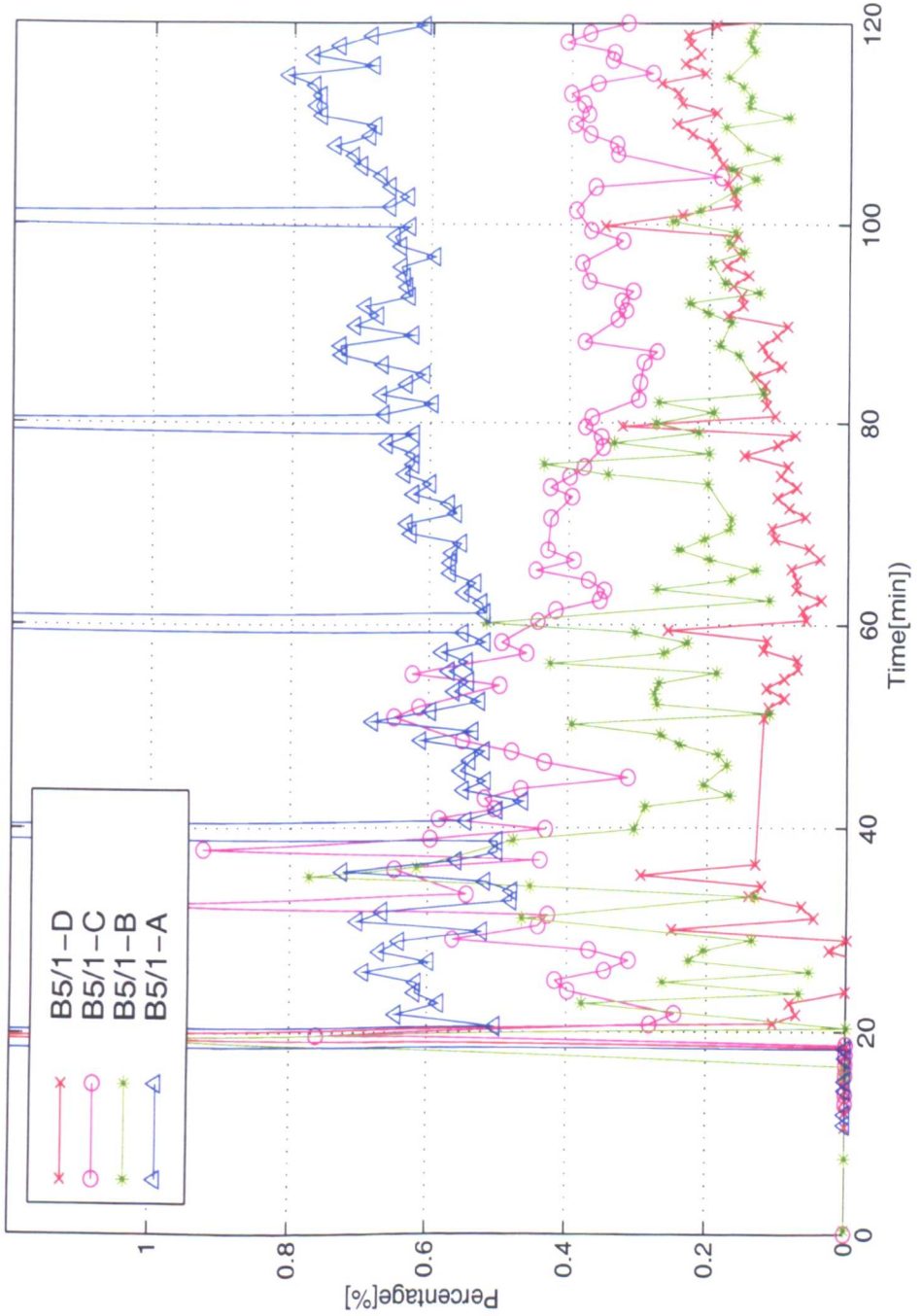


Figure 4.40: The percentage of total volume of TiB_2 particles added to the melt which are detected with LiMCA in the experiments shown in Figure 4.27.

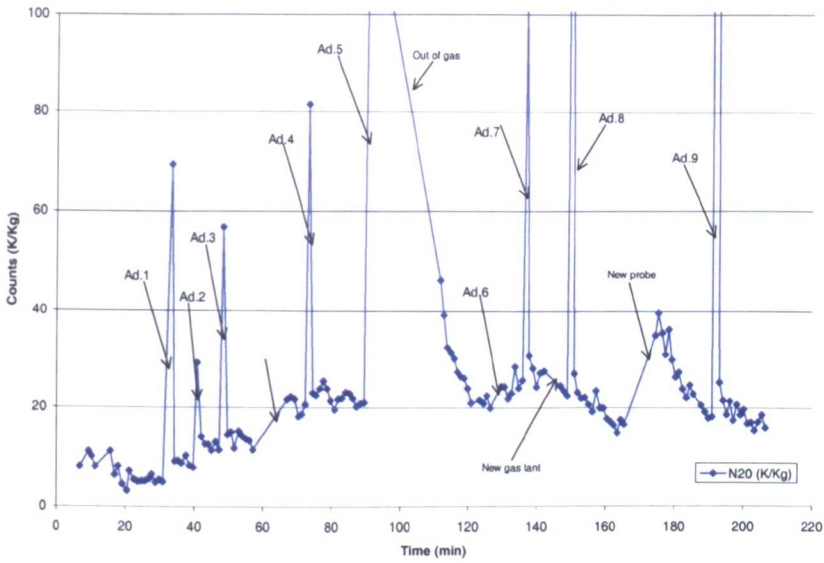


Figure 4.41: The particle count (N20) in experiment *TiB-11*. Grain refiner Al-3Ti-0.2B. The additions are shown in Table A.9

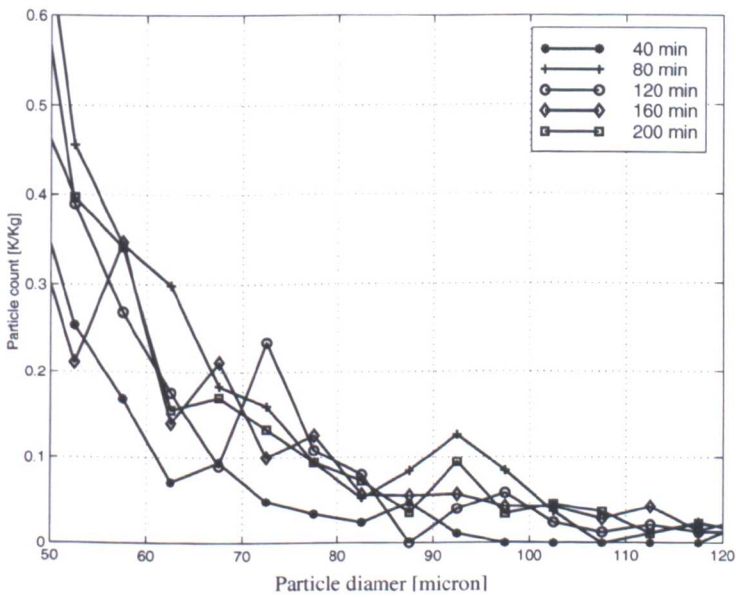


Figure 4.42: The size distribution from experiment *TiB-1* at different times.

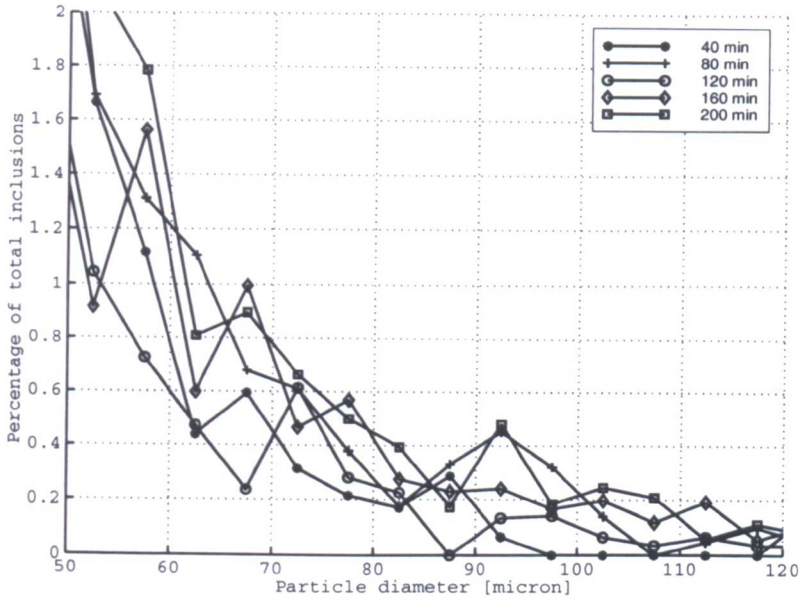


Figure 4.43: The normalised size distribution from experiment *TiB-1* at different times.

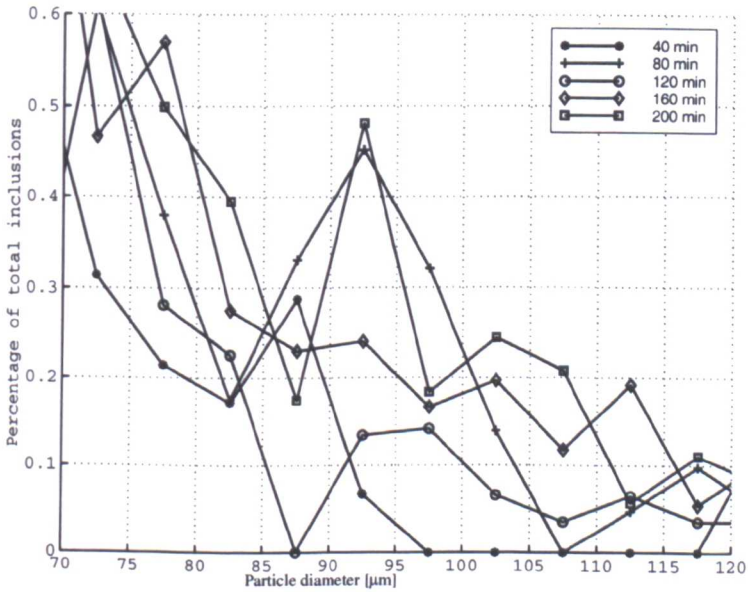


Figure 4.44: The normalised size distribution from experiment *TiB-1* at different times focusing on the particle size range 70 – 120µm.

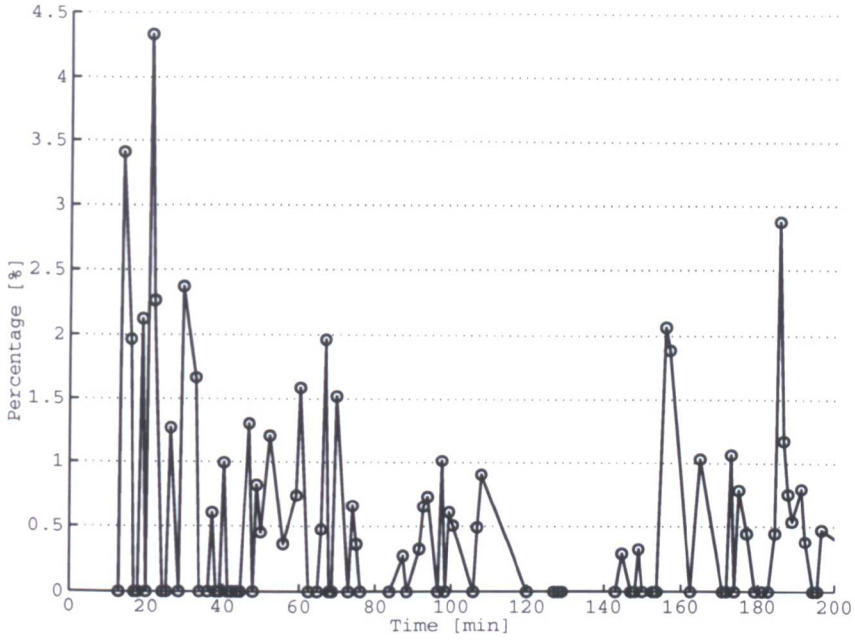


Figure 4.45: The percentage of particles larger than $110\mu\text{m}$ at different times in experiment *TiB-1*.

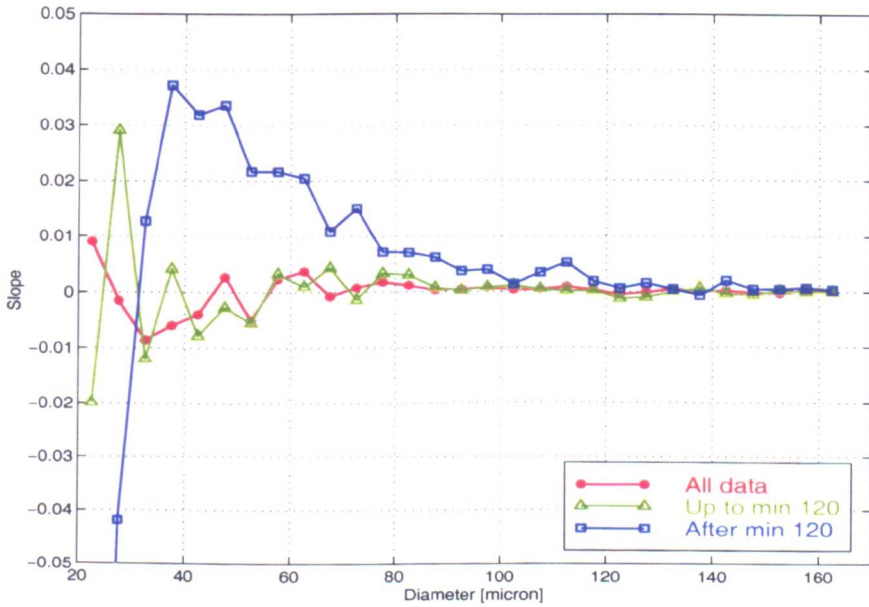


Figure 4.46: The slopes from linear fitting of each size interval at different time intervals from experiment *TiB-1*.

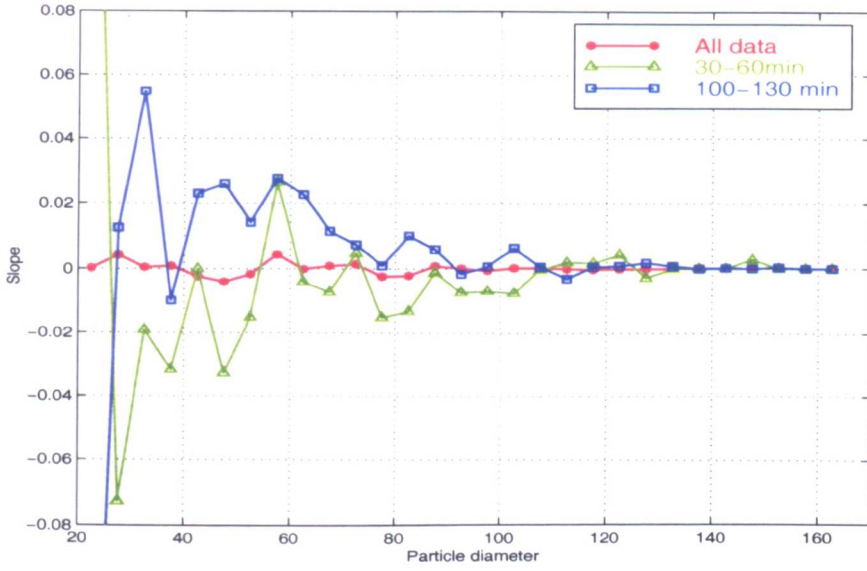


Figure 4.47: The slopes from linear fitting of each size interval at different time intervals from experiment *TiB-3*.

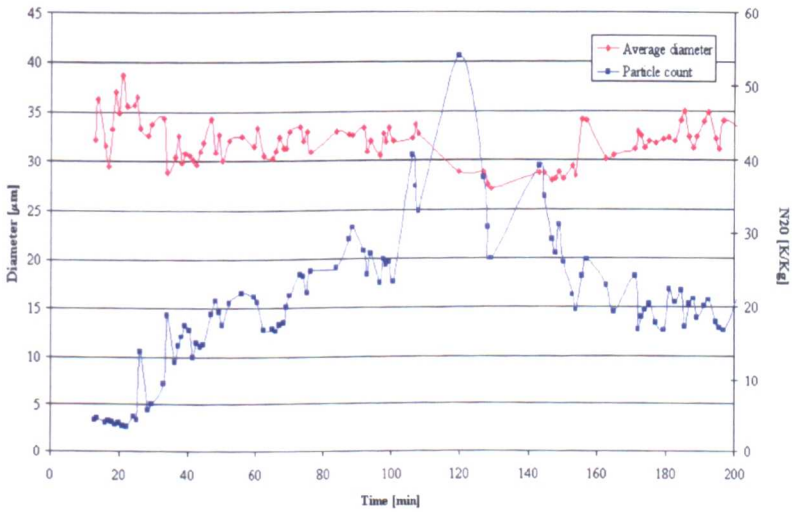


Figure 4.48: The average diameter of detected particles and the particle count in experiment *TiB-1*.

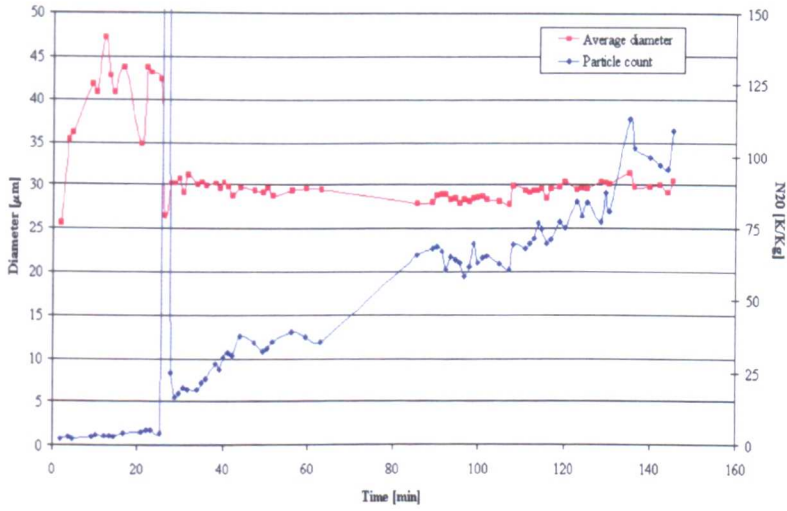


Figure 4.49: The average diameter of detected particles and the particle count in experiment *TiB-3*.

Chapter 5

Computational fluid dynamics modelling of launder systems

One of the aims of the present project is to use computational fluid dynamics (CFD) for the modelling of flow conditions and particle distribution in aluminium melts in launders. The modelling is intended to further the understanding of the distribution of particles from the master alloy in the flowing melt. The effects of particular features of launder design, such as dead-zone in corners, can also be evaluated by the model calculations. The calculated distribution can then be compared with results of experimental analysis of the melt inclusion content at different positions in the launders.

The present study will be divided into three parts:

- Modelling of flow conditions in the first launder design at the Alusuisse-Lonza casthouse in Chippis.
- Modelling of flow conditions in the second, modified, launder design at the Alusuisse-Lonza casthouse in Chippis.
- Particle tracking analysis for the first and second launders.

The reason for modelling the two launder designs, is that the experimental study of particle distribution in launders described in Chapter 6 was conducted in the first launder. The launder design was changed during the course of the project and it was, therefore, considered necessary to compare the two designs.

The software used is CFX, version 4.1 which is a registered trademark of AEA Technology Ltd [64].

5.1 Flow modelling of the first launder

Figure 5.1 shows the first launder design at the Alusuisse-Lonza casthouse in Chippis as rendered in CFX. Also, Figure 6.1 in Chapter 6 shows a photograph

of the launder. The aim of the modelling is to describe the flow pattern in the launder including velocity profiles and regions of turbulence. Approximate launder dimensions are given in Figure 5.3.

5.1.1 Numerical model

The governing fluid flow equations of mass conservation for incompressible fluids and the momentum balance are the following [58]:

$$\frac{\partial}{\partial x_i}(\rho u_i) = 0 \quad (5.1)$$

$$\frac{\partial(\rho u_i u_j)}{\partial x_i} = -\frac{\partial P}{\partial x_i} + \frac{\partial}{\partial x_j} \left[\mu_{eff} \left(\frac{\partial u_i}{\partial x_j} + \frac{\partial u_j}{\partial x_i} \right) \right] + \rho g_i \quad (5.2)$$

using Cartesian coordinates and index notation. The indexes, i and j represent the three directions of the coordinate system, here the Cartesian, which usually is termed as x, y and z .

For modelling turbulence, the standard $k - \dot{\epsilon}$ model is used [58]. There, turbulence is expressed by two transport equations for the turbulent kinetic energy, k , and its rate of dissipation $\dot{\epsilon}$. The relation between the turbulent viscosity μ_t and these two characteristics of turbulence is

$$\mu_t = C_D \rho k^2 / \dot{\epsilon} \quad (5.3)$$

where C_D is a constant used in the turbulent model.

The governing equations for k and $\dot{\epsilon}$ are

$$\frac{\partial}{\partial x_i} \left(\rho \mu_{eff} k - \frac{\mu_{eff}}{\sigma_k} \frac{\partial k}{\partial x_i} \right) = G - \rho \dot{\epsilon} \quad (5.4)$$

and

$$\frac{\partial}{\partial x_i} \left(\rho u_i \dot{\epsilon} - \frac{\mu_{eff}}{\sigma_\epsilon} \frac{\partial \dot{\epsilon}}{\partial x_i} \right) = (C_1 \dot{\epsilon} G - C_2 \rho \dot{\epsilon}^2) / k \quad (5.5)$$

where the effective viscosity comprises the laminar and turbulent components

$$\mu_{eff} = \mu + \mu_t \quad (5.6)$$

and the viscous stress generation term, G , is given by

$$G = \mu_t \frac{\partial u_j}{\partial x_i} \left(\frac{\partial u_j}{\partial x_i} + \frac{\partial u_i}{\partial x_j} \right) \quad (5.7)$$

The five empirical constants appearing in Equations 5.3 to 5.5 are given in Table 5.1 as used by Shen [57] and Joo [52].

Table 5.1: Constants used in the $k - \epsilon$ model

C_1	C_2	C_D	σ_k	σ_ϵ	Ref.
1.430	1.92	0.09	1.00	1.3	Joo [52]
1.44	1.92	0.09	1.0	1.3	Shen [57]

5.1.2 Model parameters

First, a simplified version of the first launder at Chippis was analysed. Figure 5.1 shows the launder and Figure 5.2 details the mesh in the corner region. The aim was to use this model to help to analyse the experimental results obtained for the launder which are described in Chapter 6.

Figure 5.3 shows the main dimensions of the launder system shown in Figure 5.1.

The depth of the liquid metal was set as 90mm, which is similar to that for the experiments reported in Chapter 6.

The mass flow through the launder was set to 1.0kg/s , the density of the molten aluminium is taken as 2300kg/m^3 and the viscosity is $1.2 \cdot 10^{-3}\text{Ns/m}^2$.

5.1.3 Boundary conditions

Before the modelling is started, the question of how to treat the effect of the oxide layer on the top of the melt must be answered. The possibilities are to treat the problem as a free surface flow or to include the effect of the oxide layer. Other studies [53, 56, 57] on the flow of molten aluminium have excluded the oxide layer. This results in an easier comparison with a water model, which is often used to test numerical flow models for molten metals. The geometry of the launder systems modelled in previous studies is also very different from the one in this problem. The oxide layer is relatively much larger in the present problem, i.e. the surface area of the molten metal divided by the volume of molten metal in launder. Therefore, the effect of the oxide layer is included in the present study and it is assumed to act as a non-slip wall. Thus, the boundary conditions employed are non-slip boundaries for both the walls and the oxide layer.

The inlet and the outlet of the model are defined as mass flow boundaries (Neumann boundary). At these boundaries the total mass flow rate is defined and this results in a fully developed flow at the inlet of the model. The outlet boundary conditions are fully developed flow in the outlet pipe of the launder system. There are no thermal effects included in the model which is, therefore, isothermal.

5.1.4 Mesh structure

The complexity of the corner in the model, made it necessary to construct the model with 15 blocks, which contain a total of 35,666 elements. Figure 5.4 shows the nodes of the model in plane 4 shown in Figure 5.3. The elements are distributed evenly along the launder, because the calculations did not converge with a non-uniform distribution of the elements. The geometry of the launder required a non-uniform volume of the elements. However, the average volume of each element is approximately $1.2 \times 10^{-6} m^3$. The mass source tolerance is set as 10^{-4} and the model fulfilled this constraint in 673 iterations. Figure 5.5 shows the absolute residual source sum for the momentum and mass in the model for the old launder. The total CPU time for each run is 70 minutes.

5.2 Results and discussion for the first launder

The results of the modelling of the first launder are shown in Figures 5.6-5.17. The geometrical planes in the launder for which the computation is performed are given in Figure 5.3.

The calculated velocity in Plane 1 is shown in Figure 5.6 and Figure 5.7 gives the velocity profile along the line in Plane 1 in which the max. velocity is obtained. The flow rate increases towards the centre of the cross-section of the launder. The flow is turbulent, and a comparison with the theoretical velocity profile for turbulent flow shown in Figure 2.23 confirms the similarities between the two profiles. The turbulent core region is relatively flat and the velocity gradient is steep in the laminar sub-layer near the walls.

Figure 5.8 shows the velocity in Plane 2 looking in the direction of flow. The effect of the corner is clearly demonstrated. The maximum flow rate is now observed nearer the outer edge of the launder with respect to the corner.

Figures 5.9 and 5.10 show the velocity in Planes 3 and 4, respectively. The effect of the corner is diminishing along the launder and the maximum velocity location is moving back towards the centre line.

Figures 5.11 and 5.12 show a cross-section along the launder at the outlet denoted by Plane 5 in Figure 5.3. The flow rate is highest in the centre of the main launder. It then increases in the outlet tube, because the cross-sectional area of the outlet tube is smaller than the area of the launder. This is further demonstrated by the velocity profile shown in Figure 5.13.

Figures 5.14 and 5.15 show the velocity in the first corner of the launder looking down on Plane 6, 30mm below the surface. The turbulent kinetic energy is shown in Figure 5.16 for the same conditions. The figures clearly demonstrate the dead-zone effect at the corner, which may be expected to become a source of inclusion and agglomerate enrichment of the melt therein.

Finally, Figure 5.17 shows the velocity in the first corner of the launder looking down on Plane 7, 60mm below the surface. The launder is narrower at this depth than at 30mm. The results are similar to those at 30mm depth except that there is slightly more flow into the dead-zone.

It is interesting to note that the calculations show the vortex formation, which was expected in the dead-zone at the corner. In there, the grain refining particles may be expected to become entrapped possibly resulting in agglomeration and a higher concentration of the grain refiner than in the main metal flow.

5.3 Flow modelling of the second launder

The first launder was replaced during the course of this project. The new design is shown in Figure 5.18. The second launder is significantly different from the first launder. There are two corners, with angles of 55.7 and 34.3 degrees respectively, instead of one 90 degree corner. Also the dead-zone at the corner has been removed. The depth in the melt was increased from 90mm in the old design to 100mm in the new design. The cross-sectional area of the second launder is smaller than that of the first one, which results in approximately 20% higher average velocity of the melt.

There were three main reasons for the change in the launder system. The first was a change in the layout of the cast-house in order to make more space available. The second was the change in the cross-section area of the launder which increases the velocity of the molten aluminium and thereby reduces cooling of the melt when flowing through the launder. The third was the removal of the dead-zone at the corner of the first launder, a consequence of the modelling study reported in Section 5.2.

In this section, the numerical model of the second launder system is presented and it is compared with the first launder in order to estimate the difference between these two types of launder systems.

5.3.1 Model parameters, boundaries and mesh structure

The model used is the same as in Section 5.1 and all thermophysical parameters and boundary conditions are the same. However, the model was made of three blocks, instead of 15 before, because the soft corners were more adaptable to the modelling. The outlet pipe was also neglected in the new model design.

The mesh size for this launder is not uniform. The grid is coarse near the inlet, outlet and in the middle of the part connecting the two corners, i.e. the length of each element along the launder is variable. The grid becomes finer as it approaches the corners, and it is very fine at the corners. The nodes in the cross-section of the launder near the inlet are shown in Figure 5.19. The spacing of the nodes is similar to the spacing in the old model.

The problem was solved with two different mesh specifications. The fine grid had 13,000 elements compared to 3,250 in the course grid. The nodes in Figure 5.19 are from the finer mesh. The mass source tolerance is 10^{-4} and the solution was reached in 122 iterations for the course grid and 997 iterations for fine grid. A difference in the numerical results of those two models was negligible, i.e. less than 2%. The results presented here are from the solution with the finer mesh.

5.4 Results and discussion for the second launder

Figure 5.18 shows the outline of the second launder. Corner 1 is 55.7 degrees and corner 2 is 34.3 degrees. The height of the melt in the launder is estimated to be same as in the first launder, i.e. 90mm. The cross-section is changed with the radius at the bottom being 40mm instead of 60mm in the old launder.

In this section, only the velocity profiles for the new corners are presented and the velocity profile for the cross-section of the launder without any disturbance from corners. The velocity profiles for the two corners are shown at two different depths. Figure 5.20 shows the two depths. The height of the aluminium is 90mm. $Y=0$ denotes depth of 60mm and $Y=0.03$ denotes depth of 30mm. Those two depths are chosen because the old launder showed some difference in the velocity profiles at different depth.

Figures 5.21 and 5.22 show the velocity in corner 1 at a depth of 60mm and Figures 5.24 and 5.23 show the velocity at the depth of 30mm. There is very little difference between the velocity profiles at different depths. The velocity is highest at the inner part of the corner itself, and that is expected for flow around corners. The region of maximum velocity then moves to the outer edge of the launder similar to the behaviour for the first launder in Figure 5.15.

Figures 5.25 and 5.26 show the velocity in corner 2 at the depth of 60mm and Figures 5.27 and 5.28 show the velocity at a depth of 30mm. There is some difference between the profiles at different depth. At the depth of 60mm the speed rises above 0.065m/s in a small section at the inner part of the corner, but at 30mm the velocity does not reach that value. The reason for this is that the launder is slightly narrower at the depth of 60mm.

Figure 5.29 shows the velocity in a cross-section of the launder with undisturbed flow. The velocity is highest near the centre of the launder and decreases towards the walls as expected.

5.5 Particle tracking

In the particle transport model, the total flow of the particulate phase is modelled by tracking a small number of particles through the continuum fluid. It is assumed that the particle volume fraction is sufficiently small that it does not disturb the flow field calculated in the liquid phase. This leads to the Lagrangian approach where the particle tracking is essentially implemented as post processing calculation in the steady state liquid flow field.

5.5.1 Equations for position

This section describes the equations that are solved in a particle transport model in CFX. For ease of tracking each particle position and the location where it crosses control volume boundaries, the tracking is carried out in computational space. In this space, the equations for position have the form:

$$\frac{d\xi}{dt} = \mathbf{C} \quad (5.8)$$

where ξ is computational position, t is time and \mathbf{C} is computational velocity.

The computational velocity vector is obtained from the physical velocity of the particles \mathbf{u} by calculating the Jacobian of the coordinate transformation from the vertices of the control volume and using equation:

$$\mathbf{C} = \left(\frac{\partial \mathbf{x}}{\partial \xi} \right)^{-1} \mathbf{u} \quad (5.9)$$

where \mathbf{x} is the position vector in space.

In order that this transformation is continuous across the control volume boundaries, the Jacobian is calculated continuously from the discrete information available directly on edges of control volumes using Hermite interpolation within each block on the grid. This method can also be used across block boundaries, but for complicated block structures this may be impossible. The physical velocity of the particle is always smooth across such boundaries.

5.5.2 Momentum equation for particle transport

The equations for the rate of change in the velocity of the particle come directly from Newton's second law:

$$m \frac{d\mathbf{u}}{dt} = \mathbf{F} \quad (5.10)$$

where \mathbf{F} is the force on the particle, and m its mass.

The major component of this force is the drag exerted on the particle by the

continuous phase. This has the form:

$$\mathbf{F}_D = \frac{1}{8} \pi d^2 \rho C_D |\mathbf{v}_R| \mathbf{v}_R \quad (5.11)$$

where the drag factor is given by

$$C_D = 24 \frac{1 + 0.15 Re^{0.687}}{Re} \quad (5.12)$$

The particles Reynolds number is defined by

$$Re = \frac{\rho |\mathbf{v}_R| d}{\mu} \quad (5.13)$$

Here d is the particles diameter, ρ and μ are the density and viscosity in the continuum and v_R is the relative velocity of the two phases.

There are additional forces on the particle, which can be included in the calculation:

1. A pressure gradient force

$$\mathbf{F}_P = -\frac{1}{4} \pi d^3 \nabla P \quad (5.14)$$

where P is the pressure in the continuous phase.

2. A buoyancy force

$$\mathbf{F}_B = \frac{1}{6} \pi d^3 (\rho_p - \rho) \mathbf{g} \quad (5.15)$$

where ρ_p is the density of the particle and g is the gravitational acceleration.

3. The added mass force

$$\mathbf{F}_A = -\frac{1}{12} \pi d^3 \rho_p \frac{d\mathbf{u}}{dt} \quad (5.16)$$

4. A rotating coordinates term

$$\mathbf{F}_R = \frac{1}{6} \pi d^3 \rho_p (-2\mathbf{w} \times \mathbf{u} - \mathbf{w} \times \mathbf{w} \times \mathbf{x}) \quad (5.17)$$

The pressure gradient force, the added mass force and the rotating coordinates term are small and need not be included in this case. However, the buoyancy force is important so the main forces acting are assumed to be F_B and F_D .

5.5.3 Turbulent dispersion

The effect of turbulence can be included in the particle transport model. The continuum velocity in the momentum equations above is taken to be the mean

velocity plus a contribution due to turbulence. The turbulence is assumed to be made up of a collection of randomly directed eddies. The variance of the speed of the eddies is taken to be twice the turbulent kinetic energy $2k$ [65]. The eddy lifetime t_E is given by

$$t_E = 1.5^{\frac{1}{2}} C_\mu^{\frac{3}{4}} \frac{k}{\varepsilon} \quad (5.18)$$

and the eddy length l_E by

$$l_E = C_\mu^{\frac{3}{4}} \frac{k^{\frac{3}{2}}}{\varepsilon} \quad (5.19)$$

where C_μ is a turbulence model constant and ε is the energy dissipation rate. In the present analysis turbulence modelling was included otherwise the particle dispersion would not have been correctly introduced.

5.6 Results and discussion of particle tracking

The main object modelling of the particle distribution in the first launder was to study the trapping of particles in the vortices generated in the dead-zone at the corner and at the outlet. This required the tracking of particles over long distances and available computer time did not allow turbulence to be included in the calculation. The simulation is, therefore, based on particle flow without turbulent dispersion which estimates the average particle trajectory through model. An uniform particle distribution is assumed though the cross-section at the inlet. The density of the particles is chosen as that of TiB_2 particles which is $4520\text{kg}/\text{m}^3$.

In the analysis of the corner and outlet of the first launder, particles of two size groups were added to the melt, with $3.25\mu\text{m}$ and $7.75\mu\text{m}$ diameter respectively. The time limit for the simulation was 250 seconds. Figure 5.30 shows the 90 degrees corner from the first launder seen from the top. It is difficult to estimate from this figure how much effect the vortex in the dead-zone has on the particles. Some particles are seen to circulate in the vortex, while others collide with the walls. In the model the particles are assumed not to bounce elastically off the walls, i.e. they have a sticking coefficient of 1, but this may not occur in practice.

Figure 5.31 shows the outlet of the first launder, seen from the side (Plane $z=0$ see Figure 5.3). The majority of the particles enters the outlet pipe and only four of them travel past the outlet.

In the second modified launder the main emphasis is on simulating the initial particle dispersion after injection from a point source. The results shown here are obtained using turbulent dispersion of the particles in the straight section of the launder upstream of the corners.

Results for three particles diameters, 2, 5 and $10\mu\text{m}$, are shown for the second launder. It must be noted that the drag effect of the solid grain refiner rod on the melt flow conditions is not included. This will be discussed further later in

next section. However, the calculations should give a good approximation of the nature of initial particle dispersion in the straight part of the launder.

Figures 5.32 and 5.33 show the difference in the paths of $5\mu\text{m}$ and $10\mu\text{m}$ particles, simulated for 30 seconds. The initial number of particles is forty in each case. The particles originate in a point source situated 55mm below the surface in the middle of the launder. This type of melting behaviour of master alloy rods is likely to be a reasonable approximation [48]. The particles are well dispersed after this period of time and the effect of gravity is clearly visible. The $10\mu\text{m}$ particles tend to settle more rapidly than the $5\mu\text{m}$ particles. Only one $5\mu\text{m}$ particle appears to reach the top surface but none of the $10\mu\text{m}$ particles.

Figure 5.34 shows a simulation of the flow of $2\mu\text{m}$ particles flowing through the second launder system in Chippis. The number of particles is 200. The simulation is terminated after 5, 10 and 15 seconds. This is done to evaluate the dispersion of the particles with time. The velocity field from the flow analysis showed fluid speed of $\approx 60\text{ mm/m}$ in the centre of the launder. Figure 5.34 (a) shows that after 5 seconds, the particles have travelled a distance from 250 to 350mm in the launder. Figure 5.34 (b) shows that after 10 seconds, the main body of the particles has traveled from 500 to 600mm. The particles seem to be well dispersed after 10 seconds or after traveling half a metre.

Figure 5.35 shows the same results as in Figure 5.34 viewed along the axis of the launder. The particles are well dispersed after 10 seconds. This angle shows that the particles tend to be on the inner side of the launder, which is the effect of the subsequent bend in the launder system. An interesting feature is that the particles tend not to reach the top surface due to the effect of gravity. A high number of particles seem to strike the bottom section of the launder during the first 15 seconds, this is discussed further below.

Figure 5.36 shows the percentage of the $2\mu\text{m}$ particles that collide with the walls of the launder as a function of time. These are the results from the simulations displayed in the previous figures. In these calculations, the particles do not bounce elastically of the walls, but in reality a proportion may be expected to do that. After five seconds, no particles have collided with the walls, after ten seconds 42 of 200 or 21% have collided with the walls and after 15 seconds, 72 particles or 36% have hit the walls. These results are somewhat surprising, after the main bulk of the $2\mu\text{m}$ particles has traveled approx. 800-900mm in the launder, 36% have hit the walls. As noted before, most of the particles will probably bounce of the walls in practice, but these results indicate that a substantial portion collides with the walls. The surface conditions of the launder may affect the particle behaviour when they hit the walls, and this may be an interesting project for further studies.

5.7 Effect of the grain refining rod

In practice the particles are injected not at a point but are released from a dissolving grain refiner rod. Observations of flow past cylinders have shown that vortices are formed and shed periodically downstream of the cylinder. Hence, at given time, the detailed flow pattern might appear as shown on Figure 5.37. In this figure a vortex is in the process of formation near the top of the cylinder. Below and to the right of the first vortex is another vortex, which was formed and shed a short time before. Thus the flow process in the wake of the cylinder involves formation and shedding of vortices alternately from one side and then the other. The vortices are called Kármán vortices, after a paper by Kármán from 1911, explaining this alteration to be a stable configuration for vortex pairs. Beginning for $Re_D > 35$, the vortex streaks occur in almost any bluff-body flow and persist over a wide range of Reynolds numbers as shown in Figure 5.38. Re_D is a Reynolds number based on the diameter of the cylinder and it is defined as

$$Re_D = \frac{\rho U D}{\mu} \quad (5.20)$$

As the Reynolds number increases, the wake becomes more complex and turbulent, but the alternate shedding can still be detected at $Re_D = 10^7$. For the second launder, the velocity of the flow in the centre has been estimated to be 0.06 m/s and the diameter of the grain refining rod is 0.09 m . This gives $Re_D = 1071$, which is higher than the cases displayed in Figure 5.38. This suggests that the effect of the rod should be significant for the particle dispersion in its wake, giving a more effective dispersion than calculated in Section 6.3.

The frequency of the vortex shedding has been evaluated experimentally. The frequency is given in terms of the Strouhal number St , and this in turn is a well known function of the Reynolds number. Thus, the shedding cycle takes place during the time that main flow moves approximately five cylinder diameters. Here the Strouhal number is defined as

$$St = \frac{fD}{U} \quad (5.21)$$

where f is the frequency of the shedding of vortices from one side of the cylinder, in Hz , D is the diameter of the cylinder and U is the mean free velocity. Figure 5.39 shows the experimental results of vortex shedding [51]. With $Re_D \approx 10^3$, this gives $St = 0.22$, which again gives $f = 1.46 \text{ Hz}$. A possibility for the numerical model to simulate the shedding of the vortexes, would be to set the $t_E = 1/1.46$ (Eq. 5.18), which would set the life of the vortices in the wake equal to 0.68 seconds. However, this gives the ratio between the turbulent kinetic energy and the dissipation rate as 0.28. This ratio has not been seen in the calculations so far, but it might occur when a cylinder is added to the launder

system. This ratio is much higher when the flow is undisturbed in the launder, which means much longer time between each change in direction of the particles.

There are still some difficulties in creating a useful mesh of the launder system with a cylinder included, so there are no simulation results presented for that case.

5.8 Further discussion

The flow conditions of the molten aluminium in the first and second launders at Chippis have been modelled using computational fluid dynamics. The model was then expanded to include particle tracking analysis in order to visualize the dispersion of particles entering the melt from the grain refining rod. This analysis gives a good indication of the dispersion mechanism and offers an insight into the results of the experimental studies for the first launder presented in the following chapter. Although dispersion was only modelled in the second launder, it is expected to be very similar in the first launder since it occurs in the first 0-1000mm, i.e. the straight section (see Figure 5.3).

The flow conditions in the launders described by the model calculations are in a general agreement with the conditions expected from fluid dynamics. The effect of the corners on the flow profile and the vortex formation in the dead-zone are good examples of such behaviour.

In the particle distribution analysis, there are several interesting observations. First, the vortex in the dead-zone in the first launder entraps particles from the flowing melt. This may result in an enrichment of constituents from the master alloy in this zone. Therefore, this may give rise to conditions for increased agglomeration of the grain refining particles. The agglomerates could either settle in the dead-zone or re-enter the flowing melt. As previously discussed, this was one of the reasons for the change in the launder design at Chippis.

Another interesting feature is the effect of gravity on the particle distribution. This results in a practically particle free top zone in the melt. Samples taken from the top of the melt are, therefore, not representative for the whole melt at that position in the launder. This also demonstrates that an even distribution of the particles is not achieved in the launder itself. Therefore, if the distribution is even in the casting unit, the outlet pipe must act as an effective particle distributor.

In the present calculation, the insoluble particles from the master alloy rod achieve the most random distribution after approx. 10-15 seconds or after travelling less than one metre along the launder. Therefore, any additional length of the launder after the addition point has no positive effect on the distribution. Considering agglomeration in the melt, the time from addition to solidification should be as small as possible but this must be balanced by other considerations

such as the settling out of inclusions together with agglomerates which may have originated in the master alloy. In practice, the time from the master alloy addition to solidification of the melt, i.e. the holding time, has been found to have pronounced effect on the grain size of the cast metal [2] when Al-Ti-B master alloys are employed and this is the main factor in determining the addition point of the master alloys in industry [23]. The dissolution time for the soluble $TiAl_3$ particles must also be taken into account. It is considered by industry to be approx. $40\mu m/min$ [23] and work by the author [48] indicated a similar order of magnitude. Therefore, the dissolution time for the large $TiAl_3$ particles (20- $100\mu m$) is the governing factor for the minimum holding time rather than the particle distribution of the insoluble particles. Considering a $TiAl_3$ particle of $100\mu m$ in diameter, the dissolution time is 75 seconds. By using an average melt velocity of $40mm/sec$ the distance travelled by the particle before dissolution is 3 meters. In practice, the distance will be less because the $TiAl_3$ particles take some time to reach the average melt velocity.

The high collision rate of the particles with the walls of the launders is another point of interest. This effect has not been studied by industry as far as known. The main question is whether the particles bounce elastically off the wall or are attached there. Considering the calculated collision rate, the majority must bounce off the walls.

Much work remains to be done on the particle tracking analysis. The effect of turbulence in the corner zones remains to be calculated and the effect of the grain refining rod on the flow has to be included. Later it is also necessary to expand the model to include heat transfer and natural convection. Finally, it would be of value to study the particle behaviour at the walls of the launders since the present analysis shows a high collision rate of the particles with the walls.

5.9 Tables and figures

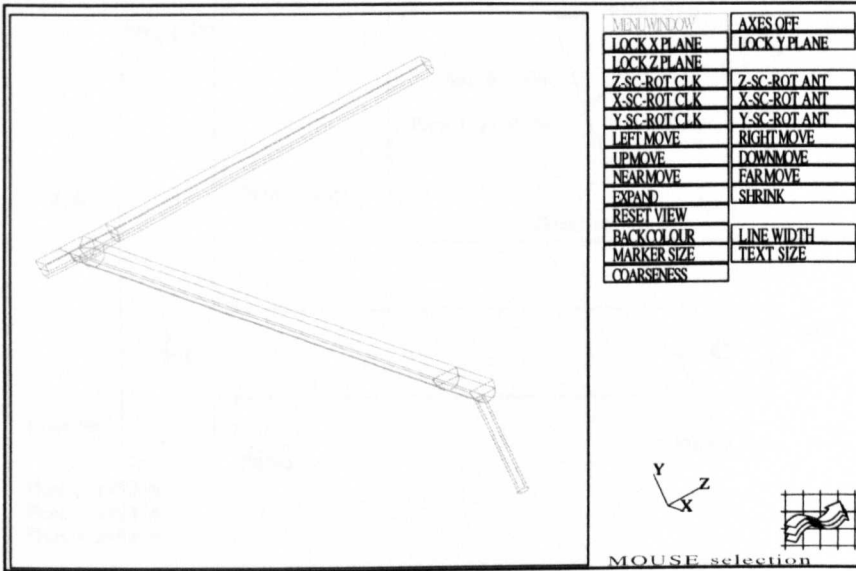


Figure 5.1: Outlines of the launder as seen in CFX.

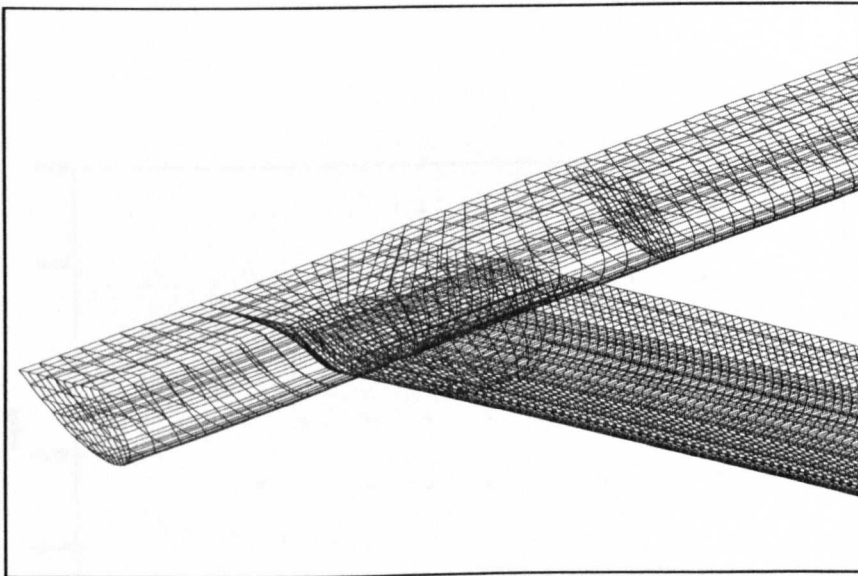


Figure 5.2: Mesh of the corner of the old launder as seen in CFX

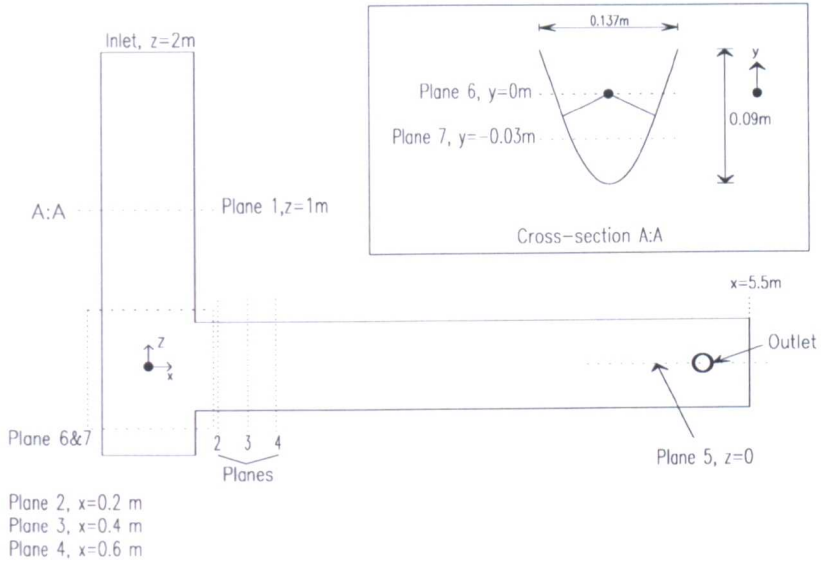


Figure 5.3: Definition of planes in the old launder system. Planes 6 and 7 are 30 and 60mm below the surface respectively.

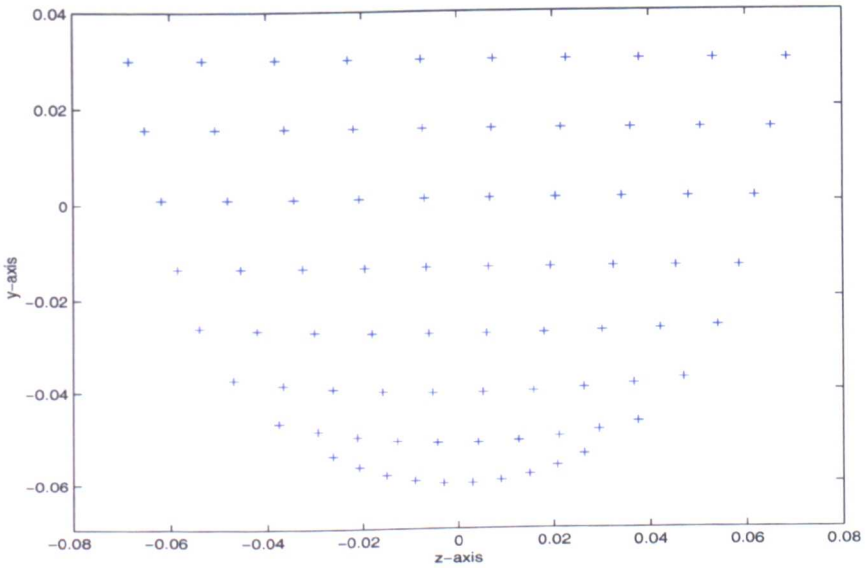


Figure 5.4: The nodes in plane 4 shown on Figure 5.3.

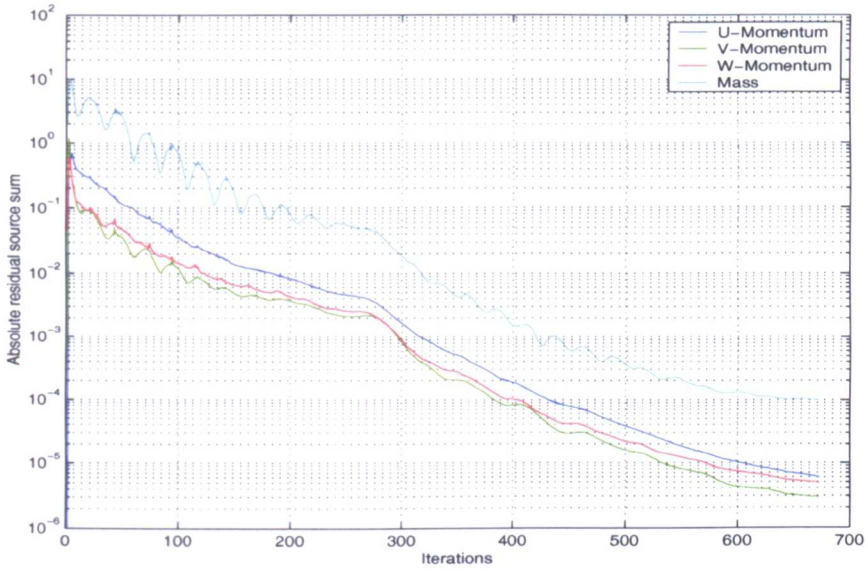


Figure 5.5: The absolute residual source sum for the momentum and mass in the model for the first launder.

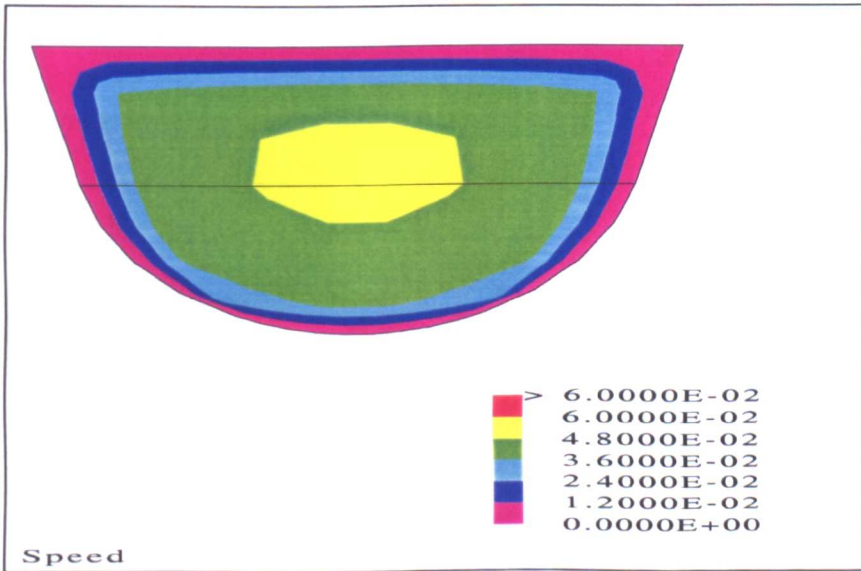


Figure 5.6: Velocity in plane 1. The color code is such that the yellow color defines the interval between 4.8×10^{-2} and 6.0×10^{-2} . Units are in *m/s*.

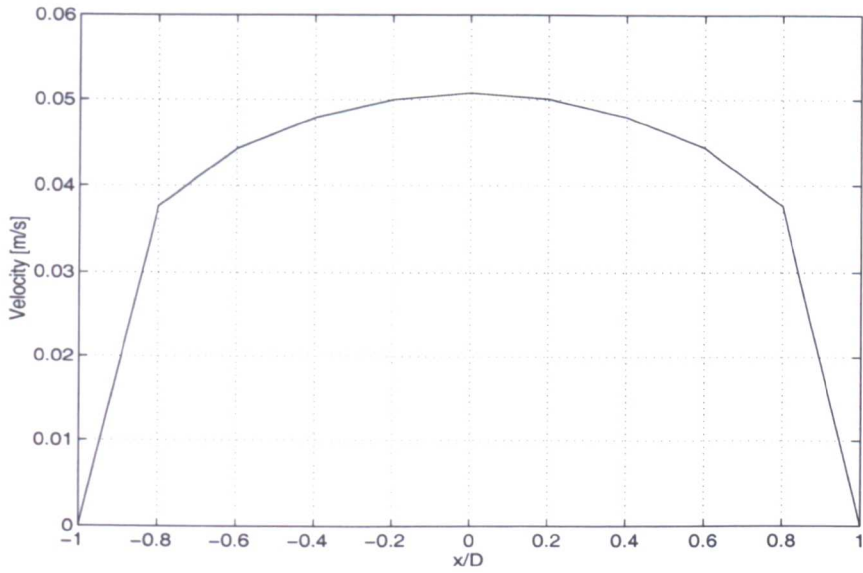


Figure 5.7: Velocity profile of plane 1, where maximum speed is obtained. D is the half length of this plane and x is the position in that direction.

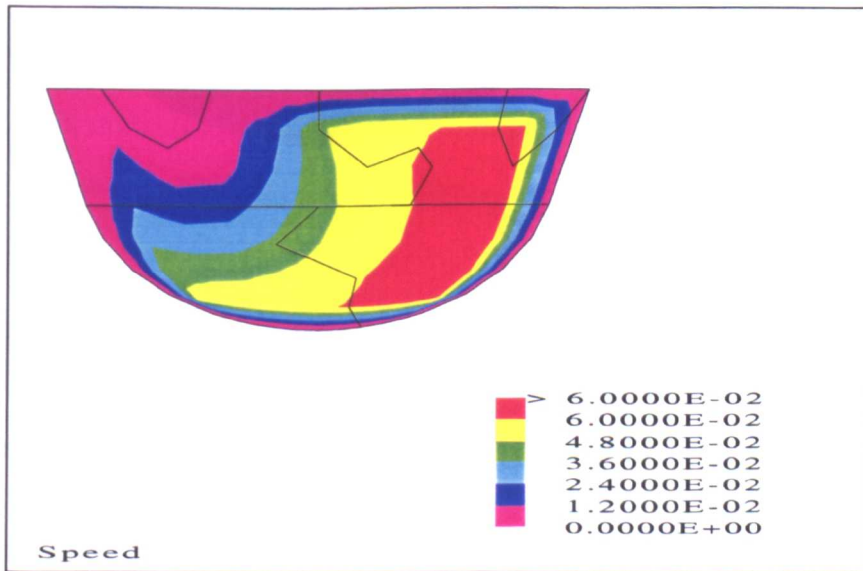


Figure 5.8: Velocity in plane 2, looking in the direction of flow. Units are in m/s.

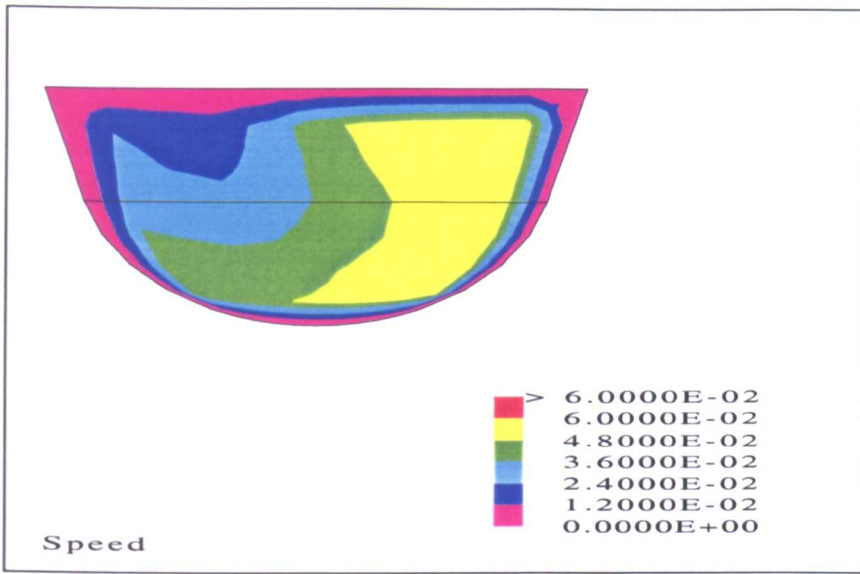


Figure 5.9: Velocity in plane 3, looking in the direction of flow. Units are in *m/s*.

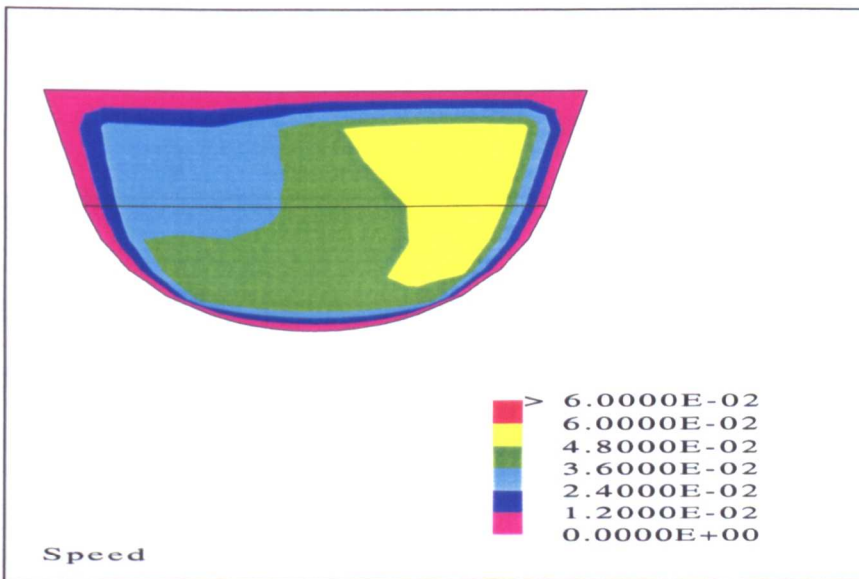


Figure 5.10: Velocity in plane 4, looking in the direction of flow. Units are in *m/s*.

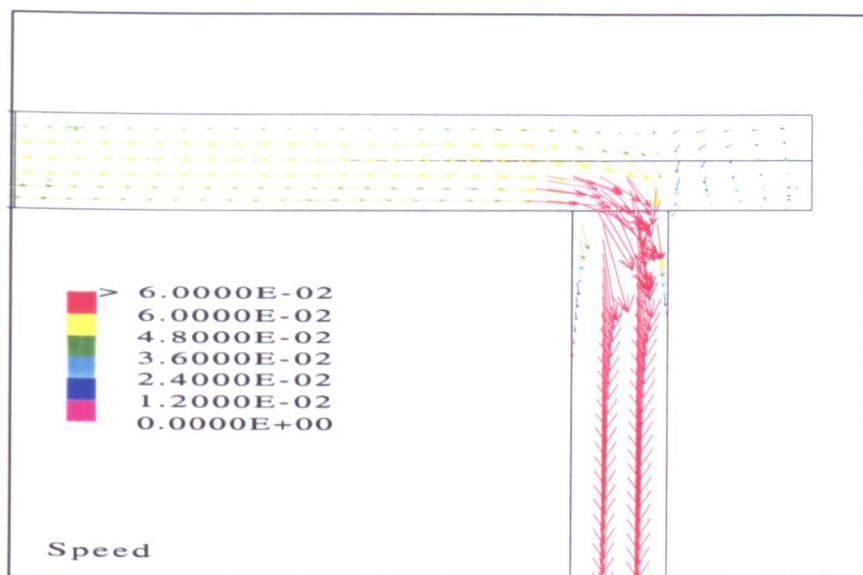


Figure 5.11: Velocity at the outlet of the launder, i.e. plane 5. Units are in *m/s*.

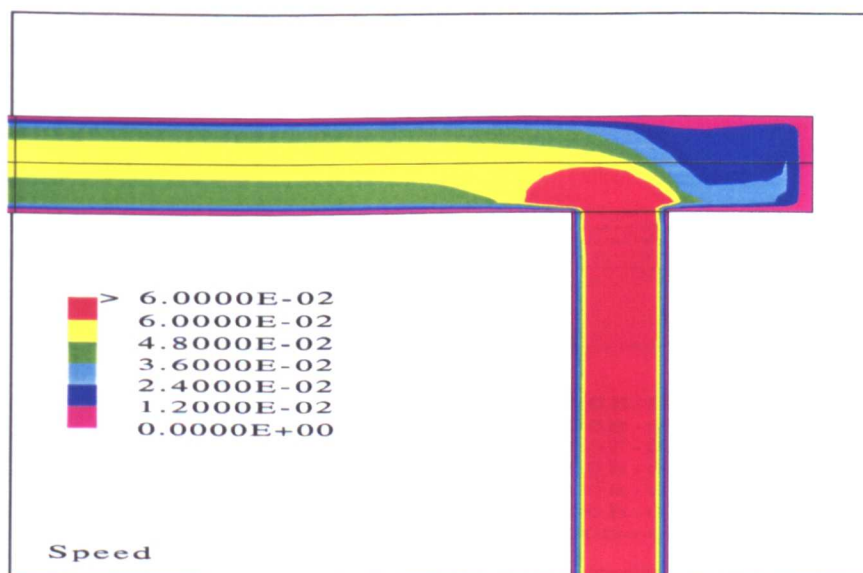


Figure 5.12: Velocity at the outlet of the launder, i.e. plane 5. Units are in *m/s*.

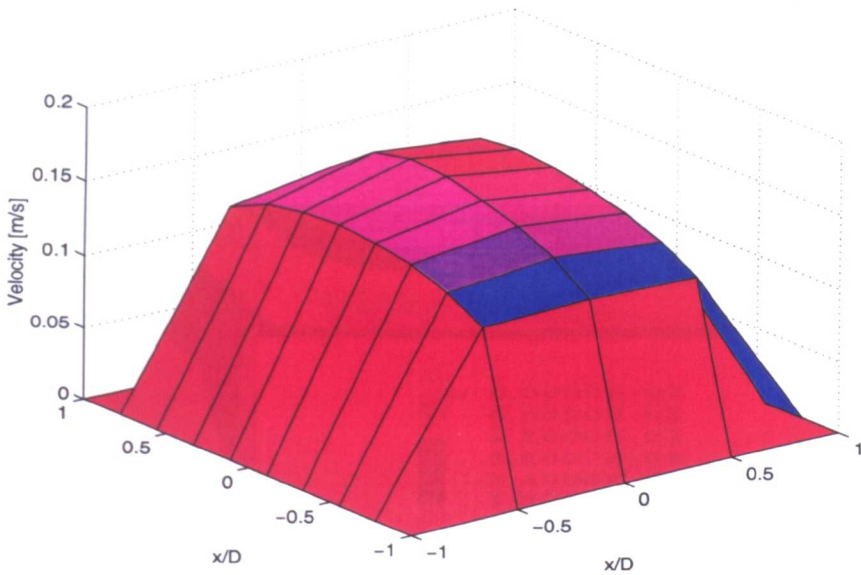


Figure 5.13: Velocity profile in the outlet pipe.

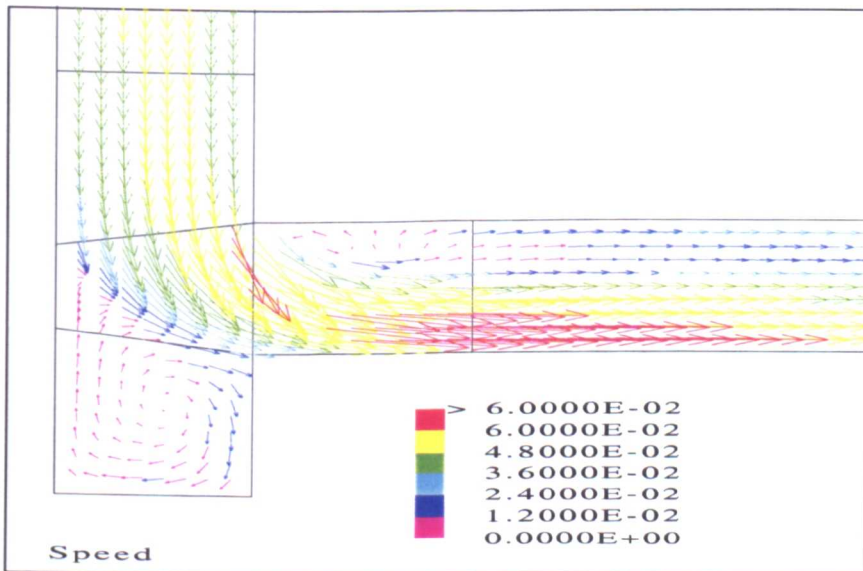


Figure 5.14: Velocity in the corner 30mm below the surface, i.e. plane 6. Units are in *m/s*.

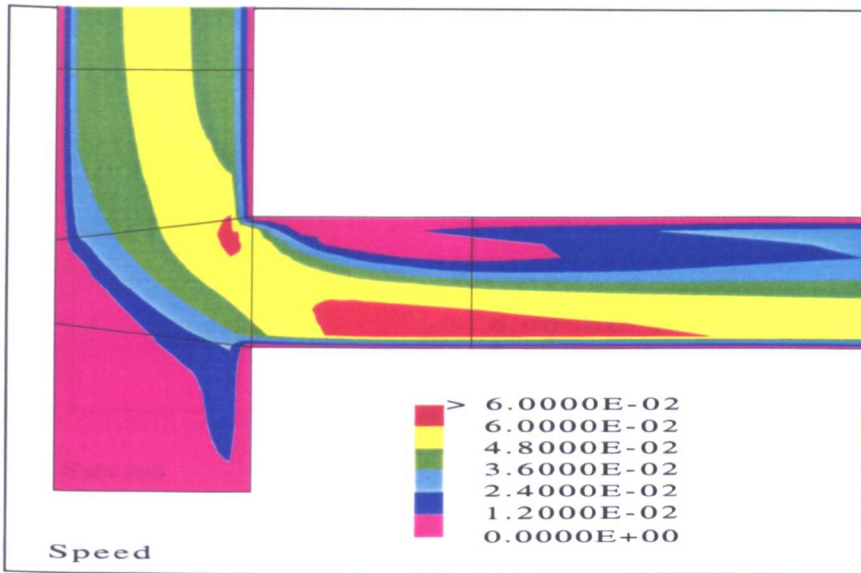


Figure 5.15: Velocity in the corner 30mm below the surface, i.e. plane 6. Units are in m/s .

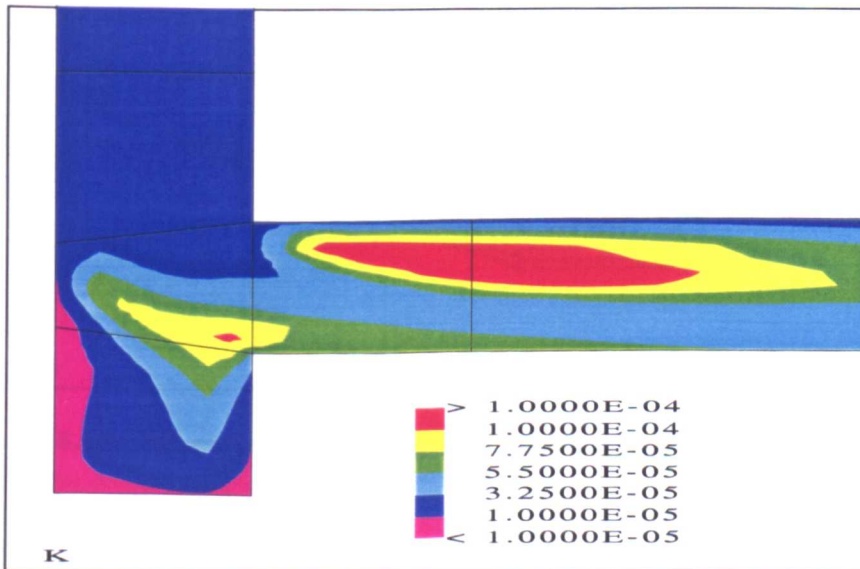


Figure 5.16: Turbulent kinetic energy in the corner 30mm below the surface, i.e. plane 6. Units are in m^2/s^2 .

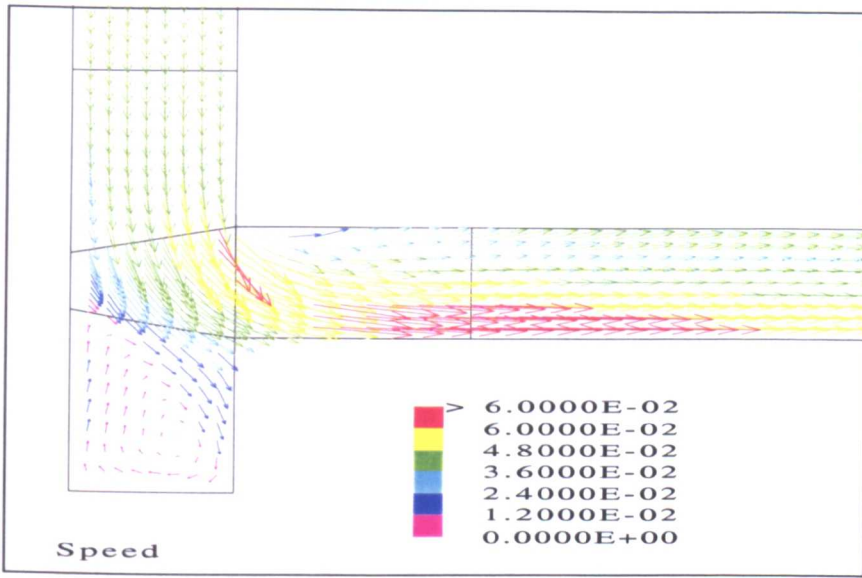


Figure 5.17: Velocity in the corner 60mm below the surface, i.e. plane 7. Units are in *m/s*.

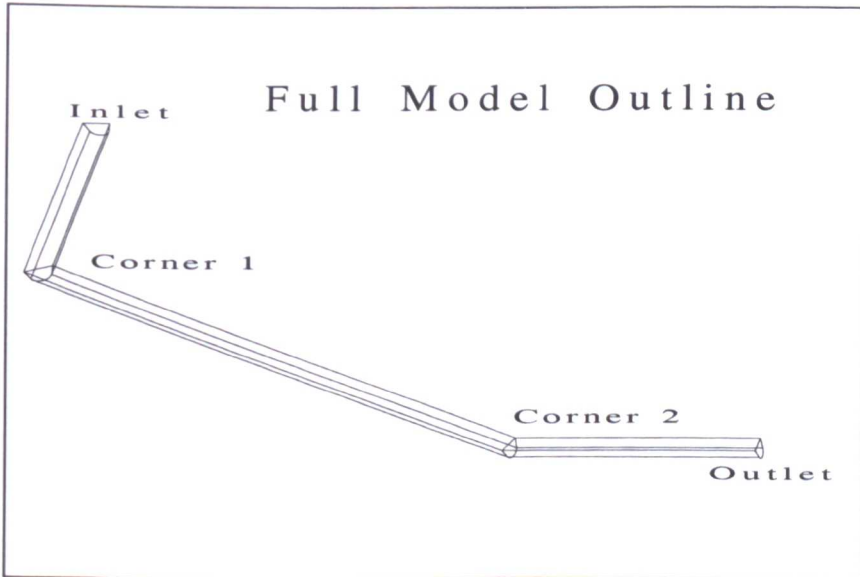


Figure 5.18: Full model outline of the new launder system.

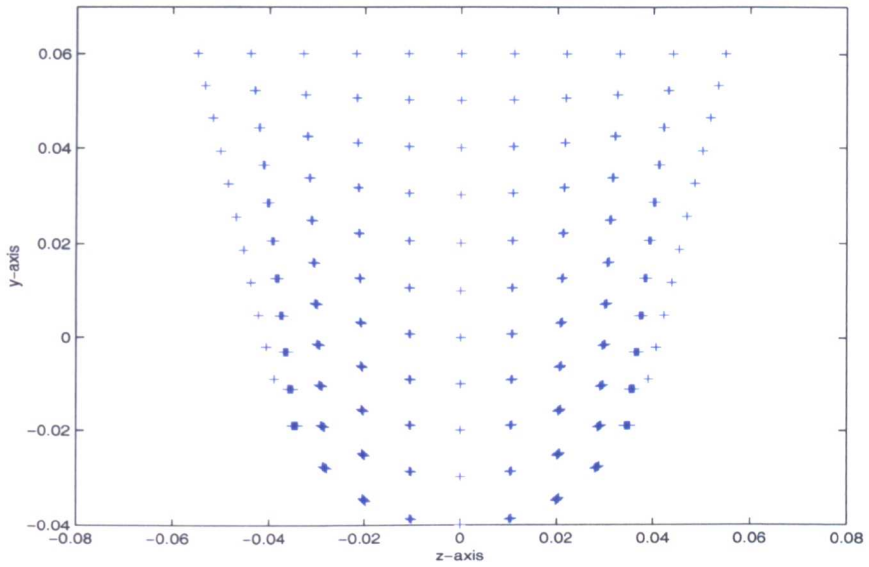


Figure 5.19: The nodes in plane in the straight inlet part of the second launder.

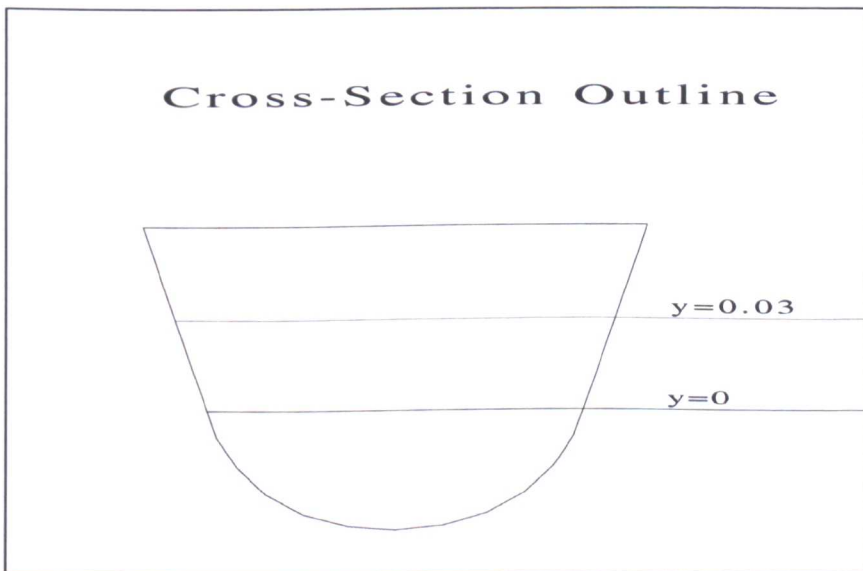


Figure 5.20: Cross-section of the new launder model. Planes $y=0.03$ and $y=0$ are 30mm and 60mm below the surface respectively.

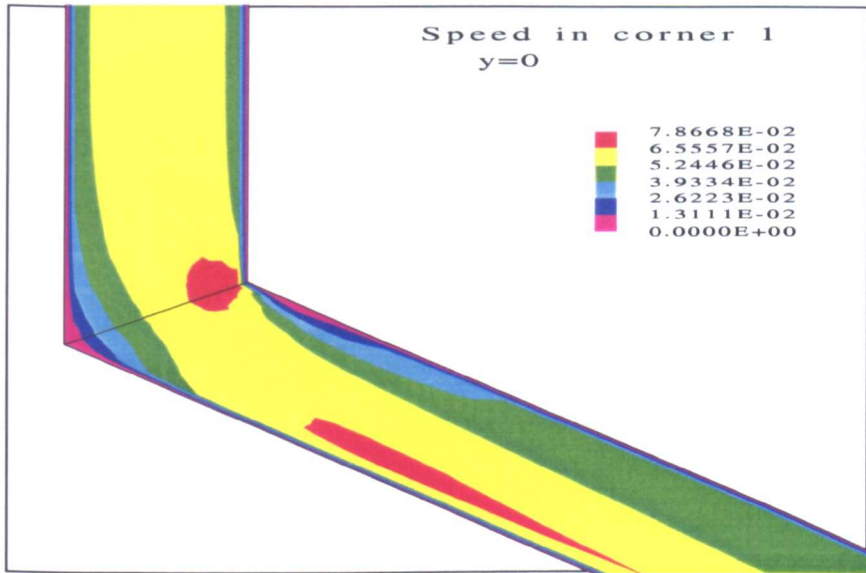


Figure 5.21: Velocity in the first corner of the launder, plane $y=0$, 60mm below the surface.

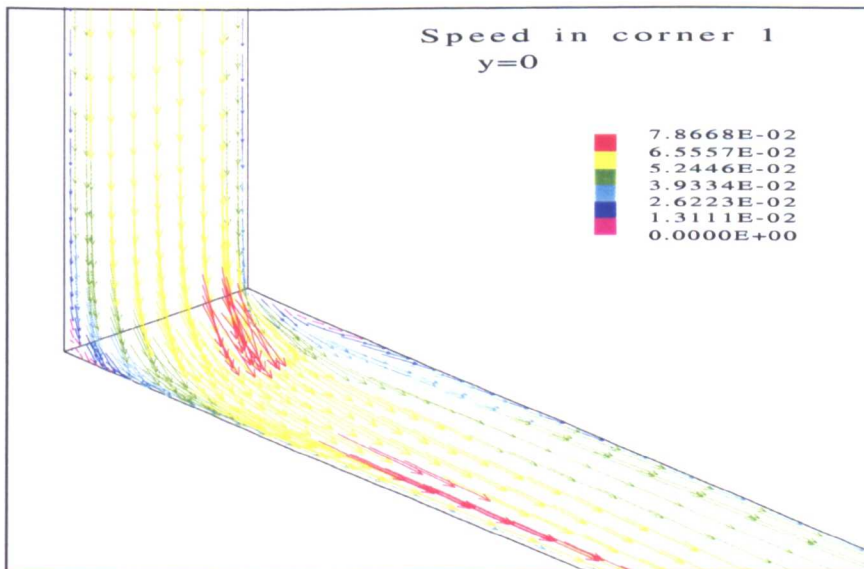


Figure 5.22: Velocity in the first corner of the launder, plane $y=0$, 60mm below the surface.

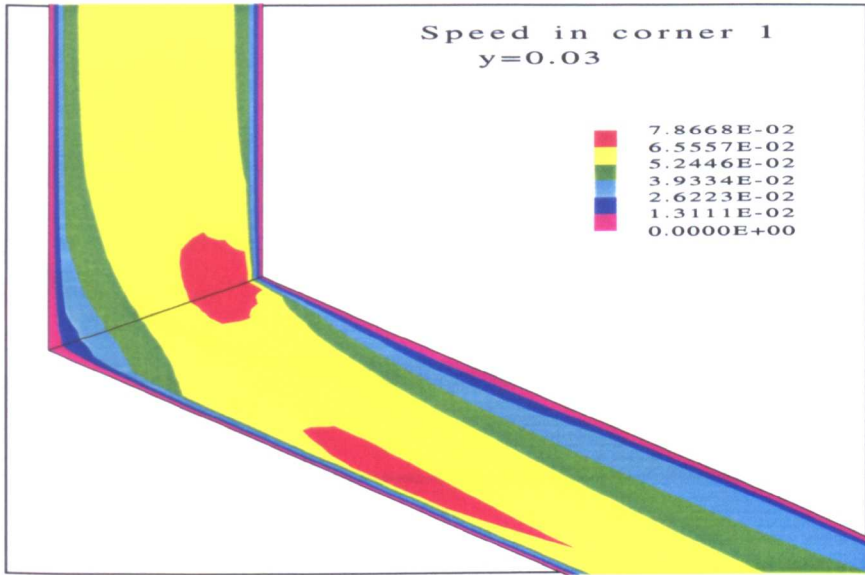


Figure 5.23: Velocity in the first corner of the launder, plane $y=0.03$, 30mm below the surface.

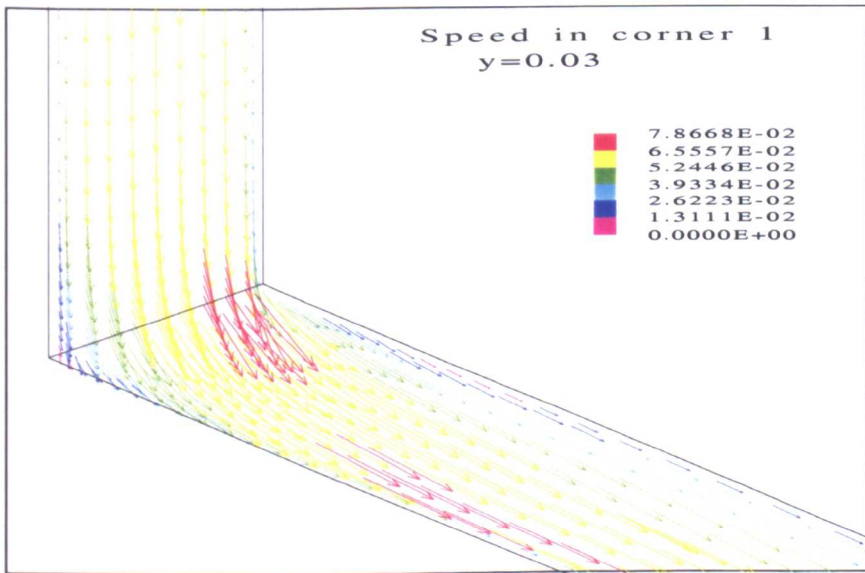


Figure 5.24: Velocity in the first corner of the launder, plane $y=0.03$, 30mm below the surface.

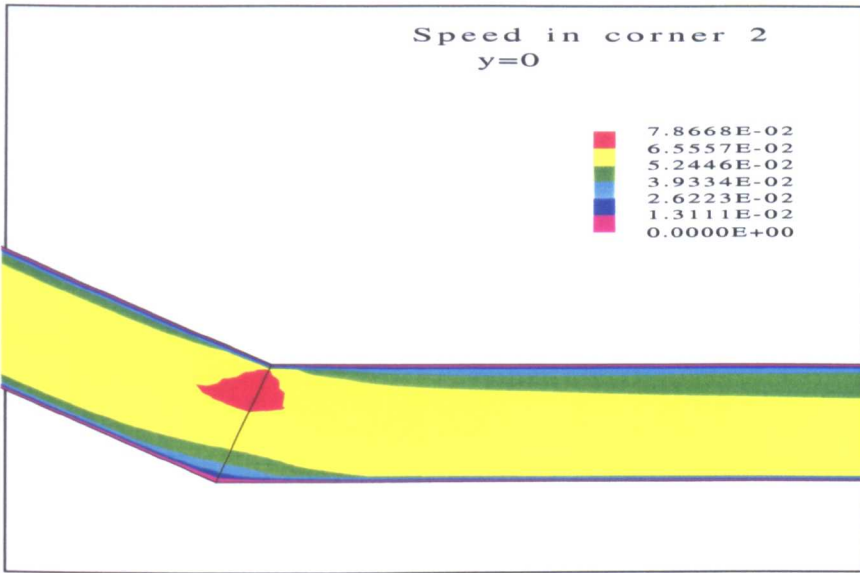


Figure 5.25: Velocity in the second corner of the launder, plane $y=0$, 60mm below the surface.

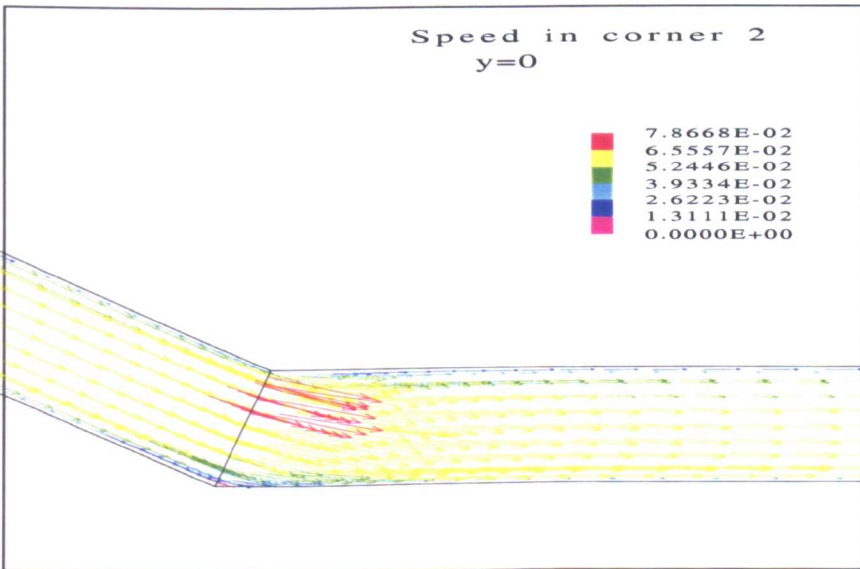


Figure 5.26: Velocity in the second corner of the launder, plane $y=0$, 60mm below the surface.

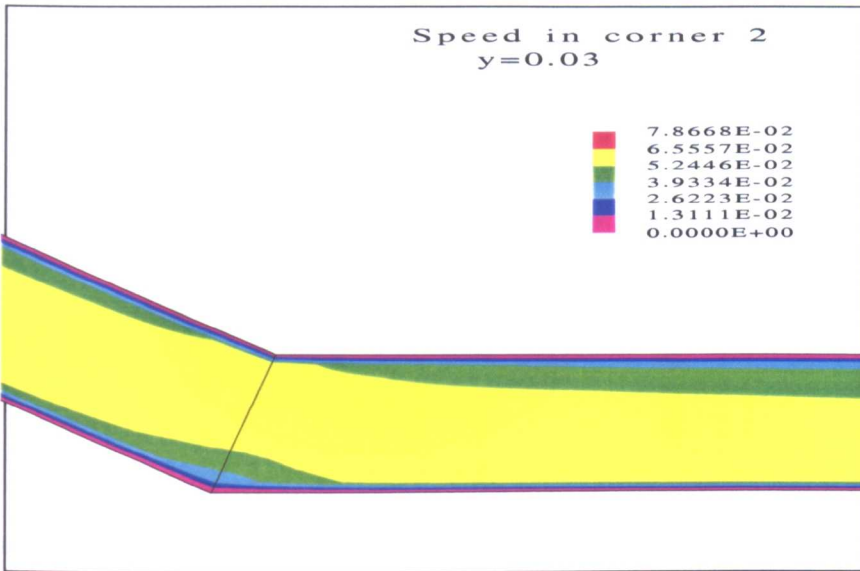


Figure 5.27: Velocity in the second corner of the launder, plane $y=0.03$, 30mm below the surface.

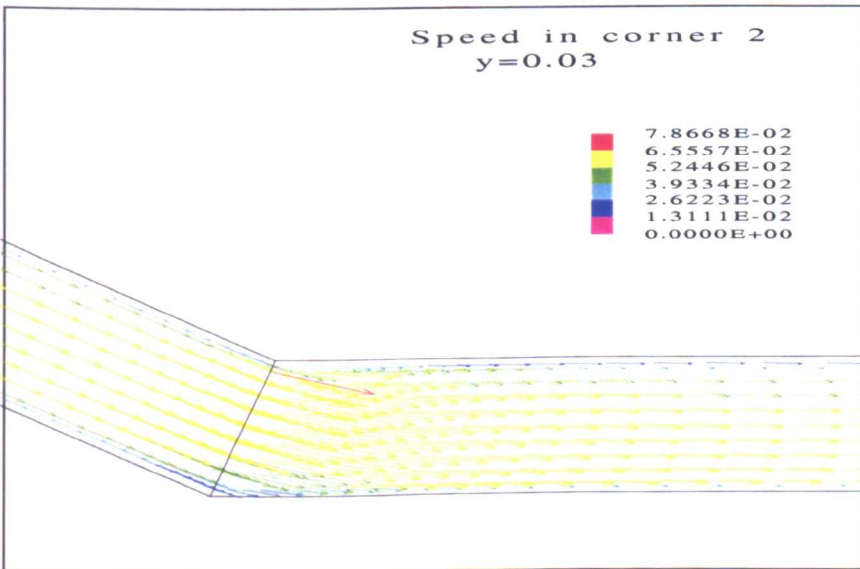


Figure 5.28: Velocity in the second corner of the launder, plane $y=0.03$, 30mm below the surface.

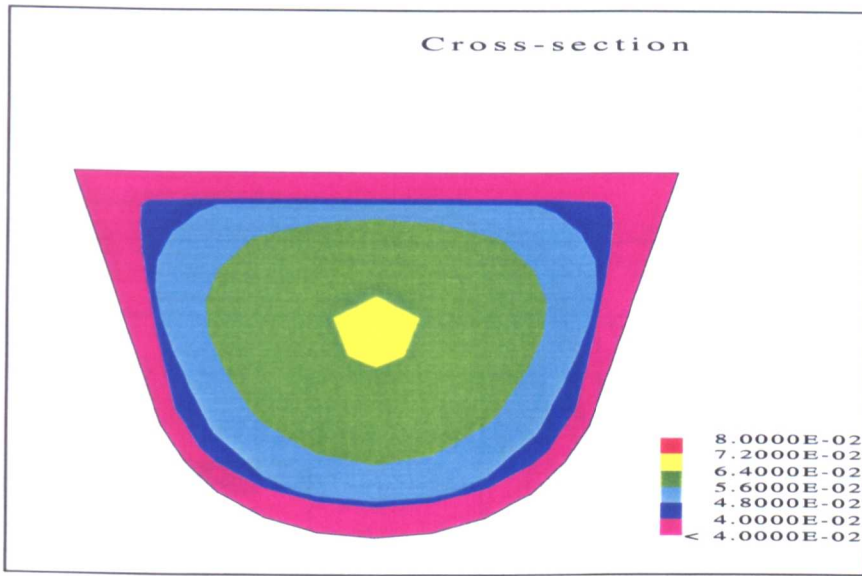


Figure 5.29: Velocity in the cross-section of the launder with undisturbed flow.

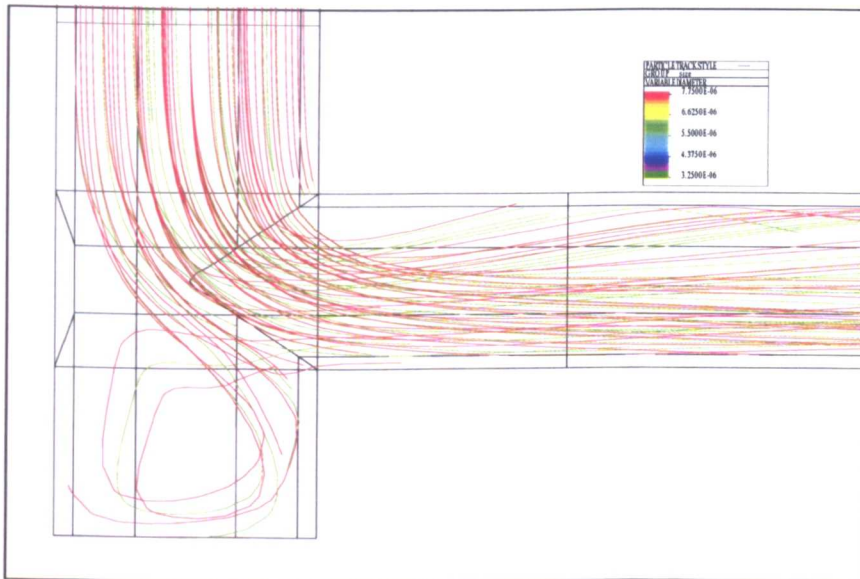


Figure 5.30: Particle tracks at the corner, seen from top. The color of the lines shows the size of the particles. Red is $7.75\mu\text{m}$ and green is $3.25\mu\text{m}$. The time limit is 250 sec.

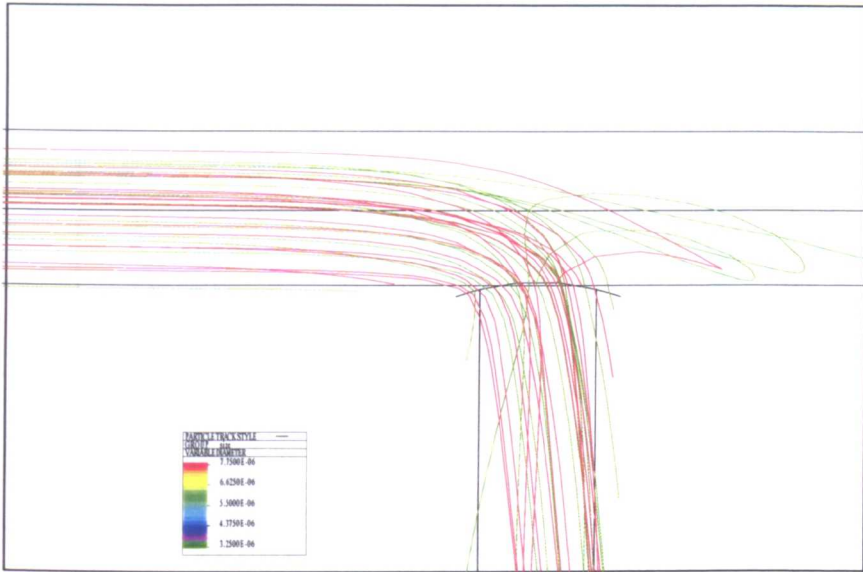


Figure 5.31: Particle tracks near the outlet, seen from the side. The color of the lines shows the size of the particles. Red is $7.75\mu\text{m}$ and green is $3.25\mu\text{m}$. The time limit is 250 sec.

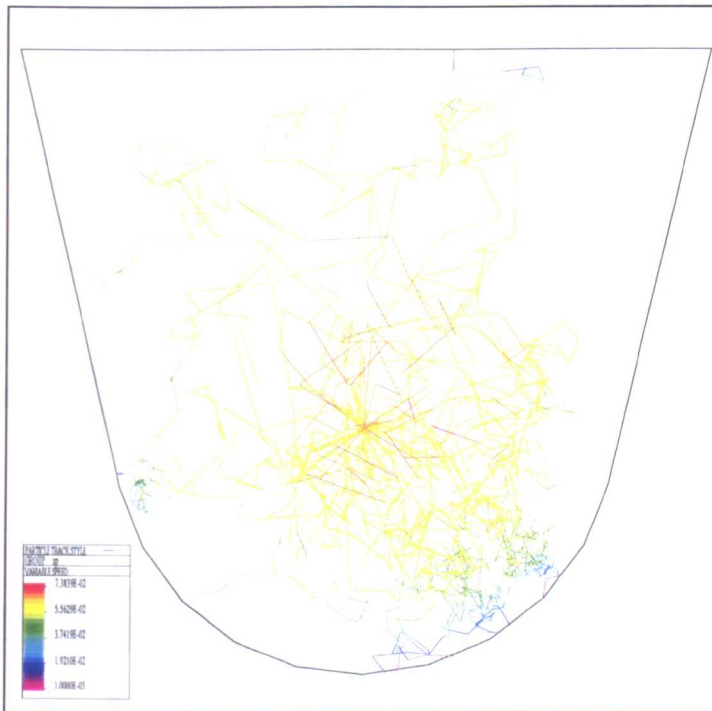


Figure 5.32: The paths of $5\mu\text{m}$ particles in straight launder in 30 seconds. The color of the lines denotes the velocity of the particles. Red is the highest velocity, approximately $7.3 \times 10^{-2} \text{m/s}$.

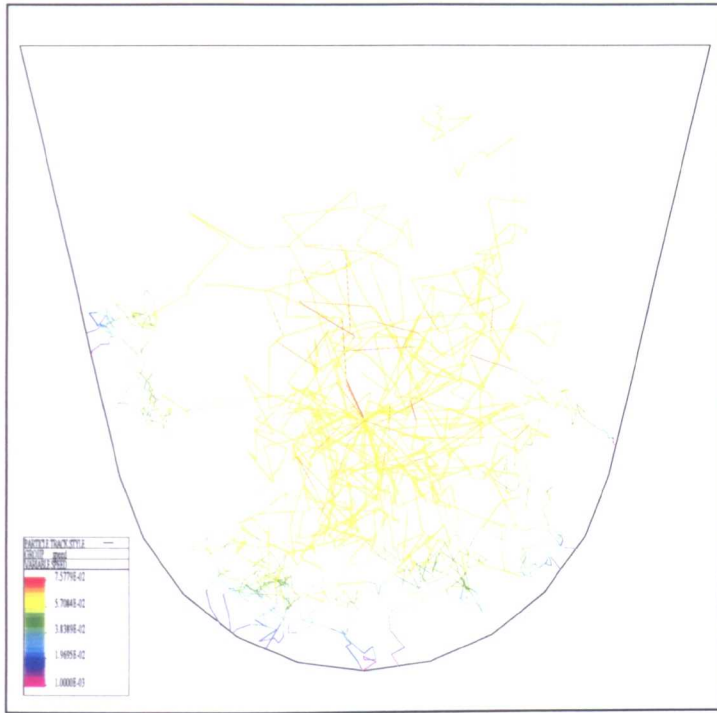
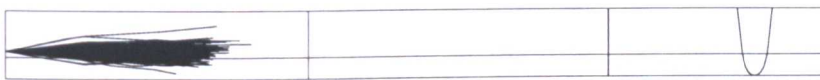
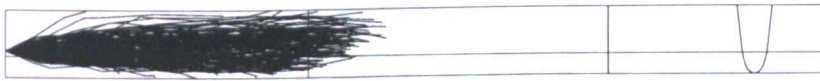


Figure 5.33: The paths of $10\mu\text{m}$ particles in straight launder in 30 seconds. The color of the lines denotes the velocity of the particles. Red is the highest velocity, approximately $7.3 \times 10^{-2} \text{m/s}$.



(a) 5 sec

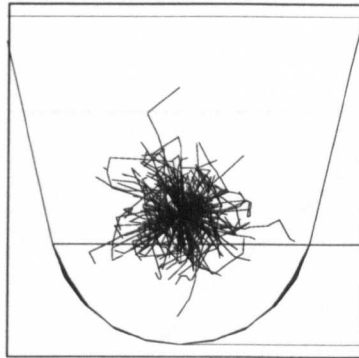


(b) 10 sec

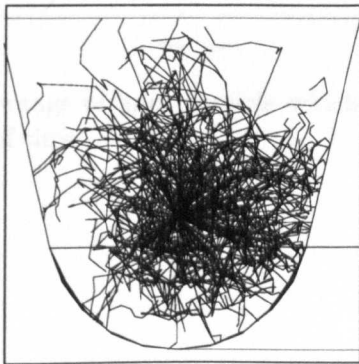


(c) 15 sec

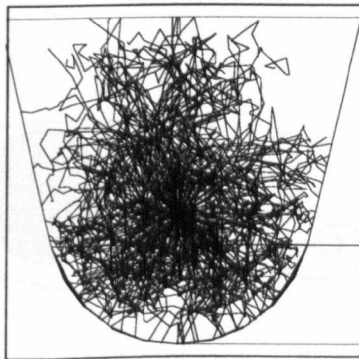
Figure 5.34: Particles flowing in the new launder, 5, 10 and 15 seconds after the addition. Particle diameter $2\mu\text{m}$. Distance between vertical lines is 500mm.



(a) 5 sec



(b) 10 sec



(c) 15 sec

Figure 5.35: Particles flowing in the new launder, 5, 10 and 15 seconds after the addition. Particle diameter $2\mu m$.

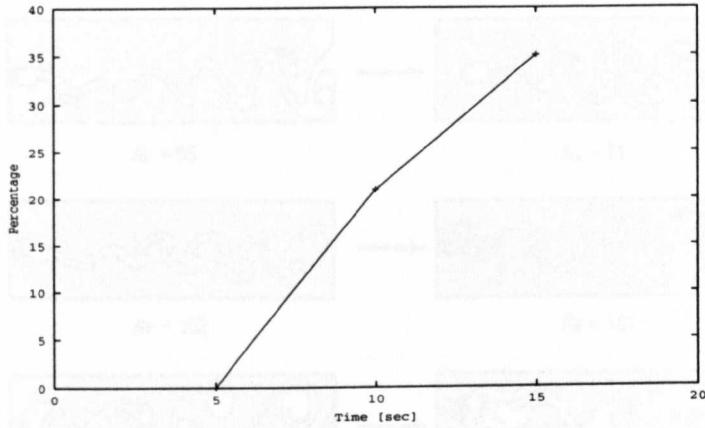


Figure 5.36: The percentage of $2\mu\text{m}$ particle which crash into the wall as a function of time.

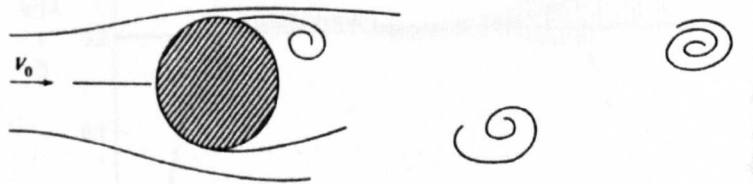


Figure 5.37: Formation of a vortex behind a cylinder [51].

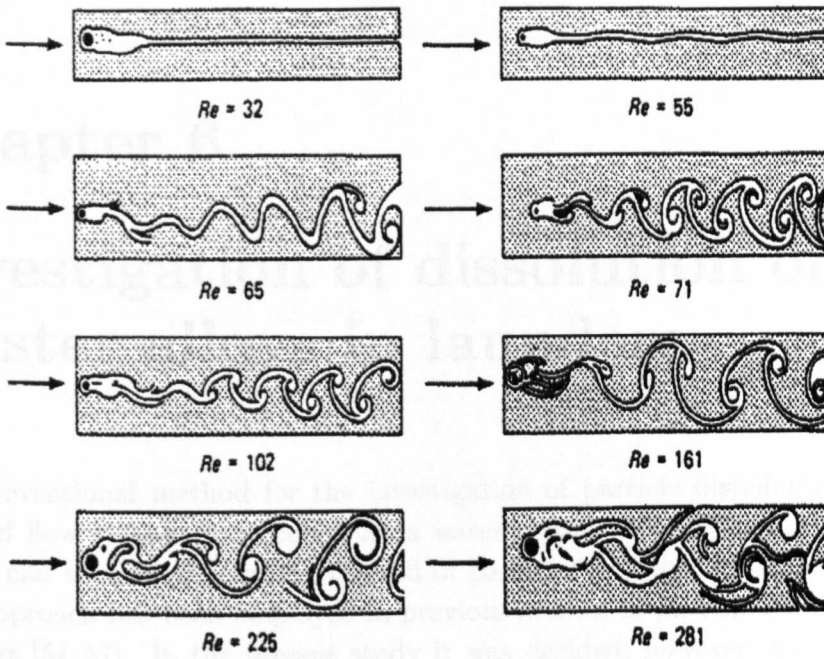


Figure 5.38: The effect of Reynolds number on the flow past a cylinder. [After Homann (1936)] [51].

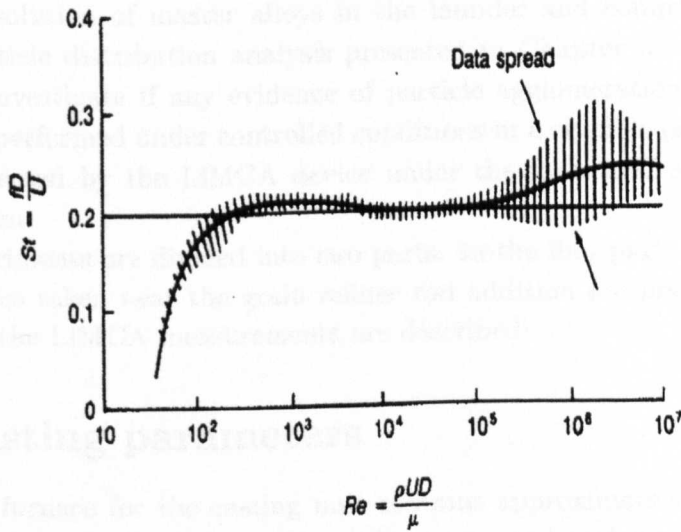


Figure 5.39: Measured Strouhal number for vortex shedding frequency behind a circular cylinder [51].

Chapter 6

Investigation of dissolution of master alloys in launders

The conventional method for the investigation of particle distribution models for fluid flow systems is to construct a water model of the system. The distribution can then be studied by the aid of particles and dye added to the flow. This approach has been employed in previous studies of particle distribution in launders [54, 57]. In the present study it was decided, however, to attempt to obtain support for the particle distribution analysis presented in Chapter 5 by performing a study of the industrial system containing molten aluminium with grain refiner added in rod form.

The experiments presented in this chapter were carried out in the first launder at Chippis. The launder geometry is described in Figures 5.1 and 5.3. The main purpose of this part of the project was to investigate the particle distribution from the dissolution of master alloys in the launder and compare the results with the particle distribution analysis presented in Chapter 5. An additional aim was to investigate if any evidence of particle agglomeration, found in the experiments performed under controlled conditions in a crucible (see Chapter 4), could be detected by the LiMCA device under the industrial conditions in a launder system.

The experiments are divided into two parts. In the first part, chemical analysis of samples taken near the grain refiner rod addition are presented. In the second part, the LiMCA measurements are described.

6.1 Casting parameters

The holding furnace for the casting unit contains approximately ten tonnes of melt for each cast. In the furnace, the melt was treated with an IRMA process, i.e. fluxing the melt with a blend of argon and chlorine gas for 25–30 minutes. After the gas treatment there was a holding time of 60 minutes and subsequently the flow to the casting machine was started. The time for the casting was approx.

70 minutes. The ingot size was 425 x 900mm which is typical for billets intended for rolling mills. The casting speed was 60 mm/min.

The first launder layout was described in Chapter 5 (see Figures 5.1 and 5.3). Figure 6.1 shows the position of the grain refiner rod in the launder. The melting zone of the rod was estimated to be at a depth of 70mm [48].

The height of the melt was 90mm in the part of the launder used for the experiments. This gives an average velocity of the melt around 45 mm/sec calculated from the average mass flow. The Reynolds number can then be calculated as 13,550 in the launder using Equation 2.15. Therefore, the flow is turbulent as assumed in the flow model analysis (see Section 5.1.1).

Three types of master alloy rods were available for this study. Two were the Al-5Ti-1B alloys labelled as *B5/1-B* and *B5/1-D* in the LiMCA experiments in the crucible described in Chapter 4 and the third was the Al-3Ti-0.2B alloy denoted as *B3/.2-A* in the same experiments. Two of these gave very low particle counts in the crucible, i.e. *B5/1-B* and *B5/1-D*, or approximately 1K/Kg for 0.035 wt% titanium addition (see Table 4.3). The third, *B3/.2-A*, gave a count of 3K/Kg for a 0.02wt% addition. Master alloys with a higher particle count in Table 4.3 could have been more suitable for these experiments but they were not available at the time.

6.2 Sampling of flowing melts

There are inherent difficulties in obtaining representative samples from a flowing fluid in order to obtain a measure of heterogeneous particle distribution in the system. Any instrument inserted into the fluid disturbs the flow profile and, therefore, disrupts the particle distribution. Some attempts were made in the present study to construct devices to insert into the melt in the launder to obtain representative samples below the surface. These were in principle based on devices utilising a flow-through principle employed to study particle distribution in geothermal steam pipelines in Iceland [66]. In brief, the devices proved unsuccessful in the severe environment of a flowing melt.

The only standard device available for sampling the melt for chemical analysis was a spoon as there was no metal sucking device (see Figure 4.5) available at the time. The samples were taken as near the surface as possible in order to minimise disturbances to the flow profile. Before each sample was taken the aluminium oxide layer on top of the melt had to be pushed away with the spoon. Then the spoon was dipped into the melt, care being taken not to go more than about 10-25 mm below the surface. Considering these limitations the samples can only be considered to give the best available indication of the composition of the melt at or near the surface under undisturbed flow conditions.

Table 6.1: List of the experiments showing the titanium addition and titanium concentration achieved.

<i>Experi- ment</i>	<i>Master alloy</i>	<i>Titanium content</i>		
		<i>Furnace measured [wt%]</i>	<i>Target addition [wt%]</i>	<i>Outlet measured [wt%]</i>
<i>TiB-21</i>	<i>B5/1-B</i>	0.0009	0.0050	0.0061
<i>TiB-22</i>	<i>B5/1-D</i>	0.0012	0.0050	0.0060
<i>TiB-23</i>	<i>B5/1-D</i>	0.0012	0.0050	0.0054
<i>TiB-24</i>	<i>B3/.2-A</i>	0.0016	0.0045	0.0034
<i>TiB-25</i>	<i>B3/.2-A</i>	0.0020	0.0045	0.0049
<i>TiB-26</i>	<i>B5/1-B</i>	0.0028	0.0050	0.0059
<i>TiB-27</i>	<i>B5/1-B</i>	0.0028	0.0050	0.0067

Table 6.2: Titanium distribution into TiB_2 and $TiAl_3$ in the master alloys.

<i>Grain refiner</i>	<i>Ti addition</i>	<i>Ti in TiB_2</i>	<i>Ti in $TiAl_3$</i>
Al-5Ti-1B	50 g/t	22.14 g/t	27.86 g/t
Al-3Ti-0.2B	45g/t	6.64 g/t	38.36 g/t

6.3 Chemical analysis

There were seven experimental runs and Table 6.1 gives a description of each experiment. Table 6.2 shows approximately how the titanium is distributed between the two phases TiB_2 and $TiAl_3$. The specification for the aluminium base metal is given in Table 6.3. An alternating current spark analysis was employed for the chemical measurements with an estimated accuracy of $\pm 3\%$.

The aim of the chemical analysis was to evaluate the dispersion of titanium and boron from the grain refiner rod addition. Figures 6.2 and 6.3 show the position of the sampling points in the launder. As the figures show, the samples are taken upto 500mm from the grain refiner addition point and very near the surface. One sampling position, i.e. point 1, was situated 200mm in front of the grain refiner rod for comparison.

The definition of an increment in the titanium concentration at each sampling point is given as:

$$\Delta C_m[\%] = \frac{C_m - C_0}{C_p - C_0} * 100 \quad (6.1)$$

where C_m is the titanium concentration measured at the point of interest (2-14) as shown in Figure 6.3, C_0 is the concentration measured at point 1 and C_p is

the concentration measured in the launder near the casting machine given as the outlet level in Table 6.1.

Figures 6.4 and 6.5 show the average titanium increment at each measuring position along the launder for master alloys Al-5Ti-1B and Al-3Ti-0.2B respectively. The measurements are given in Table B.1 in Appendix B. The measured titanium increment is always well below 100%. The increase is higher at the centre than near the walls as expected. It is also higher for the Al-5Ti-1B master alloy than for the Al-3Ti-0.2B alloy. There is considerable scatter in the results, however, and some of this can possibly be explained by uncertainties associated with the sampling procedure as discussed in Section 6.2. The general trend that appears from the results near the walls is that the titanium increment increases along the launder. In the centre, there is even more scatter in the results, possibly due to the formation of Kármán eddies in the wake of the master alloy rod (see Section 5.7). The effect of these eddies can possibly be distinguished in the oxide layer on the surface of the melt in Figure 6.1. Looking again at Figures 6.4 and 6.5, the latter shows a trend in the centre towards an increase in the titanium increment along the launder but in the former no trend can be established. According to the particle distribution model, practically no TiB_2 particles should reach the top surface layer of the melt (see Figures 5.32 and 5.33). If the same behaviour is assumed for the $TiAl_3$ particles, the titanium increase should be solely due to dissolved $TiAl_3$. This will be discussed further in Section 6.5.

No detectable increase was observed in the boron concentration at the sampling points. This is in line with the particle tracking analysis in Section 5.3.4. The TiB_2 particles can be assumed to be practically insoluble and they have a higher density than $TiAl_3$. On the other hand, they are much smaller (see Chapter 3). Therefore, a more effective mixing of the TiB_2 particles would be expected considering the particle tracking theory and they should be more likely to reach the top surface. The inference could be drawn that no $TiAl_3$ particles should reach the surface either and that the titanium increase measured above is only due to the effects of dissolved titanium. However, this is unlikely at all test positions as discussed in Section 6.5.

One sample was taken in the dead zone at the corner of the launder in experiment *TiB-26* (see Figure 6.7). The sampling position is approx. 1460mm away from the grain refiner addition point. The flow analysis in Chapter 5 showed a vortex formation in the dead zone where it was predicted that particles could accumulate. At this point an increase in the boron concentration at the surface was observed. The concentration had increased from 0.0002 wt% in the base metal to 0.00073 wt%, where the target value was 0.0010 wt%. The titanium increment was measured as 142% in the corner for the same sample. This is a clear indication of enrichment of the melt in the vortex as discussed in Section 6.5.

Table 6.3: Chemical analysis of the base metal in experiments *TiB-21* to *TiB-27*. The balance is aluminium.

<i>Element (wt %)</i>									
Si	Fe	Cu	Mn	Mg	Cr	Ni	Zn	Ti	B
0.01	0.06	0.0012	0.0014	0.0008	0.0015	0.0045	0.0034	0.0014	0.0002

6.4 LiMCA measurements

The LiMCA device was employed to investigate four of the experiments shown in Table 6.1, i.e. experiments *TiB-23*, *TiB-24*, *TiB-25* and *TiB-26*. Figure 6.6 shows measurements being taken with the LiMCA device. The measuring positions are shown in Figure 6.7. The depth of insertion of the probe was approximately 50mm. It should be noted that the LiMCA measures only inclusions larger than 20 μ m in size as previously discussed.

Before the results are presented it must be stressed that these experiments are carried out with an industrial grade of melt and in an industrial casting unit. Therefore, the conditions of the melt are not as well defined as in the LiMCA tests in the crucible described in Chapter 4. There are two main points of difference. One is that the inclusion content in the melt is a function of time during each experiment due to settling of inclusions in the furnace during the casting process. The second is that the grain refiner addition is much lower in industrial practice than employed in the tests in the crucible. Thus, the target master alloy additions in the launder shown in Table 6.1 are only about 15-20% of the normal additions to the crucible described in Table 4.1.

The results for the particle count measured with the LiMCA device are shown in Figures 6.8, 6.10, 6.12 and 6.14. The time scale in the figures shows the time at which each measurement was taken, measured from the beginning of the casting process. The measurements always start and end at position 1 which is upstream of the master alloy addition point. The results at this position, therefore, show the inclusion content in the melt without the grain refiner and they give a clear indication of the change in the inclusion content in the melt with time during each experiment. The measured values vary between experiments. They range between 1.2-5.8 K/Kg at the beginning and they are generally below 0.3 K/Kg at the end. This behaviour is normally encountered in industrial practice but the values obtained vary between production units (see Section 2.5). The values obtained here can be considered to be relatively low for an industrial grade of melt [31].

As Figures 6.8, 6.10, 6.12 and 6.14 show, the only clear indications of an increase in the particle count due to the grain refiner addition appear at points 2, 3 and 4. This is probably due to undissolved $TiAl_3$ particles. At the other

points there are hardly more particles detected than should be expected without a grain refiner addition considering the inclusions measurements at position 1. One exception is seen in Experiment *TiB-25* (Figure 6.12) at position 5 where slight indications of additional particles can possibly be distinguished from the scatter in the measurements due to the inherent inclusions count. Therefore, most of the $TiAl_3$ particles have probably dissolved at these latter points down to a size of less than $20\mu\text{m}$.

It is impossible to establish any effect of TiB_2 clusters coming from the master alloy rod in these experiments due to the inclusions content of the original melt. It can be seen, however, in the latter stages of each experiments that the melt at the positions downstream of the grain refiner seldom reaches the low final particle count at position 1 upstream of the grain refiner. Whether this is partly due to the effect of clusters from the master alloy rods cannot be determined with the present experimental approach.

The maximum probability of finding the effect of TiB_2 clusters formed in the melt is at positions 7 and 8 due to possible cluster formation and accumulation in the vortex in the dead zone and these clusters subsequently reentering the main flow. Unfortunately, the LiMCA head could not be located at position 7 due to other equipment in the cast house. Looking at Figure 6.13 for the *B3/.2-A* master alloy, there is a peak in the particle count at position 8. The size distribution at this point in Figure 6.13 also shows a tendency towards an increased particle size. This will be discussed further in Section 6.5.

Figures 6.9, 6.11, 6.13 and 6.15 show the size distribution for four different points in each cast. The size distribution in the base metal before the grain refiner addition at position 1, is similar for each experiment. Apart from position 8 in Figure 6.13, there is no obvious correlation between the small changes in the size distribution observed at different measuring points after the addition of the grain refiner.

Finally, samples for PoDFA analysis were taken from the melt in the same experimental runs as for the LiMCA tests. The samples were taken at the inlet and outlet of the launder at the end of each experimental run. The results are shown in Table 6.4. The STIC value is a measure of the inclusion content as discussed in Section 2.4.4. It is evident from these results that the master alloys increase the particle content of the melts, even though the particles are not detected by the LiMCA device, i.e. they are less than $20\mu\text{m}$ in diameter.

6.5 Discussion

The chemical analysis of the samples taken from the surface of the melt offer important insight into the particle distribution from the master alloy addition.

First, the absence of any detectable increase in the boride concentration at

Table 6.4: PoDFA analysis at the inlet and outlet of the launder. The experiments are the same as for the LiMCA tests, *TiB-23* to *TiB-26*. The samples were taken at the end of each experimental run.

<i>Experiment</i>	<i>Sampling position</i>	<i>STIC</i>
<i>TiB-23</i>	Inlet	0.03
<i>TiB-23</i>	Outlet	0.06
<i>TiB-24</i>	Inlet	0.04
<i>TiB-24</i>	Outlet	0.07
<i>TiB-25</i>	Inlet	0.06
<i>TiB-25</i>	Outlet	0.08
<i>TiB-26</i>	Inlet	0.04
<i>TiB-26</i>	Outlet	0.05

the top surface of the melt shows that few if any TiB_2 particles have reached the surface, even after travelling 500 mm from the master alloy addition point. This is in agreement with the particle distribution analysis presented in Chapter 5 where the effect of gravity prevented the particles from reaching the top surface even under the conditions of fully developed distribution profile as shown in Figures 5.32 and 5.33. The results, therefore, clearly support the particle distribution model.

The results from the titanium measurements are more difficult to interpret. In this case both the effect of the dissolution of the $TiAl_3$ particles and the movement of undissolved $TiAl_3$ must also be considered. The particle distribution analysis applies for the undissolved particles but not for the mixing of the dissolved titanium where, for instance, the effect of gravity does not apply. The TiB_2 particles are assumed to be practically insoluble as before (see Section 2.3.2).

The general trend in the measurements for the Al-3Ti-0.2B master alloy in Figure 6.5 appears to be consistent with the expected behaviour. The titanium increment at the surface increases along the launder both in the centre and near the walls. According to the proposed particle distribution model, the increase should be due to titanium from dissolved $TiAl_3$ as the undissolved particles should not reach the top surface. The results can, therefore, be explained as follows. As soon as the $TiAl_3$ particles are released from the master alloy they start to dissolve. If the industrially assumed dissolution rate of $40 \mu m/min$ [23] is applied, approximately $1.5 \mu m$ layer is dissolved from each particle in a 100 mm length of the launder. Thus, all particles up to $15 \mu m$ in diameter have dissolved after travelling a distance of 500mm. The turbulent eddy currents and the Kármán eddies (see Section 5.7) are the main factors in the mixing of the dissolved titanium both laterally and vertically. The maximum theoretical

increase in the titanium increment for the Al-3Ti-0.2B master alloy addition is 84% assuming the target addition, a complete mixing of the titanium from the $TiAl_3$ particles and using the titanium distribution between $TiAl_3$ and TiB_2 given in Table 6.2. The measured titanium increment is well below this limit in all cases. The results are, therefore, not seen to contradict the particle distribution analysis.

The results for the Al-5Ti-1B master alloy presented in Figure 6.4 are more difficult to understand. The maximum theoretical increase in the titanium increment for the target addition of this alloy is 56%, assuming complete mixing of the titanium from the $TiAl_3$ and using the distribution between $TiAl_3$ and TiB_2 given in Table 6.2. The measured increase in the titanium increment was, therefore, expected to be lower for this alloy than for the Al-3Ti-0.2B alloy. A comparison between Figures 6.4 and 6.5 indicates the reverse behaviour. There is no apparent explanation for the observed behaviour since the dissolution rate of the $TiAl_3$ particles should be the same for both types of master alloys. The size distribution of $TiAl_3$ is similar in both alloy types and the experimental conditions are the same as far as known.

The results near the walls for the Al-5Ti-1B master alloy show a similar trend towards an increase along the launder as for the Al-3Ti-0.2B alloy. The results from the centre are, on the other hand, impossible to explain without assuming that $TiAl_3$ particles are reaching the surface. The dissolution rate of $TiAl_3$ is not fast enough to bring about the observed increase in the titanium increment only 100 mm after the master alloy addition. The most likely explanation is that the vertical movement in the melt in these experiments is more pronounced than in the Al-3Ti-0.2B experiments. The question then arises why this did not also affect the distribution of the TiB_2 particles.

The questions posed by the results from the titanium measurements could possibly have been answered by metallographical analysis of the samples. Such a study combined with an investigation of improved sampling techniques for flowing melts is an interesting project for further studies of launder systems.

The measurements in the dead zone at the corner of the launder, showing a titanium increment of 135% and a boron increment of 66% at the surface, are another interesting feature in support of the particle distribution analysis. There, it was predicted that particles would become entrapped in the vortex formed in the dead zone resulting in enrichment of the melt of the constituents of the grain refiner (see Figure 5.30). The distance from the grain refiner addition point to the sampling point was 1460 mm and the average flow rate 45 mm/sec. It therefore takes the particles 32 seconds to reach the corner. Assuming the dissolution rate for $TiAl_3$ as $40\mu m/min$ as before, $TiAl_3$ particles larger than about $40\mu m$ in diameter should not be completely dissolved at this point. As there are $TiAl_3$ particles larger than this in the grain refiner (see Chapter 3) both $TiAl_3$ and TiB_2 particles are expected to enter the vortex in the dead zone. The

measurements support this. The titanium increment shows a clear indication of melt enrichment and the boron increment is also much higher than expected for a surface sample by comparison with other measurements in the launder. As previously discussed, the dead zone was omitted in the design of the second launder at Chippis partly as a result of this study.

Analysis of the LiMCA measurements are to some extent hampered by the varying inclusions count for the basic melt as shown by the results for test position 1 in Figures 6.8, 6.10, 6.12 and 6.14. The peaks in the particle count at positions 2,3 and 4 are probably $TiAl_3$ particles which have not been dissolved down to a size of less than $20\mu m$ at these points. The distance from the grain refiner addition point to these positions is 840mm so by using similar calculations as above, the time for the particles to reach these points is approx. 19 seconds. Again, using the dissolution rate of $40\mu m/min$ a layer of $13\mu m$ will dissolve from the $TiAl_3$ particles in this time. The particles must be larger than $20\mu m$ to be detectable by the LiMCA device so that the $TiAl_3$ particles in the grain refiner must be larger than about $46\mu m$ to remain detectable at these points. Such $TiAl_3$ particles are present in the master alloys as discussed in Chapter 3.

In experiment *TiB-25* the results also show an indication of particles remaining in the melt at test position 5 in addition to the signal received from the inclusions in the base metal. The particles take a shorter time to reach test position 5 than position 6 due to the shorter distance and also due to the higher flow rate at the inside of the corner as predicted by the flow analysis (see Figure 5.14). These particles are, therefore, probably also $TiAl_3$ particles remaining larger than $20\mu m$. These results can be considered to support the industrial assumed dissolution rate for $TiAl_3$, i.e. $40\mu m/min$, if the measured particles are assumed to be $TiAl_3$ as can be considered to be the most likely case. As the LiMCA measurements were always ended at position 1 no samples for metallographic tests were obtained from the LiMCA tube to support this conclusion.

There is no clear evidence in the LiMCA measurements supporting the observations from the experiments in the crucible in Chapter 4, that TiB_2 particle clusters enter the melt from the master alloys. The alloys employed in this study produced a low increase in the particle count in the crucible (1-3 K/Kg) using target additions that were approximately 5-7 times higher than in the present experiments in the launder. Therefore, the effect of clusters originating in the master alloys must be expected to be masked by the count obtained from the inclusions in the basic melt. It should be noted, however, that the LiMCA measurements after the master alloy addition point seldom reach the low value observed at position 1 at the end of each experimental run even in the final stages of the runs. It cannot be excluded, therefore, that clusters from the master alloys play a role in the observed particle count after the addition point.

The maximum probability of finding evidence of particle agglomeration in the melt is at position 8, since position 7 could not be used. This is due to the

possible cluster formation in the vortex in the dead zone and the clusters then moving into the main flow as previously discussed. There are indications of an increased particle count at position 8 as compared with position 9, especially in the second experiment using master alloy *B3/.2-A*, which gave the highest particle count in the experiments in the crucible of all the master alloys tested in the launder. The size distribution of the particles at this position also shows a tendency towards an increase. This could be the effect of clusters coming from the dead zone in the corner. Metallographic studies of samples from the LiMCA tube would be required to clarify this point as an accumulation of inclusions in the dead zone can also be considered to occur.

Further studies of particle distribution in an industrial launder system are interesting to consider. It would be necessary to have two LIMCA devices, one located before the master alloy addition point and one after the addition. The latter LiMCA would be situated only at one position in the launder in each run since the movement of the head is extremely difficult due to possible freezing of the melt in the tube. Metallographic samples could then be taken at the end of each run from the LIMCA tube to study the metallography of the detected particles. The master alloys should be selected as those giving the highest particle count in the tests in the crucible described in Chapter 4 and possibly more than one rod could be employed in order to increase the master alloy addition.

6.6 Figures

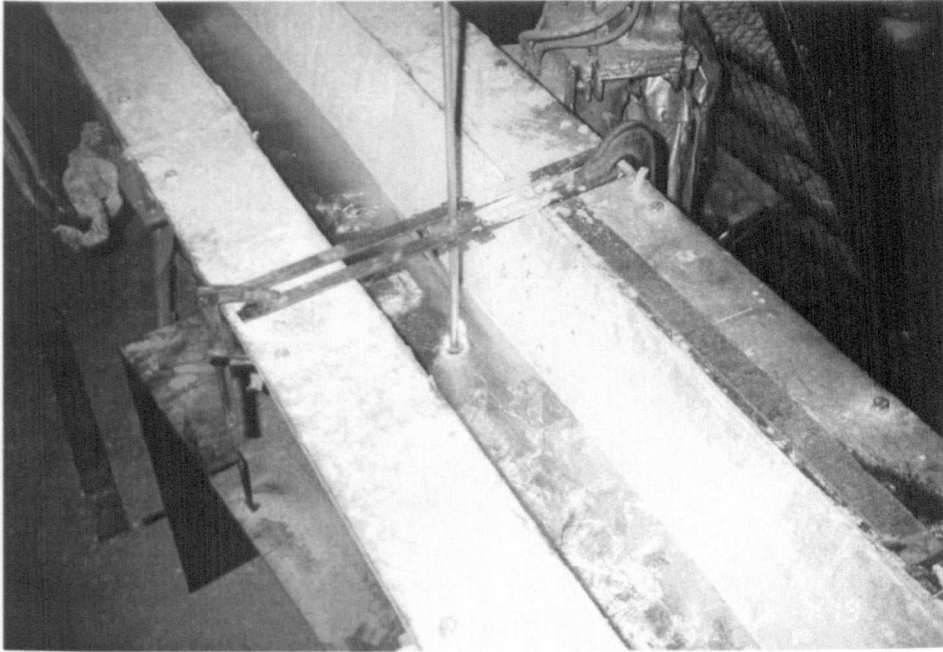


Figure 6.1: The addition point of the grain refiner rod into the transfer launder.

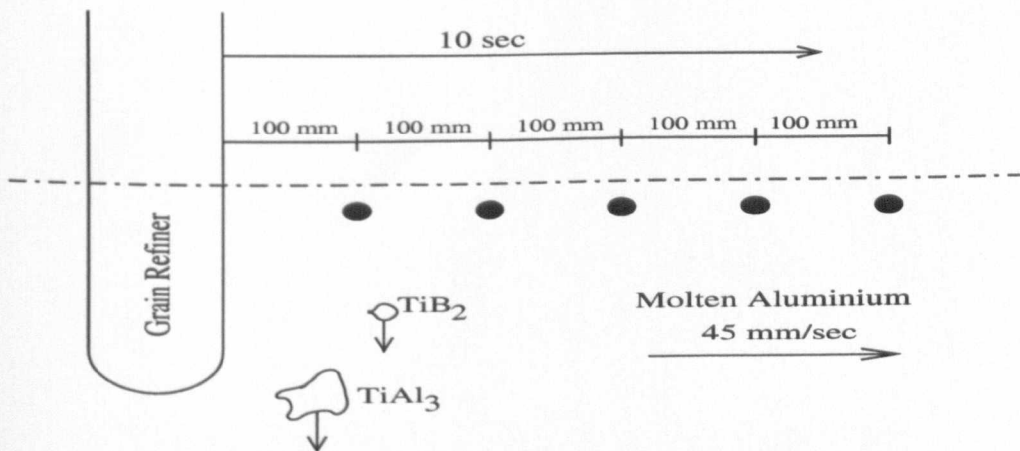


Figure 6.2: Measurement points for the chemical analysis. The samples are taken at the surface. The grain refiner is continuously added at the point of insertion.

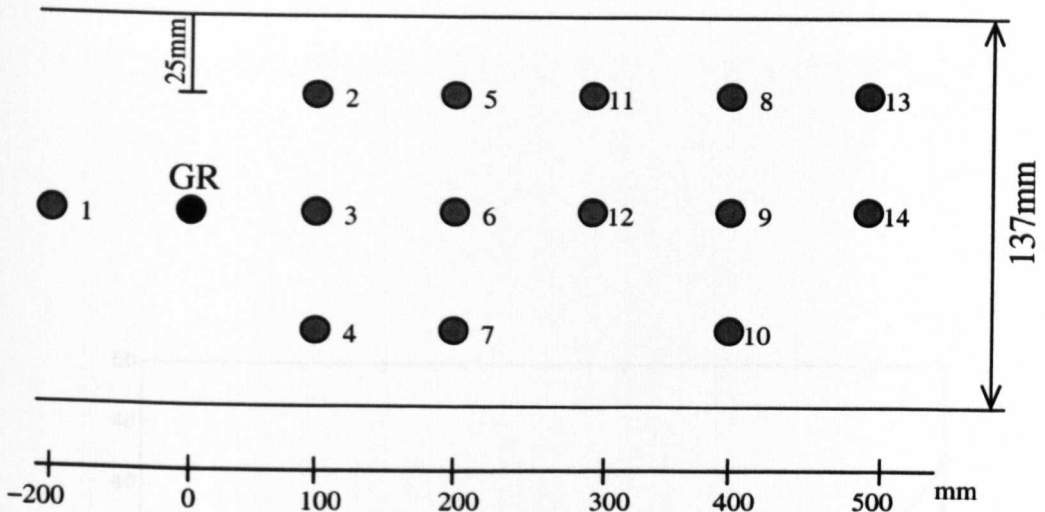


Figure 6.3: Measurement points for the chemical analysis. The samples are always taken at the surface.

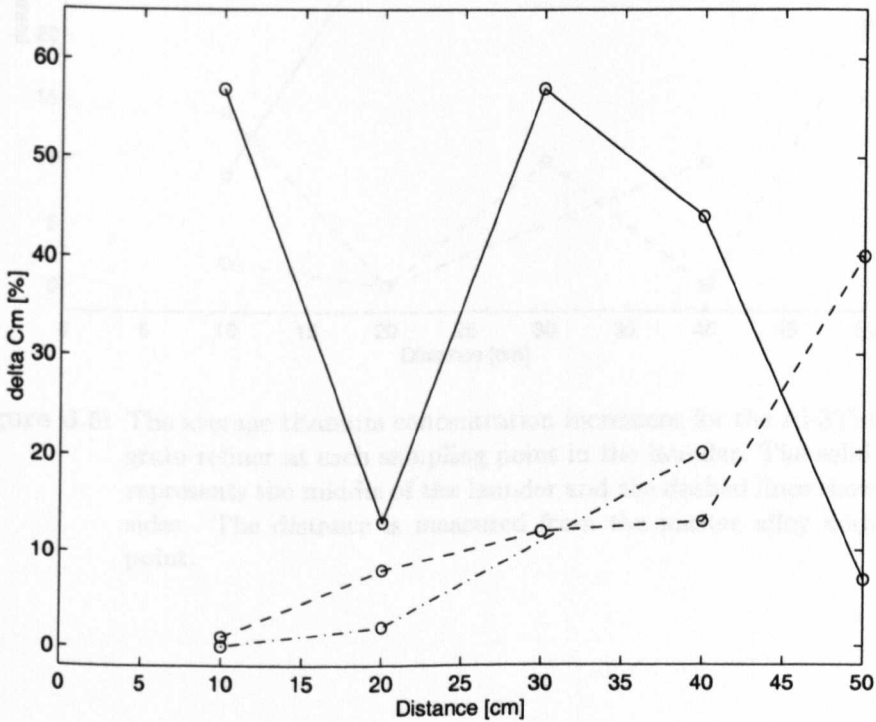


Figure 6.4: The average titanium concentration increment for the Al-5Ti-1B grain refiners at each sampling point in the launder. The solid line represents the middle of the launder and the dashed lines show the sides. The distance is measured from the master alloy addition point.

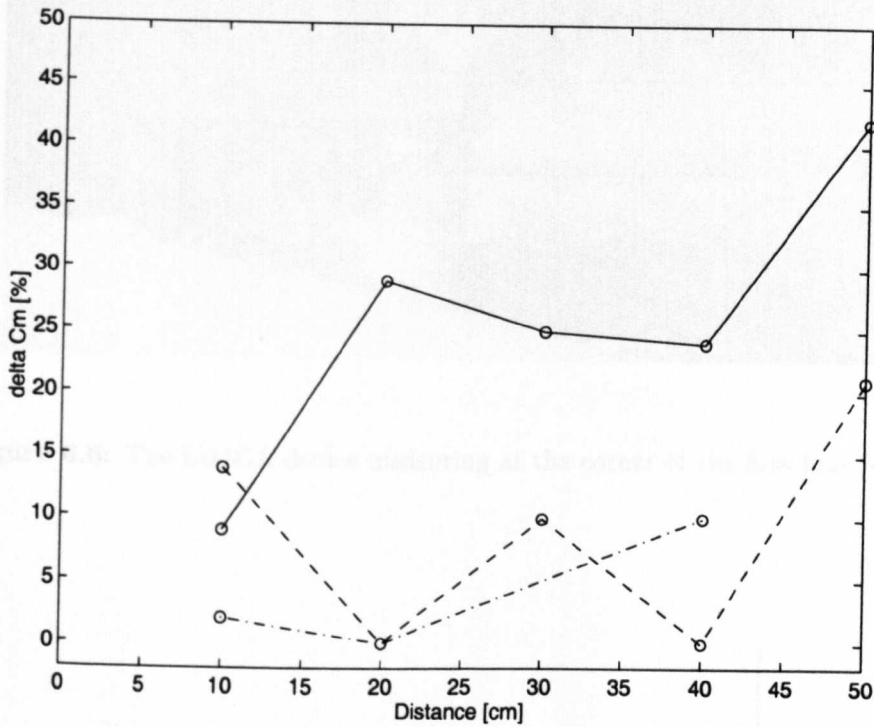


Figure 6.5: The average titanium concentration increment for the Al-3Ti-0.2B grain refiner at each sampling point in the launder. The solid line represents the middle of the launder and the dashed lines show the sides. The distance is measured from the master alloy addition point.

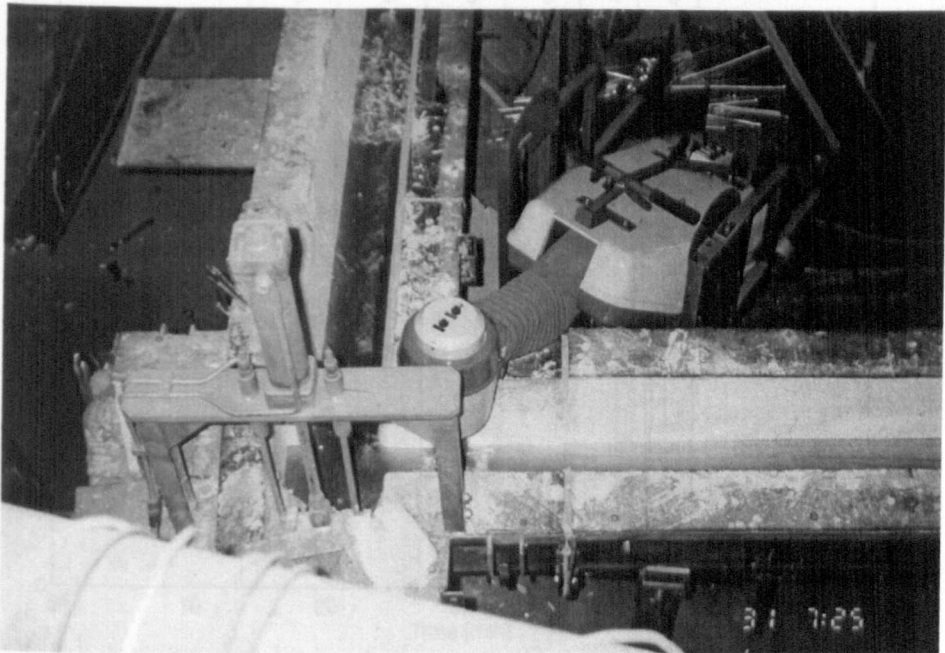


Figure 6.6: The LiMCA device measuring at the corner of the first launder.

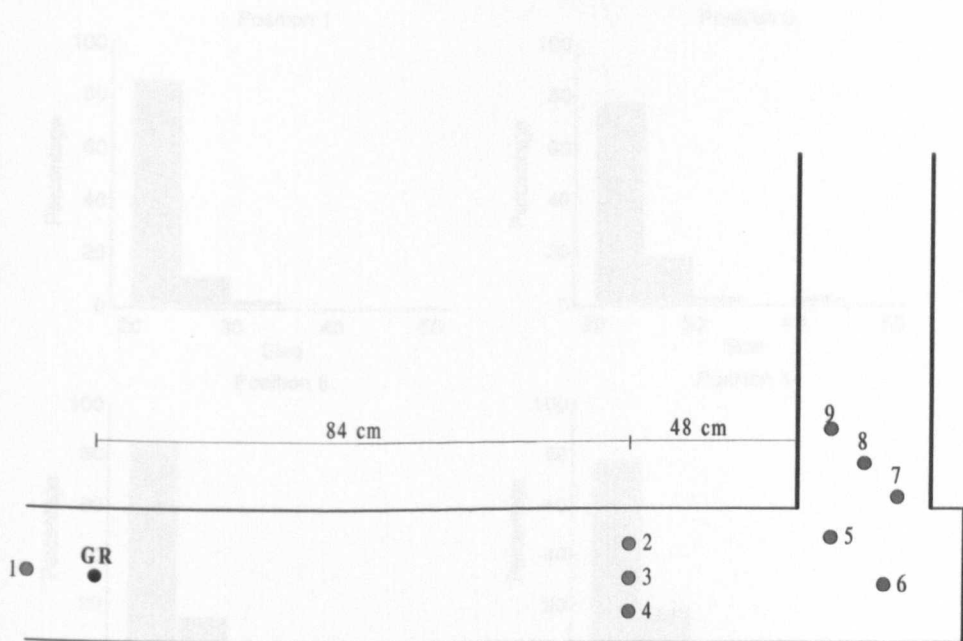


Figure 6.7: Measurement points for LiMCA. One sample for chemical analysis was taken in the corner at the right.

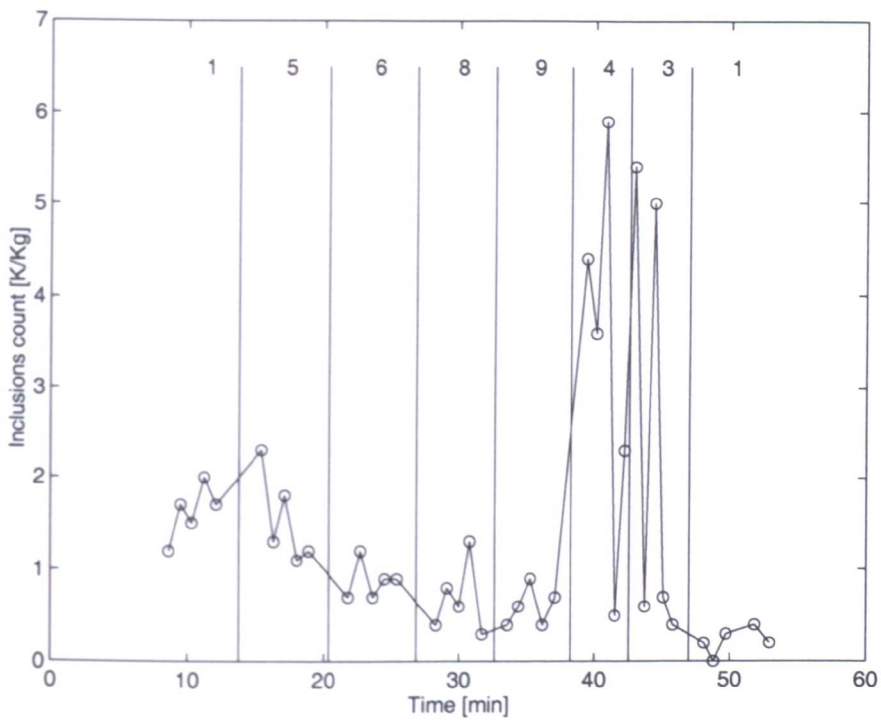


Figure 6.8: Particle count (N20) for experiment *TiB-23*. Grain refiner *B5/1-D*. The numbers refer to measurement position.

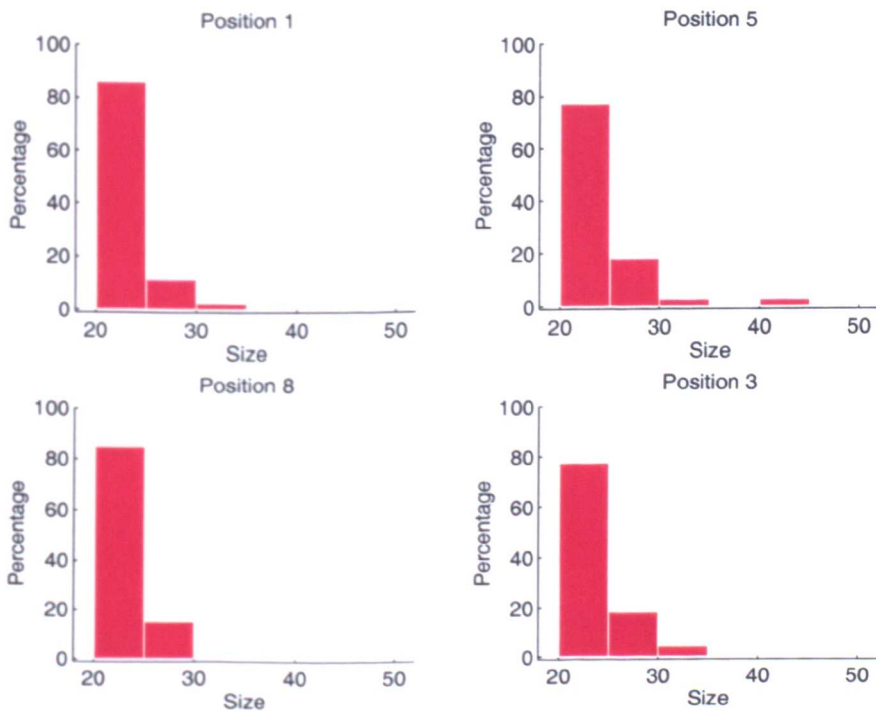


Figure 6.9: Size distribution for experiment *TiB-23*. Grain refiner *B5/1-D*. Measurement positions 1, 5, 8 and 3. The size is in μm .

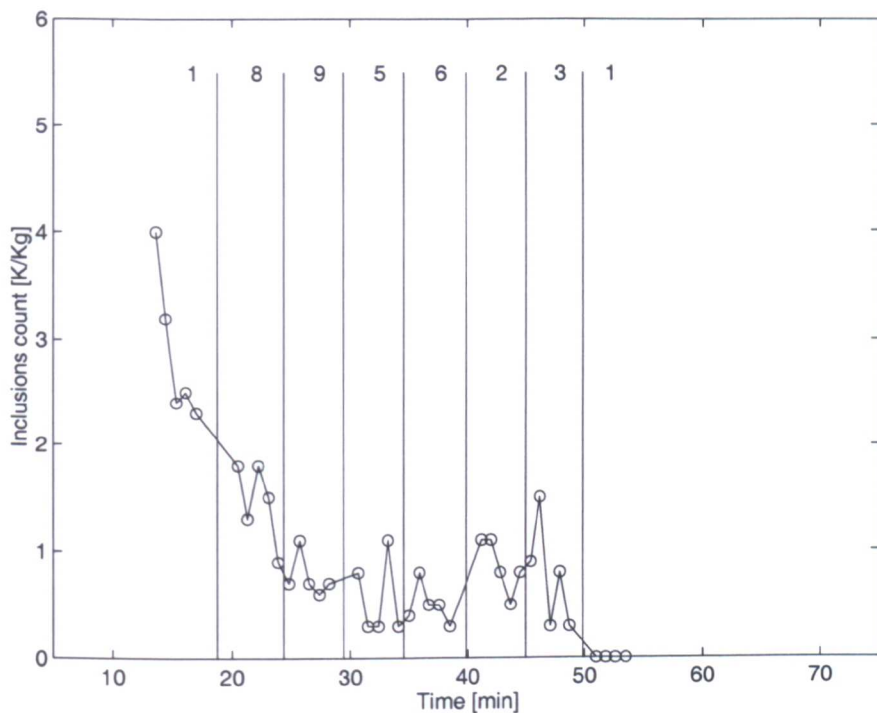


Figure 6.10: Particle count (N20) for experiment *TiB-24*. Grain refiner *B3/.2-A*. The numbers refer to measurement position.

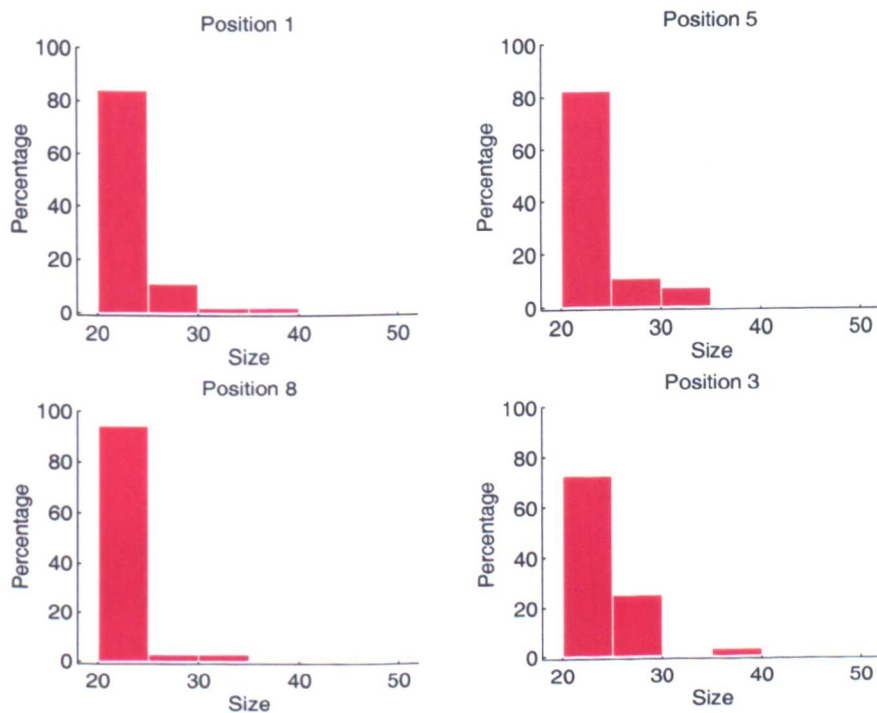


Figure 6.11: Size distribution for experiment *TiB-24*. Grain refiner *B3/.2-A*. Measurement positions 1, 5, 8 and 3. The size is in μm .

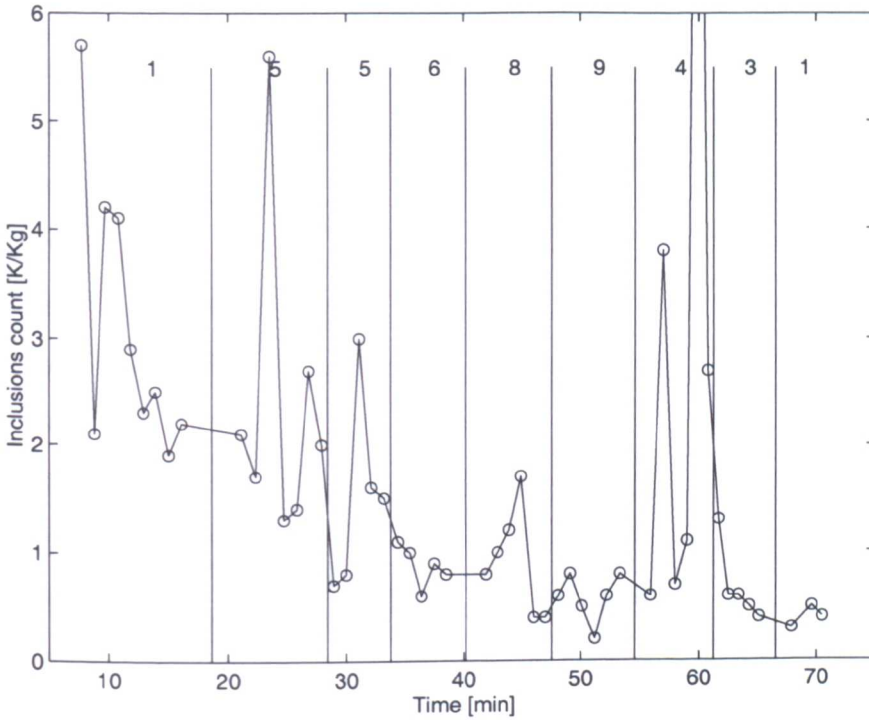


Figure 6.12: Particle count (N20) for experiment *TiB-25*. Grain refiner *B3/.2-A*. The numbers refer to measurement position.

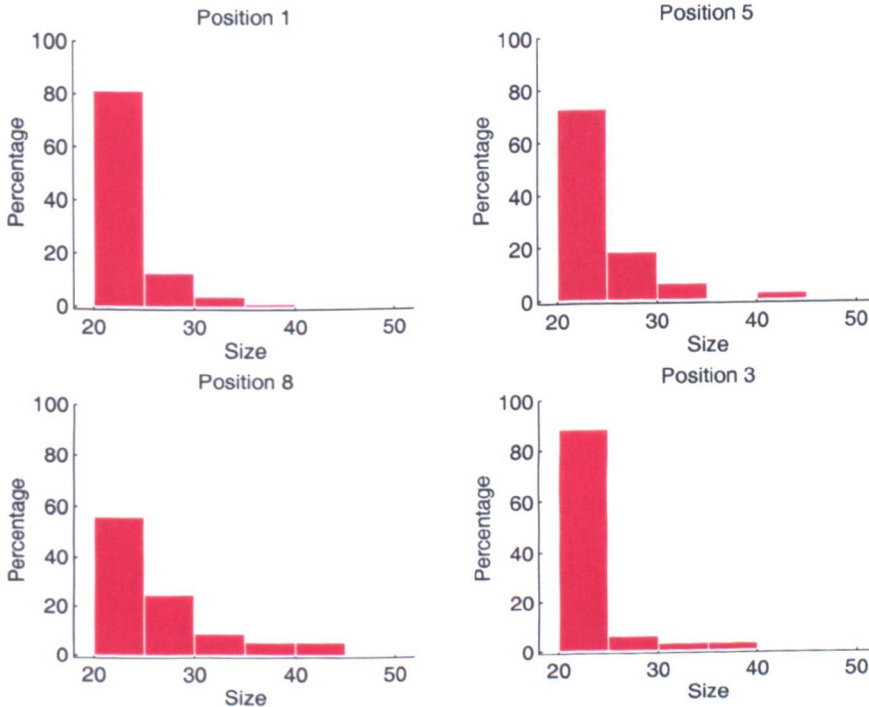


Figure 6.13: Size distribution for experiment *TiB-25*. Grain refiner *B3/.2-A*. Measurement positions 1, 5, 8 and 3. The size is in μm .

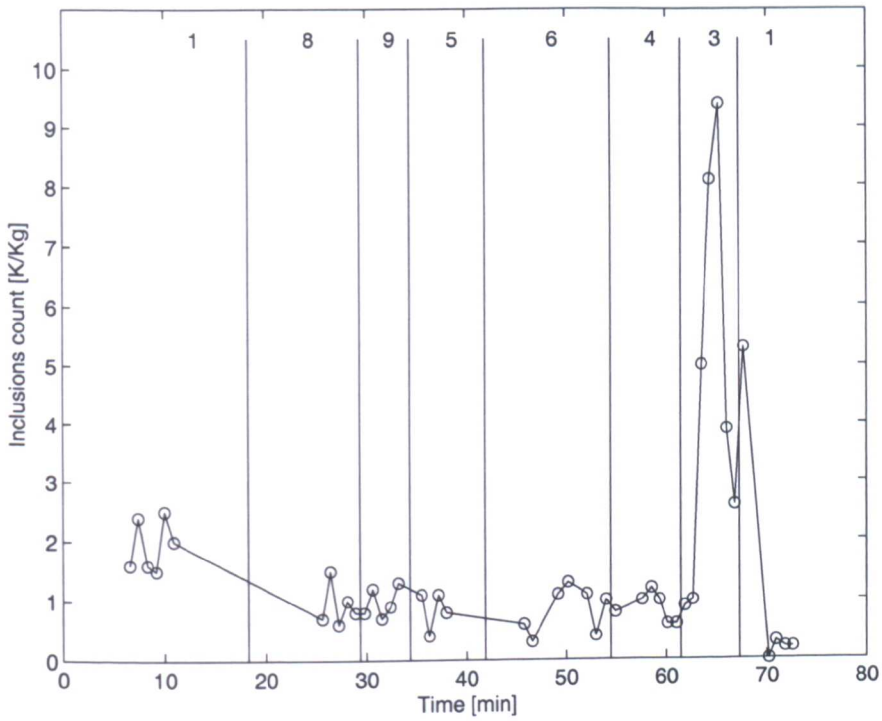


Figure 6.14: Particle count (N20) for experiment *TiB-26*. Grain refiner *B5/1-B*. The numbers refer to measurement position.

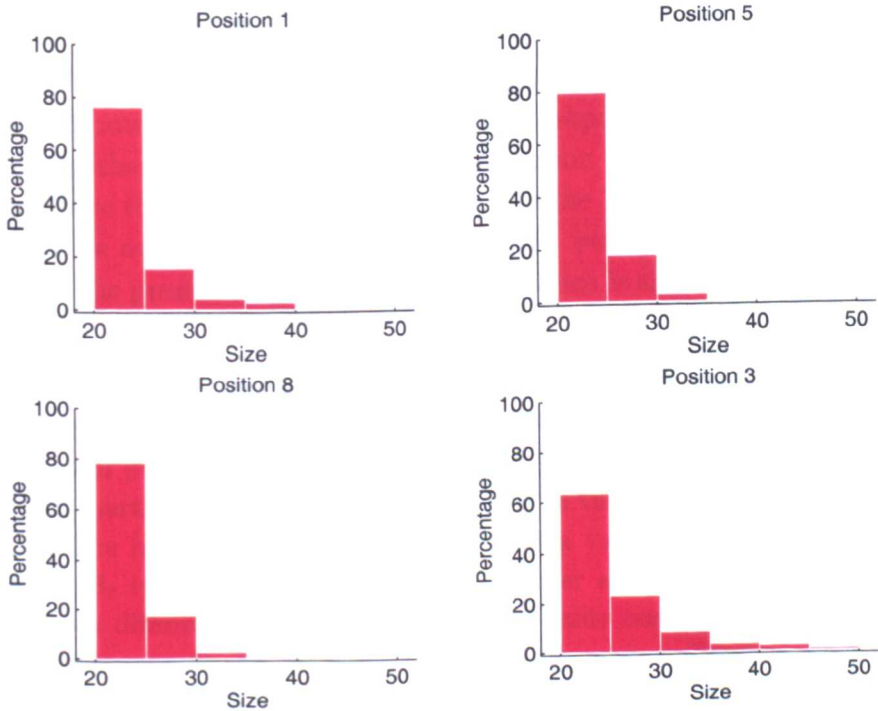


Figure 6.15: Size distribution for experiment *TiB-26*. Grain refiner *B5/1-B*. Measurement positions 1, 5, 8 and 3. The size is in μm .

Chapter 7

Conclusions

The metallographical study of different types of master alloys has clearly revealed the presence of particle clusters both in Al-Ti-C and Al-Ti-B master alloys rods. The particles forming the clusters have been shown to be insoluble or partly soluble TiC and TiB_2 particles, respectively.

EDX analysis of the TiC particle clusters show the presence of oxide, presumably aluminium oxide. It is concluded that the TiC particles are possibly held together in some way by the oxide. The largest TiC cluster found by microscopy was $50 \times 90\mu\text{m}$ and oxide strings up to $1000\mu\text{m}$ in length were detected in a high oxide Al-Ti-C master alloy. These clusters are much larger than those previously reported in the literature ($2\mu\text{m}$).

In the Al-Ti-B master alloys, the TiB_2 particle clusters contained oxygen, fluorine and potassium. It has previously been proposed that the TiB_2 particles are held together by fluoride salts. By comparison with the TiC clusters, it is suggested here that the possible role of oxide in the TiB_2 agglomeration process should not be overlooked. The size of the TiB_2 particle clusters found by microscopy in the present study was up to $20\mu\text{m}$ which is similar to that previously reported.

Al-5Ti-1B master alloys from different manufacturers showed differences in the quantity of impurities containing oxide and fluoride salts. Furthermore, the distribution of phases varied especially with respect to texturing and alignment of the TiB_2 particles. The texturing is a result of the manufacturing process for the rods. The impurities in the alloys showed a varying degree of association with the TiB_2 texture lines. The Al-Ti-C master alloys also showed texturing but the main difference was observed in their oxide content. It was concluded that the difference in the microstructure of the master alloys would probably result in differences being observed in the quantity of clusters when the alloys are dissolved in an aluminium melt.

The experimental set-up which was developed for the LiMCA tests in a cru-

cible proved to be a suitable tool for comparing the behaviour of different master alloys with respect to particle cluster formation. The particle count as measured by LiMCA after the master alloy addition can be divided into three regions with respect to time. Immediately after addition of the master alloys into commercially pure aluminium melt, a peak response is obtained with the peak lasting for 1-2 minutes. For the Al-Ti master alloy the particle count then returned to the former baseline observed prior to the addition. The peak response was attributed to the soluble $TiAl_3$ particles in the alloys. For the Al-Ti-C and Al-Ti-B master alloys, on the other hand, the particle count did not return to the baseline after the peak response but remained at some higher value. This value or step response varied between the types of these master alloys and it was concluded that the increase in the particle count was a function of the quantity of clusters of TiC and TiB_2 particles, respectively, introduced into the melt by the master alloys. The size of the clusters as measured by LiMCA was in the range of 20-100 μ m. These clusters are, therefore, much larger than those generally observed by microscopy of master alloys. The presence of individual larger clusters cannot be excluded but they do not appear in a sufficient quantity to be noted in the LiMCA results. The percentage of the total TiB_2 and TiC volume additions to the melt that is found in the clusters, as measured after the step response, is less than 3%.

The quantity of clusters determined by the step response can be related to the microstructure of the master alloy rods. Thus, the Al-5Ti-1B master alloy containing the largest quantity of impurities gave the highest step response in the particle count. The same type of alloy produced with a textured TiB_2 distribution and with the impurities concentrated along the TiB_2 lines gave the second highest step. An alloy with a similar TiB_2 texturing, but a more random distribution of the impurities, gave much lower results. For the case of the Al-3Ti-0.15C master alloys, an increased oxide content gave a higher step response in the particle count. These observations are especially significant in showing that the experimental method can be employed for testing the quality of master alloys with respect to clusters present in the alloy rods and, therefore, for improving their quality.

The correlation of the microstructure and the cluster content of the master alloy rods supports the conclusion that oxide plays an important role in the cluster formation in the Al-Ti-C master alloy rods and the impurities containing oxide and fluoride salts in the Al-Ti-B rods.

The LiMCA tests also confirm that further agglomeration of the clusters and particles occurs in the melt after the step response both for Al-Ti-C and Al-Ti-B master alloys. The rate of increase in the particle count was measured up to 0.8 (K/Kg)/min. The measured rate values are deceptive, however, since

there is no way of estimating the effect of the rate of settling on the results. No correlation could be found between the observed rate of further agglomeration and the microstructure of the master alloys. Further studies of this process would require the effects of settling and the particle collision rate to be included.

A reduction in the rate of stirring of the melt in the LiMCA experiments reduced the measured rate of further agglomeration in the melt. The shift in the particle size distribution towards smaller particles at the lower stirrer speed indicates that increased settling plays an important part in the lower agglomeration rate observed with reduced stirring. Lower particle collision rate at the low stirrer speed can also be of importance.

The use of computational fluid dynamics techniques as an important tool in the modelling of flow conditions and particle distribution in aluminium melt in launders has been confirmed. Two launder designs were modelled. In the first design the effect of vortex formation in the dead-zone at a corner of the launder was demonstrated. The probability of particle trapping and melt enrichment in the vortex zone was confirmed and an increased agglomeration rate in the melt in that region was predicted. The results influenced the second modified launder design, where the dead-zone at the corner was omitted. Particle dispersion from a point source simulating the probable dissolution of a master alloy rod was also modelled. An effective distribution was achieved within 1000mm from the source of particle introduction. The results also predict that a fully dispersed particle distribution is achieved before the large $TiAl_3$ particles are dissolved. The analysis showed the effect of gravity on the particle distribution with very few particles reaching the top surface of the melt. A high rate of particle collisions with the walls of the launder was also observed with the conclusion being made that the surface conditions of the launders could play a role in the particle distribution behaviour.

Finally, the preliminary LiMCA measurements in the first launder and the chemical analysis of samples taken from the flowing melt generally support the flow and particle distribution modelling. The measurements point towards melt enrichment in the corner vortex zone and some indications of an increased agglomerate concentration in the melt after the corner were also obtained.

Chapter 8

Future work

The TiC and TiB_2 particle clusters found to be present in master alloy rods both by microscopy and by LiMCA tests are an interesting subject for further study. Oxide and fluoride salts have been proposed as some form of binders for the particles in the clusters but the binding mechanism is not known. The oxide is presumably aluminium oxide and should be in solid form in the melt. The fluoride salts, on the other hand, are probably in fluid form. A further study of the actual forces involved in the binding mechanism and the strength of the bonds is a most interesting subject for further study.

The individual TiC and TiB_2 particles are hard substances. The question then arises whether the particle clusters are also hard entities or if the bonding is weak enough for them to crumble when the melt is filtered or later in the solid metal under an applied force such as in the metal forming operations. This is in effect an addition to the above study of the binding mechanism.

The quantity of clusters determined by the step response in the LiMCA particle count can be related to the microstructure of the master alloys. Further correlation of the microstructure with the LiMCA measurements can possibly be combined with measurements of the grain refining efficiency of the master alloys. This presents another important subject for future work.

The rate of agglomeration of particles and clusters in the aluminium melt does not appear to be directly related to the microstructure of the master alloys. For further studies of this process the effect of the particle collision rate and particle settling must be introduced into the analysis.

The use of computational fluid dynamics techniques for flow and particle modelling will undoubtedly increase in the future. With an increased computer power more complicated flow problems can be solved. This can include the effect of particle collisions with the walls of the launders using different sticking factors and also the dissolution kinetics of the $TiAl_3$ particles. The effect of equipment such as filters and inline degassing units often present in the launder could also

be modelled.

Finally, LiMCA measurements of the master alloy addition in launders offers an interesting scope for further work. This requires the use of two LiMCA devices simultaneously. One is necessary to measure the change in the particle content of the melt entering the launder as this will change during the casting process. The second LiMCA can then be employed to monitor the particle distribution along the launder. Thus, the same volume element of melt can be compared at different locations in the launder by allowing for the flow rate. Using this method all changes in the particle distribution along the launder could possibly be monitored.

Bibliography

- [1] M.M. Ali and A.A. Mostafa. Improvement of the aluminium cell lining behaviour by using SiC. In *Light Metals*, pages 273–278, 1997.
- [2] T. Abel Engh. *Principles of Metal Refining*. Oxford University Press, Oxford, 1992.
- [3] M.W. Meredith, A.L. Greer, P.V. Evans, and R.G. Hammertonm. The generation of Al-Fe dilute aluminium alloys with different grain refining additions. In *Light Metals*, pages 811–817, 1999.
- [4] J.R. Guttery and W. Evans. A new generation of fluxing in aluminium melting and holding furnaces. In *Light Metals*, 1994.
- [5] I. Ventre and J. Rolland. Replacing ceramic foam filtration by an alpur s1000 in-line treatment : a winning bet at cableries de lens. In *Light Metals*, pages 1245–1251, 1995.
- [6] R.M. Smith, P. Flisakowsky, A. Henry, and I. Ventre. Process improvements obtained through the unstationation and use of the sx-3000 degassing unit. In *Light Metals*, pages 1223–1226, 1995.
- [7] M.M. Niedzinski, E.M. Williams, D.D. Smith, and L.S. Aubrey. Staged filtration evaluation at an aircraft plate and sheet manufacturer. In *Light Metals*, pages 1019–1030, 1999.
- [8] M. Syvertsen, F. Frisvold, T.A. Engh, and D.S. Voss. Developement of compact deep bed filter for aluminium. In *Light Metals*, pages 1049–1055, 1999.
- [9] M.M. Guzvoski, G.K. Sigworth, and D.A. Granger. *Metallurgical Transactions A*, 18A:603–619, 1987.
- [10] D.G. McCartney. Grain refining of aluminium and its alloys using inoculants. *International Materials Review*, 34:247–260, 1989.
- [11] M.A. Kearns, S.R. Thistlethwaite, and P.S. Cooper. Recent advances in understanding the mechanism of aluminum grain refinement by TiBAl master alloys. In *Light Metals*, pages 713–720, 1996.
- [12] I. Maxwell and A. Hellawell. *Acta Metall*, 23:229–237, 1975.

- [13] P. Schumacher and A.L. Greer. High-resolution transmission electron microscopy of grain-refining particles in amorphous aluminium alloys. In *Light Metals*, page 745, 1996.
- [14] D.A. Granger. In *Refining and alloying of liquid aluminium and ferro-alloys*, pages 231–244. Norwegian Institute of Technology, 1985.
- [15] A. Hellawell. In *Solidification and Casting of Metals*, pages 161–168. The Metals Society, 1979.
- [16] L.F. Mondolfo. *Aluminum alloys, Structure & Properties*. Butterworth, London, UK, 1976.
- [17] S.R. Thistlethwaite, D. Hadlet, and J.C. Hoff. In *Light Metals*, pages 1169–1178, 1985.
- [18] G.T. Campbell, S.A. Danilak, S.R. Thistlewaite, and P. Fisher. In *Light Metals*, pages 831–836, 1992.
- [19] C.D. Mayes, D.G. McCartney, and G.J. Tatlock. Observations on the microstructure and performance of an Al-Ti-C grain-refining master alloy. *Materials Science and Engineering*, A188:283–290, 1994.
- [20] A.J. Whitehead, S.A. Danilak, and D.A. Granger. Development of a commercial Al-3Ti-0.15C grain refining master alloy. In *Light Metals*, pages 785–793, 1997.
- [21] P. Hoefs, A.H. Green, P.C. van Wiggeren, W. Schneider, and D. Brandner. Development of an improved AlTiC master alloy for the grain refining of aluminium. In *Light Metals*, pages 777–784, 1997.
- [22] A. Cibula. *J. Inst. Met.*, 76:321–360, 1949–50.
- [23] London & Scandinavian Metals Ltd (LSM), Private communications, 1997–1999., 1997.
- [24] M.S. Lee, B.S. Terry, and P. Grieveson. Interfacial phenomena in the reaction of Al-B, Al-Ti-B and Al-Zr-B alloys with $kf - al_3$ and $naf - alf_3$ melts. *Metallurgical Transactions B*, 24B:947–953, 1993.
- [25] A.M. Bunn. *Grain refinement in aluminium alloys*. PhD thesis, University of Cambridge, 1998.
- [26] J.C. Bailey, F.T. Coyle, and W.G. Lidman. Size and distribution of TiB₂ particles in titanium–boron–aluminum grain refiner alloys. In *Annual meeting of the metallurgical Society, Cast shop technology IV*, Phoenix, AR, USA, 1988.
- [27] Th. Gudmundsson. *Agglomeration of TiB₂ particles in liquid aluminium*. PhD thesis, University of Nottingham, 1996.

- [28] Kirk-Othmer, *Encyclopedia of chemical technology*, volume 23. John Wiley & Sons, 1983.
- [29] D. Sampath, P.G.J. Flick, J. Pool, W. Boender, and W. van Rijswijk. Sampling of aluminium melts and detection of nonmetallic inclusions using LAIS. In *Light Metals*, pages 817–821, 1996.
- [30] ARDC-SÉCAL. *Determination of PoDFA inclusions concentrates*, 1990.
- [31] Alusuisse - Lonza Technical Centre, Switzerland, Private communications., 1996-1998.
- [32] G.T. Campbell and S.A. Sutker. Effect of various polishing techniques on the evaluation of TiB_2 distribution in titanium-boron-aluminum grain refiners. In *Light Metals*, pages 739–747, 1987.
- [33] D. Doutre, B. Gariépy, J.P. Martin, and G. Dubé. Aluminium cleanliness monitoring: Methods and applications in process development and quality control. In *Light Metals*, pages 1179–1195, 1985.
- [34] ABB-Bomem Inc., <http://www.bomem.com>, 2000.
- [35] P.S. Mohanty, R.I.L. Guthrie, and J.E. Gruzleski. Studies on the fading behavior of Al-Ti-B master alloys and grain refinement mechanism using LiMCA. In *Light Metals*, pages 859–868, 1995.
- [36] E.U. Comerford and G. Béland. Extended user's experience with the LiMCA technology to continuously monitor and improve can body stock quality. In *Light Metals*, pages 1083–1091, 1994.
- [37] C. Dupuis and R. Dumont. The impact of LiMCA technology on the optimization of metal cleanliness. In *Light Metals*, pages 997–1002, 1993.
- [38] J-P. Martin and F. Painchaud. On-line metal cleanliness determination in molten aluminum alloys using the LiMCA II analyser. In *Light Metals*, pages 915–920, 1994.
- [39] L.A. Strom, J.W. Black, R.I.L. Guthrie, and C. Tian. Non-ferrous alloy filtration efficiency study of fully sintered reticulated ceramics utilizing LiMCA and LAIS. In E.R. Cutahall, editor, *Light Metals*, pages 1092–1100, 1991.
- [40] N.J. Keegan, W. Schneider, H.P. Krug, and V. Dopp. Evaluation of the efficiency of ceramic foam and bonded particle cartridge filtration systems. In *Light Metals*, pages 973–982, 1997.
- [41] N.J. Keegan, W. Schneider, and H.P. Krug. Evaluation of the efficiency of fine pore ceramic foam filters. In *Light Metals*, pages 1031–1040, 1999.
- [42] G. Parker, T. Williams, and J. Black. Production scale evaluation of a new design ceramic foam filter. In *Light Metals*, pages 1057–1062, 1999.

- [43] R.W. DeBlois and C.P. Bean. Counting and sizing of submicron particles by the resistive pulse technique. *The review of scientific instruments*, 41:909–916, July 1970.
- [44] F. Painchaud. Prediction of the reproducibility between data from two LiMCA II analysers operated side by side, 1994.
- [45] *Encyclopedia of Chemical Technology, 3rd edition*, volume 23. John Wiley, 1983.
- [46] BOMEM Inc. *LiMCA II instrument, Installation & training, Technical presentation*, 1995.
- [47] J-P. Martin and R.I.L. Guthrie. Settling of inclusions in casting furnaces. In *Second Australian Asian Pacific course and conference on aluminium melt treatment and casting*, pages 21:1–21:24, 1–4 July 1991.
- [48] E.J. Asbjornsson, D.G. McCartney, and T.I. Sigfusson. Melting and dissolution of master alloys, Unpublished results, 1998.
- [49] J.M. Drezet. *Direct chill and electromagnetic casting of aluminium alloys: Thermomechanical effects and solidification aspects*. PhD thesis, EPFL, 1996.
- [50] J. Szekely. *Fluid flow phenomena in metals processing*. Academic Press, Inc. (London) LTD., London, 1979.
- [51] J.A. Roberson and C.T. Crowe. *Engineering fluid mechanics*. Houghton Mifflin Company, USA, 1990.
- [52] S. Joo and R.I.L. Guthrie. Inclusion behaviour and heat-transfer phenomena in steelmaking tundish operations: Part 1. aqueous modeling. *Metallurgical Transactions B*, 24B:755–765, October 1993.
- [53] S. Joo and R.I.L. Guthrie. Inclusion behaviour and heat-transfer phenomena in steelmaking tundish operations: Part 2. mathematical model for liquid steel in tundishes. *Metallurgical Transactions B*, 24B:767–777, October 1993.
- [54] S. Joo and R.I.L. Guthrie. Inclusion behaviour and heat-transfer phenomena in steelmaking tundish operations: Part 3. computational approach to tundish design. *Metallurgical Transactions B*, 24B:777–788, October 1993.
- [55] J. Szekely and N. El-Kaddah. Turbulent recirculating flow in metals processing. In *International Seminar on Refining and Alloying of Liquid Aluminium and Ferro-Alloys*, pages 249–266, Trondheim Norway, August 26–28 1985.
- [56] J. Szekely and O.J. Ilegbusi. *The physical and mathematical modeling of tundish operations*. Springer-Verlag, Berlin, 1989.

- [57] F. Shen, J.M. Khodadadi, S.J. Pien, and X.K. Lan. Mathematical and physical modeling studies of molten aluminum in a tundish. *Metallurgical Transactions B*, 25B:669–680, October 1994.
- [58] H.K. Versteeg and W. Malalasekera. *An introduction to computational fluid dynamics. The finite volume method*. Longman Scientific & Technical, England, 1995.
- [59] F.A. Acosta B, A.H. Castillejos E, E. Ruis A., M. Méndez N, and J.C. Escobedo B. A study of the role of fluid velocity and particle size on deep bed filtration behaviour. In *Light Metals*, pages 823–830, 1996.
- [60] International Aluminium Institute, <http://www.world-aluminium.org>, 2000.
- [61] J.O Goldstein et.al. *Scanning Electron Microscopy and X-ray analysis*. Plenum Press, New York, 1984.
- [62] *Metals Handbook. Ninth Edition. Volume 9, Metallography and Microstructure*. ASM International, Metals Park, Ohio, 1985.
- [63] J.M. Coulson and J.F. Richardson. *Chemical Engineering, 4rd edition*, volume 2. Pergamon Press, 1989.
- [64] AEA Technology. *CFX 4.1. User guide*, 1995.
- [65] AEA Technology. *CFX 4.1. Flow solver User guide*, 1995.
- [66] The National Energy Authority of Iceland (Orkustofnun), Private communications, 1996., 1996.

Appendix A

Supplement to Chapter 4

Table A.1: Chemical analysis of the base metal in the experiments presented in Chapter 4 before addition of the master alloy portions. The balance can be considered to be aluminium.

<i>Experi- ment</i>	<i>Element (wt %)</i>									
	Si	Fe	Cu	Mn	Mg	Cr	Ni	Zn	Ti	B
<i>Ti-1</i>	.049	.06	.0006	.0006	.0005	.0005	.0036	.0037	.0048	.0003
<i>Ti-2</i>	.043	.07	.0003	.0006	.0003	.0016	.0041	.0033	.0021	.0002
<i>TiC-1</i>	.048	.07	.0003	.0007	.0003	.0015	.0042	.0033	.0047	.0002
<i>TiC-2</i>	.048	.07	.0003	.0006	.0003	.0013	.0040	.0033	.0048	.0002
<i>TiC-3</i>	.052	.08	.0004	.0007	.0003	.0015	.0044	.0040	.0045	.0002
<i>TiC-4</i>	.048	.07	.0003	.0011	.0003	.0013	.0051	.0033	.0038	.0004
<i>TiC-5</i>	.042	.06	.0002	.0006	.0007	.0013	.0042	.0033	.0052	.0003
<i>TiB-1</i>	.06	.08	.0003	.0009	.0002	.0008	.0044	.0044	.0086	.0016
<i>TiB-2</i>	.053	.12	.0006	.0012	.0004	.0010	.0039	.0036	.0054	.0007
<i>TiB-3</i>	.052	.11	.0012	.0019	.0003	.0015	.0045	.0076	.0033	.0005
<i>TiB-4</i>	.042	.06	.0002	.0007	.0003	.0006	.0035	.0033	.0043	.0002
<i>TiB-5</i>	.043	.07	.0003	.0007	.0003	.0007	.0037	.0032	.0052	.0004
<i>TiB-6</i>	.043	.06	.0002	.0007	.0003	.0008	.0037	.0032	.0062	.0006
<i>TiB-7</i>	.042	.06	.0002	.0007	.0002	.0007	.0037	.0033	.0061	.0005
<i>TiB-8</i>	.06	.09	.0003	.0011	.0003	.0025	.0051	.0044	.0032	.0002
<i>TiB-9</i>	.054	.08	.0003	.0010	.0002	.0010	.0043	.0042	.011	.0015
<i>TiB-10</i>	.054	.09	.0003	.0010	.0002	.0008	.0044	.0042	.0049	.0002
<i>TiB-11</i>	.042	.07	.0003	.0010	.0003	.0010	.0042	.0042	.0049	.0004
<i>TiB-12</i>	.042	.07	.0003	.0006	.0002	.0007	.0037	.0033	.0044	.0005

Table A.2: The additions in experiments *Ti-1* and *Ti-2*. Grain refiner Al-6Ti.

Experiment	Addition no.	Time of addition (min)	Addition weight (g)	Ti content	
				target (wt %)	measured (wt %)
<i>Ti-1</i>	1	24	37.2	0.03	
	2	62	37.4	0.06	
	3	80	37.1	0.09	
	4	123	38.3	0.12	0.12
	5	137	36.5	0.15	
	6	145	36.5	0.18	
	7	160	38.2	0.21	0.20
	8	189	38.0	0.24	
	9	200	36.9	0.27	
	10	255	38.3	0.30	0.30
<i>Ti-2</i>	1	12	190.5	0.15	
	2	43	75.4	0.21	
	3	60	37.7	0.24	0.24
	4	86	38.0	0.27	0.25
	5	115	38.5	0.30	0.29

Table A.3: The additions in experiments *TiC-1* and *TiC-2*. Grain refiner Al-6Ti-0.03C.

Experiment	Addition no.	Time of addition (min)	Addition weight (g)	Ti content	
				target (wt %)	measured (wt %)
<i>TiC-1</i>	1	20	65.7	0.05	.07
<i>TiC-2</i>	1	20	64.3	0.05	
	2	40	66.9	0.10	
	3	60	69.4	0.15	
	4	80	69.7	0.20	
	5	100	67.5	0.25	0.26

Table A.4: The additions in experiments *TiC-3*, *TiC-4* and *TiC-5*. Grain refiner Al-3Ti-0.15C.

Experiment	Master alloy	Addition no.	Time of addition (min)	Addition weight (g)	Ti content	
					target (wt %)	measured (wt %)
<i>TiC-3</i>	C3/.15-A	1	20		0.035	
		2	40		0.070	
		3	60		0.105	
		4	80		0.140	
		5	100		0.175	0.163
<i>TiC-4</i>	C3/.15-A	1	20	89.1	0.035	0.039
<i>TiC-5</i>	C3/.15-B	1	20	90.1	0.035	0.039

Table A.5: Chemical analysis of each melt in experiments *TiB-1* to *TiB-10* after the last addition of the Al-Ti-B master alloy portions. The balance is aluminium.

Experiment	Element (wt %)									
	Si	Fe	Cu	Mn	Mg	Cr	Ni	Zn	Ti	B
<i>TiB-1</i>	.053	.09	< .001	< .001	< .001	< .001	.004	.004	.035	.0031
<i>TiB-2</i>	.051	.13	< .001	< .001	.001	.001	.004	.004	.17	.026
<i>TiB-3</i>	.050	.11	.001	.001	.001	.001	.004	.008	.18	.31
<i>TiB-4</i>	.045	.07	.0004	.0003	.0004	.0006	.0035	.0045	.17	.027
<i>TiB-5</i>	.045	.07	.0004	.0003	.0003	.0006	.0035	.0046	.16	.026
<i>TiB-6</i>	.046	.07	.0003	.0005	.0003	.0008	.0036	.0045	.16	.025
<i>TiB-7</i>	.045	.07	.0003	.0002	.0003	.0006	.0035	.0040	.14	.018
<i>TiB-8</i>	.054	.09	< .001	< .001	.001	.003	.005	.005	.16	.024
<i>TiB-9</i>	.055	.09	< .001	< .001	< .001	.001	.004	.004	.14	.018
<i>TiB-10</i>	.052	.09	< .001	< .001	.001	.001	.004	.004	.050	.0042

Table A.6: The additions in experiments *TiB-1*, *TiB-2* and *TiB-3*. Grain refiner Al-5Ti-1B.

Experiment	Master alloy	Addition no.	Time of addition (min)	Addition weight (g)	Ti content	
					target (wt %)	measured (wt %)
<i>TiB-1</i>	B5/1-B	1	25	30.1	0.02	
		2	33	30.7	0.04	.027
<i>TiB-2</i>	B5/1-B	1	25	302.7	0.20	.16
<i>TiB-3</i>	B5/1-B	1	25	306.1	0.20	.17

Table A.7: The additions in experiments *TiB-4*, *TiB-5*, *TiB-6* and *TiB-7*.
Grain refiner Al-5Ti-1B.

Experiment	Master alloy	Addition no.	Time of addition (min)	Addition weight (g)	Ti content	
					target (wt %)	measured (wt %)
<i>TiB-4</i>	B5/1-D	1	20	60.8	0.035	
		2	40	61.1	0.070	
		3	60	61.0	0.105	
		4	80	60.9	0.14	
		5	100	61.7	0.175	0.17
<i>TiB-5</i>	B5/1-C	1	20	60.6	0.035	
		2	40	60.9	0.070	
		3	60	61.3	0.105	
		4	80	61.6	0.14	
		5	100	60.9	0.175	0.15
<i>TiB-6</i>	B5/1-B	1	20	60.0	0.035	
		2	40	60.9	0.070	
		3	60	60.9	0.105	
		4	80	60.7	0.14	
		5	100	61.5	0.175	0.15
<i>TiB-7</i>	B5/1-A	1	20	60.3	0.035	
		2	40	60.8	0.070	
		3	60	60.9	0.105	
		4	80	61.0	0.14	
		5	100	60.2	0.175	0.13

Table A.8: The additions in experiments *TiB-8*, *TiB-9* and *TiB-10*. Grain refiner Al-5Ti-1B.

Experiment	Master alloy	Addition no.	Time of addition (min)	Addition weight (g)	Ti content	
					target (wt %)	measured (wt %)
<i>TiB-8</i>	B5/1-B	1	20	60.0	0.04	
		2	40	59.8	0.08	
		3	60	60.5	0.12	
		4	80	60.9	0.16	
		5	100	61.7	0.20	0.16
<i>TiB-9</i>	B5/1-A	1	20	58.1	0.04	
		2	40	60.3	0.08	
		3	60	58.3	0.12	
		4	80	58.4	0.16	
		5	100	59.0	0.20	0.13
<i>TiB-10</i>	B5/1-C	1	20	59.4	0.04	
		2	40	61.0	0.08	0.05

Table A.9: The additions in experiments *TiB-11*. Grain refiner Al-3Ti-0.2B.

Experiment	Master alloy	Addition no.	Time of addition (min)	Addition weight (g)	Ti content	
					target (wt %)	measured (wt %)
<i>TiB-11</i>	B3/.2-A	1	32	51.3	0.02	
		2	41	52.7	0.04	
		3	49	50.7	0.06	
		4	72	51.6	0.08	0.078
		5	89	51.1	0.10	
		6	130	51.3	0.12	0.11
		7	138	51.2	0.14	
		8	150	52.5	0.16	
		9	194	103.0	0.20	0.198

Appendix B

Supplement to Chapter 6

Table B.1: Measured titanium concentration in experiment *TiB-21*.

Position	Distance	C _m	C _p	C _o	C _m %
Center	100 mm	0.0038	0.0061	0.0014	51
Center	200 mm	0.0020	0.0061	0.0014	13
Center	300 mm	0.0042	0.0061	0.0014	60
Center	400 mm	0.0032	0.0061	0.0014	38
Center	500 mm	0.0018	0.0061	0.0014	9
Side 1	100 mm	0.0016	0.0061	0.0014	4
Side 1	200 mm	0.0017	0.0061	0.0014	6
Side 1	300 mm	0.0018	0.0061	0.0014	9
Side 1	400 mm	0.0022	0.0061	0.0014	17
Side 1	500 mm	0.0033	0.0061	0.0014	40
Side 2	100 mm	0.0013	0.0061	0.0014	< 0
Side 2	200 mm	0.0016	0.0061	0.0014	4
Side 2	400 mm	0.0022	0.0061	0.0014	17

Table B.2: Measured titanium concentration in experiment *TiB-22*.

Position	Distance	C _m	C _p	C _o	C _m %
Center	100 mm	0.0042	0.0060	0.0014	61
Center	200 mm	0.0018	0.0060	0.0014	9
Center	300 mm	0.004	0.0060	0.0014	57
Center	400 mm	0.0036	0.0060	0.0014	48
Center	500 mm	0.0017	0.0060	0.0014	6
Side 1	100 mm	0.0011	0.0060	0.0014	< 0
Side 1	200 mm	0.0015	0.0060	0.0014	2
Side 1	300 mm	0.0020	0.0060	0.0014	13
Side 1	400 mm	0.0021	0.0060	0.0014	15
Side 1	500 mm	0.0032	0.0060	0.0014	7
Side 2	100 mm	0.0015	0.0060	0.0014	2
Side 2	200 mm	0.0013	0.0060	0.0014	< 0
Side 2	400 mm	0.0025	0.0060	0.0014	24

Table B.3: Measured titanium concentration in experiment *TiB-23*.

Position	Distance	C _m	C _p	C _o	C _m %
Center	100 mm	0.0036	0.0054	0.0014	53
Center	200 mm	0.0021	0.0054	0.0014	18
Center	300 mm	0.0033	0.0054	0.0014	48
Center	400 mm	0.0034	0.0054	0.0014	50
Center	500 mm	0.0015	0.0054	0.0014	3
Side 1	100 mm	0.0014	0.0054	0.0014	0
Side 1	200 mm	0.0018	0.0054	0.0014	10
Side 1	300 mm	0.0021	0.0054	0.0014	18
Side 1	400 mm	0.0018	0.0054	0.0014	10
Side 1	500 mm	0.0032	0.0054	0.0014	45
Side 2	100 mm	0.0014	0.0054	0.0014	0
Side 2	200 mm	0.0015	0.0054	0.0014	3
Side 2	400 mm	0.0020	0.0054	0.0014	15

Table B.4: Measured titanium concentration in experiment *TiB-24*.

Position	Distance	C _m	C _p	C _o	C _m %
Center	100 mm	0.0016	0.0034	0.0014	10
Center	200 mm	0.0020	0.0034	0.0014	30
Center	300 mm	0.0020	0.0034	0.0014	30
Center	400 mm	0.0019	0.0034	0.0014	25
Center	500 mm	0.0022	0.0034	0.0014	40
Side 1	100 mm	0.0017	0.0034	0.0014	15
Side 1	200 mm	0.0013	0.0034	0.0014	< 0
Side 1	300 mm	0.0016	0.0034	0.0014	10
Side 1	400 mm	0.0014	0.0034	0.0014	0
Side 1	500 mm	0.0018	0.0034	0.0014	20
Side 2	100 mm	0.0014	0.0034	0.0014	0
Side 2	200 mm	0.0013	0.0034	0.0014	< 0
Side 2	400 mm	0.0016	0.0034	0.0014	10

Table B.5: Measured titanium concentration in experiment *TiB-25*.

Position	Distance	C _m	C _p	C _o	C _m %
Center	100 mm	0.0017	0.0049	0.0014	9
Center	200 mm	0.0025	0.0049	0.0014	31
Center	300 mm	0.0021	0.0049	0.0014	20
Center	400 mm	0.0023	0.0049	0.0014	26
Center	500 mm	0.0029	0.0049	0.0014	43
Side 1	100 mm	0.0019	0.0049	0.0014	14
Side 1	200 mm	0.0013	0.0049	0.0014	< 0
Side 1	300 mm	0.0018	0.0049	0.0014	11
Side 1	400 mm	0.0011	0.0049	0.0014	< 0
Side 1	500 mm	0.0022	0.0049	0.0014	23
Side 2	100 mm	0.0015	0.0049	0.0014	3
Side 2	200 mm	0.0014	0.0049	0.0014	0
Side 2	400 mm	0.0017	0.0049	0.0014	9

Nomenclature

Symbol	Meaning	SI Units
A_1, A_2	Constants	
C	Computed velocity	m/s^{-1}
C_D	Drag factor	
C_i	Constants in turbulence model	
C_m	Measured concentration	
C_o	Inlet concentration	
C_p	Outlet concentration	
d	Diameter	m
D	Diameter	m
f	Frequency	Hz
f	Volume fraction	
F	Force	N
F_D	Force of drag	N
F_P	Pressure gradient force	N
F_B	Buoyancy force	N
F_A	Added mass force	N
F_R	Rotational force	N
g	Gravity	ms^{-2}
G	Viscous stress generation	
I	Electric current flow rate	A
k	Turbulent kinetic energy	m^2s^{-2}
k_1, k_2	Constants	
N_{20}	Count of particles larger than $20\mu m$ presented as thousands per kilo of melt [K/Kg]	
$N_{20-25\mu m}$	Count of 20-25 μm particles [K/Kg]	
$\dot{N}_{20-25\mu m}$	Normalized count of 20-25 μm particles	
l_E	Eddy length	m
L	Length	m
m	Mass	kg
R	Electical resistance	Ω

Symbol	Meaning	SI Units
Re	Reynolds number	
S	Size of a sample	
St	Strouhal number	
t	Time	sec
t_E	Eddy lifetime	sec
u	Velocity	
V	Volume	m^3
V	Voltage	V
x_i	Cartesian coordinates	
\mathbf{x}	Position vector	

Greek Characters

Symbol	Meaning	SI Units
β	Density of particle population	
$\dot{\epsilon}$	Turbulence dissipation rate	$m^2 s^{-3}$
μ	Dynamic viscosity	Nms^{-1}
μ	Mean of distribution	
μ_t	Turbulence viscosity	Nms^{-1}
μ_{eff}	Effective viscosity	Nms^{-1}
ξ	Computational position	
ρ	Density	kg/m^{-3}
ρ	Electrical resistivity of molten aluminium ($25 \times 10^{-8} \Omega m$)	
σ	Standard deviation	
$\sigma_k, \sigma_\epsilon$	Constants in $k - \dot{\epsilon}$ model	

Master alloys

Symbol	Meaning
$B3/0.2-A$	Al-3Ti-0.2B master alloy from producer A
$B3/0.2-B$	Al-3Ti-0.2B master alloy from producer B
$B5/1-A$	Al-5Ti-1B master alloy from producer A
$B5/1-B$	Al-5Ti-1B master alloy from producer B
$B5/1-C$	Al-5Ti-1B master alloy from producer C
$B5/1-D$	Al-5Ti-1B master alloy from producer D
$C3/0.15-A$	Al-3Ti-0.15C master alloy from producer A
$C3/0.15-B$	Al-3Ti-0.15C master alloy from producer B

Publications and lectures

Publications

Asbjornsson E.J., McCartney G.M., Sigfusson T.I., Bristow D. and Gudmundsson T., *Studies on the dissolution of Al-Ti-C master alloy using LiMCA*, Light Metals, Editor: Dr. Eckert C.E., California, pages 705-710, 1999.

Asbjornsson E.J., Sigfusson T.I. and Gudmundsson T., *Dreifing endurkristollunaragna i albrad (Distribution of Grain Refiner Particles in Aluminium Melt)*, Physics in Iceland IX, Annual conference of the Icelandic Physics Society, Editor: Olafsson A., Reykjavik, pages 153-161, 1999.

Asbjornsson E.J., Dispersion of Grain Refiner Particles in Molten Aluminium, Technical Reports 1-6, Nottingham, 1996-1999.

Lectures

Titanium boron in molten aluminium, Lecture for the technical staff at ISAL aluminium casthouse, March, 1998.

Dissolution of grain refiners, Alusuisse Casthouse Workshop, Alusuisse Singen, Germany, 5-6 October, 1998.

List of Tables

2.1	A comparison between aluminium metals from a Hall-Heroult electrolytic cells and three-layer electrolysis with respect to impurities [2].	8
2.2	A list of detectable inclusions in molten aluminium. Size is in μm	16
2.3	Comparison of the LiMCA and PoDFA techniques [46]	23
2.4	Properties of molten aluminium and steel in launders.	26
3.1	Classes and main types of master alloys.	42
3.2	Chemical analysis of the Al-6Ti master alloy.	44
3.3	Chemical analysis of the Al-5Ti-1B master alloys.	45
3.4	Analysis of the microstructure of the Al-5Ti-1B master alloys.	46
3.5	Chemical analysis of the Al-3Ti-0.2B master alloys.	47
3.6	Chemical analysis of the Al-3Ti-0.15C master alloys.	48
3.7	Chemical analysis of the Al-6Ti-0.03C master alloy.	49
4.1	List of the experiments.	78
4.2	A comparison of the percentage of TiC particles detected after the first step response and 30 minutes after the additions for the Al-Ti-C master alloys.	88
4.3	The increase in the particle count produced by the step response after the first addition.	94
4.4	A comparison of the detected volume of TiB_2 and TiC particles after the first step response for the Al-5Ti-1B and Al-3Ti-0.15C master alloys. The additions correspond to 0.035% increase in titanium.	99
5.1	Constants used in the $k - \epsilon$ model.	132
6.1	List of the experiments showing the titanium addition and titanium concentration achieved.	165
6.2	Titanium distribution into TiB_2 and $TiAl_3$ in the master alloys.	165
6.3	Chemical analysis of the base metal in experiments $TiB-21$ to $TiB-27$. The balance is aluminium.	167
6.4	PoDFA analysis at the inlet and outlet of the launder. The experiments are the same as for the LiMCA tests, $TiB-23$ to $TiB-26$. The samples were taken at the end of each experimental run.	169

A.1	Chemical analysis of the base metal in the experiments presented in Chapter 4 before addition of the master alloy portions. The balance can be considered to be aluminium.	191
A.2	The additions in experiments <i>Ti-1</i> and <i>Ti-2</i> . Grain refiner Al-6Ti.	192
A.3	The additions in experiments <i>TiC-1</i> and <i>TiC-2</i> . Grain refiner Al-6Ti-0.03C.	192
A.4	The additions in experiments <i>TiC-3</i> , <i>TiC-4</i> and <i>TiC-5</i> . Grain refiner Al-3Ti-0.15C.	193
A.5	Chemical analysis of each melt in experiments <i>TiB-1</i> to <i>TiB-10</i> after the last addition of the Al-Ti-B master alloy portions. The balance is aluminium.	193
A.6	The additions in experiments <i>TiB-1</i> , <i>TiB-2</i> and <i>TiB-3</i> . Grain refiner Al-5Ti-1B.	193
A.7	The additions in experiments <i>TiB-4</i> , <i>TiB-5</i> , <i>TiB-6</i> and <i>TiB-7</i> . Grain refiner Al-5Ti-1B.	194
A.8	The additions in experiments <i>TiB-8</i> , <i>TiB-9</i> and <i>TiB-10</i> . Grain refiner Al-5Ti-1B.	194
A.9	The additions in experiments <i>TiB-11</i> . Grain refiner Al-3Ti-0.2B.	195
B.1	Measured titanium concentration in experiment <i>TiB-21</i>	196
B.2	Measured titanium concentration in experiment <i>TiB-22</i>	197
B.3	Measured titanium concentration in experiment <i>TiB-23</i>	197
B.4	Measured titanium concentration in experiment <i>TiB-24</i>	198
B.5	Measured titanium concentration in experiment <i>TiB-25</i>	198

List of Figures

2.1	The Hall-Heroult reduction cell [1].	29
2.2	Casthouse layout.	29
2.3	An overview of the aluminium manufacturing process [60].	30
2.4	Relation between hydrogen content and porosity for sand-cast bars, 25mm diameter, of aluminium and aluminium alloys. [2]	31
2.5	A cross-section of an ingot showing a typical fir-tree structure. Etched in 10% NaOH at 70°C for 20 minutes. [2]	31
2.6	Sectional view of a staged ceramic foam filter. [7]	32
2.7	Cylindrical filter unit containing a gas-lift pump. The melt levels and flow pattern are indicated. [8]	32
2.8	Portions of tranverse sections through two ingots of alloy 6061 that were direct chill semicontinuous cast. (a) Ingot cast without a grain refiner. (b) Ingot showing fine equiaxed grain structure that was cast with a grain refiner [2].	33
2.9	(a) The Al-Ti phase diagram [16]. (b) The aluminium rich end of the phase diagram	33
2.10	Scematic view of a hexagonal TiB_2 particle [25].	34
2.11	Cluster of TiB_2 particles in a Al-5Ti-1B master alloy denoted as $B5/1-B$ in the present study.	34
2.12	Size distribution of TiB_2 particles chemically extracted from an Al-5Ti-1B master alloy [26].	35
2.13	Scematic view of an octahedral TiC particle [19].	35
2.14	Cross-section of a PoDFA filter showing TiB_2 particles. The magnification is 200X.	36
2.15	Pouring of a PoDFA sample.	36
2.16	(a) Schematic of LiMCA operation. (b) Resistive pulse principle for the particle size measurement.	37
2.17	Diameter of the spherical particle as a function of the voltage variations.	37
2.18	Reproducibility of LiMCA with constant sample size of 17.5 g. The solid line is the overall reproducibility, the dashed line is the statistical reproducibility and the dashed-dotted line is the instrumental reproducibility.	38
2.19	Reproducibility of LiMCA with constant inclusion count. Dashed line 2×10^3 inclusions per kilogram (2 K/Kg) and solid 1×10^3 inclusions per kilogram (1 K/Kg).	38

2.20	Effect of settling on the inclusions concentration measured by LiMCA at the exit of a tilting furnace [47].	39
2.21	Effect of settling on the inclusions concentration measured by LiMCA in the launder of a manufacturing casthouse. Prior settling time 60 minutes. Grain refiner Al-5-Ti-1B.	39
2.22	Effect of settling on the inclusions concentration measured by LiMCA in the launder of a manufacturing casthouse. Prior settling time 60 minutes. Grain refiner Al-5-Ti-1B.	40
2.23	Estimated velocity profile for turbulent flow in the vicinity of a solid surface.	40
2.24	Computed velocity vectors in the vicinity of the bend for the original tundish at (a) free surface ($z/D=3.2$), (b) $z/D=2.4$, and (c) $z/D=1.6$ [57].	41
3.1	Typical design of a scanning electron microscope (SEM) for secondary electron imaging [62].	52
3.2	Types of electron-beam-excited electrons and radiation used in a SEM and the depth of the region below the specimen surface from which information is obtained [62].	52
3.3	Polished surfaces of the Al-6Ti master alloy. Magnification 50x and 200x. The grey particles are $TiAl_3$ and the dark spots are impurities.	53
3.4	TiB_2 cluster in the B5/1-B master alloy. EDX spectra of spots A, B and C, are shown in Figures 3.5, 3.6 and 3.7.	54
3.5	The EDX spectrum of spot A in Figure 3.4. The unmarked large peak between Al and K is 2xAl peak.	54
3.6	The EDX spectrum of spot B in Figure 3.4. The unmarked peak between Al and K is 2xAl.	55
3.7	The EDX spectrum of spot C in Figure 3.4.	55
3.8	TiB_2 cluster in the B5/1-A master alloy marked "A". EDX spectra of spots A and B which is in the α -phase, are shown in Figures 3.9 and 3.10.	56
3.9	The EDX spectrum of spot A in Figure 3.8. The unmarked peak between Al and K is 2xAl.	56
3.10	The EDX spectrum of spot B in Figure 3.8. The unmarked peak between Al and K is 2xAl.	57
3.11	Polished surfaces of the B5/1-A master alloy. Magnification 50x and 200x. The large particles are $TiAl_3$ and the small particles are TiB_2 . The dark spots are inclusions containing aluminium oxide and fluoride salts.	58
3.12	Polished surfaces of the B5/1-B master alloy. Magnification 50x and 200x. The large particles are $TiAl_3$ and the small particles are TiB_2 . The dark spots are inclusions containing aluminium oxide and fluoride salts.	59

3.13 Polished surfaces of the <i>B5/1-C</i> master alloy. Magnification 50x and 200x. The large particles are $TiAl_3$ and the small particles are TiB_2 . The dark spots are inclusions containing aluminium oxide and fluoride salts.	60
3.14 Polished surfaces of the <i>B5/1-D</i> master alloy. Magnification 50x and 200x. The large particles are $TiAl_3$ and the small particles are TiB_2 . The dark spots are inclusions containing aluminium oxide and fluoride salts.	61
3.15 Backscatter view of polished sample of the <i>B5/1-A</i> master alloy. EDX spectrum of the inclusion marked with an A is shown in Figure 3.16. The large blocky particle is $TiAl_3$ and the small white particles are TiB_2	62
3.16 The EDX spectrum of spot A in Figure 3.15.	62
3.17 Backscatter view of polished sample of the <i>B5/1-A</i> master alloy. EDX spectrum of the inclusion marked with an A is shown in Figure 3.18. The large blocky particles are $TiAl_3$ and the small white particles are TiB_2	63
3.18 The EDX spectrum of spot A in Figure 3.17.	63
3.19 Polished surfaces of the <i>B3/.2-A</i> master alloy. Magnification 50x and 200x. The large particles are $TiAl_3$ and the small particles are TiB_2 . The dark spots are inclusions containing aluminium oxide and fluoride salts.	64
3.20 TiC cluster in the <i>C9/.15-B</i> rod marked "A". EDX spectra of spots A and B which is in the α -phase, are shown in Figures 3.21 and 3.22.	65
3.21 The EDX spectrum of spot A in Figure 3.20.	65
3.22 The EDX spectrum of spot B in Figure 3.20.	66
3.23 TiC cluster in the <i>C9/.15-A</i> rod marked "A". EDX spectra of spots A and B which is in the α -phase, are shown in Figures 3.24 and 3.25.	66
3.24 The EDX spectrum of spot A in Figure 3.23.	67
3.25 The EDX spectrum of spot B in Figure 3.23.	67
3.26 TiC particle cluster in <i>C9/.15-A</i> . The size of the cluster is $10 \times 20 \mu m$. EDX spectra of spots 1, 2 and 3, are shown in Figures 3.27, 3.28 and 3.29.	68
3.27 EDX spectrum of spot 1 in Figure 3.26.	68
3.28 EDX spectrum of spot 2 in Figure 3.26.	69
3.29 EDX spectrum of spot 3 in Figure 3.26.	69
3.30 Backscatter image of TiC particle clusters in <i>C9/.15-A</i> . The large block particles are $TiAl_3$. Two groups of TiC are seen, one long and narrow at the top and one $90 \times 50 \mu m$ in the middle. EDX spectra of spots A, B and C, are shown in Figures 3.32, 3.33 and 3.34.	70
3.31 EDX spectrum of the whole surface in Figure 3.30. A significant level of oxygen is observed. The unmarked peak between Al and Ti is $2xAl$	70

3.32	EDX spectrum of spot A in Figure 3.30. A significant level of oxygen is observed.	71
3.33	EDX spectrum of spot B in Figure 3.30. A significant level of oxygen is observed.	71
3.34	EDX spectrum of spot C in Figure 3.30. A significant level of oxygen is observed. The unmarked peak between Al and Ti is $2xAl$	72
3.35	Polished surface of the C9/.15-A master alloy. The large particles are $TiAl_3$ and the small ones are TiC . The dark streaks and spots are oxides.	73
3.36	Polished surface of the C9/.15-B master alloy. The large particles are $TiAl_3$ and the small ones are TiC . The dark spots are oxides.	74
3.37	Polished surface of Al-6Ti-0.03C master alloy. The large particles are $TiAl_3$ and the the dark spots are oxides. No TiC particles can be distinguished.	75
4.1	The experimental setup. The upper diameter of the crucible was 200mm and the depth of the melt was approximately 200mm. The width of the impeller head was 80mm and it was positioned approximately 150mm below the surface. The depth of the LiMCA probe was approximately 80mm.	104
4.2	The flow profiles in a rectangular crucible [63], with rotor offset from centre.	104
4.3	The experimental setup in operation. The impeller shaft is entering the melt on the left and the LiMCA head on the right.	105
4.4	The experimental setup in operation, focusing on the LiMCA head entering the melt.	105
4.5	Metal sucking device.	106
4.6	The particle count in experiment Ti-1. Grain refiner Al-6Ti. Each addition point is labelled with the number of the addition. The additions are shown in Table A.2.	106
4.7	The particle count in experiment Ti-2. Grain refiner Al-6Ti. Each addition point is labelled with the number of the addition. The additions are shown in Table A.2.	107
4.8	Cross-section of a sample taken with a metal sucking device, fifteen minutes after experiment Ti-1. The large grey blocky particles are $TiAl_3$. Magnification 200X.	107
4.9	Cross-section of a sample taken from the LiMCA probe after experiment Ti-2. The large grey blocky particles are $TiAl_3$. Magnification 200X.	108
4.10	The EDX spectrum of the large particle in Figure 4.9.	108
4.11	The EDX spectrum of the α -phase of the base metal in Figure 4.9. The unmarked peak between Al and Ti is $2xAl$	109
4.12	The Stokes settling rate for spherical particles in a stagnant aluminium bath.	109

- 4.13 The particle count (N_{20} = Particles larger than $20\mu\text{m}$) in experiment *TiC-1*. Grain refiner Al-6Ti-0.03C. The additions are shown in Table A.3 110
- 4.14 The particle count (N_{20}) in experiment *TiC-2*. Grain refiner Al-6Ti-0.03C. The additions are shown in Table A.3 110
- 4.15 The normalized size distribution in experiment *TiC-1*, one, ten and twenty minutes after the addition, respectively. 111
- 4.16 The particle count per kg of the Al-6Ti-0.03C master alloy in experiment *TiC-1* one minute after the addition of the master alloy. 111
- 4.17 The particle count (N_{20}) in experiment *TiC-3*. Grain refiner Al-3Ti-0.15C. The master alloy is of type *C3/.15-A*. The additions are shown in Table A.4 112
- 4.18 The inclusion count (N_{20}) in experiment *TiC-4* and *TiC-5* Grain refiner Al-3Ti-0.15C. The additions are shown in Table A.4 . . . 112
- 4.19 A *TiC* cluster in fractured sample from the LiMCA tube taken at the end of experiment *TiC-3*. The sample is unpolished. EDX spectra at points A, B and C are shown in the following figures. . 113
- 4.20 EDX spectrum at point B in the *TiC* particle cluster shown in Figure 4.19. 113
- 4.21 EDX spectrum at point C in the *TiC* particle cluster shown in Figure 4.19. 114
- 4.22 EDX spectrum at point A outside the *TiC* particle cluster shown in Figure 4.19. 114
- 4.23 The volume of the detected particles shown in Figure 4.18. . . . 115
- 4.24 The normalized size distribution for the master alloy *C3/.15-A* in experiment *TiC-4*, calculated one, ten and twenty minutes after the additions shown in Figure 4.18 115
- 4.25 The normalized size distribution for the master alloy *C3/.15-B* in experiment *TiC-5*, calculated one, ten and twenty minutes after the additions shown in Figure 4.18 116
- 4.26 The particle count (N_{20}) with two small additions in the beginning of the measurements (solid line, experiment *TiB-1*) and two series with high titanium content added in the beginning (dashed lines, experiments *TiB-2* and *TiB-3*). The master alloy was *B5/1-B*. The additions are shown in Table A.6. 116
- 4.27 The particle count from experiments *TiB-4* to *TiB-7*, the additions give 0.035 wt% Ti at minutes 20, 40, 60, 80 and 100. The additions are shown in Table A.7. 117
- 4.28 The particle count from experiments *TiB-8* to *TiB-10*, the additions give 0.04 wt% Ti at minutes 20, 40, 60, 80 and 100. The rotor speed is 40 RPM. The additions are shown in Table A.8. . . 118
- 4.29 The particle count (N_{20}) from Figure 4.28 showing only the first addition. 118
- 4.30 A *TiB₂* cluster in fractured sample from the LiMCA tube taken at the end of experiment *TiB-4*. The sample is unpolished. EDX spectra at points A, B and C are shown in the following figures. . 119

4.31	EDX spectrum at spot A in the TiB_2 particle cluster shown in Figure 4.30. The peak in the spectrum overlapping the symbol O is a low energy titanium peak ($L\alpha$).	119
4.32	EDX spectrum at spot B in the TiB_2 particle cluster shown in Figure 4.30.	120
4.33	EDX spectrum at spot C inside the TiB_2 particle cluster shown in Figure 4.30.	120
4.34	The average size distribution for each master alloy after the first addition in Figure 4.29.	121
4.35	The normalized size distribution of detected particles for each master alloy after the first addition shown on Figure 4.29.	121
4.36	The volume of particles as a function of diameter, ranging from 20-150 μ m.	122
4.37	The estimated volume of TiB_2 particles detected in experiment $TiB-1$, shown in Figure 4.26.	122
4.38	The estimated volume of TiB_2 particles detected in the experiments $TiB-2$ and $TiB-3$, shown in Figure 4.26.	123
4.39	The percentage of total volume of TiB_2 particles added to the melt which are detected with LiMCA in the experiments shown in Figure 4.28.	123
4.40	The percentage of total volume of TiB_2 particles added to the melt which are detected with LiMCA in the experiments shown in Figure 4.27.	124
4.41	The particle count (N20) in experiment $TiB-11$. Grain refiner Al-3Ti-0.2B. The additions are shown in Table A.9	125
4.42	The size distribution from experiment $TiB-1$ at different times.	125
4.43	The normalised size distribution from experiment $TiB-1$ at different times.	126
4.44	The normalised size distribution from experiment $TiB-1$ at different times focusing on the particle size range 70 – 120 μ m.	126
4.45	The percentage of particles larger than 110 μ m at different times in experiment $TiB-1$	127
4.46	The slopes from linear fitting of each size interval at different time intervals from experiment $TiB-1$	127
4.47	The slopes from linear fitting of each size interval at different time intervals from experiment $TiB-3$	128
4.48	The average diameter of detected particles and the particle count in experiment $TiB-1$	128
4.49	The average diameter of detected particles and the particle count in experiment $TiB-3$	129
5.1	Outlines of the launder as seen in CFX.	143
5.2	Mesh of the corner of the old launder as seen in CFX	143
5.3	Definition of planes in the old launder system. Planes 6 and 7 are 30 and 60mm below the surface respectively.	144
5.4	The nodes in plane 4 shown on Figure 5.3.	144

5.5	The absolute residual source sum for the momentum and mass in the model for the first launder.	145
5.6	Velocity in plane 1. The color code is such that the yellow color defines the interval between 4.8×10^{-2} and 6.0×10^{-2} . Units are in <i>m/s</i>	145
5.7	Velocity profile of plane 1, where maximum speed is obtained. D is the half length of this plane and x is the position in that direction.	146
5.8	Velocity in plane 2, looking in the direction of flow. Units are in <i>m/s</i>	146
5.9	Velocity in plane 3, looking in the direction of flow. Units are in <i>m/s</i>	147
5.10	Velocity in plane 4, looking in the direction of flow. Units are in <i>m/s</i>	147
5.11	Velocity at the outlet of the launder, i.e. plane 5. Units are in <i>m/s</i>	148
5.12	Velocity at the outlet of the launder, i.e. plane 5. Units are in <i>m/s</i>	148
5.13	Velocity profile in the outlet pipe.	149
5.14	Velocity in the corner 30mm below the surface, i.e. plane 6. Units are in <i>m/s</i>	149
5.15	Velocity in the corner 30mm below the surface, i.e. plane 6. Units are in <i>m/s</i>	150
5.16	Turbulent kinetic energy in the corner 30mm below the surface, i.e. plane 6. Units are in m^2/s^2	150
5.17	Velocity in the corner 60mm below the surface, i.e. plane 7. Units are in <i>m/s</i>	151
5.18	Full model outline of the new launder system.	151
5.19	The nodes in plane in the straight inlet part of the second launder.	152
5.20	Cross-section of the new launder model. Planes $y=0.03$ and $y=0$ are 30mm and 60mm below the surface respectively.	152
5.21	Velocity in the first corner of the launder, plane $y=0$, 60mm below the surface.	153
5.22	Velocity in the first corner of the launder, plane $y=0$, 60mm below the surface.	153
5.23	Velocity in the first corner of the launder, plane $y=0.03$, 30mm below the surface.	154
5.24	Velocity in the first corner of the launder, plane $y=0.03$, 30mm below the surface.	154
5.25	Velocity in the second corner of the launder, plane $y=0$, 60mm below the surface.	155
5.26	Velocity in the second corner of the launder, plane $y=0$, 60mm below the surface.	155
5.27	Velocity in the second corner of the launder, plane $y=0.03$, 30mm below the surface.	156
5.28	Velocity in the second corner of the launder, plane $y=0.03$, 30mm below the surface.	156
5.29	Velocity in the cross-section of the launder with undisturbed flow.	157

5.30	Particle tracks at the corner, seen from top. The color of the lines shows the size of the particles. Red is $7.75\mu\text{m}$ and green is $3.25\mu\text{m}$. The time limit is 250 sec.	157
5.31	Particle tracks near the outlet, seen from the side. The color of the lines shows the size of the particles. Red is $7.75\mu\text{m}$ and green is $3.25\mu\text{m}$. The time limit is 250 sec.	158
5.32	The paths of $5\mu\text{m}$ particles in straight launder in 30 seconds. The color of the lines denotes the velocity of the particles. Red is the highest velocity, approximately $7.3 \times 10^{-2}\text{m/s}$	158
5.33	The paths of $10\mu\text{m}$ particles in straight launder in 30 seconds. The color of the lines denotes the velocity of the particles. Red is the highest velocity, approximately $7.3 \times 10^{-2}\text{m/s}$	159
5.34	Particles flowing in the new launder, 5, 10 and 15 seconds after the addition. Particle diameter $2\mu\text{m}$. Distance between vertical lines is 500mm.	159
5.35	Particles flowing in the new launder, 5, 10 and 15 seconds after the addition. Particle diameter $2\mu\text{m}$	160
5.36	The percentage of $2\mu\text{m}$ particle which crash into the wall as a function of time.	161
5.37	Formation of a vortex behind a cylinder [51].	161
5.38	The effect of Reynolds number on the flow past a cylinder. [After Homann (1936)] [51].	162
5.39	Measured Strouhal number for vortex shedding frequency behind a circular cylinder [51].	162
6.1	The addition point of the grain refiner rod into the transfer launder.	173
6.2	Measurement points for the chemical analysis. The samples are taken at the surface. The grain refiner is continuously added at the point of insertion.	173
6.3	Measurement points for the chemical analysis. The samples are always taken at the surface.	174
6.4	The average titanium concentration increment for the Al-5Ti-1B grain refiners at each sampling point in the launder. The solid line represents the middle of the launder and the dashed lines show the sides. The distance is measured from the master alloy addition point.	174
6.5	The average titanium concentration increment for the Al-3Ti-0.2B grain refiner at each sampling point in the launder. The solid line represents the middle of the launder and the dashed lines show the sides. The distance is measured from the master alloy addition point.	175
6.6	The LiMCA device measuring at the corner of the first launder. .	176
6.7	Measurement points for LiMCA. One sample for chemical analysis was taken in the corner at the right.	176
6.8	Particle count (N20) for experiment <i>TiB-23</i> . Grain refiner <i>B5/1-D</i> . The numbers refer to measurement position.	177

6.9	Size distribution for experiment <i>TiB-23</i> . Grain refiner <i>B5/1-D</i> . Measurement positions 1, 5, 8 and 3. The size is in μm	177
6.10	Particle count (N20) for experiment <i>TiB-24</i> . Grain refiner <i>B3/.2-A</i> . A. The numbers refer to measurement position.	178
6.11	Size distribution for experiment <i>TiB-24</i> . Grain refiner <i>B3/.2-A</i> . Measurement positions 1, 5, 8 and 3. The size is in μm	178
6.12	Particle count (N20) for experiment <i>TiB-25</i> . Grain refiner <i>B3/.2-A</i> . A. The numbers refer to measurement position.	179
6.13	Size distribution for experiment <i>TiB-25</i> . Grain refiner <i>B3/.2-A</i> . Measurement positions 1, 5, 8 and 3. The size is in μm	179
6.14	Particle count (N20) for experiment <i>TiB-26</i> . Grain refiner <i>B5/1-B</i> . B. The numbers refer to measurement position.	180
6.15	Size distribution for experiment <i>TiB-26</i> . Grain refiner <i>B5/1-B</i> . Measurement positions 1, 5, 8 and 3. The size is in μm	180